Measurements of the Structure of Turbulent Premixed and Stratified Methane/Air Flames

M. S. Sweeney

Magdalene College
University of Cambridge

A dissertation submitted to the University of Cambridge
for the degree of Doctor of Philosophy

May 2011

Measurements of the Structure of Turbulent Premixed and Stratified Methane/Air Flames

M. S. Sweeney

The influence of stratification on the structure of turbulent methane/air combustion is investigated using experimental data from laboratory scale burners: a weakly turbulent slot burner, and a higher turbulence co-annular swirl burner. The degree of stratification can be controlled independently of the overall fuel/air flow rate. The resulting measurements of scalar and velocity fields provide detailed test cases for existing and emerging turbulent flame models, covering a range of u'/S_L from 1 to 10, turbulence intensities from 5 to 60 %, and stratification ratios from 1 to 3.

Simultaneous Rayleigh/Raman/CO-LIF measurements of temperature and major species concentrations — CH_4, CO_2, CO, H_2, H_2O and O_2 — along a line are used to investigate the structure of a series of flames in both the slot and swirl burners. Concurrent cross-planar OH-PLIF allows thermal gradients to be angle corrected to their three-dimensional values. Finally, non-reacting and reacting velocity fields complete the flame database.

The behavior of major species concentrations in the slot and swirl burner with respect to temperature is found to agree well on the mean with unstrained premixed laminar flame calculations. Scalar means conditioned on stoichiometry also show good agreement, aside from hydrogen which is enhanced under stratified conditions. Surface density function and scalar dissipation are lower than calculated values in all cases, suggesting that turbulence-induced thickening dominates the effect of increased strain.

Metrics commonly used to derive flame surface density (FSD) were investigated. FSD may be determined using a statistical method based on measurements of temperature and its gradient, or a geometric method based on 2D temperature or LIF imaging. A third metric, an extension of the geometric method, is proposed. Good agreement is observed between the three metrics.

The current database provides the first detailed high resolution scalar measurements for premixed and stratified flames. The data analysis provides insight into the physics of stratification: for the flames considered, the effects of stratification appear to be surprisingly small compared to those of turbulence, even at significant stratification ratios. The datasets provide a means of validating current and future computational turbulent combustion models.

Declaration

This dissertation is the result of my own work and includes nothing which is the outcome of work done in collaboration except where specifically indicated in the text. It has not been submitted for another qualification to this or any other university. The full length of this thesis is 51 926 words and includes 89 figures.

M. S. Sweeney
October 12, 2011

Keywords: Turbulent Combustion, Stratified Combustion, Premixed Combustion, Laser Diagnostics, OH-PLIF, Flame Surface Density, V-Flame, Swirl, Methane/Air, Curvature, Equivalence Ratio, PIV.

Acknowledgements

I would like to thank Professor Simone Hochgreb, my supervisor, for taking a chance on someone without any prior exposure to the field of combustion, and for carefully curating my project from inception to finish. She has been patient when I have been confused, supportive when I have been lost, and congratulatory when I have succeeded!

I would also like to acknowledge the contribution of Dr. Robert Barlow of Sandia National Laboratories, USA. In addition to enabling me to take detailed multi-scalar measurements of the highest caliber at his laboratory[a], he has been a constant source of wisdom on aspects of research both experimental and theoretical. Similar gratitude is owed to Bob Harmon, Rob's technologist, and Matt Dunn, his current post-doc, and Guanghua Wang, his previous post-doc.

I thank the Department of Engineering, EPSRC and Rolls Royce for their financial contributions to this work, the Leverhulme Trust for an International Network Grant, and Magdalene College for keeping a roof over my head. Without the help of these institutions I could never have remained in higher education, nor traveled the world to demonstrate my research.

Thanks is also due to everyone in the Heat Gallery for providing both education and entertainment, often in equal measure; Chong, Hemanth, Inkyu, Isil, James, Jim, Ray, Isil. To Tristan, thank you for pointing me towards this project, putting in a good word for me with Simone, and being good banter throughout.

Above all else I'd like to thank Oli for always being there for me, both as a colleague and as a friend. The experiences we have shared over the past few years, from turbulence to tea-breaks, are among my fondest memories of Cambridge.

---

[a] Work at Sandia was supported by the United States Department of Energy, Office of Basic Energy Sciences, Division of Chemical Sciences, Geosciences and Biosciences. Sandia National Laboratories is a multiprogram laboratory operated by Sandia Corporation, a Lockheed Martin Company, for the United States Department of Energy under contract DE-AC04-94-AL85000.

To Jim Scott, who always wanted to be an engineer

Contents

Nomenclature

The page number indicates the first mention of each symbol/acronym. All units are SI unless stated otherwise.

Roman Symbols

A_e	Exit area	124
c	Progress variable	9
c_OH	OH progress variable	58
Da	Damköhler number	86
F	Finite difference coefficient	75
h	Enthalpy	9
$\mathbf{i}$, $\mathbf{j}$ and $\mathbf{k}$	Orthogonal coordinate system	54
I	Signal intensity	57
I	Turbulence intensity	124
Ka	Karlovitz number	86
L	Length scale	124
L_turb	Turbulent length scale	11
$\mathbf{n}$	Flame normal vector	53
$\lvert\nabla c\rvert$	Progress variable gradient, surface density function	63
P	Probability density function	63
P_w	Wetted perimeter	124
R	Radius	122
r	Radal location in swirl burner	42
Re	Reynolds number	124
s	Distance along the flame front	56
S_L	Laminar flame speed	11
$\mathbf{t}$	Flame tangent	53

T	Temperature	7
U	Mean velocity	23
u'	Velocity fluctuation	11
u'/S_{L}	Turbulence intensity	11
$\overline{U}$	Mean absolute velocity	115
$\mathbf{x}$	Line measurement axis	54
x	Distance from centreline in slot burner	42
Y	Mass fraction	7
Z	Mixture fraction	18
z	Axial location in slot burner and swirl burner	42

Greek Symbols

α	Thermal diffusivity	77
χ_c	Scalar dissipation rate	77
Δ	Full width half maximum	139
δ	Flame thickness	11
δ_{t}	Turbulent flame thickness	188
η_{K}	Kolmogorov length scale	124
κ_{d}	Discrete two-dimensional local curvature	56
κ_{c}	Continuous two-dimensional local curvature	57
∇	Gradient	63
ν_{K}	Kolmogorov velocity scale	124
Ω	Inter-plane angle	54
ϕ	Equivalence ratio	14
ψ	Arbitrary scalar	75
$\underline{\phi}$	Lookup table corrected equivalence ratio	66
Φ	Linear bridged equivalence ratio	69
τ_{K}	Kolmogorov time scale	124
θ	Solid angle between line measurement axis and 3D flame normal	54
ζ	Number of thinning operations	59

Subscripts

1	Inner wall of annulus	122
1	Fuel stream	61
2	Outer wall of annulus	122
2	Oxidizer stream	61

3	Location of peak axial velocity	122
b	Burned	7
s	Bilger	61
e	Equilibrium	64
F	Fuel	7
g	Global	59
K	Kolmogorov	124
L	Laminar	11
n	Nominal	62
O	Oxidizer	7
P	Product	7
s	Stoichiometric	61
T	Turbulent	86
t	Turbulent	124
u	Unburned	7
x	Two-dimensional projection (of gradient)	63

Chemical Species

Al_2O_3	Aluminum Oxide	23
CH_4	Methane	7
CO_2	Carbon dioxide	9
CO	Carbon monoxide	9
H_2O	Water	33
N_2	Nitrogen	33
Nd:YaG	Neodymium-doped yttrium aluminum garnet	44
O_2	Oxygen	9

Acronyms

BML	Bray-Moss-Libby flamelet model	12
CFM	Coherent flame model	12
CMC	Conditional moment closure	12
CTA	Constant temperature anemometry	33
FSD	Flame surface density	12
FWHM	Full Width Half Maximum	31
HWA	Hot wire anemometry	33
LDV	Laser Doppler velocimetry	16

LIF	Laser induced fluorescence	22
LES	Large eddy simulation	12
MFC	Mass flow controller	29
PIV	Particle image velocimetry	14
PLIF	Planar laser induced fluorescence	14
Pdf	Probability density function	12
RMS	Root mean squared	16
RANS	Reynolds-averaged Navier Stokes	12
SB	Cambridge Stratified Slot Burner	27
SNR	Signal to noise ratio	57
SwB	Cambridge Stratified Swirl Burner	39

"I tried, didn't I? Goddammit, at least I did that!"

— R. P. McMurphy, in *One Flew Over The Cuckoo's Nest* by Ken Kesey

Chapter 1

Introduction

Worldwide energy consumption is approximately 16.5 TW based on recent figures[a], and is steadily increasing due to the rapid advancement of newly industrialized countries such as China, India and Brazil. Combustion of fossil fuels accounts for the vast majority of energy production (67 %), with natural gas combustion contributing approximately 22 % of total energy production.

Combustion of fossil fuels is primarily used in power generation (e.g. coal power stations and gas turbine power stations) and transportation (e.g. motor vehicles and jet engine aviation), and as such plays an important role in modern life. The combustion of energy-dense hydrocarbon fuels is required to meet the high power requirements of these applications. The combustion process is intrinsically linked with the production of undesirable byproducts, whether in the form of ozone-damaging nitrous oxides (NOx), unburned hydrocarbons and other combustion-related pollutants. Scientific concern and public awareness of the environmental impact of human activity has risen substantially over the past half century, with the result that many governments have implemented

---

[a] Energy consumption figures based on the most recent (2008) figures released by the U.S. Energy Information Administration (`http://tonto.eia.doe.gov/`).

increasingly stringent emissions limits for combustion applications. Combustion systems now aim to have stable combustion with low levels of the previously mentioned pollutants, without compromising fuel efficiency to a serious degree.

Achieving these often ambitious goals is one of the key challenges facing energy production, prompting significant research endeavors from both industry and academia. Though it has been an area of active investigation since the 19th century, it is only relatively recently that experimental diagnostics have been able to probe the internal structure of the flame and that computational power has advanced to the point that combustion may be simulated. Theoretical combustion modeling has made great strides in the past three decades, with a number progressing to computational models with industrial applications. However, there remain many areas in combustion where the understanding of the underlying physics is not yet fully closed.

Practical combustion applications, whether by accident or design, commonly feature reactant mixture fields that exhibit spatial variation in composition. Such conditions are defined as stratified in the present work. However, the fundamental science underpinning stratified combustion remains poorly characterized and understood relative to other combustion regimes. There is a paucity of high quality stratified combustion datasets to assist model validation and development. This lack of validation hinders the emergence of future computational models from current theoretical models. It also imposes a penalty on the development of novel stratified devices, as current physical models have unknown accuracy.

1.1 Objectives

The overall objective of this project is to provide further insight into the fundamental physics governing stratified combustion. Stratification may influence the evolution of chemical species within the flame, and also chemical-turbulence interactions. These potential effects can be investigated through detailed analysis of key combustion quantities derived from experimental measurements.

The specific objectives of the present work are:

i) To design and test a turbulent stratified swirl burner with characteristics suitable for model validation.

ii) To generate experimental datasets suitable for identifying the effect of stratification on combustion.

iii) To develop a suite of validated data processing algorithms enabling the extraction of key combustion quantities from experimental data.

iv) To derive insight into the fundamentals of stratified combustion through detailed comparison of comparable premixed and stratified results.

v) To package experimental data into open-access datasets for use in validation of emerging combustion models.

1.2 Thesis Overview

Chapter 2 provides a concise review of the main concepts relevant to the study of turbulent stratified combustion. The literature is discussed where relevant to highlight both consensus and discord within the combustion community in these areas.

Chapter 3 describes the two turbulent burners (a V-flame slot burner and a co-annular swirl burner) used in the present work, the operating conditions surveyed in each, and the experimental methodologies employed. Measurement uncertainties are detailed to quantify any systematic errors.

Chapter 4 covers the data processing used to calculate various derived quantities relevant to the study of combustion (e.g. curvature) from the raw experimental data. Background is supplied for non-standard and novel algorithms, implementation details are discussed, and thorough error analysis applied where feasible to calculate propagated uncertainties for the derived quantities.

The influence of stratification on combustion is investigated using data from a weakly turbulent V-flame in Chapter 5. The interaction between turbulence and the effect of stratification is also examined. Similar analysis is provided in Chapter 6 for data from the swirl burner.

An investigation of the congruence of three metrics which can be used to calculate flame surface densities from experimental data is presented in Chapter 7. As this chapter makes use of data from both the slot and swirl burners, it is presented after the data used to calculate the flame surface densities have been shown (Chapter 5, Chapter 6).

Finally, the primary findings of the present work are presented in Chapter 8. Suggestions on the potential avenues for future work are also detailed.

Chapter 2

Background

Combustion has been an area of active research for many decades, resulting in a large body of available literature. In general the research has focused on premixed flames, where the fuel and oxidizer are fully mixed prior to ignition, and non-premixed flames, where combustion takes place at the interface between separate fields of fuel and oxidizer. Stratified combustion, a subset of premixed combustion where the fully mixed fuel/oxidizer field exhibits a spatial composition gradient, has been the subject of relatively few studies, despite the practical relevance of stratification in real world combustion systems [1–5]. This stratification may be intentional, giving acceptable flame stability in overall lean combustion. It may be due to physical design constraints, which may impose limits on the mixing length for the fuel and oxidizer. There is a pressing need to advance the understanding of stratified combustion and its underlying physics, and this thesis focuses on a series of experiments which aim to further this understanding. The following section provides the necessary background material to put this research and subsequent discussion of results in context.

A brief overview of the various modes of combustion is provided in the following section to expand on the brief descriptions given previously. The state of premixed and stratified turbulent combustion research is then assessed, providing a framework against which the merits of the current work can be evaluated. Key studies and findings in both the experimental and modeling domains are presented. Finally, a concise review of material pertaining to the laser diagnostics techniques used in the present work is given.

2.1 Modes of Combustion

Combustion is defined as an exothermic chemical reaction between fuel and oxidizer. The process may be subdivided into a number of different modes. The most basic division is between premixed or non-premixed combustion. The strict definition of premixed combustion states that fuel and oxidizer must be completely mixed on a molecular level; in practice, flows in which there is no significant variation in composition are said to be premixed. An example of this is a premixed Bunsen burner flame. This may be obtained by fully opening the air inlet at the base of the Bunsen burner, allowing complete mixing of air and fuel before flow reaches the burner exit. In non-premixed combustion, the fuel and oxidizer are separate and the flame stabilizes at the stoichiometric interface that arises due to molecular diffusion between the two fields. A classic example of this is the yellow flame generated by a candle as evaporated fuel (typically paraffin in modern candles) diffuses into ambient air.

The next level of classification is into either fuel-lean, stoichiometric, or fuel-rich combustion. Stoichiometric combustion occurs when fuel and oxidizer are present in the correct ratio for complete reaction to take place between them, with no shortage of either fuel or oxidizer. In lean combustion there is an excess of oxidizer relative to the amount of fuel, and vice-versa for rich combustion.

Between the extrema of premixed and non-premixed combustion, one can find situations in which the fuel stream is partially mixed with oxidizer, either intentionally (e.g., to suppress soot), or by the natural evaporation and turbulent mixing processes taking place prior to reaching a zone of flame stabilization. In this work, the term stratified combustion is considered to be a subset of premixed combustion provided the mixture is entirely fuel-rich or fuel-lean. Flames propagate through fuel/oxidizer fields which though fully premixed exhibit significant spatial variation in air/fuel ratio. This form of combustion is referred to by a number of terms in the literature — “stratified”, “partially premixed”, “stratified premixed”, “imperfectly premixed” — but to avoid confusion and to aid brevity will be referred to as stratified combustion throughout this thesis.

The present work is primarily concerned with identifying the effects of stratification on turbulent CH_4/air combustion. Turbulent premixed combustion at comparable operating conditions (flow rates, global and local stoichiometry etc) provides reference cases against which the extent of these effects may be evaluated. Both modes of combustion are examined in more detail in the following sections, with a particular focus on the current state of the literature on stratified combustion in the experimental and modeling domains.

2.2 Laminar Premixed Combustion

A basic understanding of the structure of laminar premixed flames is useful in the study of their turbulent counterparts, and also of turbulent stratified flames. A laminar premixed flame may be considered to comprise three parts: unburned reactants, burned products, and a thin layer separating the two. An idealized thermal profile across a laminar flame front is shown in Figure 2.1. The layer separating the burned and unburned gases may be subdivided into three regions; the preheat zone, the reaction zone and the equilibration zone.

The bulk of the chemical reactions occur in the reaction zone, which is typically

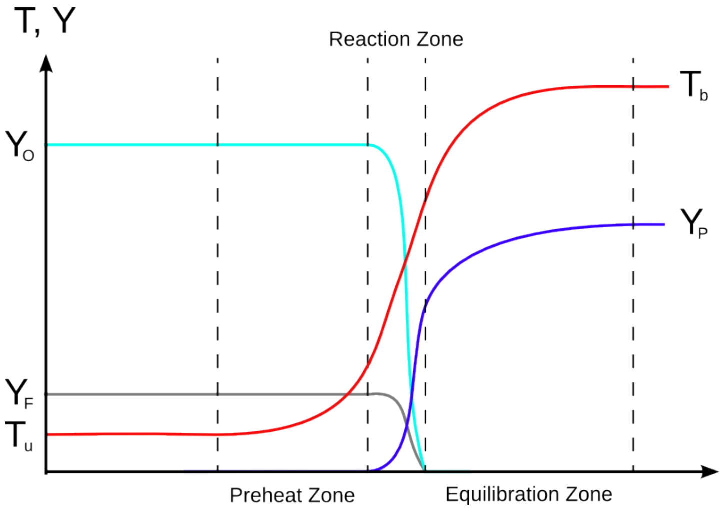

Figure 2.1: Schematic showing the structure of a laminar premixed flame, adapted from Cant *et al* [6]. T is temperature, Y is mass fraction, and the subscripts u, b, O, F and P refer to unburned, burned, oxidizer, fuel and product quantities respectively.

sub-millimeter in thickness. The conversion of unburned to burned gases takes place via a number of intermediary reactions. The region between the unburned reactants and the reaction zone is known as the preheat zone. The temperature is raised by the conduction of heat and radicals from the reaction zone, but not to a level sufficient to overcome the activation energy of most combustion reactions. Therefore there is little chemical activity in this region. The equilibration zone is where much of the net heat release in laminar premixed combustion occurs, via the formation of products by the recombination of intermediate species, and it is in this region that most species achieve chemical equilibrium.

When describing the evolution of various quantities within a flame, laminar or otherwise, it is often easier to work in terms of a progress variable c. The progress variable is a scalar, defined such that it has a value of zero in unburned reactants ($c_{\mathrm{u}} = 0$) and unity in the burned products ($c_{\mathrm{b}} = 1$). Various measures of progress variable have been defined, with the majority using a normalization of temperature or chemical species concentration to define c. Some commonly used progress variables are listed below:

$$c\,(h) = \frac{h - h_\mathrm{u}}{h_\mathrm{b} - h_\mathrm{u}} \tag{2.1}$$

$$c\,(T) = \frac{T - T_\mathrm{u}}{T_\mathrm{b} - T_\mathrm{u}} \tag{2.2}$$

$$c\,(Y_\mathrm{O}) = 1 - \frac{Y_\mathrm{O} - Y_{\mathrm{O}_\mathrm{b}}}{Y_{\mathrm{O}_\mathrm{u}} - Y_{\mathrm{O}_\mathrm{b}}} \tag{2.3}$$

$$c\,(Y_\mathrm{F}) = 1 - \frac{Y_\mathrm{F} - Y_{\mathrm{F}_\mathrm{b}}}{Y_{\mathrm{F}_\mathrm{u}} - Y_{\mathrm{F}_\mathrm{b}}} \tag{2.4}$$

$$c\,(Y_\mathrm{P}) = \frac{Y_\mathrm{P} - Y_{\mathrm{P}_\mathrm{u}}}{Y_{\mathrm{P}_\mathrm{b}} - Y_{\mathrm{P}_\mathrm{u}}} \tag{2.5}$$

where Y_P is often taken to be $Y_{[\mathrm{CO}+\mathrm{CO}_2]}$. Equation 2.1 is often approximated by Equation 2.2. The thermal progress variable $c\,(T)$ is often used where temperature measurements are available. Strictly speaking it is only valid in adiabatic, incompressible flows with near-unity Lewis number, as otherwise the relationship between c and T is not unique [6]. However it is often applied in the experimental literature to cases outside of this narrow definition. The choice of scalar basis has an influence on the behavior of progress variable and its gradient, as shown in Figure 2.2. When comparing results in c-space from other sources care should be taken to ensure that the same basis is used. The current work uses a modified form of Equation 2.2 which allows c to be applied to stratified flows where the fuel/oxidizer composition is not constant. This is detailed in Chapter 4.

2.3 Turbulent Premixed Combustion

In turbulent premixed combustion, the fuel and oxidizer streams are mixed prior to any combustion events such that the stoichiometry of the combined fluid is homogeneous in

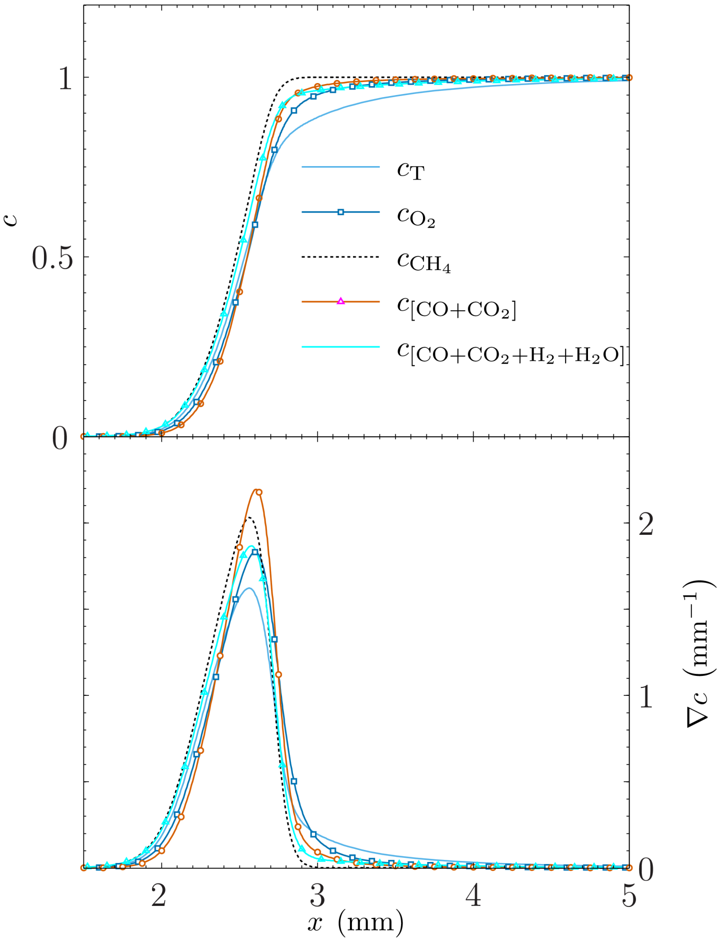

Figure 2.2: Comparison of progress variable c using a variety of scalar basis. Data is obtained from unstrained laminar premixed flame calculations in a methane/air field where $\phi = 0.73$.

space. In practice however a certain degree of inhomogeneity is permissible before the system may no longer be classified as premixed. This form of combustion is common in real world applications, and will be familiar to anyone who has ever used a gas cooking stove, or a Bunsen burner with a fully open air supply.

A reacting front (flame front) propagates towards unburned mixture at a speed determined by the local temperature, pressure, and stoichiometry. In order to stabilize the flame in a stationary burner, it is desirable to balance this propagation with a bulk motion of the premixed field. In this case the shape of the mean flame brush is governed by the laminar burning velocity relative to the bulk velocity of the flow.

The addition of turbulence to the laminar premixed flame has a number of potential effects, which may act in concert or against each other. For example, the flame front will typically become convoluted, which has the effect of increasing flame surface area and hence propagation due to increased reaction rates. However, if turbulent eddies penetrate the preheat zone, the interplay between reactive and diffusive processes within the flame may be locally altered, which can lead to a reduction in propagation rate.

The characteristics of turbulent premixed flames may be broadly classified based on the relationship between the turbulence intensity u'/S_{L} and the turbulent length scale (normalized by the corresponding laminar flame thickness) $L_{\mathrm{turb}}/\delta_{\mathrm{L}}$, as shown by the modified Borghi diagram in Figure 2.3.

Numerous models have been proposed and applied to the simulation of turbulent premixed combustion. These include, in order of increasing complexity: Bray-Moss-Libby (BML) flamelet modeling [7]; Flame Surface Density (FSD) modeling [8, 9]; G-equation modeling [10]. BML modeling is centered on the probability density function of the progress variable, $\mathrm{P}(c)$, and its behavior in the limit of infinitely thin flamelets. FSD modeling quantifies the surface-to-volume ratio at a specific value of progress variable within the flamelet. It assumes that the flamelet is controlled by local stoichiometry and

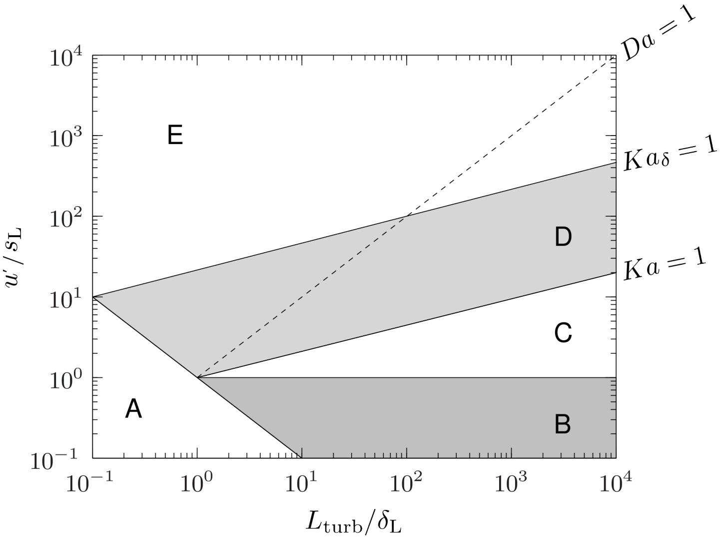

Figure 2.3: Modified Borghi diagram for classifying turbulent flames: A, laminar flames; B, wrinkled flamelets; C, corrugated flamelets; D, thin reaction zones; E, broken reaction zones.

strain, and that the area is governed by turbulence. The G-equation approach shows some similarities to FSD modeling, but offers a greater degree of flexibility. It is based on a non-reacting scalar variable G, which is used to define the flame surface via a level-set approach.

Premixed turbulent combustion modeling has typically been expressed in a Reynolds-Averaged Navier Stokes (RANS) framework, though Large Eddy Simulation (LES) approaches have become more common recently. It is beyond the scope of the present work to describe each of these methods in detail; a good review can be found in [6]. Veynante *et al* [11] give an excellent synopsis of turbulent combustion modeling at the turn of the millennium, while Echekki *et al* [12] provide a more recent and extensive treatment.

Note that in comparison to diffusion flames, there is still a paucity of high quality experimental datasets available for turbulent premixed model validation. This is in part due to practical difficulties, as it is only in recent years that the optical resolution of temperature and species measurements has become sufficiently refined to allow the structure of thin, premixed turbulent flame fronts to be probed. This has hindered premixed model validation in the past, though the situation is continually improving.

2.4 Stratified Combustion

As mentioned earlier in the present chapter, practical combustion applications and model combustors designed to study relevant phenomena at atmospheric pressure typically operate in a stratified regime [1–5, 13–15]. This stratification may be intentional, giving acceptable flame stability in overall lean combustion, or it may be due to physical design constraints, which may impose limits on the mixing length for the fuel and oxidizer. It may also occur simply by accident of design. Advancing the understanding of stratified combustion is important due to this practical relevance. This section provides a brief overview of the key experimental and numerical findings on stratification to date.

2.4.1 Experimental Studies on Stratification

2.4.1.1 Laminar Stratified Combustion

Various studies support the idea that stratification increases the lean flammability limits in comparison to equivalent premixed cases. Kang and Kyritsis [16] measured the laminar displacement speed of a flame front through a lean stratified mixture and found that depending on the degree of stratification imposed, the lean flammability limit could be lowered to $\phi = 0.4$, significantly below the established value of $\phi = 0.5$ [17]. As the flame propagates towards and below the conventional flammability limit, combustion is supported by heat released when the flame burned through mixture closer in composition to stoichiometric. The extension of the lean flammability limit where a stratified mixture field has been induced has also been reported for spark-ignition engines [18, 19].

Furthermore, both Kang and Kyritsis [16] and Gallizzi and Escudié [20] (in laminar V-flame experiments) found that laminar flame speeds are increased beyond the expected values based on local stoichiometry, which they attributed to the presence of a nearby stoichiometric zone.

2.4.1.2 Turbulent Stratified Combustion

The effect of stratification on low turbulence ($u'/S_\mathrm{L} \sim \mathcal{O}(1)$), low Reynolds number lean flames has been investigated recently in a small number of studies. Renou *et al* [21] studied the behavior of unsteady flame kernels propagating through carefully tailored equivalence ratio gradients in overall lean flames, and found that stratification increased the flame propagation rate. The local variation in burning velocity was accompanied by an increase in flame front wrinkling relative to premixed flames, with a corresponding broadening of curvature distributions. Pasquier *et al* [22] studied the propagation of flames through stratified lean turbulent propane mixtures in a combustion bomb. These studies followed the fuel concentration ahead of the flame and the local velocity in 2D planar laser induced fluorescence (PLIF) and particle image velocimetry (PIV) measurements in premixed and stratified mixtures. The results showed that flame propagation was influenced by the stoichiometry history of the mixture, whereby locally lean mixtures burn faster if pockets of richer mixtures were burned through earlier in the flame's propagation history.

Robin *et al* [23] studied a rod-stabilized V-flame supplied with a Gaussian distribution of mean equivalence ratio. Each branch of the flame propagates across the stratified mixture field, which decreases in fuel/air ratio from a central peak to air at the edges. Rayleigh scattering was used to obtain the temperature field, and the flow was seeded with acetone to obtain the mixture fraction using PLIF. The analysis of flame thickness and curvature indicates that the presence of stratification in lean flames leads to a decrease in flame thickness, which is attributed to an additional stretch component arising from differential flame propagation speeds. Anselmo-Filho *et al* [24] used a low turbulence, rod-stabilized slot burner flame (as in the present work) to investigate the effect of stratification on geometric flame properties. Analysis of curvature data from a large interrogation window indicates that probability density functions (pdfs) of curvature are broadened by stratification, and that the flame surface density is increased relative to the premixed case across a wide region of the flame.

The combustion research community has begun to look at the behavior of stratified flames at more practically relevant turbulence levels, with a number of recent experimental studies examining results from novel turbulent stratified burners [25–29].

Seffrin *et al* [25] introduced an axisymmetric concentric-tube burner designed to allow the investigation of flames at high Reynolds numbers ($Re \sim \mathcal{O}\left(10^4\right)$). Laser Doppler velocimetry (LDV) and particle image velocimetry were used to characterize the velocity field for a number of operating conditions. The structure of these flames were investigated by Böhm *et al* [26] using Rayleigh scattering, and the resulting mean and RMS profiles of temperature indicated a lower turbulent burning speed in the stratified case relative to the corresponding premixed case. However it is worth noting that the equivalence ratio at the intersection of the mixing layer and the mean flame brush was significantly lower in the stratified case ($0.6 < \phi < 0.9$) than in the premixed ($\phi = 0.9$), and hence this result may be solely due to the premixed flame burning through lean mixture of higher equivalence ratio than the stratified case. This makes it difficult to draw any solid conclusions as to the influence of stratification on the turbulent burning velocity in this experiment. Examining instantaneous temperature profiles and corresponding OH-PLIF images, Böhm *et al* conclude that the effect of stratification on temperature profiles is secondary to that of the actual three-dimensional flame front geometry due to turbulence. Additionally they found that curvature distributions trended similarly with stratification to those reported by Anselmo-Filho *et al* [24].

Flame surface density measurements obtained from the axisymmetric co-annular burner used in the current work (see Chapter 3) were presented in [27]. Though the study investigated methods of deriving FSD rather than the effects of stratification on said quantity, the result shown indicated that stratification attenuated FSD in non-swirling flows; similar reductions were not evident in the swirling results. Galizzi *et al* [28] studied a stratified turbulent rod-stabilized V-flame, carrying on from their previous work on laminar stratified flames [20]. The main effects of stratification observed were changes to the velocity field, with burned gases being accelerated towards the flame front opposite the stratified zone. Vena *et al* [29] examined the effects of equivalence ratio gradients on the topology of flame fronts in a turbulent iso-octane/air V-flame. They observed variations in curvature distributions that were less significant than those reported elsewhere in the methane/air literature. Their main conclusion was that while stratification may effect the overall structure and instantaneous behavior of globally stoichiometric flames, the effects on curvature may be limited in locally stoichiometric flames.

2.4.2 Numerical Studies on Stratified Combustion

A number of numerical studies have examined the behavior of partially premixed and stratified flames, from 1D laminar to 3D turbulent flows. Pires da Cruz *et al* [30] originally investigated the behavior of freely-propagating methane flames through step changes in stoichiometry. The findings are in agreement with experimental results from laminar flames below the stoichiometric point: lean flames traveling from a richer mixture to a leaner mixture (back-supported) travel faster than expected based on their local mixture fraction. Flame propagation is enhanced by diffusion of additional heat and radicals from higher enthalpy regions to lower enthalpy regions. Thus, the flame speeds of flames propagating away from the stoichiometric point are faster than those propagating towards it. This acceleration allows back-supported lean flames to propagate below the lower flammability limit. When burning towards stoichiometric in rich cases, flames are also influenced by the diffusion of molecular and atomic hydrogen from the rich to the stoichiometric side of the flame. This further accelerates flame propagation, despite the lower temperatures of the rich flame. In general, the acceleration effect due to enrichment was found to be on the order of 10-20% of the local flame speed.

Marzouk *et al* [31] investigated the role of stratification by calculating laminar opposed flow propane/air flames subjected to a gradient in equivalence ratio and strain. Similarly to Pires da Cruz *et al* [30], they observed that lean flames can be supported by richer flames via diffusion of heat and radicals to burn beyond the premixed flammability limit, and that the rate of heat release is correspondingly higher than expected from the local equivalence ratio. Furthermore, their investigation of the dynamic behavior of back-supported flames showed that greater equivalence ratio gradients allow the flame to propagate through increasingly lean mixtures, again by virtue of the diffusion of heat and radicals. Richardson *et al* [32] systematically investigated the behavior of steady, stabilized strained flames with fresh reactants on one side and burned products on the other, where the opposed streams have different equivalence ratios. They conclude that the effect of equivalence ratio gradients on steady flames is primarily due to the modified radical pool flux rather than heat. Further, they conclude that the unsteady behavior of stratified flames is different from that of premixed flames, and that the response to variable strain is a function of the relative response of diffusion and reaction times, which are affected by the equivalence ratio gradient.

The effect of stratification in turbulent combustion has been considered using direct numerical simulations (DNS) in several studies. Hèlie and Trouvé [33] have performed 3D, single-step chemistry DNS of mean stoichiometric propane/air stratified flames with various initial mixture fraction distributions and length scales. They found that the flame surface density was unaffected by stratification, and that the lowering of the overall reaction rate relative to the homogeneous case was entirely due to deviation from stoichiometry and the corresponding reduction in local reaction rate. Poinsot *et al* [34] performed three-dimensional reduced chemistry simulations of turbulent stratified propane/air flames with a Gaussian distribution of mixture fraction centered at $Z = 0.049$ ($\phi = 0.8$). They concluded that the main effect of stratification is to enhance heat release via the production of flame surface area via flame stretch. The difference between the findings in [33] and [34] is primarily due to the assumed mean stoichiometry. Poinsot *et al* [34] also notes that the induced stretch by partial premixing is small, and that this effect should be overwhelmed by flow stretch at high turbulence levels.

Haworth *et al* [35] performed two-dimensional complex chemistry simulations of turbulent propane stratified flames for a stoichiometric mean equivalence ratio. The study demonstrated the two-stage spatial structure of stratified flames, and concluded that there was no difference in overall heat release rate between homogeneous and stratified conditions. Jimenez *et al* [36] extended that work, by varying the length scale and the mean equivalence ratio of stratification. The study showed that both the global and the local rates of heat release are affected by the scale and distribution of mixture fraction fluctuation, the effect depending on the mean equivalence ratio.

Computational models that are simple extensions of premixed modeling approaches have been applied to stratified systems with some success [14, 15, 23, 37–39], and more extensive approaches bridging regimes have also been proposed [40, 41]. Still, the availability of detailed experimental data for model development and validation is very limited, and the state of modeling for stratified combustion is less advanced than that for non-premixed or fully premixed combustion. Furthermore, fundamental questions regarding the structure and dynamics of turbulent stratified flames remain unanswered. In particular, issues of whether the flame structure is affected by local equivalence ratio gradients commensurate with flame or turbulence structures have yet to be fully understood.

2.5 Laser Diagnostics of Combustion

The measurement capabilities of experimental combustion research have advanced rapidly over the past thirty years as ever more refined laser diagnostics systems became technologically and commercially viable. Early experiments were constrained by the power and repetition rate of lasers, the optical resolution of light collection devices, and the data storage available. The result of this was that many early surveys were by necessity limited to single species measurements at a point, which were laboriously traversed across radial and axial locations in order to develop profiles of the mean and fluctuation. Modern systems allow for high speed stereoscopic velocity characterization, for planar or line imaging of major species and temperature, and much more. Crucially such methods allow for temporally and spatially resolved measurements to be made in turbulent reacting flows without perturbing the flow field.

The principles underlying the main diagnostic techniques used in this work are presented in the following subsections. More detailed accounts of each of the techniques are available in the literature, and the treatment by Eckbreth [42] is recommended for the interested reader.

2.5.1 Rayleigh Scattering

Rayleigh scattering is the elastic scattering of light by particles whose major dimension is an order of magnitude smaller than the wavelength of the incident light. Mie scattering will occur if the particles are larger than this cut-off value. A dipole moment is induced in an atom or molecule when it is hit by a laser beam of suitable wavelength. This moment is strongly aligned with the polarization of the particle's electric field. When the dipole moment relaxes, light at the same wavelength as the incident light is emitted (elastic scattering).

In a single species measurement volume, the probability of light being scattered by a particle is given by its Rayleigh cross-section. In combustion experiments, where multiple species are present simultaneously, the effective Rayleigh cross-section must be calculated before any quantitative results can be obtained from Rayleigh scattering experiments. The effective cross-section is the mole fraction weighted sum of the Rayleigh cross-sections of each species in the measurement volume. The intensity of the light emitted from a gaseous sample is directly proportional to the product of the intensity of the incident light, the effective Rayleigh cross-section of the impinged gas, and the summation of the number densities of species in the gas.

Provided sufficient knowledge of the local composition is available, it is possible to determine the local temperature or density from Rayleigh measurements. Where detailed knowledge of the local composition is not feasible due to experimental constraints, it is possible to overcome this issue by choosing a fuel mixture such that the effective cross section is close to unity. In the current work local measurements of major species are used to determine the effective Rayleigh cross-section, and hence the temperature.

Rayleigh measurements have been applied with increasing frequency to both premixed [27, 43–48] and stratified systems [23, 26, 27, 47, 49].

2.5.2 Raman Scattering

Raman scattering is an inelastic process, as the incident and emitted radiation are of different wavelengths. Incident light may cause a change in the vibrational, rotational or electronic energy levels of an impinged atom or molecule. Light of a different (typically lower) frequency is emitted when the atom or molecule relaxes to either an elevated energy level (Stokes scattering) or a lower energy level (anti-Stokes scattering) relative to the original energy state. In combustion diagnostics we are primarily concerned with changes in the vibrational modes.

The signal obtained from Raman scattering is typically much smaller than that from other forms of scattering, as the vibrational Raman scattering cross-sections are less than 0.1 % of those for Rayleigh scattering. This requires very large laser energies, spread out over wider pulses than those provided by conventional commercial grade lasers, thus limiting its widespread use. The Raman cross-section is a function of the incident light, and the Raman signal from each species is directly proportional to the product of this cross-section and the number density of the species.

A further complication to Raman scattering measurements is that measurements from a specific species are prone to interference from other species. An example of interference in species relevant to combustion diagnostics is that of CH_4 on O_2. Many combustion relevant interferences are detailed in [50]. Fluorescence from soot precursors is another source of interference in Raman measurements. Fortunately this can be avoided by selecting operating conditions which minimize sooting (i.e. operating in globally lean conditions).

Despite the difficulties associated with Raman scattering measurements, they have been successfully applied to a range of turbulent combustion systems including premixed [47], partially premixed [51, 52], and stratified [47] flames. The current work makes extensive use of species measurements obtained from Raman scattering diagnostics.

2.5.3 Laser Induced Fluorescence

Laser induced fluorescence, or LIF, is a commonly applied technique in the field of experimental combustion. Molecules are induced into an excited energy state by the application of laser light at a particular frequency. Provided the excited atom or molecule does not undergo a quenching collision first, after a specific period the particle will fluoresce isotropically. This isotropy enables planar imaging of species (PLIF) to be performed. There are few species that can fluoresce at practically accessible wavelengths, which limits the application of this technique.

Quenching collisions significantly decrease the LIF signal, which complicates the quantification of LIF measurements. In order to correct for signal degradation due to quenching it is necessary to have simultaneous measurements of temperature and the colliding molecules relevant to the flow under investigation. The present work makes use of OH-PLIF and two-photon CO-LIF, qualitatively in the case of the former and semi-quantitatively in the latter.

2.5.4 Particle Image Velocimetry

Particle image velocimetry, or PIV, is a non-intrusive laser diagnostic which allows a flow field to be characterized through the sequential imaging of seed particles in the flow illuminated by laser light. The flow field is seeded with particles whose size and properties are chosen to allow them to follow the motion of the fluid under investigation without perturbing it. The particles should be roughly uniform in diameter, as the signal obtained scales with the square of their major dimension. The current work makes use of sub-micrometer diameter alumina particles (Al_2O_3).

Two images of the particles in the flow field are obtained in quick succession, by illuminating the seeded field using a sheet of laser light, imaging the reflected light using an optical collection system, and repeating the process after a suitable separation time. This separation time is tuned such that the average displacement of the particles is only a few pixels ($\sim 3-5$) between the two images. Interrogation windows are then traversed over the image pairs, and correlation algorithms are used to determine the velocities in the field. The use of interrogation windows limits the resolution of PIV measurements, as typically a minimum window size of 32×32 pixels is required for accurate results.

Single camera PIV can only provide the components of velocity in the imaging plane (i.e. U_{x}, U_{y}). This is reasonable for applications where the out-of-plane component is small, such as in radially symmetric non-swirling flames. It is necessary to use stereoscopic PIV (SPIV) in cases where this is not true.

2.6 Summary

The present chapter has given a brief overview of the topics in order to put the current work in context. First, an overview of the various modes of combustion was given. This provided definitions of premixed and stratified combustion, which form the focus of the present work. The key findings in the stratified literature, experimental and numerical, were presented to assist interpretation of the results and discussion shown later on in Chapter 5 and Chapter 6 by the reader, regardless of their field of specialization.

Chapter 3 presents the two burners surveyed experimentally in the present work. Their geometry and the operating conditions surveyed are described in full. The experimental methods used to obtain data from the flames in these burners are also detailed. The following chapter (Chapter 4) is closely linked to Chapter 3, focusing on the data analysis techniques applied to the experimental data to derive quantities such as curvature, flame surface density, and scalar dissipation rate.

Chapter 3

Experimental Details

This chapter provides an overview of the burners and experimental methods used to generate the premixed and stratified flame data studied in subsequent chapters. The chapter is divided into two main sections, each focusing on a particular burner. These sections outline the design, operating conditions, and experimental methods applied to each burner. The first burner (Section 3.1) is a stratified slot burner that generates a weakly turbulent rod-stabilized V-flame with variable stratification. This burner was designed and fabricated as part of a previous PhD programme. The second burner (Section 3.2) is a co-annular swirl burner that allows turbulent bluff-body stabilized flames of variable stratification and swirl to be investigated.

The experiments performed on the burners may be broken down into multi-scalar measurements and velocity characterization. There is considerable overlap in the experimental details of the multi-scalar measurements as they were performed in the Turbulent Combustion Laboratory[a] using broadly similar equipment and techniques. As such the methods are described in depth for the slot burner experiments (Section 3.1.3), while only major differences are detailed for the swirl burner (Section 3.2.3). Note that the

---

[a] Sandia National Laboratories, Livermore, CA, USA

velocity characterization in the slot burner was performed during a previous PhD program, and is included to put the analysis of scalar measurements presented in Chapter 5 in context.

3.1 Cambridge Stratified Slot Burner

3.1.1 Burner Design

The Cambridge Stratified Slot Burner is a rectangular slot burner, similar in geometry to others used elsewhere in the premixed [53, 54] and stratified [21, 49] literature. The attraction of this design is that it is one of the simplest geometries for investigating turbulent stratified combustion; the flow field can be considered to be approximately two-dimensional, with the mixing layer between streams of different stoichiometry generating a spatial gradient in equivalence ratio. The flame is stabilized on a rod, which results in an open-air turbulent V-flame that intersects the mixing layer mentioned previously. The lack of a combustion chamber allows complete optical access to the areas of interest. The geometry of the burner and the turbulence generating grid are simplified to ensure that it is attractive to simulate using either modeling or DNS methods.

Burner Geometry: The apparatus, originally described in [47, 55], consists of a planar slot burner comprising 6 parallel slots; each slot is a channel 5 mm wide and 50 mm deep separated by 0.3 mm metal slits, through which fuel/oxidizer mixtures can flow (Figure 3.1 and Figure 3.2). The outer slots are used to carry an air co-flow to prevent entrainment of ambient air. One pair of inner slots carries a richer mixture, ϕ_{r}, and the remaining inner pair carries a controlled leaner mixture, ϕ_{l}. Premixed or stratified flow fields are achieved by distributing a constant volumetric flow rate of air equally across

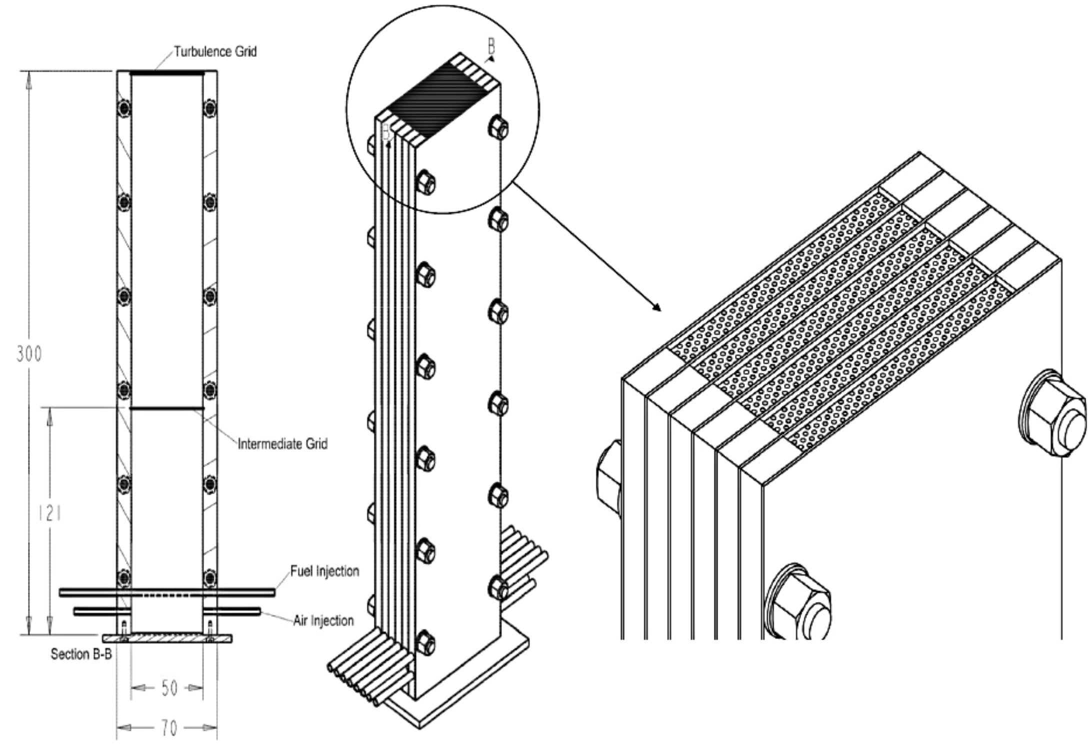

Figure 3.1: Schematic of the stratified slot burner (*SB*) showing internal structure, reproduced from Anselmo Filho *et al* [55]. All dimensions in mm and to scale.

the inner four slots and adjusting two methane flow rates to give the desired operating conditions.

Grid & Flame Stabilizing Rod: A wire mesh grid with a 1.02 mm square pattern and 79% open area is attached to the burner mouth to generate turbulence in the reactant streams. A Ø1.5 mm flame stabilizing rod is placed downstream of the burner mouth ($z = 10\,\mathrm{mm}$), offset from the burner center-line ($x = 2\,\mathrm{mm}$). The rod ensures that intersection of the mixing layer and the flame brush occurs before the entrainment of co-flow air into the region of interest, far enough downstream of the rod to avoid interference with the laser sheets.

The slot burner is referred to as *SB* in the rest of this work.

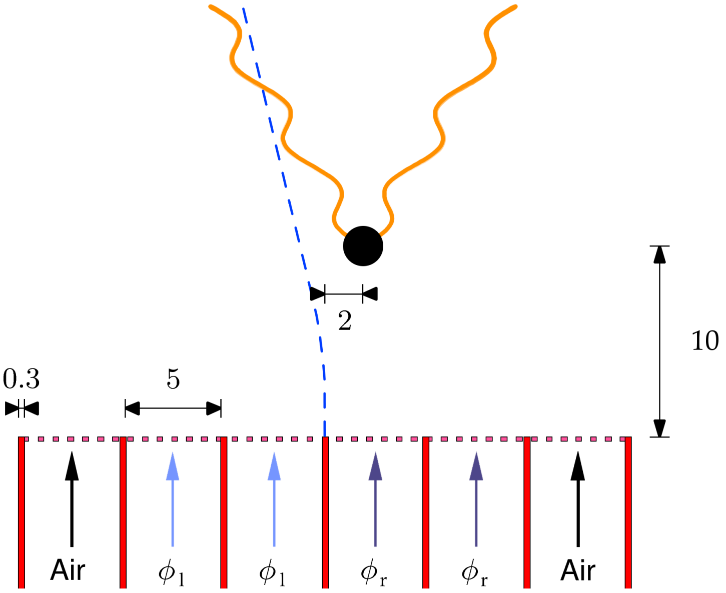

Figure 3.2: Schematic of the exit geometry of the stratified slot burner (SB) showing location of flame stabilization rod ●, V-flame ———, mixing layer ┄┄┄, and turbulence generating grid at exit. CH_4/air slots are marked with open arrows, and co-flow air slots with closed arrows. ϕ_l is the lean flow and ϕ_r the rich flow in stratified cases. All dimensions in mm and to scale.

3.1.2 Operating Conditions

The burner was run in premixed and stratified regimes for a range of flow rates at a nominal global equivalence ratio $\phi_\mathrm{g} = 0.73$. Three cases are investigated in this thesis; a premixed case, $fs1$, a moderately stratified case, $fs4$, and a highly stratified case, $fs6$. The heat load was kept fixed at 7.1 kW, and stratification was achieved by keeping air flow rates constant and varying the split of methane to the reactant flows. The operating conditions are summarized in Table 3.1. Before moving on it is worth noting that lean stratified combustion can be further broken down into back- and front-supported regimes. Back-supported combustion occurs when the products are closer to stoichiometric than the reactants, and vice-versa for front-support. The current work deals exclusively with back-supported flames, and all stratified cases described subsequently

Table 3.1: Operating conditions and bulk flow rates at 1 atm, 294 K. Volumetric flow rate of air includes co-flow air supply.

Flame	Combustion Regime	ϕ_l	ϕ_r	$\phi_\mathrm{r}/\phi_\mathrm{l}$	CH_4 Flow 1 (l/min)	CH_4 Flow 2 (l/min)	Air Flows (l/min)
$fs1$	Premixed	0.73	0.73	1.00	6.58	6.58	85.0
$fs4$	Stratified	0.51	0.95	1.86	4.61	8.55	85.0
$fs6$	Stratified	0.37	1.10	3.00	3.29	9.87	85.0

will be assumed to be back-supported except where otherwise stated.

Flow control: The gas flows for the multi-scalar measurements (Section 3.1.3) were metered using mass flow controllers. These mass flow controllers were calibrated against laminar flow elements to within 1 % of reading. The velocity measurements (Section 3.1.4) used Roxspur NGX series glass variable area rotameters. These rotameters have a specified accuracy of ±3.0 % of reading scale. Each rotameter was factory-calibrated for appropriate gas and flow rate. The rotameters were recalibrated against Bronkhorst EL-Flow F-203AC series thermal mass flow controllers (MFCs) to correct for back-pressure in the system. The MFCs have an accuracy of ±0.5 % of reading and ±0.1 % of full scale.

3.1.3 Multi-scalar Laser Diagnostics

Multi-scalar laser diagnostics in the slot burner were carried out at Sandia National Laboratories by R. S. Barlow. The diagnostics setup allows for the line measurement of temperature (Rayleigh scattering) and major species (Raman scattering) with simultaneous cross planar OH-PLIF. The experimental setup is illustrated in Figure 3.3. This setup has previously been described in [47, 56, 57].

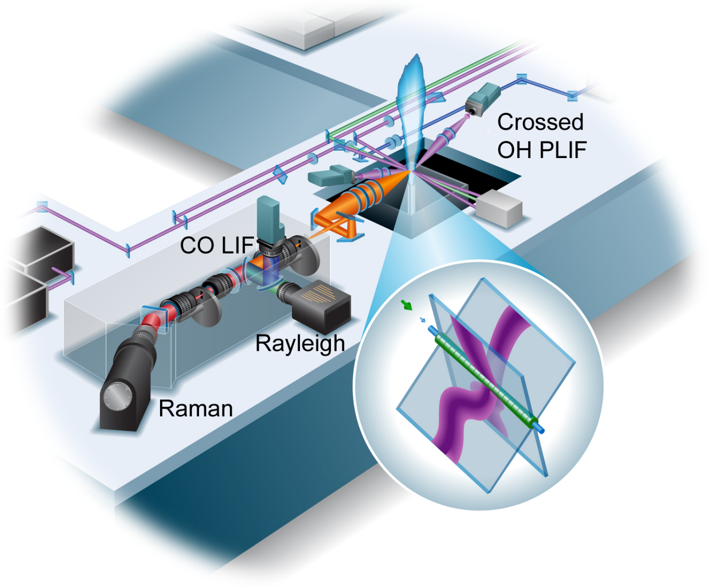

Figure 3.3: Illustration demonstrating the optical system at Sandia National Laboratories for combined Raman/Rayleigh/CO-LIF line measurements with simultaneous cross-planar OH-PLIF imaging.

Line Imaging of Temperature and Major Species: Beams from four frequency doubled Nd:YAG lasers were used for Raman and Rayleigh line imaging, yielding a total energy of 1.8 J/pulse in the probe volume. The focus had a diameter of ~ 0.22 mm ($1/e^2$). The beam diameter was ~ 0.24 mm at the ends of the 6 mm length of the measured segment. CO was excited at 230.1 nm (two photons), with the UV laser beam aligned on the same axis as the Nd:YAG laser beams.

A single detection unit housed CCD cameras for Raman, Rayleigh, and CO-LIF. A pair of 150 mm diameter achromats (Linos Photonics, f/2 and f/4) imaged a portion of the laser beam into the apparatus. The main internal components included two custom-built motor-driven chopper wheels, six commercial camera lenses, and a transmission grating. The two chopper wheels were locked in frequency and phase to a master controller, which also generated timing signals for the lasers and cameras. The "slow" wheel (3 000 RPM, 300 µs FWHM gate) was located at the focus of the collection lens pair to provide gating for the Rayleigh camera. A 1-inch diameter leaf shutter (35 ms) at the entrance to the detection unit allowed just one laser exposure during each camera cycle. The image acquisition rate was 5 Hz, while lasers fired at 10 Hz. Relay lenses and beam splitters separated the wavelengths of interest and refocused the respective images onto the Rayleigh detector, the intensified CO-LIF detector, and the stationary slit of the "fast" wheel (21 000 RPM, 3.9 µs FWHM gate) for the Raman spectrometer. The CCD cameras were the same as those used in [47], with the non-intensified, low-noise, cryogenically-cooled Raman detection array (Princeton Instruments VersArray 1300B, with CryoTiger Cooling Unit operated at −110 °C) being most critical for the overall system performance.

The four camera lenses in the optical train between the slow wheel and the Raman CCD array were 85 mm f/1.8, 50 mm f/1.4, 85 mm f/1.4, and 135 mm f/2. The lenses in front of the Rayleigh and CO cameras were 85 mm f/1.8 and 50 mm f/1.4, respectively. Nikon lenses were used throughout, with the exception of the 135 mm Canon lens. A long-pass filter separated the wavelength range monitored by the Raman camera ($\sim$ 550 nm to 700 nm) from the Rayleigh scattering (532 nm) and CO fluorescence ($\sim$ 480 nm to 488 nm). A second long-pass filter split the CO and Rayleigh signals, and 10 nm bandpass filters centered at 484 nm and 532 nm were used in front of the respective camera lenses.

The custom transmission grating (Kaiser Optical) for the Raman spectrometer was 76 mm square, with anti-reflection coating and design specifications of 1 200 lines/mm, 625 mm center wavelength, and 22° incident and refracted angles. Efficiency specifications were approximately 0.78, 0.90 and 0.78 for wavelengths of 565 nm, 625 nm and 685 nm, respectively.

The optical resolution was determined primarily by the pair of achromatic lenses at the front end of the collection system. The measured line-spread function at best focus was $\sim 40\,\mu\text{m}$ FWHM for each system at fixed wavelength, using a knife edge method [58]. Final focusing of each camera was accomplished using a laser-drilled target with a linear pattern of 50 µm holes on 200 µm centers, located on the plane bisecting the laser alignment aperture. For the Raman system, a neon lamp was used to back-illuminate the target, producing an array of dots in the detected image and allowing convenient optimization of focus across the array. The effective resolution is influenced by the presence of a flame in the collection path, and it is reduced when the flame normal is not aligned with the beam due to the finite beam diameter. The spacing of binned pixels along the laser axis was 105 µm, 20 µm and 101 µm for the Raman, Rayleigh, and CO-LIF measurements respectively.

Cross-planar OH-PLIF: The instantaneous 3D orientation of the flame was determined using planar imaging of OH fluorescence from two crossed laser sheets that intersected along the multi-scalar line measurement axis [24, 56]. A dye laser was pumped using a frequency-doubled Nd:YaG laser, the frequency of which was doubled to 283.5 nm. The output beam was split into two separate 1 mJ beams, and one beam was optically delayed by 40 ns to ensure the fluorescence from each would not interfere with the other. The beams were reshaped using sheet-forming optics and crossed such that the inter-plane angle was 60° and their intersection axis was coincident with the line measurement window. 10-element UV lenses (CERCO 45 mm f/1.8) were combined with intensified CCD cameras (Andor) to image the fluorescence obtain by the excitation of the $Q_1\,(8)$ line of the OH molecules. The imaged region for each plane was 10 mm by 8 mm, with a resolution of 0.15 mm/pixel.

Experimental Error: Calibrations for the line-imaged measurements were based on cold flows, heated flows, laminar jet diffusion flames, and flat CH_4/air flames of known stoichiometry. Estimates of accuracy were based on uncertainties in calibration flow conditions and repeatability of measurement. Table 3.2 lists uncertainties based on estimated accuracy and the standard deviation (precision) of averaged measurements.

Table 3.2: Uncertainties in scalar measurements based on measurements in calibration flows, arranged in order of descending accuracy.

Scalar	Accuracy, Δ (%)	Precision, σ (%)	Calibration Flow
T	2	0.75	$\phi = 0.97,\ T = 2\,185\,\mathrm{K}$
N_2	2	0.7	
H_2O	3	2.4	
CO_2	4	3.2	
ϕ	5	2.2	
CO	10	4.5	$\phi = 1.28,\ T = 20\,450\,\mathrm{K}$
H_2	10	7.5	

3.1.4 Velocity Characterization

Velocity characterization in the slot burner was performed by P. Anselmo-Filho, and is detailed in full in [55]. A brief synopsis will be given in order to assure the reader as to the reliability of the velocity data presented later on. Axial velocities in the cold flow were characterized by hot wire anemometry (HWA) operating in constant temperature anemometry (CTA) mode. The main disadvantages of HWA are that it is by definition an intrusive procedure (unlike laser diagnostic methods), that it can only be used in cold flow conditions, and that it is significantly more difficult to measure two or three component velocities than single component velocities due to the increased complexity in accurately calibrating measurements. Only one-dimensional velocity measurements were made in the slot burner.

Principles of Operation: The basic principle of HWA is that the probe is cooled by the flow of the fluid about it, which reduces its resistance. In CTA mode, the applied voltage is varied with the changing resistance to ensure the probe maintains a constant temperature. This voltage is measured and may be converted to a velocity measurement. The technique requires calibration procedures to be followed prior to making any measurements.

HWA Setup: The velocity characterization used a single normal probe (Dantec Dynamics 55P16), 5 µm in diameter and 1.25 mm in length. The operating range for this probe was 0.05 m/s to 500 m/s, making it a suitable choice for the velocities expected in the flow. The probe was connected to a Dantec Dynamics 56C01 CTA unit with a 56C17 CTA bridge and a 56N20 signal conditioner using a standard BNC cable. The voltage signal from the CTA system was recorded using a digital acquisition board (National Instruments PCI 6035E).

HWA Calibration: The calibration rig was based on that used by Johnstone *et al* [59], and comprised a low angle diffuser, a cylindrical settling chamber with two flow stabilization screens, and a nozzle with exit diameter 25.58 mm and contraction ratio of $25 : 1$. The laboratory temperature was kept constant at $20 \pm 1\,^{\circ}\mathrm{C}$, while the calibration airflow was maintained at $20 \pm 2\,^{\circ}\mathrm{C}$. The air flow was metered using a Bronkhurst El-Flow F-203AC thermal mass flow controller (MFC), which had a factory calibration of ±0.5 % of reading plus ±0.1 % full scale. The calibration methodology detailed in [59] was iterated until the calibration error was within 0.5 %. This procedure generated a polynomial fit between the measured voltage and velocity.

HWA Measurements: The sampling frequency was chosen to be 100 kHz to ensure the flow was temporally resolved, as the cutoff frequency was measured to be 50 kHz. The sample time was 40 s, giving a sample size of 4×10^6. These values were chosen to ensure statistically independent samples. The experimental error in the mean velocity measurements due to the effects of spatial resolution was estimated to be about 1.0 %, assuming isotropic turbulence. When combined with probe calibration error, the combined error was determined to be roughly 3.0 %.

Velocity profiles were taken by traversing the probe in increments of 0.5 mm along a line parallel to the burner exit and $z = 15$ mm downstream of it. Note that hot flow properties for the slot burner are currently unavailable. A systematic PIV measurement campaign is planned for the future.

3.2 Cambridge Stratified Swirl Burner

3.2.1 Burner Design

The slot burner provided a good introduction to the behavior of stratified flames, and at conditions which could be reasonably simulated by DNS. It has also attracted interest from RANS modelers [60]. However, the turbulence intensity of the flames surveyed (Re $\sim$ 2 000) are not really comparable with those seen in practical combustion systems. The simulation of flames in burners at more realistic turbulence levels have become ever more viable with the advance of computational power, the refinement of existing models and the emergence of newer models. A burner with substantially higher flow rates (and Reynolds numbers) was designed to investigate the effect of stratification in a more representative flow. The burner was designed to provide flows with a variable degree of swirl to allow the turbulence levels to be varied for a given level of stratification; this was to allow any potential turbulence dependences of stratification in this geometry to be identified. It has the potential to assist flame stabilization, as in practical combustors, allowing more extreme stratified conditions to be investigated than would otherwise be possible. This latter avenue of research was not pursued in the current work.

The swirl burner is shown in plan view in Figure 3.4; key components are labeled and will be referenced in braces, {}, in the following discussion. It consists of two annular channels through which fuel/oxidizer mixtures can flow, and a large (382 mm diameter) co-flow of filtered air to prevent the entrainment of ambient air. Air flow in the co-flow is conditioned in the following way. First, it is passed through 3 perforated disks {M}, the first of which has 3 mm diameter holes with 40% open area, while the subsequent pair has 1.5 mm diameter holes with 25% open area. The flow is then straightened by passing it through a 38.1 mm deep honeycomb section {L} with 3 mm holes and 75% open area. Finally any clustered particles are filtered using two mesh gauze {K}, the first of which has 1.2 mm square holes and 70% open area, while the second has 1 mm square holes with 40% open area.

The annuli are formed by three concentric tubes {E-G}. The exit geometry is shown in Figure 3.5. The innermost tube {G} is terminated in a ceramic cap {J}. This acts as a central bluff body which aids flame stabilization. The use of ceramic material ensures that heat losses to the bluff body are minimized, and the conditions are assumed to be close to adiabatic.

A locating collar {D} is used to ensure that the major axes of the tubes are coincident. The outer tube {E} is aligned relative to the middle tube {F} using a set of three 60 µm diameter pins arranged at 120°. The diameter of the pins was selected as a compromise between structural strength and the desire to minimize disturbance to the flow. The perturbation of the flow was further reduced by placing the locating collar a number of hydraulic diameters upstream of the burner exit.

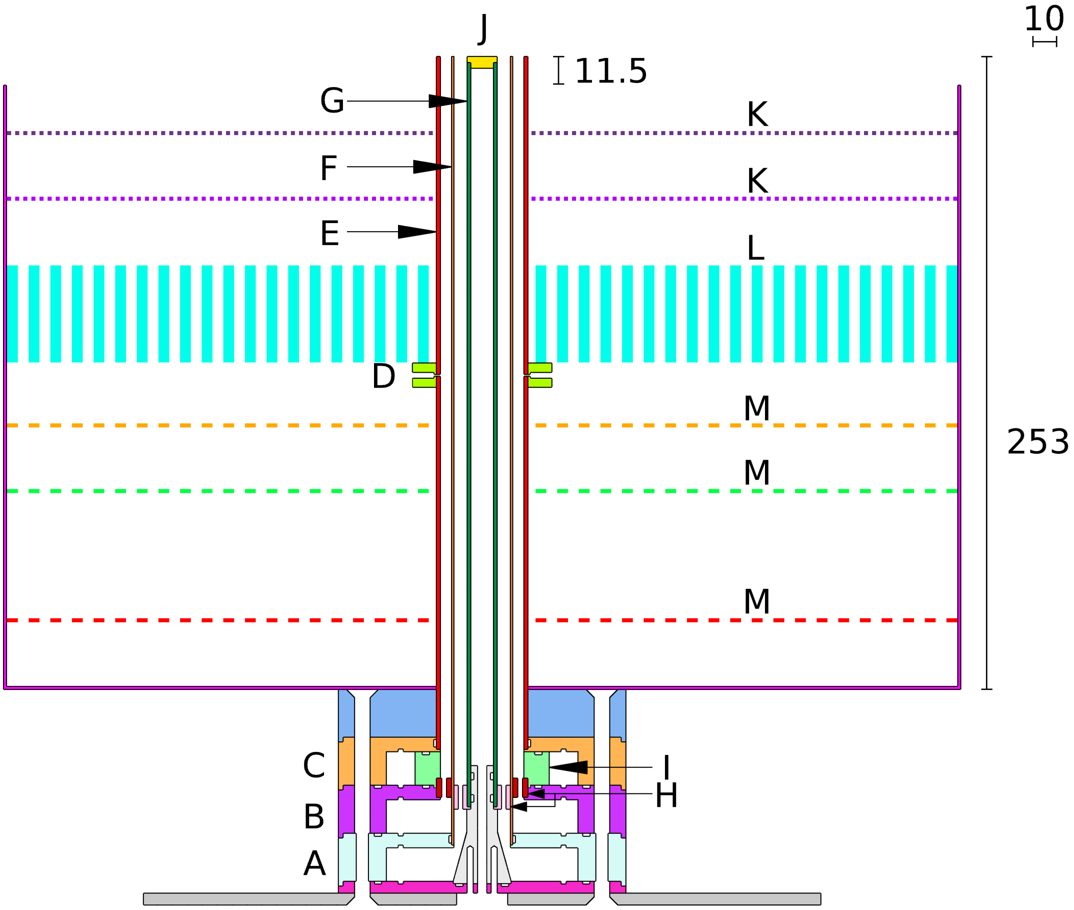

Figure 3.4: Elevation of the stratified swirl burner (SwB). A: inner annulus plenum; B: outer annulus axial flow plenum; C: outer annulus swirl flow plenum; D: locating collar; E: outer tube; F: middle tube; G: inner tube; H: flow straighteners; I: swirl generating collar; J: ceramic cap; K: wire mesh; L: honeycomb section; M: perforated disk. Flow fittings are omitted for clarity. All dimensions are to scale and in mm.

The pins are slotted through holes in the locating collar and the outer tube, and the relative position of the middle tube is controlled by varying the depth to which the pins are screwed into the locating collar. A transparent cap with concentric markings corresponding to the desired positions of the various tubes was placed on the outer tube to assist location. Another set of three pins, offset by 30° to the previously mentioned set, are used to locate the inner tube relative to the outer one following a similar procedure.

Flow to the inner annulus is supplied via a plenum {A} at the base of the burner.

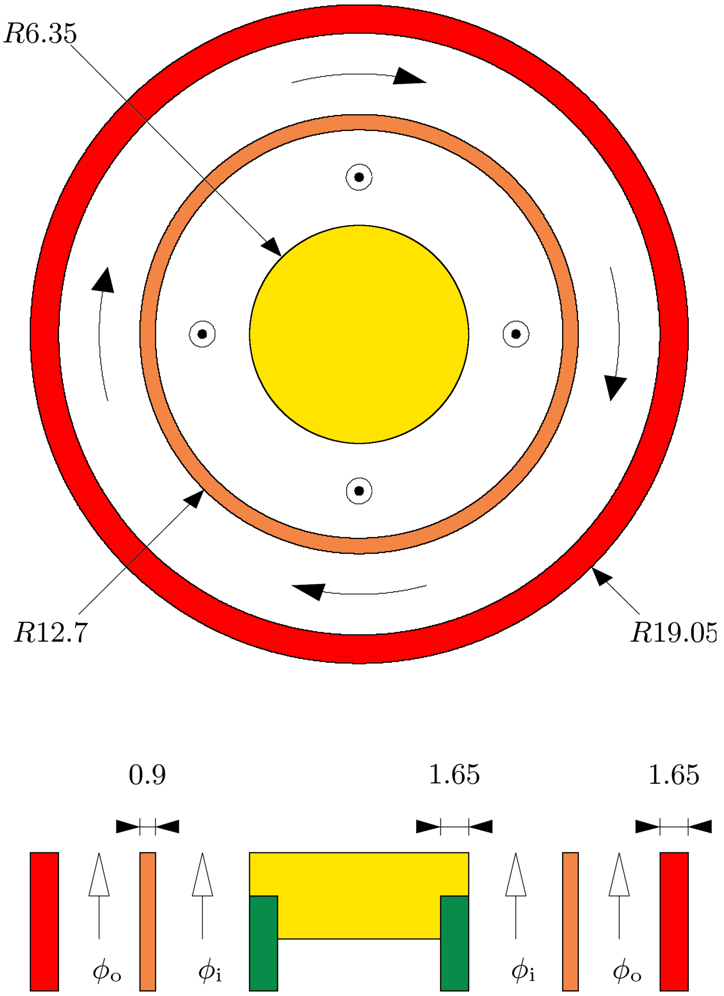

Figure 3.5: Plan view of the exit geometry in the stratified swirl burner (SwB), showing a plan view and a cross section through the burner axis. The curved vectors in the plan view show the direction of swirling flows in the outer annulus, while the out of page vectors show the axial flow in the inner annulus. All dimensions are to scale and in mm

Though plenum's primary purpose is to channel flow from the supply lines to the inner annulus, it also quietens the flow structures in the lines on entrance to the burner. The plenum also ensures that any fuel/oxidizer that is incompletely mixed before exiting the supply lines is fully mixing prior to entering the annulus. The outer annulus is fed by the middle and upper plenums {B, C} in the burner. If the middle plenum {B} is used in isolation, then the resulting outer annulus flow is axial. A variable degree of swirl can be introduced to the outer flow by passing a percentage of the overall outer annulus flow through upper plenum {C}. Gas from the upper plenum joins the outer annulus through a swirl collar {I}, via a radially symmetric pattern of inlets angled at 30° to the annulus. These angled jets induce a tangential component to the axial flow from the middle plenum, generating a swirling flow at the burner mouth.

Flow straightening plates {H} are fitted to the inner and outer annulus close to the plenums supplying axial flow. The plates have a number of small through-holes arranged in a radially symmetric pattern, with major axes parallel to those of the annuli. Turbulence is generated by the changes in sectional area as flow passes through the plates, and the pressure drop across them is sufficient that the downstream flow is more uniform than in the absence of the plates.

The distance between the flow straighteners and the burner exit was a compromise between the need for a long axial length to ensure that turbulence is fully developed, the practical challenges long burner geometries pose for laser diagnostics, and the decay of swirl and turbulence intensity with distance. The development length is over 25 diameters in both annuli, which is sufficient to give fully developed turbulent flow with greater hydraulic Reynolds numbers than the slot burner at exit in a moderately compact geometry, with significant levels of swirl achievable.

The swirl burner is referred to as SwB in the rest of this work. This should not be confused with SB, which refers to the slot burner detailed in Section 3.1.1.

3.2.2 Operating Conditions

A matrix of operating conditions was created for experiments using the swirl burner, as shown in Table 3.3. These conditions were chosen to allow the investigation of flames in premixed and stratified regimes, with or without swirl. Bulk velocities were chosen to maximize the Reynolds numbers in the flows given the physical constraints imposed by the mass flow controllers available and the maximum throughput of the laboratory air supply. The total power load is 33.6 kW, with the fractional load being 0.25 for the inner fuel/air stream and 0.75 for the outer fuel/air stream.

The bulk velocity in the outer annulus, U_o , was held at twice the value of the velocity in the inner annulus, U_i , in order to generate substantial levels of shear between the two flows and ensure thorough mixing of the flows near to the burner mouth ($U_\mathrm{i} = 8.31\,\mathrm{m/s}$, $U_\mathrm{o} = 18.7\,\mathrm{m/s}$). Co-flow air was supplied around the outer annulus with a bulk velocity $U_\text{co-flow} = 0.4\,\mathrm{m/s}$ to prevent the entrainment of ambient air. The Reynolds numbers ($\mathrm{Re} = \rho U L/\mu$) derived from the bulk velocities and the exit geometry are $\mathrm{Re}_\mathrm{i} = 5\,960$ for the inner annulus and $\mathrm{Re}_\mathrm{o} = 11\,500$ for the outer annulus.

The stratification ratio $\phi_\mathrm{i}/\phi_\mathrm{o}$ was varied from 1 for premixed cases to 3 for highly

Table 3.3: Operating conditions for Cambridge Stratified Swirl Burner. In all cases U_i is 8.31 m/s and U_o is 18.7 m/s, and the $U_\text{co-flow}$ is 0.4 m/s.

Flame	$Q_\mathrm{tg}/Q_\mathrm{t}$	$\phi_\mathrm{i}/\phi_\mathrm{o}$	ϕ_i	ϕ_o	ϕ_g
$SwB1$	0.0	1	0.75	0.75	0.75
$SwB2$	0.25				
$SwB3$	0.33				
$SwB4$	0.4				
$SwB5$	0.0	2	1.0	0.5	
$SwB6$	0.25				
$SwB7$	0.33				
$SwB8$	0.4				
$SwB9$	0.0	3	1.125	0.375	
$SwB10$	0.25				
$SwB11$	0.33				
$SwB12$	0.4				
$SwB13$	0.0	1	1.0	1.0	1.0
$SwB14$	0.25				
$SwB15$	0.33				
$SwB16$	0.40				

stratified cases. The swirl ratio $Q_{\mathrm{tg}}/Q_{\mathrm{t}}$ was varied between 0 for non-swirling flow to 0.4 for highly swirling flow. The 0.4 swirl ratio cases were found not to stabilize reliably in the stratified cases and so are not considered in the remainder of the present work.

The gas flows in all experiments were metered using mass flow controllers. In the case of the multi-scalar measurements (Section 3.2.3), the MFCs were calibrated against laminar flow elements to within 1 % of reading. All the controllers used for the velocity characterization were Alicat[b] mass flow controllers, with factory calibration specifying accuracies within ±0.8 % of reading and ±0.2 % of full scale.

3.2.3 Multi-scalar Laser Diagnostics

The basic operation of the multi-scalar laser diagnostic system for the SwB experiments was similar to that detailed in Section 3.1.3, with the main difference being an improvement to the OH-PLIF imaging setup. A pair of UV aplanat lenses with AR-coating (CVI APMQ-500-100) were used with the Andor CCD cameras detailed in Section 3.1.3 to image OH fluorescence from the flame. The imaged area was smaller than in the previous experiments, with each plane being 8 mm by 4 mm, but the resolution was approximately three times finer at 48 µm/pixel. The spacings of the binned temperature and species measurements along the laser axis were marginally different to the previous experiment; 103 µm, 20 µm and 101 µm for the Raman, Rayleigh, and CO-LIF measurements respectively. The uncertainties in the revised diagnostics system are similar to those in the slot burner experiments, and are given in Table 3.4. The multi-scalar experiments were carried out with the additional assistance of M. J. Dunn.

Multi-scalar data were taken in two separate campaigns. First, the temperature, equivalence ratio and species profiles were mapped out in space by taking measurements

---

[b] For further details on the Alicat MFCs please refer to `http://www.alicatscientific.com/products/gas-flow-controller.php`

in overlapping windows along the radial direction for various heights above the burner mouth ($z = 10\,\mathrm{mm}$, $z = 20\,\mathrm{mm}$, ...). These measurements were downsampled to a uniform pixel resolution of 103 µm. 300 shots were taken in each measurement window, with an additional 1 200 shots taken at the mean flame front position for each axial location. The measurement locations for both campaigns are shown schematically in Figure 3.6.

Preliminary analysis of these images identified the axial and radial locations at which the mixing layer intersected the mean flame bush. Further data was taken at these locations; 5 000 and 30 000 shots were taken for premixed and stratified cases respectively. More data was taken for stratified cases than for premixed cases to improve results conditioned on local equivalence ratio in Chapter 6. This data was recorded by oversampling at a sampling resolution of approximately 20 µm. The data was then processed

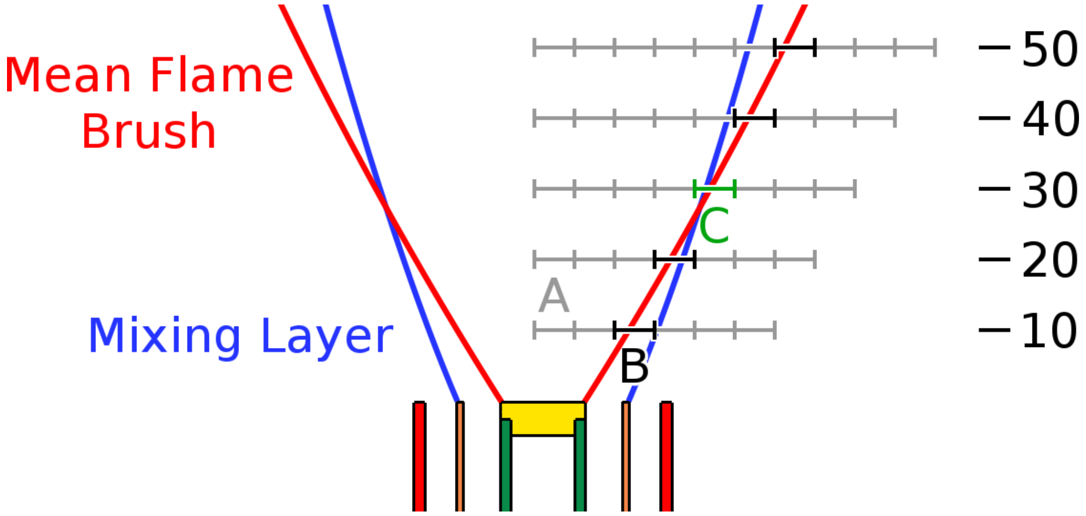

Figure 3.6: Illustration of measurement locations for multi-scalar diagnostics campaigns in swirl burner (*SwB*). A: 103 µm measurement window (300 shots); B: 103 µm measurement window (1 500 shots); C: 20 µm measurement window (5 000 shots in premixed cases, 30 000 shots in stratified cases). Note that the line measurement window C lies at the intersection of the mixing layer and the mean flame brush. All line measurement windows approximately 6 mm in length and overlap slightly (overlap omitted for clarity). All dimensions are to scale and in mm.

Table 3.4: Uncertainties in scalar measurements in *SwB* based on measurements in calibration flows, arranged in order of descending accuracy. Uncertainties are determined from measurements in premixed CH_4/air flat flame where $\phi = 1.28$ and $T = 2\,050\,\mathrm{K}$. Precision in the wavelet denoised data is shown in parentheses.

Scalar	Accuracy, Δ (%)	Precision, σ (%)	SNR
T	2	0.7 (0.5)	150 (200)
N_2	2	0.8 (0.5)	130 (190)
H_2O	3	2.0 (1.1)	50 (88)
CO_2	4	3.5 (2.2)	29 (45)
ϕ	5	1.5 (1.2)	65 (86)
CO	10	5.9 (4.2)	16 (23)
H_2	10	6.3 (4.3)	17 (24)

using wavelet filtering to remove the noise caused by the oversampling. Details on this technique will be published in [61]. Note that effective spatial resolution of the measurements is roughly 60 µm and is limited by the optical resolution of the imaging system, the laser beam diameter, and blurring effect of the flame itself, which is difficult to evaluate. However the wavelet filtered 20 µm data allows smooth gradients to be obtained at the 60 µm spacing. The precision of these wavelet filtered data is improved relative to the downsampled 103 µm data (the accuracy is unchanged), as shown in Table 3.4.

3.2.4 Velocity Characterization

Velocity characterization in *SwB* was performed using two-dimensional particle image velocimetry (PIV), giving the velocity components in the axial and radial directions. Three-dimensional stereo PIV measurements were performed but results from these experiments are omitted due to concerns over the accuracy of the results obtained. There were issues with obtaining high quality images of the seed particles in both cameras which were not surmountable due to the time constraints on the use of the stereo equipment. As such only results from the two-dimensional PIV measurements will be presented in the current work; this should be borne in mind when considering results from the swirling cases, which have a substantial component of velocity in the tangential direction.

3.2.4.1 2D velocity surveys

Preliminary velocity characterization was carried out by M. S. Sweeney using particle image velocimetry. The inner annulus, outer annulus, and co-flow were each seeded with 1 µm calcined aluminum oxide particles. The seeding was achieved by passing a portion of each air flow through simple turbulent jet seeders (see Figure 3.7). The seeders were based on a design by M. J. Dunn which had proven successful in previous experiments. It had the advantages of being suitable for relatively high flow rates, easily reloaded with seed particles, and simple and cheap to fabricate. Air enters through a 12.7 mm inlet at the base of the seeder. It is then forced through a number of small diameter holes near the wall of the main body. This creates a number of turbulent jets, which aerosolize the seed powder in the main body. This seeded flow passes through a perforated plate before exiting through a 12.7 mm outlet.

These particles were illuminated using a double-pulsed Nd:YaG laser (Litron Nano PIV) operating at 532 nm. The vertical laser sheets had sub-millimeter thickness at the burner centerline. Each pulse was separated by a dt of 16 µs. The dt value was chosen using an iterative parameter optimization process to ensure that the typical displacement of particles within the flow between each pulse was 3 pixel to 5 pixel. This is a standard procedure in PIV experiments, and it is necessary for sensible velocities to be derived from the data using correlation algorithms.

The light scattered by the seed particles was imaged using a CCD camera (LaVision Imager Pro X 4M) fitted with a Nikon AF Micro Nikkor 60 mm lens (f/4) and a 50 mm interference filter centred about 532 nm (0.5 nm FWHM). The imaged field was 69.3 mm wide by 69.3 mm tall, with a pixel resolution of 34.1 µm. Sample shots (both non-reacting

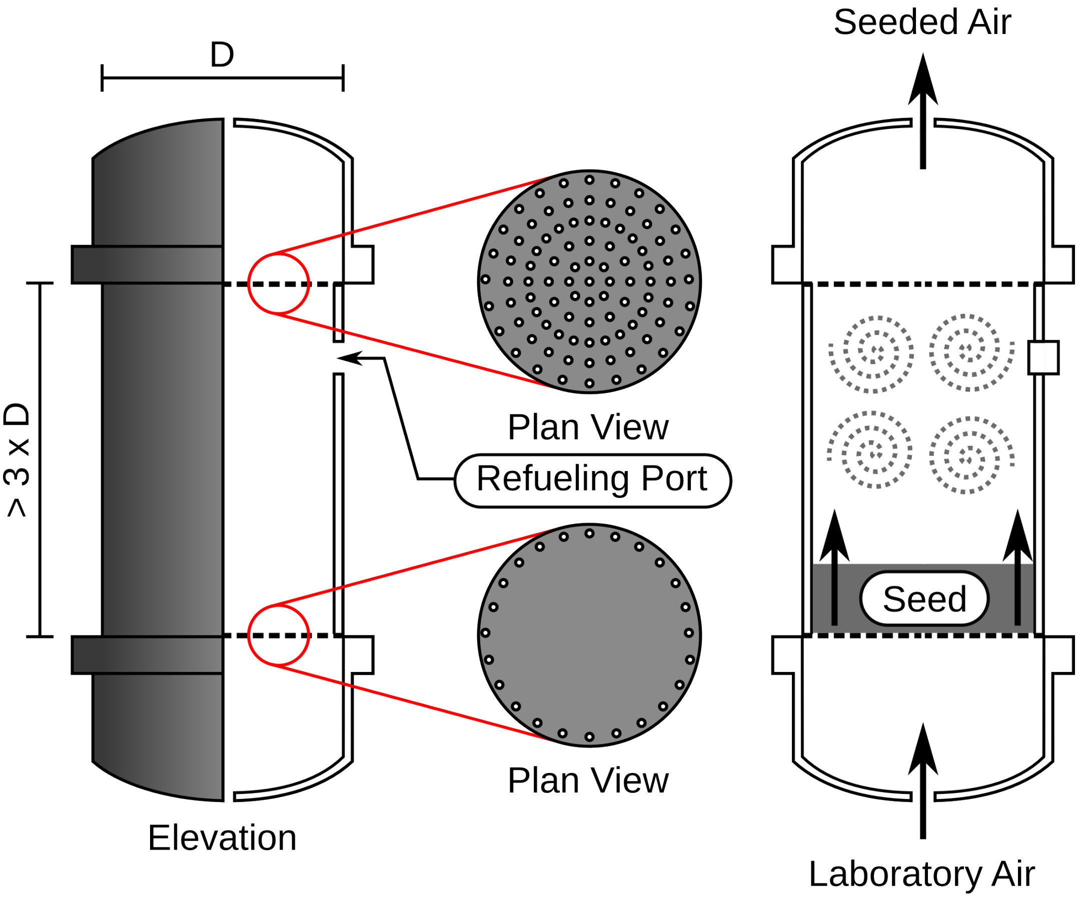

Figure 3.7: Illustration of seeder design. Dimensions are not to scale, and were varied based on the capacity required by the flow rates in the corresponding air supply. The perforated disks shown in plan view have a blockage ratio of 50 % and hole diameters of 1 mm; the hole patterns shown are for illustrative purposes.

and non-reacting) are shown for $SwB1$ in Figure 3.8. The sample shots also highlight potential issues with the reacting measurements. The signal intensity is significantly lower than in the non-reacting case, while the expansion of hot gas results in low seed density within the hot products. The results from the non-reacting cases are expected to be of higher accuracy than those from the reacting cases for these reasons.

Note that data below $z = 5\,\text{mm}$ was found to be unusable due to the high amounts of light reflected from seed particles that accumulate on the central bluff-body due to its associated recirculation zone. To prevent this interference, and any possible damage

Table 3.5: Number of instantaneous velocity fields recorded in PIV measurements of the reacting swirl burner cases.

SwB	1	2	3	5	6	7	9	10	11	13	14	15
#	5 000	2 000	1 000	5 000	2 000	2 000	5 000	1 000	2 000	5 000	2 000	1 000

to the imaging equipment, a light block was attached to the outside of the co-flow. This shielded the central bluff body from any incident laser light, and accounts for the absence of signal in the sample shots near to $z = 0\,\mathrm{mm}$.

The PIV system was run at 7.5 Hz, and the raw images were processed using LaVision software (DaVis 7.4). Algorithmic mask generation was used to constrain calculations to relevant areas in each image, and vectors were calculated using single-pass cross-correlation with a 32×32 window size and 50% overlap. This gives vector field resolution of 0.55 mm[c]. Muli-pass cross-correlation was not performed due to time constraints on the use of the LaVision-licensed workstation. 2 000 shots were taken in each of the non-reacting cases. 1 000 to 5 000 shots (Table 3.5) were taken in the reacting cases depending on the quality of signal obtained in the PIV images, and the time constraints mentioned previously.

3.3 Summary

The present chapter has detailed two separate stratified burners and the experimental campaigns applied to them. The first, SB, is a weakly turbulent rod-stabilized V-flame slot burner. The second, SwB, is a much more turbulent co-annular swirl burner. Operating matrices varying the stratification level (and the swirl level in the case of SwB)

---

[c] The resolution of the PIV measurements in terms of the smallest velocities it can resolve with adequate accuracy could be determined by investigating the frequency spectra obtained from the instantaneous velocity fields. However this analysis is non-trivial and due to time constraints has not been attempted in the present work.

have been detailed. Advanced multi-scalar laser diagnostics were applied to flames in both burners to measure temperature, equivalence ratio, and major species. Velocity characterization was performed using hot wire anemometry in the case of SB (experiments carried out by P. Anselmo-Filho) and two-dimension particle image velocimetry in the case of the swirl burner. These data require further processing to calculate the quantities which will be examined in later chapters (such as flame surface density, scalar dissipation rate and local curvature); details of the data analysis are given in Chapter 4.

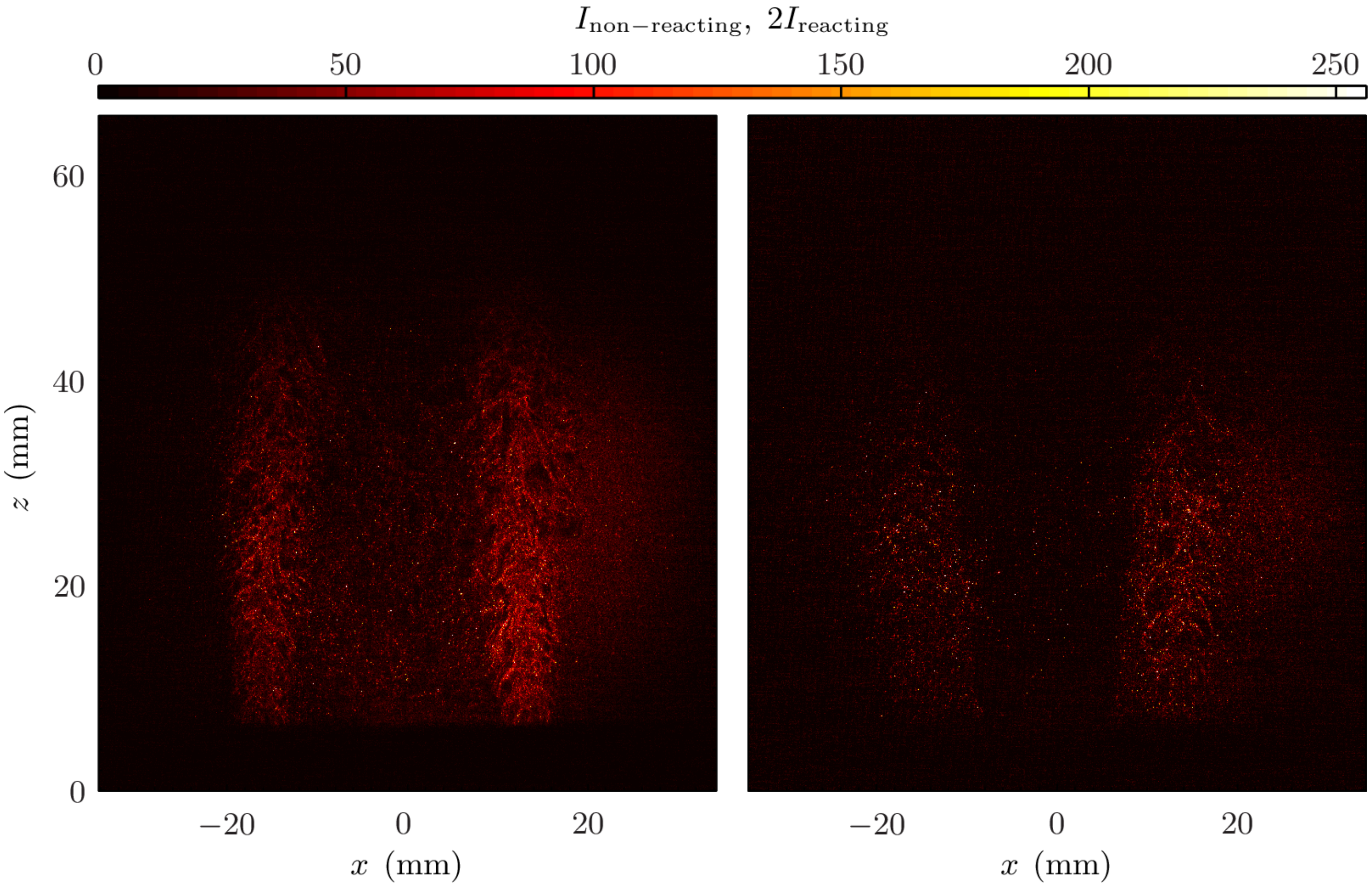

Figure 3.8: Randomly selected PIV shots from the non-reacting (left) and reacting (right) premixed non-swirling $SwB1$ case in the swirl burner.

Chapter 4

Data Processing Methodology

The data generated by the multi-scalar laser diagnostics detailed in the previous chapter provide a great deal of information on the instantaneous and mean structure of the CH_4/air flames surveyed. However, further processing is required to obtain many of the quantities relevant to combustion from the multi-scalar data. It is important to have a clear explanation of all data processing used, as the method of determining certain quantities (e.g., curvature) can affect the derived values to a non-trivial degree. Furthermore the details are necessary in the interests of reproducibility, enabling any future experimental and modeling investigations to make like-for-like comparisons with the results in the present work if so desired.

The data processing has been divided into three broad sections: OH image processing, scalar data processing, and flame surface density methods. The OH images obtained during the multi-scalar laser diagnostics provide information on the local topology of the flame. They can also be converted into two-dimensional progress variable images. A description of the image processing methods applied to the OH-PLIF data is given in Section 4.1.

The species data is used to calculate the equivalence ratio using a mole balance between hydrocarbon and oxygen mole fractions. The mixture fraction may be calculated using similar methods. These quantities as defined in the present work show substantial deviations through the flame front due to the effects of differential diffusion. This poses issues for conditioning results on local equivalence ratio, particularly in the stratified cases. Section 4.2 provides the definitions used in the present work for Z and ϕ, as well as the methodology employed to mitigate the differential diffusion effects mentioned previously. The progress variable, c, is defined and the methods used to derive scalar gradient terms such as scalar dissipation rate are also given.

Finally, three different metrics used to obtain flame surface density results from the experimental data are presented in Section 4.3. This data processing makes use of both the OH-PLIF images and the multi-scalar measurements. These metrics are compared and contrasted in Chapter 7.

4.1 OH Image Processing

The OH-PLIF images obtained during the experimental campaigns detailed in Chapter 3 are useful in their own right as they provide a qualitative impression of the regime the flame is operating in. The degree of wrinkling or convolution is easily observed, and any evidence of local extinction can be identified. As much of the OH production takes place within the reaction zone of the flame, the concentration of OH correlates reasonably well with the progress of reaction, and hence can provide a visual measure of the flame thickness. Although these are all qualitative uses of the OH-PLIF images, significant amounts of quantitative information may also be obtained from them. Various image processing techniques are employed to derive quantitative values for curvature, three-dimensional flame normal, and OH-based progress variable from the raw images, and these are detailed in the following subsections.

4.1.1 Pre-processing

The OH-PLIF images as recorded need a certain degree of pre-processing to obtain normalized images which allow subsequent processing (e.g., the extraction of OH contours) to be performed robustly. A sample unprocessed image is shown in Figure 4.1a. Note that the background level is significantly greater than zero counts.

The following steps, common in processing OH-PLIF images in the literature [27, 47, 62, 63], are applied to the raw images:

i) Background correction

ii) Laser power profile correction

iii) Normalization

Background correction is performed by taking a number of dark images (recorded with the laser shuttered) and averaging to get a mean dark image (Figure 4.1b) which is subtracted from the raw images.

There is a clear attenuation of signal in the top and bottom quarters of the raw image, due to the non-uniform distribution of power in the laser sheet. The sheet typically has a Gaussian power profile, for which corrections must be made.

To correct for these intensity variations, images are taken above a premixed stoichiometric CH_4/air flat flame at near adiabatic conditions in the product region ($\sim 30\,\mathrm{mm}$ downstream of the burner exit). The imaged region has an approximately constant OH concentration, and hence the intensity profile of the beam can be obtained. A sample mean sheet correction image is shown in Figure 4.1c. By dividing the raw OH image by the mean sheet it is possible to correct for the intensity variation seen in the raw image (Figure 4.1d). Finally the OH images are normalized between 0 and 1.

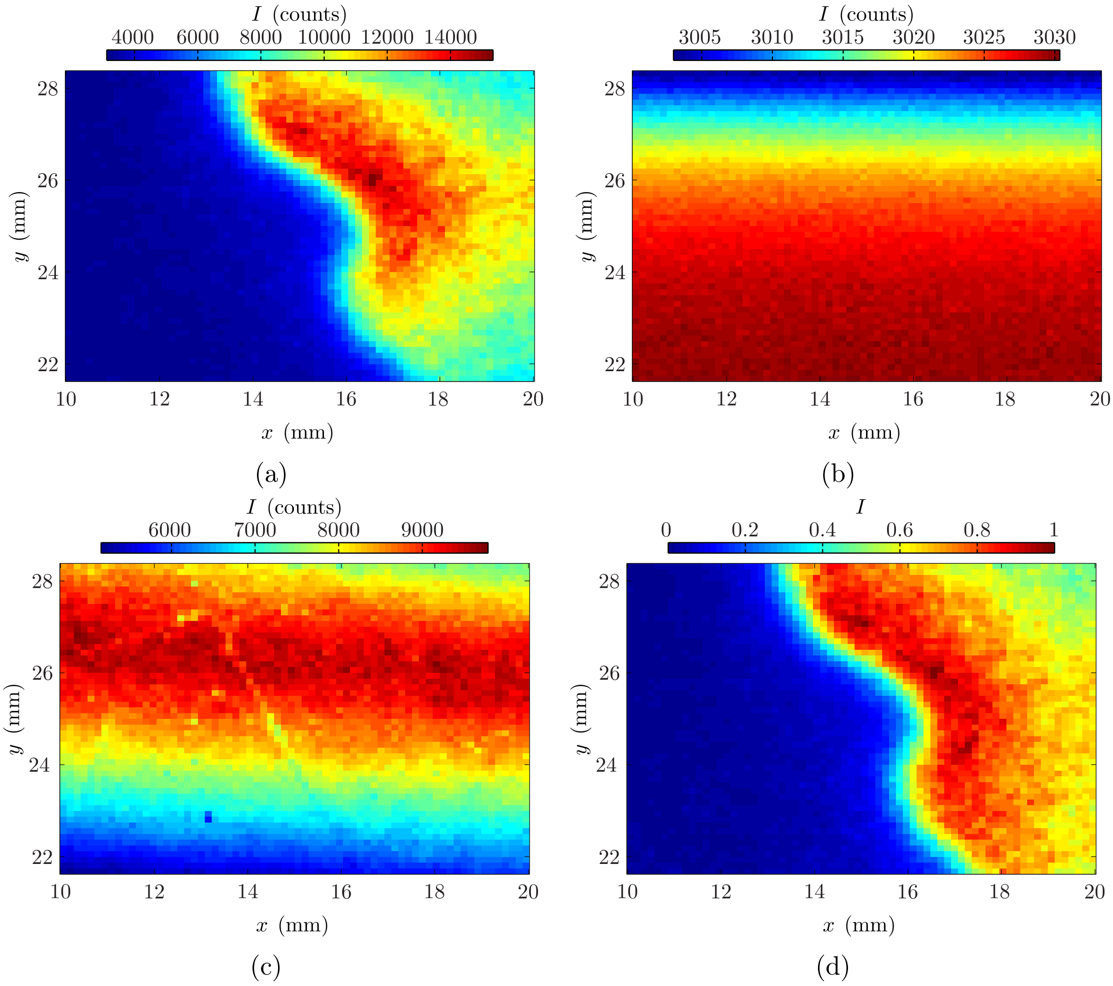

Figure 4.1: (a) Raw OH-PLIF image, (b) dark image, (c) sheet correction image, and (d) corrected OH-PLIF image.

4.1.2 Flame Front Extraction

OH-PLIF images are commonly used to derive flame fronts from experiments [24, 27, 56, 57, 63]. The flame front is defined as the contour of maximum OH gradient. This approach was taken to process the slot burner images, using an augmented Canny edge detection algorithm with autonomous parameter selection [62]. This method gives the optimal gradient-derived flame front in OH-PLIF images without *a priori* parameter selection, though it incurs significant computational cost.

This algorithm was deemed too computationally intensive relative to the accuracy benefits for processing the larger swirl burner image sets. A simpler threshold-based methodology was employed instead. Preliminary flame fronts were obtained in each image using a basic Canny edge detection algorithm with pre-determined parameters. The median OH value along the preliminary fronts was then used to threshold the image, and the final flame fronts were derived from the thresholded images. Flame fronts generated using the thresholding method on a sample set of 100 OH images from the premixed $SwB1_{30}$ case gave similar curvature values ($\overline{\kappa} = 0.05$ mm^{-1}, $\sigma_\kappa = 0.74$ mm^{-1}) to those obtained using the augmented Canny method ($\overline{\kappa} = 0.02$ mm^{-1}, $\sigma_\kappa = 0.83$ mm^{-1}), and were processed two orders of magnitude faster.

4.1.3 Flame Normal

Flame front geometry and the angle between the crossed planes were used to extract the three-dimensional flame normal, $\mathbf{n}$, at the line measurement axis [56, 57]. The normal was determined by resolving the two-dimensional flame tangents ($\mathbf{t_1}$, $\mathbf{t_2}$) in each plane from the 2D image coordinate system into the 3D laboratory coordinate system (Figure 4.2), and taking their cross product:

$$\begin{aligned}\mathbf{n} &= \mathbf{t_1} \times \mathbf{t_2} \\ &= \overbrace{(\dot{x}_1\ \mathbf{i} + \dot{y}_1 \sin\Omega\ \mathbf{j} + \dot{y}_1 \cos\Omega\ \mathbf{k})}^{\mathbf{t_1}} \times \overbrace{(\dot{x}_2\ \mathbf{i} - \dot{y}_2 \sin\Omega\ \mathbf{j} + \dot{y}_2 \cos\Omega\ \mathbf{k})}^{\mathbf{t_2}} \qquad (4.1)\end{aligned}$$

where 2Ω is the angle subtended by the crossed planes (here $\Omega = 30°$), the subscripts 1 and 2 correspond to the two OH-PLIF planes, and the coordinates $\mathbf{i}$, $\mathbf{j}$ and $\mathbf{k}$ are as shown in Figure 4.2. The normal vector, $\mathbf{n}$, is orientated such that it points from the products into the reactants. The angle θ between $\mathbf{n}$ and the line measurement axis,

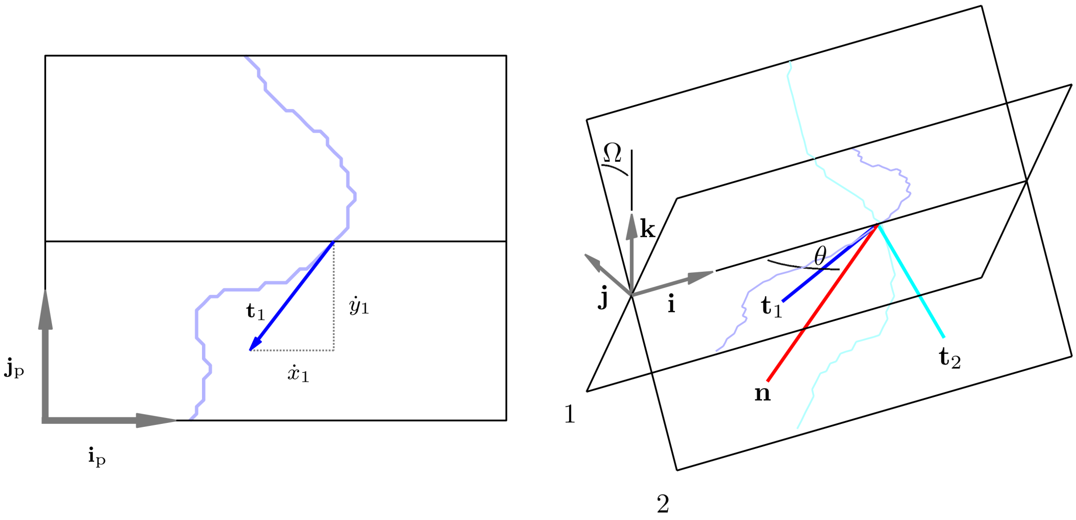

Figure 4.2: Planar coordinate system (*left*) and laboratory coordinate system (*right*). Note that $\mathbf{i}_\mathrm{p} = \mathbf{i}$ and $\mathbf{j}_\mathrm{p} = \sin\Omega\mathbf{j} + \cos\Omega\mathbf{k}$.

$\mathbf{x} = (1\ \mathbf{i} + 0\ \mathbf{j} + 0\ \mathbf{k})$, may be evaluated using the dot product rule:

$$\begin{aligned}\theta &= \arccos\left(\frac{\mathbf{n}\cdot\mathbf{x}}{|\mathbf{n}||\mathbf{x}|}\right) \\ &= \arccos\left(\mathbf{n}\cdot\mathbf{x}\right) \qquad (4.2)\end{aligned}$$

4.1.4 Curvature

Two methods of obtaining local 2D measurements of curvature from the OH-PLIF data are detailed in the following sections. These comprise a discrete method, which defines the curvature along the flame fronts defined in Section 4.1.2, and a continuous method which gives curvature throughout the imaged area. Note that these methods only provide two-dimensional analogues of the true three-dimensional curvature, and give neither the principal components of curvature nor related quantities. A potential avenue for determining the three-dimensional principal curvatures is described briefly in Chapter 8.

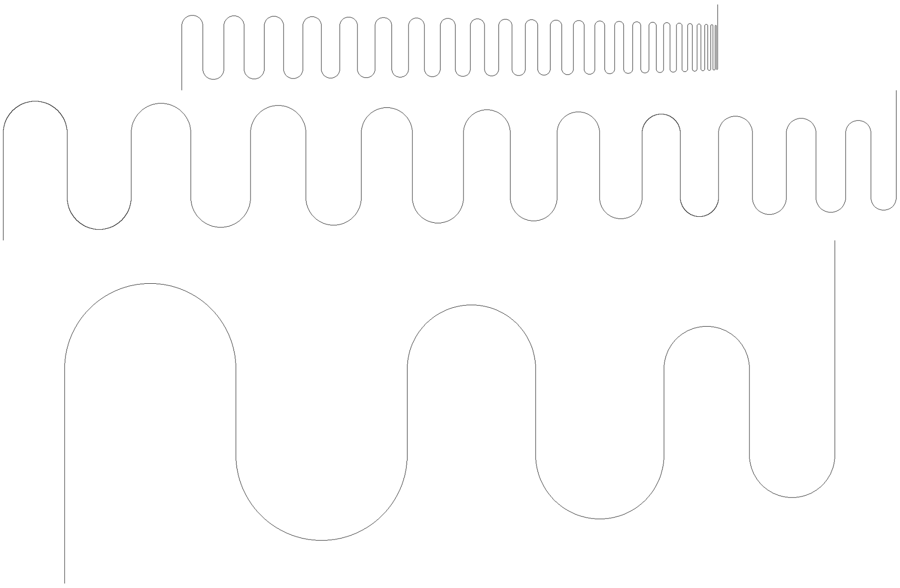

Figure 4.3: Curvature calibration images consisting of single pixel flame fronts with radii of between 2 and 200 pixel.

However the implementation of this technique is incomplete at the time of writing, and a more complete discussion of the methodology is beyond the scope of the present work.

4.1.4.1 Discrete Curvature

Each flame front contour was indexed using a simple 8-directional search algorithm, and the resulting x and y coordinates were indexed using the distance along the front, s. Third order polynomials were fitted to each x and y data point with respect to s using 14 neighboring points. The order of the fit and the number of points used were selected based on a sensitivity analysis using images of curves with known curvature[a]. The calibration images used are shown in Figure 4.3. The curves vary systematically from radii of curvature of 2 pixel to 200 pixel, which correspond to ranges of curvatures of $0.017\,\mathrm{mm}^{-1} \leq |\kappa| \leq 3.3\,\mathrm{mm}^{-1}$ $\left(0.05\,\mathrm{mm}^{-1} \leq |\kappa| \leq 10\,\mathrm{mm}^{-1}\right)$ at the OH-PLIF resolution

---

[a] The calibration images were generated by hand using GNU Image Manipulation Program [64].

of the slot (swirl) burner experiments.[b]

Indexing with respect to s prevents issues in polynomial fitting due to the fact that y is not in general a mono-valued function of x, $y \neq f(x)$. These polynomials are differentiated to determine $\dot{x} = \mathrm{d}x/\mathrm{d}s$, $\ddot{x} = \mathrm{d}^2x/\mathrm{d}s^2$, $\dot{y} = \mathrm{d}y/\mathrm{d}s$, and $\ddot{y} = \mathrm{d}^2y/\mathrm{d}s^2$ in the image coordinate system (Figure 4.2).

The discrete two-dimensional local curvature, κ_d, at any point on the flame front is given by the following expression using the quantities derived previously:

$$\kappa_\mathrm{d} = \frac{\dot{x}\ddot{y} - \dot{y}\ddot{x}}{\left(\dot{x}^2 + \dot{y}^2\right)^{\frac{3}{2}}} \tag{4.3}$$

where κ_d is taken as positive if the flame front is convex towards the reactants. The major limitation of this method is that it is only defined at the flame front itself, and hence line measurement data can only be curvature-conditioned at a single point, greatly reducing the size of potential datasets for such analysis.

4.1.4.2 Continuous Curvature

The discrete curvature described in the previous section is not well suited to conditioning other quantities as it is only defined along the single pixel flame front. A continuous measure of local 2D curvature along the line measurement window is necessary for sensible conditioning of the scalar data. Kass *et al* [65] give a definition applicable to the entire image using a formula that resembles Equation 4.3:

$$\kappa_\mathrm{c} = \frac{\frac{\mathrm{d}I}{\mathrm{d}x}^2 \frac{\mathrm{d}^2I}{\mathrm{d}y^2} - 2\frac{\mathrm{d}I}{\mathrm{d}x}\frac{\mathrm{d}I}{\mathrm{d}y}\frac{\mathrm{d}^2I}{\mathrm{d}x\mathrm{d}y} + \frac{\mathrm{d}I}{\mathrm{d}y}^2\frac{\mathrm{d}^2I}{\mathrm{d}x^2}}{\left(\frac{\mathrm{d}I}{\mathrm{d}x}^2 + \frac{\mathrm{d}I}{\mathrm{d}y}^2\right)^{\frac{3}{2}}} \tag{4.4}$$

---

[b] The OH-PLIF resolution is approximately 150 µm/pixel and 50 µm/pixel in the slot and swirl burner data respectively.

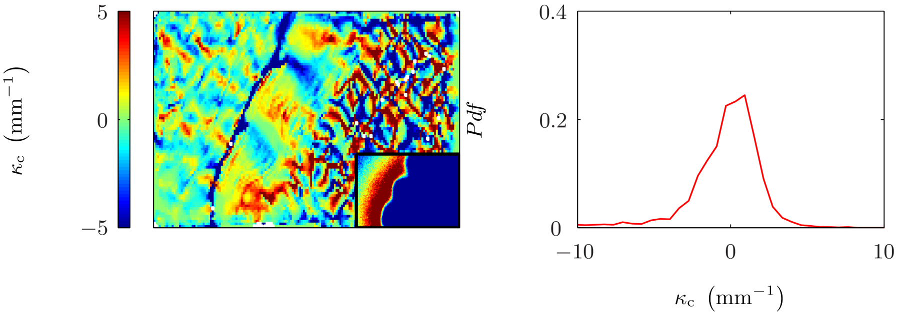

Figure 4.4: *Left to right*: Continuous curvature obtained from a sample OH-PLIF image (see inset) randomly selected from $SwB3$ at $z = 30\,\text{mm}$; corresponding distribution of continuous curvature using all data within 0.5 mm of the flame front. 50 evenly spaced bins between $-15\,\text{mm}^{-1}$ to $15\,\text{mm}^{-1}$ were used to generate the PDF.

where I is taken to be the signal intensity of the OH-PLIF image. This gives a local measure of two-dimensional curvature at every point in each OH-PLIF plane, as shown in Figure 4.4. Note that in the present work the experimental images and their gradients are smoothed using a two-dimensional median filter with a 5×5 pixel window size to prevent erroneous curvature values arising due to noise; this method is particularly noise-sensitive due to the presence of both first- and second-order differential terms. The curvature values calculated using Equation 4.4 are within the range expected for the turbulence intensities seen in the slot and swirl burner flames provided the signal to noise ratio (SNR) of the signal intensity is sufficiently high. The curvature values are interpolated to the line-based multi-scalar measurement resolution so that the scalar data can be conditioned on κ_c.

The continuous curvature values given by Equation 4.4 are not identical to the discrete measure given by Equation 4.3 even when assessed at the same location. However, the agreement is very good, as demonstrated by the sample case shown in Figure 4.5; furthermore, the correlation coefficient between κ_c and κ_d is $R = 0.914\,2$ when considering a 300 image dataset from the highly swirling premixed $SwB3$ case at $z = 30\,\text{mm}$.

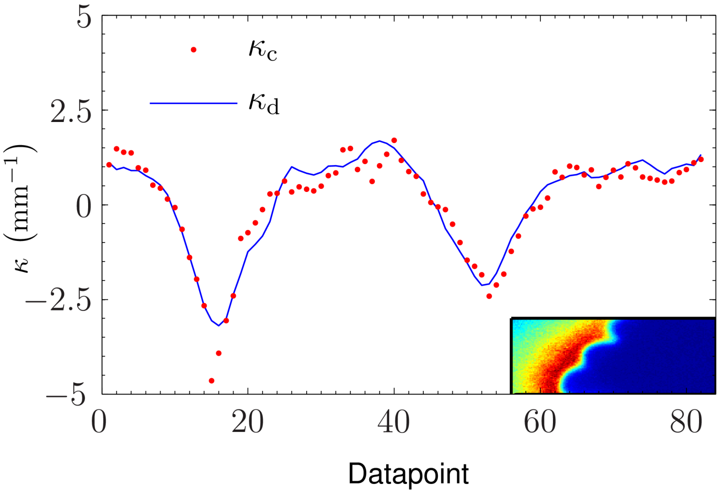

Figure 4.5: Comparison of discrete and continuous curvature methods applied to the same OH-PLIF image (see inset) from *SwB*3 30 mm downstream of the burner exit.

4.1.5 2D OH Progress Variable

OH-PLIF images are used to calculate flame surface density, as described further on in Section 4.3. However, the pre-processed images generated in Section 4.1.1 must first be converted into two-dimensional progress variable maps before they can be used to determine the flame surface density. Here the progress variable, c_{OH}, is defined as a normalization of the OH signal such that c_{OH} is zero valued in the unburned reactants, and unity valued in the products.

The level of OH in the flames surveyed is near-zero in the reactants, rises sharply in the reaction zone to a super-equilibrium peak, and decays towards final equilibrium relatively slowly in the products. Using OH as a scalar progress variable is complicated by the fact that normalization of OH by the final equilibrium value would permit $c_{\mathrm{OH}} \geq 1$ over a large area of the image. Thresholding images to identify flame regions at high OH gives poor results as the OH value may dip below the threshold on the product side due to the decay. An adjustment to the pre-processed OH images (Section 4.1.1) is necessary to produce an OH progress variable suitable for use in calculations, as follows.

The OH images are thresholded between product (foreground, $c_{\mathrm{OH}} = 1$) and reactant (background, $c_{\mathrm{OH}} = 0$) regions using the median OH signal value in pixels of high OH gradient (found using a simple Canny edge detection algorithm [66]) to determine the threshold value. This threshold value is below the minimum OH value in the equilibrium zone for the majority of cases. The perimeters of foreground regions are taken to be flame fronts. This methodology is employed over more rigorous gradient-based methods [62] to reduce computational costs. A thinning morphological operation [67] is applied iteratively to the foreground regions, eliminating a one-pixel thick perimeter from each foreground region with every iteration, until the perimeter with the maximum mean value of I_{OH} is identified; essentially defining the contour describing the super-equilibrium condition. Note that images are padded by replication at the edges to prevent problems arising where foreground regions cross the edges of the image.

The number of thinning operations, ζ, was increased until the mean OH value along foreground perimeters showed a global maximum ($\overline{\mathrm{OH}} = \mathrm{OH}_{\mathrm{g}}$ at $\zeta = N$), as shown in Figure 4.6. The maximum OH value along the perimeters for $\zeta = N$, $\mathrm{OH}_{\mathrm{max}}$, was noted. The enclosed foreground areas are taken to be product regions, and are set to $\mathrm{OH}_{\mathrm{max}}$ (plateaued). OH values between the perimeter of the plateaued region ($\zeta = N$) and the original product perimeter ($\zeta = 0$) were smoothed to avoid sudden jumps in signal by scaling the difference between the original data and $\mathrm{OH}_{\mathrm{max}}$. A Gaussian scaling function was used in the results presented in later sections. Values greater than $\mathrm{OH}_{\mathrm{max}}$ were set to 1. This operation preserves islands of products in the reactants and pockets of reactants in the products. This process defines a progress variable whereby complete reaction ($c_{\mathrm{OH}} = 1$) is strongly correlated with the location of maximum OH, which may result in discrepancies in comparisons with other progress variable definitions.

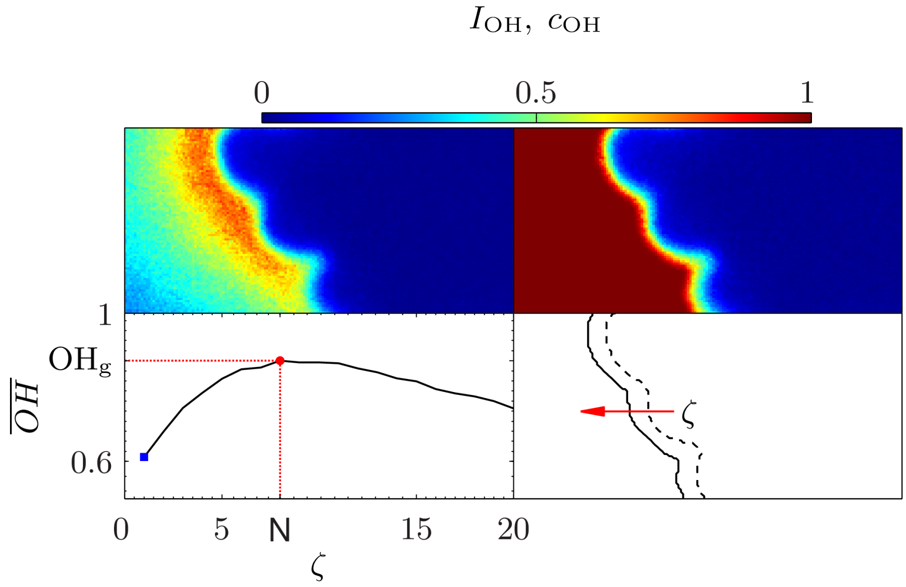

Figure 4.6: Demonstration of plateau technique applied to an OH image from $SwB11$. Clockwise from top left; pre-processed OH image; plateaued OH image; initial OH flame front ($\zeta = 0$) - - - -, perimeter at the global maximum ($\zeta = N$) ——; mean OH level along the contour associated with each degree of thinning ζ

4.2 Scalar Data Processing

The multi-scalar line measurements also require additional processing to obtain both a sensible form of equivalence ratio and also derived gradient-based quantities such as scalar dissipation rate. This section outlines the methodologies employed in the interests of reproducibility and transparency.

4.2.1 Mixture fraction and Equivalence Ratio

The mixture fraction, Z, is defined as a scalar which is conserved through a premixed flame, and is crucial to the formulation of a variety of modeling methods. In the present work mixture fraction is defined using the mass balance suggested by Bilger [68] for hydrocarbon fuels:

$$Z = \frac{2Y_{\mathrm{C}}/M_{\mathrm{C}} + 0.5Y_{\mathrm{H}}/M_{\mathrm{H}} + \left(Y_{\mathrm{O},2} - Y_{\mathrm{O}}\right)/M_{\mathrm{O}}}{2Y_{\mathrm{C},1}/M_{\mathrm{C}} + 0.5Y_{\mathrm{H},1}/M_{\mathrm{H}} + Y_{\mathrm{O},2}/M_{\mathrm{O}}} \tag{4.5}$$

where Y_{a} is the mass fraction of the sum of all measured species containing the element a, M_a is the atomic weight of element a, and the subscripts 1 and 2 refer to values in fuel and air respectively. This definition allows the mixture fraction to be approximately conserved across the reaction zone.

The present work also makes use of an equivalence ratio derived from an atomic balance as follows:

$$\phi = \frac{X_{\mathrm{CO_2}} + 2X_{\mathrm{CH_4}} + X_{\mathrm{CO}} + 0.5\left(X_{\mathrm{H_2O}} + X_{\mathrm{H_2}}\right)}{X_{\mathrm{CO_2}} + X_{\mathrm{O_2}} + 0.5\left(X_{\mathrm{CO}} + X_{\mathrm{H_2O}}\right)} \tag{4.6}$$

The equivalence ratio detailed in Equation 4.6 is the ratio of the demand for oxygen based on the local mass fractions of hydrogen and carbon to the locally available oxygen. This definition of equivalence ratio yields values that are close to those calculated using the scaled Bilger mixture fraction Z [68]:

$$\begin{aligned} \phi_{\mathrm{B}} &= \frac{Z}{1-Z}\frac{1-Z_{\mathrm{s}}}{1-Z} \\ &\approx \phi \end{aligned} \tag{4.7}$$

where the subscripts B and s refer to the Bilger definition and the stoichiometric value respectively. The relationship between Z and ϕ_{B} is approximately linear for the range of mixture fractions typically experienced within flammable methane/air flames ($0.0339 < Z < 0.0756$). This is due to Z and Z_{s} being small relative to unity, with the result that $\phi_{\mathrm{B}} \approx Z/Z_{\mathrm{s}}$.

4.2.1.1 The Effect of Differential Diffusion

Both the equivalence ratio in Equation 4.6 and the mixture fraction Z (and the derived ϕ_{B}) are constructed to be conserved scalars across a reaction zone, as carbon, hydrogen and oxygen are conserved elements across a flame. However, carbon- and hydrogen-containing species may have different molecular weights and diffuse at different rates. Hydrogen and water are smaller molecules than carbon monoxide and carbon dioxide, with the result that they may diffuse faster. This creates local imbalances in the carbon and hydrogen mass fractions at any position in the thermal ramp of a flame, such that the equivalence ratio as defined in Equation 4.6 is only approximately conserved in temperature space.

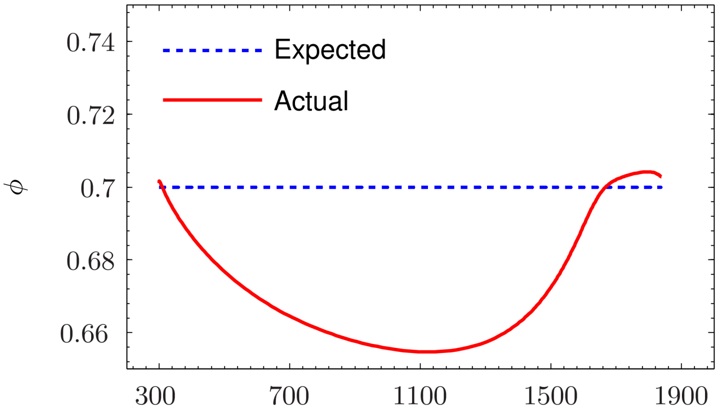

Figure 4.7: Demonstration of the effects of differential diffusion on equivalence ratio across an unstrained premixed laminar flame front. Data is taken from flame calculations with a nominal equivalence ratio of $\phi_{\mathrm{n}} = 0.7$.

Figure 4.7 demonstrates this behavior using an unstrained premixed laminar flame calculation. In the case shown the maximum deviation in equivalence ratio between the nominal and the observed value is 6.5 %; depending on the value of ϕ_{n} this peak deviation ranges from 6.0 % to 7.7 %. This is particularly relevant in the context of defining a local stoichiometry for a stratified flame, where the fuel/oxidizer ratio is by definition expected to exhibit spatial variation. Given the deviations in ϕ expected in a premixed flame, when the flame is stratified it is not possible to clearly separate the variation in ϕ due to differential diffusion effects from the spatial gradients in ϕ induced by the stratification itself.

Therefore, when comparing experimental premixed and stratified results, a correction process is required to allow for like-for-like comparisons to be made. This process should be robust, and create a framework within which rigorous comparisons conditioned on local equivalence ratio can be made. The approach employed in the present work is detailed in Section 4.2.3 after the concept of the progress variable is introduced (Section 4.2.2), which is required for some of the methodology discussed.

4.2.2 Progress Variable

The progress variable is a scalar c defined such that it has a value of zero in unburned reactants ($c_{\mathrm{u}} = 0$) and unity in the burned products ($c_{\mathrm{b}} = 1$). Typically this quantity is a normalization of temperature or chemical species concentration with respect to its values in both the burned and unburned gases. The definition of a suitable progress variable simplifies the description of the overall reaction, which involves multiple species, to a single variable which is uniquely related to the others. However the behavior of the progress variable is dependent on the choice of basis, as mentioned in Section 2.2 of Chapter 2, and hence care must be taken when comparing results in c-space from various studies.

The progress variable has many applications in premixed flame modeling. Important examples include its probability density function (pdf), a key component of Bray-Moss-Libby flamelet modeling [7], and its gradient $|\nabla c|$, which is integral to flame surface density (FSD) modeling [8, 69].

The present work makes use of a thermal progress variable, $c\left(T\right)$. In a purely premixed flame this is simply a normalization of the local flame temperature by the maximum temperature attained in the burned products and the temperature of the unburned reactants, as given in Equation 2.2 in Section 2.2 of Chapter 2[c]. However, if this is applied to a flame in which the equivalence ratio field is varying spatially, errors are introduced. Hence, the equilibrium temperature used in the calculation of the thermal progress variable must be allowed to vary with local equivalence ratio:

$$c_{\mathrm{T}}\left(x,\phi\right) = \frac{T\left(x\right)-T_{\mathrm{u}}}{T_{\mathrm{e}}\left(\phi\right)-T_{\mathrm{u}}} \tag{4.8}$$

where $T\left(x\right)$ is the local temperature, T_{u} is the temperature in the unburned reactants, and $T_{\mathrm{e}}\left(\phi\right)$ is the equilibrium flame temperature as a function of ϕ (determined from premixed unstrained laminar flame calculations[d]). This form of thermal progress variable is much more suitable for flames with a significant degree of stratification than a basic temperature normalization.

Figure 4.8 demonstrates that while there may not be substantial deviations between $c\left(T\right)$ and $c\left(T,\phi\right)$ in the pre-heat and reaction zones, there are clear differences between the two measures in the equilibration zone. In the present work the progress variable defined in Equation 4.8 is used throughout. Results presented in Chapter 5 and Chapter 6 use the differential-diffusion corrected ϕ to determine $c\left(T,\phi\right)$.

4.2.3 Differential Diffusion Correction

The effects of differential diffusion detailed in Section 4.2.1.1 require the equivalence ratio calculated from the species measurements to be corrected in order for sensible con-

---

[c] Strictly speaking, thermal enthalpy should be used; however, deviations from this definition due to the use of temperature are small.

[d] Laminar flame calculations were generated using CHEMKIN [70] and GRI-Mech 3.0 [71]

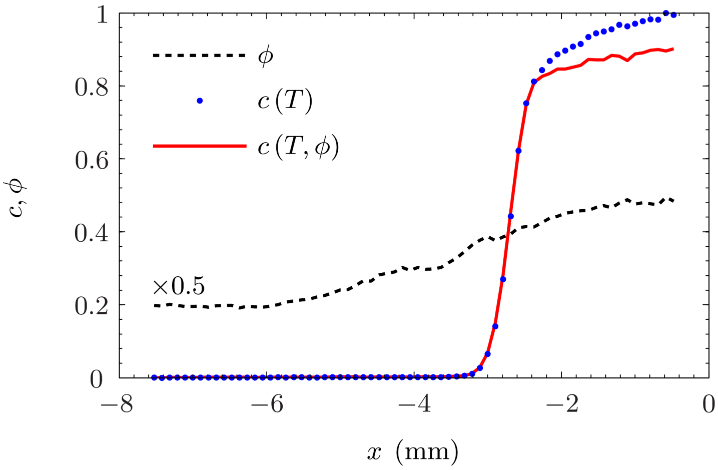

Figure 4.8: Variation in progress variable c where the equilibrium flame temperature T_{e} is based on T in the reactants ($c\,(T)$) or is taken to be a function of the local stoichiometry ($c\,(T,\phi)$). Sample data is randomly selected from the highly stratified $fs6_{25}$ case in the slot burner.

ditioning and comparison of other measured quantities to be made. Two such correction methods have been considered during the course of this research; a lookup table of correction factors based on the deviations observed in premixed laminar flame calculations, and a linear bridging function between the pre-heat zone and the equilibration zone.

The methodologies are detailed in Section 4.2.3.1 and Section 4.2.3.2 respectively. Premixed data from both the slot ($fs1$) and swirl burner ($SwB1$) are corrected using each of these methods. The lookup table method is shown to alter but not correct for the deviations in local equivalence ratio in experimental data as it fails to take into account the turbulence dependence of the differential diffusion effect; the linear bridging method is deemed more suitable in light of this and is applied to all data presented in subsequent sections.

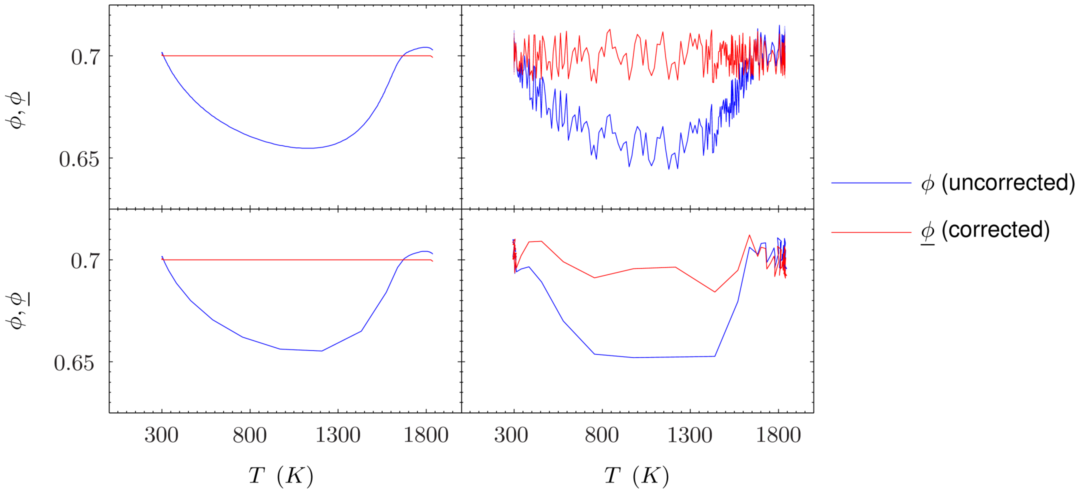

Figure 4.9: Demonstration of the differential diffusion correction using data from unstrained premixed laminar flame calculations where $\phi_\mathrm{n} = 0.7$. *Clockwise from top left*: high resolution (8 µm), smooth values from calculations; high resolution values with added noise; values downsampled to the slot burner experimental resolution (105.2 µm) with added noise; experimental resolution, smooth values.

4.2.3.1 Lookup Table Approach

A lookup table of correction factors to adjust for the effect of differential diffusion on equivalence ratio was derived from premixed unstrained laminar flame calculations. Equivalence ratio corrected using the lookup table approach is denoted in the present work by $\underline{\phi}$. The result of applying these correction factors to laminar flame calculations at high resolution and at the resolution of the multi-scalar experiments is shown in Figure 4.9. The equivalence ratio is reconstructed to the nominal values whether the original data is smooth or noisy. The noise applied has a Gaussian distribution, zero mean, and a standard deviation of 1.5×10^{-3}, which results in similar levels of point-to-point noise as that seen in the experimental data.

It is worth noting that the effects of differential diffusion on equivalence ratio are not the same across different flame conditions or types. This can be seen in Figure 4.10, which shows the effect of the correction on experimental data from: a vertical premixed

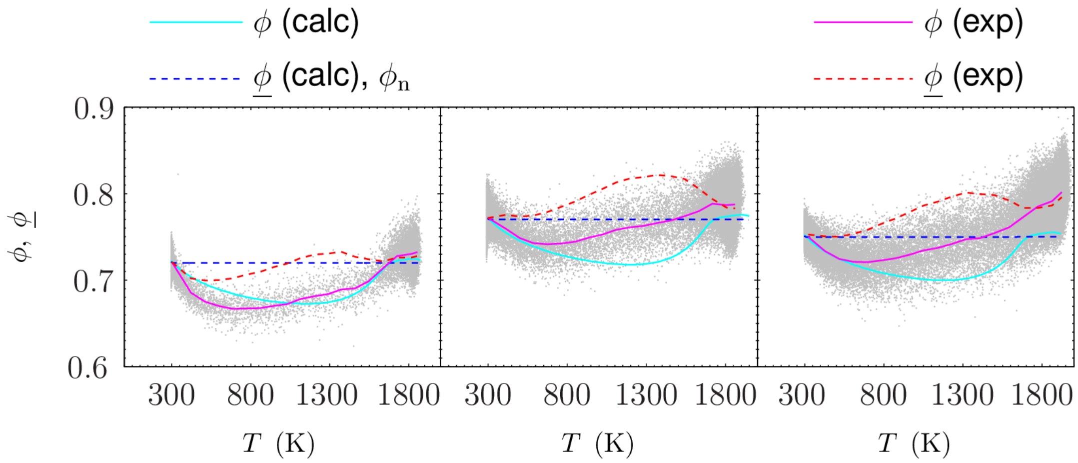

Figure 4.10: Scatter plots and mean fits of equivalence ratio from experiments on a laminar vertical premixed flame (vf), a weakly turbulent premixed flame ($fs1_{25}$), and a more turbulent premixed flame ($SwB1_{30}$), demonstrating the varying influence of differential diffusion. Calculated values from laminar unstrained flame calculations at the corresponding stoichiometry are also shown. Values of $\underline{\phi}$ are determined using a lookup table derived from calculations.

laminar methane/air flame, denoted vf in the figure; the $fs1$ case from the slot burner; and the $SwB1$ case from the swirl burner. The data in the vertical burner vf was obtained by R. S. Barlow using the same methodology as that for the swirl burner, described in Section 3.2.3 of Chapter 3. The vertical flame burner is shown for reference in Figure 4.11, and further details are given in a publication by Barlow *et al* [72] (in submission at the time of writing). The three cases listed are premixed, non-swirling flames, and are arranged in order of increasing turbulence.

Applying the correction factors obtained from flame calculations to the experimental data allows like-for-like comparisons, but still results in equivalence ratio values which vary with temperature, albeit in a different manner. It should be noted that the $SwB1$ case shows significantly elevated equivalence ratio on the product side (7.5 % greater than the mean reactant value). This is due to the effect of the recirculation zone above the central bluff-body in the swirl burner, and is discussed in depth in Chapter 6. The results

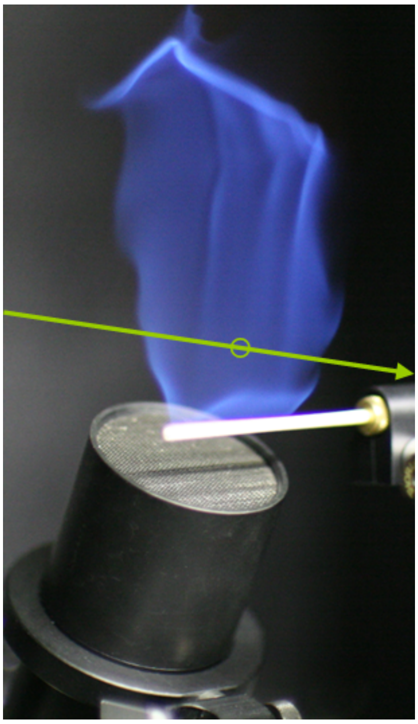

Figure 4.11: Vertical flame burner vf with multi-scalar line measurement axis shown schematically. Figure adapted from [72].

from the vertical burner and the slot burner are considered in the ensuing discussion as the influence of the elevated product-side equivalence ratio makes it difficult to evaluate the correction in the swirl burner case.

The differences between the uncorrected calculated and experimental mean values are small in the laminar case compared with the others, indicating that the differential diffusion effect may be coupled to local turbulence levels. This observation is corroborated by the analysis of differential diffusion effects by Barlow *et al* [72]. However even in the laminar flame the $\underline{\phi}$ data exhibits non-trivial variation with temperature (up to $3\,\%$ relative to ϕ_n). Without a more complete knowledge of the variables governing the differential diffusion effects, and their relative importance, the lookup table method does not appear to be a viable route for processing the equivalence ratio data, and as such is

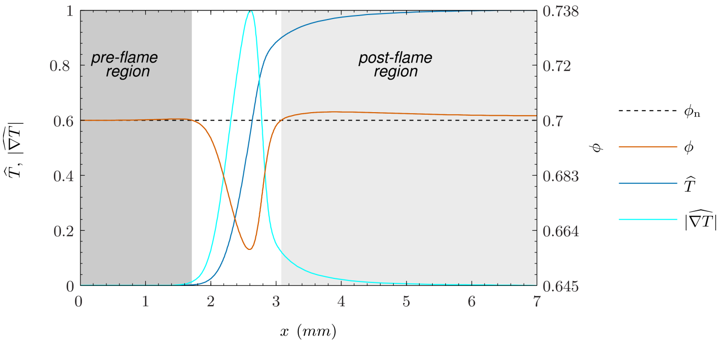

Figure 4.12: Diagram illustrating the location of the pre- and post-flame regions, where the equivalence ratio dips below its nominal value $\phi_{\mathrm{n}} = 0.7$. Normalized temperature and its gradient are also plotted.

not used further in this work.

4.2.3.2 Linear Bridging Function Approach

Figure 4.12 shows the variation of equivalence ratio in space in a premixed laminar flame calculation due to differential diffusion, as well as the normalized temperature $\widehat{T}$ and the normalized temperature gradient $|\widehat{\nabla T}|$. At the beginning of the pre-heat zone ($\widehat{T}$, $|\widehat{\nabla T}| << 1$) and near the end of the equilibrium zone ($\widehat{T} \sim 1$, $|\widehat{\nabla T}| << 1$) the equivalence ratio derived using Equation 4.6 is close to the nominal value. A possible approach to correct the equivalence ratio data as measured is therefore to linearly interpolate between the pre- and post-flame regions, where differential diffusion effects are significant. The resulting linear bridged equivalence ratio is denoted by Φ. This approach is reasonable provided the length scales associated with equivalence ratio variations due to stratification are larger than the thermal length scales of the flame.

The algorithm used to apply this linear bridging function to the experimental data is summarized in the flow chart in Figure 4.13. The temperature data is normalized using the maximum and minimum values to give $\widehat{T}$. The normalized gradient $|\widehat{\nabla T}|$ is obtained in a similar manner after applying a second order central-differencing scheme to the temperature data. These normalized quantities are thresholded to obtain estimates of the location of the pre- and post-flame regions. Figure 4.14 shows the values of the normalized quantities in premixed laminar flame calculations (taken at the locations where the equivalence ratio first dips below the nominal value on both the reactant and product side of the differential diffusion deviation) for a range of compositions.

The initial values of $\widehat{T}_1 = 0.025$, $\widehat{|\nabla T|}_1 = 0.1$ and $\widehat{T}_2 = 0.95$, $\widehat{|\nabla T|}_2 = 0.1$ were chosen empirically to determine the pre- and post-flame regions respectively. These values were selected as a compromise between the intermediary values of the thresholds, and the desire to minimize jitter in the thresholded regions due to noise in the burned and unburned gases.

After the normalized quantities are thresholded, spurious signals are removed. Isolated peaks and dips in the thresholded profiles are removed by convolution with suitable kernels, while broader troughs and peaks (up to a maximum width of three times the experimental resolution) are either eliminated or filled after being identified.

Using the thresholded profiles, the mean equivalence ratio in the pre- and post-flame regions is obtained from a three point average of the equivalence ratio data at the respective locations. These mean equivalence ratio values are used to refine the estimates of the thresholds $\widehat{T}_1$, $\widehat{|\nabla T|}$, $\widehat{T}_2$, and $\widehat{|\nabla T|}_2$ by interpolating the calculated parameters (Figure 4.14) in equivalence ratio space.

The thresholding process is then repeated using the new threshold values. The new mean equivalence ratio in the pre- and post-flame regions is compared with the old values, and the process is iterated until the mean difference between the old and new values is less than 0.5 %. Once this criterion has been fulfilled the equivalence ratio data is linearly interpolated between the two regions using the final mean equivalence ratio values. Note that the criterion was selected empirically, and a rigorous sensitivity

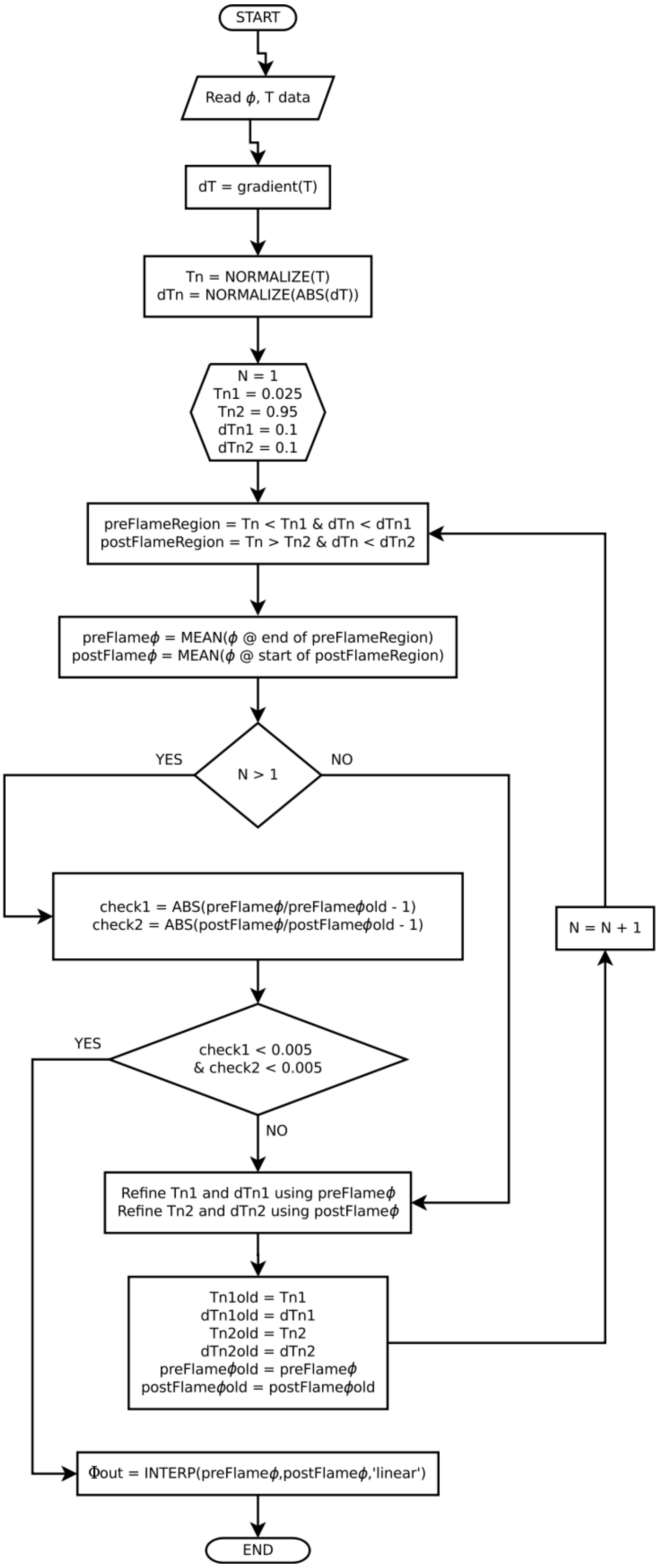

Figure 4.13: Flow chart illustrating the process flow involved in applying a linear bridging function to equivalence ratio data. Note that $\widehat{T}$ and $\widehat{|\nabla T|}$ are shown as Tn and dTn respectively.

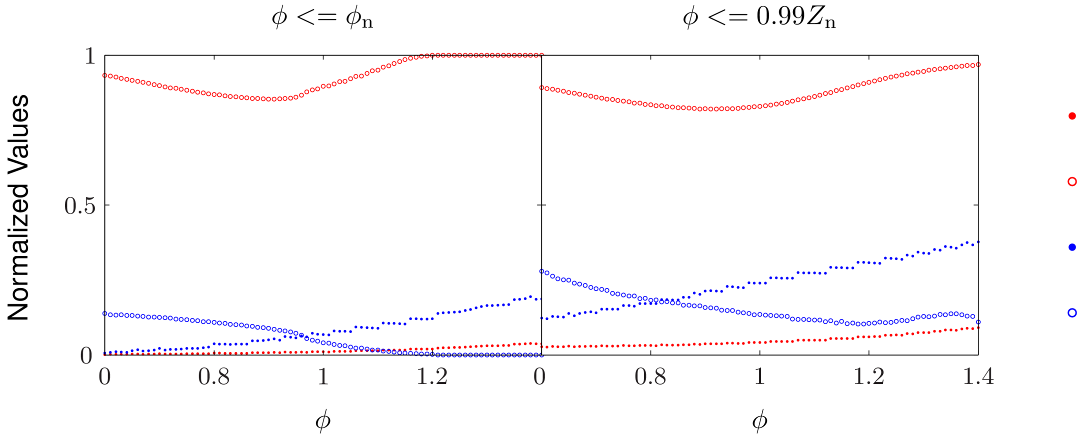

Figure 4.14: Values of normalized temperature and temperature gradient marking the locations of the pre- and post-flame regions for a range of compositions. The data are taken from laminar premixed calculations at the points where the equivalence ratio first dips below the nominal equivalence ratio (LHS) and 99 % of the nominal equivalence ratio (RHS).

analysis remains to be performed.

The algorithm as described typically takes two iterations to converge for the premixed $fs1_{25}$ case and six iterations for the highly stratified $fs6_{25}$ case, with computation times of 2.74 ms and 11.14 ms per shot respectively. It was found that by using the calculated threshold parameters at the locations where the equivalence ratio dipped below 99 % of the nominal value (RHS in Figure 4.14), the mean equivalence ratios in the pre- and post-flame regions converged to the same values and locations as when the previously described thresholds were used, but with less iterations required for the stratified cases (two instead of six). As a result the present work uses these threshold values due to the reduction in computational expense. Examples of instantaneous data from the $fs1_{25}$, $fs4_{25}$, and $fs6_{25}$ cases are shown in Figure 4.15, both raw and after the application of the linear bridging function.

The effect of the linear bridging function when considered on the mean is shown in Figure 4.16 for both the vertical flame case vf and the premixed slot burner case

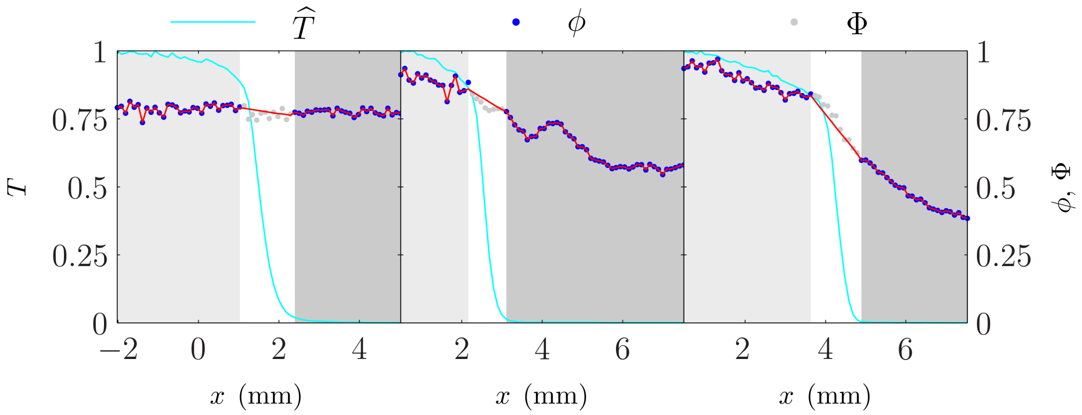

Figure 4.15: Demonstration of linear bridging function applied to equivalence ratio profiles from $fs1_{25}$, $fs4_{25}$, and $fs6_{25}$ cases (left to right). Raw equivalence ratio data is plotted with filled markers (gray within the linear bridging region, blue without), while the linear bridged data is plotted in red. Normalized temperature is plotted in cyan, and pre- and post-flame regions are shaded dark and light gray respectively.

$fs1_{25}$. The vf case yields mean values very close to the nominal equivalence ratio value Φ_n following the application of the linear bridging function. The $fs1_{25}$ case shows significantly less variation through intermediate temperature values than the uncorrected data, with the mild slope seen attributable to the uncorrected equivalence ratio data in the product region being biased high by approximately 2 %. It may be possible to correct for this discrepancy by determining the degree of bias — by comparing mean equivalence ratio at $c \approx 0$ and $c \approx 1$ — and multiplying the equivalence ratio values in the post flame region by a suitable correction factor. The robustness of such a correction has yet to be evaluated, and so the present work does not attempt to modify the post-flame equivalence ratio values.

4.2.4 Scalar Gradients

The rate of change of scalars is often of interest in combustion. The present work is only concerned with spatial gradients, as the time resolution of the multi-scalar mea-

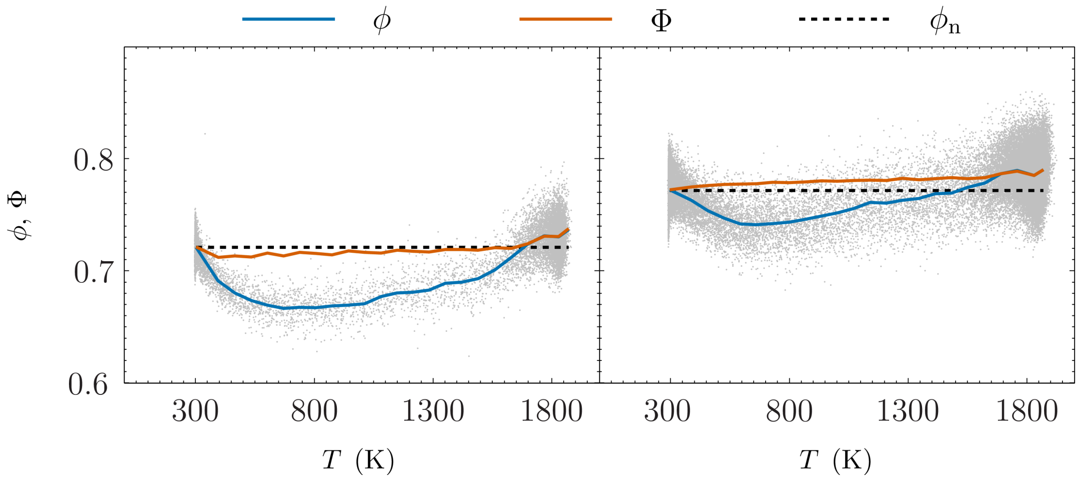

Figure 4.16: Scatter plots and mean fits of equivalence ratio from experiments on a laminar vertical premixed flame (vf) and a weakly turbulent premixed flame ($fs1_{25}$), demonstrating the effect of linear bridging the local equivalence ratio data to give the bridged equivalence ratio, Φ. The gray scatter data are instantaneous uncorrected equivalence ratio values, ϕ.

surements does not allow the calculation of valid time derivatives. The methods used to obtain these gradients are detailed in this section.

Discrete Differentiation: Scalar gradients are obtained by applying finite differencing schemes to discrete experimental data, rather than explicitly differentiating known mathematical functions. A variety of finite difference schemes are available to the experimentalist (See Table 4.1), though in the present work all gradients are obtained using a simple second order central-differencing scheme, with forward- and backward-differencing schemes applied at the edges of the line measurement data. The main motivation for using such a simple scheme is to reduce spatial averaging which increases in magnitude with differentiation scheme order due to the relatively coarse resolution of the 103 µm experimental data. The use of a second order scheme also minimizes the propagated error (higher order schemes require more points) and helps to avoid very noisy gradients in measurements from the equilibration zone, where typically the scalar data exhibits point-to-point jitter.

Order	F_{-5}	F_{-4}	F_{-3}	F_{-2}	F_{-1}	F_{-0}	F_1	F_2	F_3	F_4	F_5
2nd					$\frac{1}{2}$	0	$-\frac{1}{2}$				
4th				$-\frac{1}{12}$	$\frac{2}{3}$	0	$-\frac{2}{3}$	$\frac{1}{12}$			
6th			$\frac{1}{60}$	$-\frac{3}{20}$	$\frac{3}{4}$	0	$-\frac{3}{4}$	$\frac{3}{20}$	$-\frac{1}{60}$		
8th		$-\frac{1}{280}$	$\frac{4}{105}$	$-\frac{1}{5}$	$\frac{4}{5}$	0	$-\frac{4}{5}$	$\frac{1}{5}$	$-\frac{4}{105}$	$-\frac{1}{280}$	
10th	$\frac{1}{1260}$	$-\frac{5}{504}$	$\frac{5}{84}$	$-\frac{5}{21}$	$\frac{5}{6}$	0	$-\frac{5}{6}$	$\frac{5}{21}$	$-\frac{5}{84}$	$\frac{5}{504}$	$-\frac{1}{1260}$

Table 4.1: Central finite difference coefficients for the first derivative to varying orders of accuracy.

Angle Correction: The 3D flame normal is rarely coincident with the line measurement axis, $\mathbf{n} \cdot \mathbf{x} \neq 1$, as seen in Figure 4.2. Therefore, the gradient of any given scalar with respect to x, or $\mathbf{x}$, is expected to be smaller that the 3D value in most realizations as it is a projection of the true gradient. A first order correction is obtained by dividing gradients by the cosine of the solid angle θ between the flame normal and the line measurement axis. However, the uncertainties in the measurement are amplified by the correction as the solid angle increases, to the extent that the accuracy of the gradient values deteriorates substantially [56]. The angle-corrected gradient of any scalar ψ is thus given as $\mathrm{d}\psi/\mathrm{d}n = (\mathrm{d}\psi/\mathrm{d}x)\,/\cos\theta,\ \theta \leq \theta_{\mathrm{m}}$.

Note that for this correction to be strictly valid, the angle θ should be obtained as in Equation 4.2 using the same scalar field as the scalar whose gradient is being corrected. It is assumed in the present work that the OH field is well correlated with the temperature field in three-dimensional space. Hence the solid angle θ derived from the OH-PLIF measurements can be used to correct temperature gradients in the present work.

Resolution correction: Differentiation of discrete scalar data introduces errors in the calculation of gradients which are a function of the experimental resolution, the most notable effect of which is the systematic reduction of peak gradient values. These errors can be reduced by the use of higher order differentiation schemes, but such methods increase the propagated uncertainty in the derived gradients substantially in comparison to simple second order central-differencing, due to the increased number of sampled points. In the present work a basic resolution correction factor has been used to compensate for the effects of measuring scalars at the experimental resolution. This is not applied to the 20 µm wavelet filtered data as the attenuation is negligible.

Laminar calculations for premixed unstrained CH_4/air flames were used to generate noise-free spatial profiles of temperature, T, and another scalar, ψ, at much finer resolutions than is feasible in experiments, for a range of discrete equivalence ratios, $0.6 \leq \phi \leq 1.4$. The calculated equivalence ratios were corrected for differential diffusion effects. The scalar profiles were differentiated using a tenth order accurate scheme (See Table 4.1) to give the fine resolution gradient $\mathrm{d}\psi/\mathrm{d}x|_\mathrm{f}$. The profiles were then resampled at the experimental resolution before once differentiating using a second order scheme to calculate gradients at this resolution, $\mathrm{d}\psi/\mathrm{d}x|_\mathrm{e}$. A look-up table of ϕ, T and the resolution correction-factor $R = (\mathrm{d}\psi/\mathrm{d}x|_\mathrm{e})\,/\,(\mathrm{d}\psi/\mathrm{d}x|_\mathrm{f})$ was created, and bilinear interpolation in local temperature and equivalence ratio is performed to estimate the local resolution correction factor $R\,(T,\ \phi)$.

This correction brings the accuracy of second order differentiation schemes in line with higher order schema. This approximation is only valid where the scalar is strongly correlated with T and ϕ, which is the case for the progress variable c considered in this study. Additionally, it is assumed that correction factors obtained in laminar unstrained flames will be similar to the experimental turbulent flames for a given ϕ and T. The correction factors obtained may be biased slightly high, as turbulence has been reported to increase flame thickness relative to equivalent laminar cases [73, 74]. The final expression for the gradient of the scalar is thus:

$$|\nabla\psi| \quad = \quad \left|\frac{\mathrm{d}\psi/\mathrm{d}x}{R\cos\theta}\right| \tag{4.9}$$

The change in progress variable gradient ∇c due to this correction factor is small relative to the peak values attained through the flame ($1\,\mathrm{mm}^{-1}$ to $2.26\,\mathrm{mm}^{-1}$ in the current work); the mean magnitude of the correction is approximately $30\,\mathrm{\mu m}^{-1}$, with a maximum correction on the order of $100\,\mathrm{\mu m}^{-1}$.

Scalar Dissipation Rate: The scalar dissipation rate, χ_c, determines how quickly fluctuations in progress variable decay within the flame. Furthermore it is a measure of the mixing rate of reactants and products, and is proportional to the mean burning rate (assuming fast chemistry and mixing limited combustion). It appears directly or indirectly in both premixed [10, 11, 38, 75, 76] and nonpremixed [76–79] combustion models. It also appears as a sink term in the scalar variance equation. The mixture fraction dissipation rate, χ_Z, and the cross dissipation rate, $\chi_{Z,c}$, are also important quantities (particularly in non-premixed combustion), but are not considered further as they cannot be derived from the current experimental datasets due to the lack of information on the three-dimensional mixture fraction field. The scalar dissipation rate is given by the following expression:

$$\chi_c = \alpha|\nabla c|^2 \tag{4.10}$$

where the thermal diffusivity, α, is obtained by interpolating a lookup table of calculated values in temperature and equivalence ratio. The calculated thermal diffusivity values were taken from unstrained premixed laminar flame calculations.

4.2.5 Error analysis

The uncertainties introduced in the evaluation of the quantities detailed previously are quantified so as to understand which effects may be due to physical factors, such as flame straining and curvature, and which may be artifacts of the data analysis itself. The precision of these derived quantities, σ, are determined through the application of error propagation in conjunction with the experimental uncertainties listed in Table 3.4 and Table 3.4. The equations used are lengthy and so are detailed separately in Appendix B.

Table 4.2: Table of propagated uncertainties for derived quantities in the slot burner and the swirl burner. Uncertainties for each quantity are expressed as a percentage of the mean value of the scalar at the location of peak $|\nabla c|$.

Flame	y (mm)	$\sigma_{T_{\text{eq}}}$ (%)	σ_c (%)	σ_α (%)	$\sigma_{\|\nabla c\|}$ (%)	σ_{χ_c} (%)
$fs1$	25	0.13	1.01	1.22	2.63	5.38
	30	0.13	1.01	1.22	2.65	5.43
$fs4$	25	0.13	1.03	1.22	2.15	4.47
	30	0.14	1.03	1.22	2.65	5.39
$fs6$	25	0.13	1.03	1.23	2.06	4.30
	30	0.14	1.02	1.25	2.84	5.91
$SwB1$	10	0.89	1.40	1.16	3.84	7.75
$SwB2$	10	0.87	1.38	1.17	3.89	7.83
$SwB3$	10	0.91	1.43	1.16	5.57	9.86
$SwB5$	10	0.55	1.12	1.17	2.36	4.84
$SwB6$	10	0.52	1.09	1.18	2.41	4.91
$SwB7$	10	0.61	1.14	1.17	2.73	5.41
$SwB9$	10	0.13	0.90	1.23	3.20	6.48
$SwB10$	10	0.14	0.92	1.22	2.75	5.57
$SwB11$	10	0.38	0.98	1.21	2.89	5.67
$SwB13$	10	0.49	1.08	1.18	2.34	4.79
$SwB14$	10	0.51	1.09	1.18	2.41	4.94
$SwB15$	10	0.53	1.13	1.17	2.10	4.34

The resulting uncertainties for both the slot and swirl burner datasets are listed in Table 4.2. Uncertainties are presented at $z = 10\,\mathrm{mm}$ for the sake of brevity; these values are indicative of the propagated uncertainties at other axial locations. Uncertainties are presented for the approximately 100 µm pixel resolution data only.

4.3 Flame Surface Density

Flame surface density (FSD) is defined as the ratio of flame surface area to volume for an iso-surface of a relevant scalar. FSD plays an important role in combustion modeling. It shows up in coherent flamelet models; if the combustion device is operating in the flamelet regime, then the reaction rate in such models may be expressed in terms of the FSD. Flame surface density measurements have typically been derived from experimental data using two significantly different methods.

FSD is generally obtained from the product of the conditional progress variable probability and the conditionally-averaged progress variable gradient [8] provided that the progress variable, c, has been derived from measurements of temperature [45, 80]. This quantity, defined further on in Equation 4.11, is referred to as Σ_1 in the present section. It is referred to simply as Σ later on in Chapter 5 and Chapter 6 unless otherwise stated.

A geometric method for determining flame surface density from Rayleigh (temperature), Mie, or suitable PLIF images was proposed by Shepherd [81] and used in a number of studies [24, 81–83]. In this method, FSD is defined as the ratio of average flame front crossing length to mean flame brush area for a given mean progress variable $\bar{c}$. This quantity, henceforth referred to as Σ_2, is analogous to Σ_1, but is defined in previous studies for $c = 0.5$ only. Σ_2 can be extracted from any scalar progress variable image; OH measurements predominate [24, 81, 82], though CH has also been used [83]. Here

Σ_2 is based on OH-LIF measurements.

A third measure of flame surface density, Σ_3, is proposed further on. This is an extension of Σ_2, modified to enable direct comparison with Σ_1. These flame surface density metrics are compared in Chapter 7, and the extent to which the values they report are self-similar is investigated.

Further classes of geometric FSD measurement have been proposed by Cohé *et al* [84] and Veynante *et al* [85]. These forms are not considered in the present work due to constraints on time; however, the description of the latter in [85] implies that it is very similar in implementation to Σ_2.

To avoid any confusion in the subsequent sections, it is reiterated that three distinct definitions of flame surface density will be used in the present work. When discussing the quantity Σ, the subscript 1 (or the absense of a subscript) refers to the exact definition of flame surface density provided by Pope [8], the subscript 2 refers to the geometric definition supplied by Shepherd [81], and the subscript 3 refers to the extended geometric method. Two forms of progress variable are used: a thermal progress variable (Section 4.2.2) and an OH progress variable (Section 4.1.5). The subscripts T and OH refer to the thermal and OH progress variables respectively when discussing the quantity c.

4.3.1 Σ_1 Methodology

The statistical flame surface density, Σ_1, is defined using the exact expression derived by Pope [8]:

$$\Sigma_1\left(c;\bar{c}\right) = \mathrm{P}\left(c;\bar{c}\right)\left\langle \left|\nabla c\right|\right|_c\right\rangle\left.\right|_{\bar{c}} \tag{4.11}$$

For the evaluation of the line temperature based FSD, $\Sigma_{1,T}$, the conditional progress variable pdf $\mathrm{P}\left(c_T; \bar{c}_T\right)$ was calculated by binning the c_T data by $\bar{c}_T$ (centers at $\bar{c}_T = 0.05,\ 0.15,\ ...,\ 0.95$), and calculating the conditional probability of finding a data point within each instantaneous c_T bin (centers at $c_T = 0.05,\ 0.15,\ ...,\ 0.95$). The conditionally averaged progress variable gradient $\left\langle |\nabla c_T| |_{c_T} \right\rangle |_{\bar{c}_T}$ was found by binning the ∇c_T data in c_T and $\bar{c}_T$ as per $\mathrm{P}\left(c_T; \bar{c}_T\right)$.

Another variant of Σ_1 may be derived using the progress of reaction c_{OH}, defined using the values of the OH progress images (Section 4.1.5) along the line measurement axis, in conjunction with Equation 4.11 to give $\Sigma_{1,\mathrm{OH}}$. $\Sigma_{1,\mathrm{OH}}$ is then derived from the angle- and resolution-corrected OH gradient, ∇c_{OH}, and the conditional pdf of c_{OH}, $\mathrm{P}\left(c_{\mathrm{OH}}; \bar{c}_{\mathrm{OH}}\right)$.

4.3.2 Σ_2 Methodology

Shepherd [81] defined geometric flame surface density as:

$$\Sigma_2\left(\bar{c}\right) = L\left(\bar{c}\right) / A\left(\bar{c}\right) \tag{4.12}$$

where $L\left(\bar{c}\right)$ is the flame crossing length at the specified value of mean progress variable, and $A\left(\bar{c}\right)$ is the corresponding area. The plateaued OH images (Section 4.1.5) are thresholded at $c_{\mathrm{OH}} = 0.5$ to produce binary images of products and reactants. Flame fronts are extracted from these images using the method detailed in Section 4.1.2. Product-reactant images are then averaged to give a mean OH image, which is thresholded at $\bar{c}_{\mathrm{OH}} = 0.1, 0.2, \ldots, 0.9$. The area $A\left(\bar{c}_{\mathrm{OH}}\right)$ is determined for each threshold level. Instantaneous flame fronts are analyzed to determine the length of their intersection with each $\bar{c}_{\mathrm{OH}}$ region of the mean image, and these lengths are averaged for all images to give $L\left(\bar{c}_{\mathrm{OH}}\right)$. $\Sigma_{2,\mathrm{OH}}$ is then given by Equation 4.12.

4.3.3 Σ_3 Methodology

Σ_3 is an extension to the method proposed by Shepherd [81] and detailed in Section 4.3.2, but with a few key differences. Note that in the present work the OH progress variable is used to give $\Sigma_{3,\mathrm{OH}}$; however if Rayleigh temperature images were available it would be possible to calculate $\Sigma_{3,T}$.

The mean OH image is generated from the plateaued OH images rather than the binarized OH-PLIF images (thresholded at $c_{\mathrm{OH}} = 0.5$) to remove the influence of threshold choice. The area $A\left(\bar{c}_{\mathrm{OH}}\right)$ is determined at each $\bar{c}_{\mathrm{OH}}$ level as before. Instead of computing L at a single c_{OH} level, the crossing lengths for each instantaneous c_{OH} are found for each $\bar{c}_{\mathrm{OH}}$, and averaged to give $L\left(c_{\mathrm{OH}}, \bar{c}_{\mathrm{OH}}\right)$. The flame surface density Σ_3 is then given by:

$$\Sigma_3\left(c, \bar{c}\right) = L\left(c, \bar{c}\right) / A\left(\bar{c}\right) \tag{4.13}$$

Equation 4.13 allows results to be compared for a range of instantaneous c_{OH} as well as $\bar{c}_{\mathrm{OH}}$ in a similar vein to $\Sigma_{1,T}$, which is not possible for $\Sigma_{2,\mathrm{OH}}$. It should be noted that $\Sigma_2\left(\bar{c}_{\mathrm{OH}}\right) \approx \Sigma_3\left(c_{\mathrm{OH}} = 0.5, \bar{c}_{\mathrm{OH}}\right)$, with the differences in determining the mean OH image in each method accounting for any observed deviations.

4.4 Summary

The present chapter has detailed the data processing methods used to calculate derived quantities from the experimental data measured in the slot and swirl burners. The image processing required to calculate geometric quantities such as curvature, flame normal angle have been detailed, as well as a method of creating OH progress variable images (Section 4.1). The methods of processing the scalar data have also been shown, with a particular focus on the correction of the effect of differential diffusion on local equivalence ratio in the flame (Section 4.2) and the derivation of propagated uncertainties in the derived quantities. Finally, three flame surface density metrics have been presented (Section 4.3).

Chapter 5 focuses on the analysis of results from the slot burner, while Chapter 6 provides a similar investigation for the swirl burner. The three flame surface density metrics described in Section 4.3 are compared in Chapter 7 to evaluate their congruence.

Chapter 5

Slot Burner Results

The results for the slot burner detailed in Section 3.1.1 of Chapter 3 are organized as follows. First, non-reacting velocity measurements and derived quantities are presented. Next, the instantaneous structure of the cases investigated are illustrated with sample scalar data and associated OH-PLIF images. The overall behavior of each condition is examined using Favre-averaged profiles of temperature and species. The extent of stratification is quantified using the two-dimensional projection of the equivalence ratio gradient on the line measurement axis. State space species-temperature behavior in the turbulent flames is compared with that of premixed unstrained laminar flame calculations.

The influence of stratification on flame curvature distributions is also examined. Measured surface density function and scalar dissipation rate are compared with laminar flame calculations, for both unconditioned data and data conditioned on local equivalence ratio. Similar analyses are performed conditioned on the local curvature. Finally measurements of flame surface density derived using the Pope definition (Section 4.3.1 of Chapter 4) are presented conditioned on mean and instantaneous progress variable.

5.1 Flow Field Measurements

Velocity profiles were taken with a spatial resolution of 0.5 mm at $z = 15\,\mathrm{mm}$ downstream of the burner exit. Mean axial velocity $\overline{U}$ and turbulence intensity $u'/\overline{U}$ are shown in Figure 5.1 [55]. As mentioned previously, the data presented in this section were obtained from experiments performed by P. Anselmo-Filho, and are included for the sake of completeness. The mean velocity is reasonably uniform, with variations due to wakes from the splitter plates.

The turbulent integral length scale (L_{turb}) was calculated from the autocorrelation function of the time series of velocity. The Kolmogorov length scale (η) was estimated using Taylor's hypothesis of homogeneous isotropic turbulence. The ratio of turbulence intensity to laminar flame speed u'/S_{L} was calculated using data for methane from [86] for a mean $\Phi_{\mathrm{g}} = 0.73$. The integral scale of turbulence in the cold flow is around 2 mm

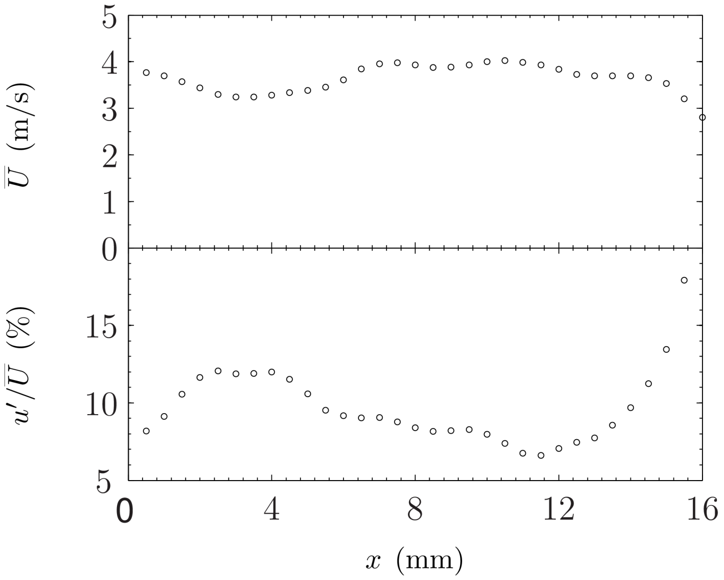

Figure 5.1: Hot wire measurements of mean vertical velocity $\overline{U}$ (top row) and turbulence intensity $u'/\overline{U}$ (bottom row) in the slot burner at $z = 15\,\mathrm{mm}$ downstream of the burner exit. The burner centerline is located at $x = 0\,\mathrm{mm}$.

Table 5.1: Mean cold flow properties derived from measurements taken at $z = 15\,\text{mm}$ downstream of the burner exit. Raw data was averaged over a cross stream region $0 < x < 16.05\,\text{mm}$.

$\overline{U}$ (m/s)	u' (m/s)	u'/S_L	L_turb (mm)	η (mm)	δ_L (mm)	Re	Re_T
3.05	0.32	1.33	1.93	0.09	0.62	2 316	38

in the measurement region, and u'/S_L is of the order unity in the flames (Table 5.1). The Damköhler number is $Da = 2.35$ and the Karlovitz number is $Ka = 0.59$, placing the flames surveyed marginally within the corrugated flamelet regime in the modified Borghi diagram (Figure 5.2).

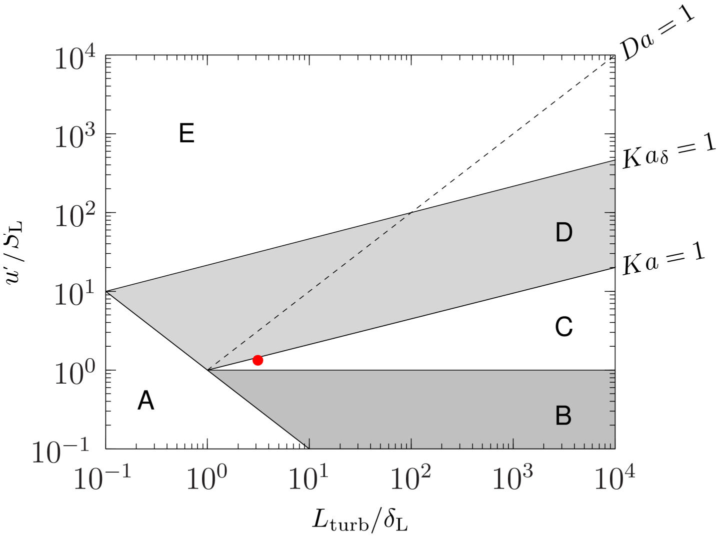

Figure 5.2: Modified Borghi diagram illustrating the main regimes of premixed combustion: A, laminar flames; B, wrinkled flamelets; C, corrugated flamelets; D, thin reaction zones; E, broken reaction zones. The flames surveyed in the slot burner operate in the corrugated flamelet regime and are shown by a red circle.

5.2 Instantaneous Flame Structure

Instantaneous sample shots of temperature, T, and linearly bridged equivalence ratio, Φ, are shown in Figure 5.3, and the corresponding images of OH-PLIF in Figure 5.4. Note that the temperature data are plotted with markers at the experimental resolution; all other quantities are plotted with lines only save for cases where overlapping data require markers for clarity. It is clear that significant gradients of Φ may arise within the reaction zone for the stratified cases.

Analysis of the data within the flame brush demonstrates that the instantaneous equivalence ratio gradients in the flame brush ($\nabla_x \Phi_{fs4_{25}} = 277\,\mathrm{m}^{-1}$ and $\nabla_x \Phi_{fs6_{25}} = 399\,\mathrm{m}^{-1}$) can be significantly higher than the mean gradients ($\overline{\nabla\Phi}_{fs4_{25}} = 81\,\mathrm{m}^{-1}$ and $\overline{\nabla_x\Phi}_{fs6_{25}} = 132\,\mathrm{m}^{-1}$). Further discussion of the extent of stratification is given in Section 5.4. These steep gradients are commensurate with the thermal and reaction zone length scales within the flame, and raise the question of whether reaction in such flames can be considered quasi-steady based on local mixture fraction, or whether their immediate environment must also be taken into account. Laminar calculations of flames with

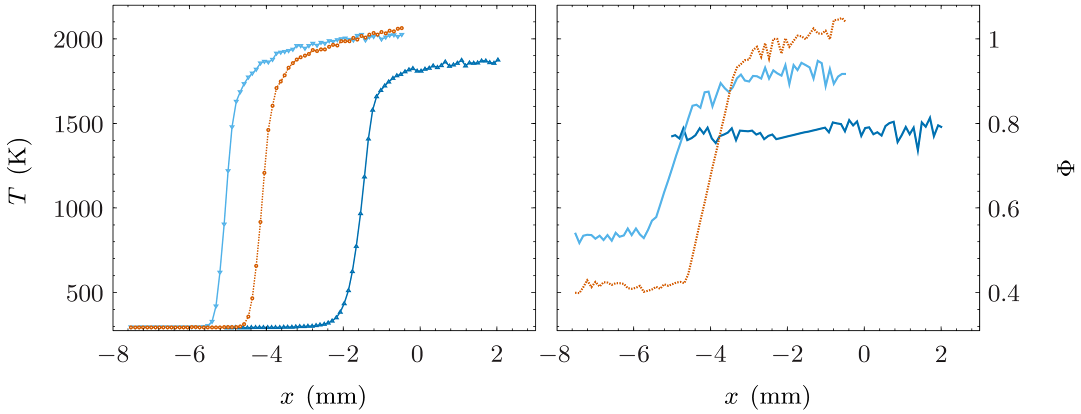

Figure 5.3: Single-shot profiles of temperature (*left*) and equivalence ratio (*right*) at 25 mm downstream of the burner exit for premixed $fs1$, ——, moderately stratified $fs4$, ——, and highly stratified $fs6$, ⋯⋯, cases.

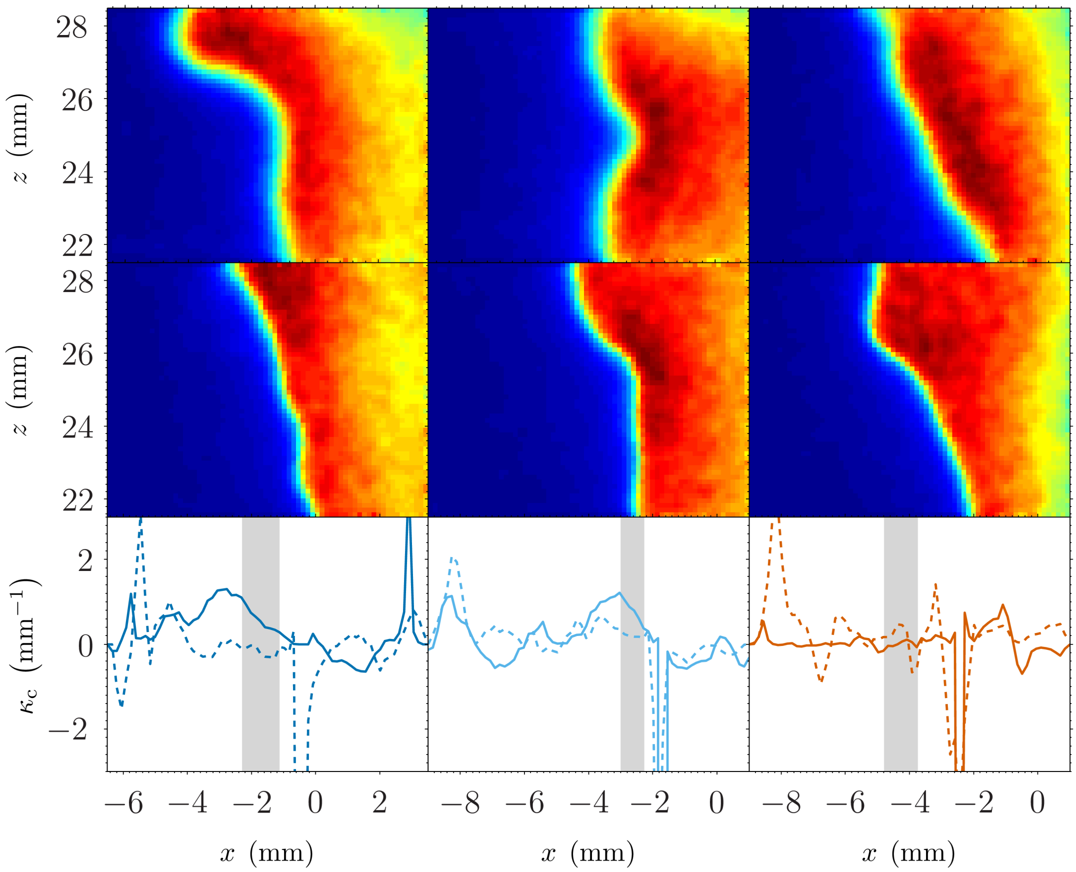

Figure 5.4: *Top and middle rows*: Single-shot OH-PLIF image pairs (randomly selected) for the premixed (*left*), moderately stratified (*middle*), and highly stratified (*right*) slot burner flames, corresponding to the instantaneous profiles shown in Figure 5.3. *Bottom row*: Continuous curvature along the line measurement axis ($z = 25\,\text{mm}$). Data from the second plane are plotted with dashed lines, and instantaneous flame brushes are marked in gray.

positive or negative mixture fraction gradients seem to indicate that non-local effects should be evident, particularly for very lean flames [30–32], with the behaviour exhibited being influenced by the history of equivalence ratios experienced by the flame.

The OH-PLIF images shown in Figure 5.4 are typical, and demonstrate the weakly turbulent nature of the flame; no pockets or examples of local flame extinction are evident. This is true of all the cases considered. The values of κ_c along the line measurement axis demonstrate the potential pitfalls of using the continuous form of curvature to condition experimental data, as substantial deviations from the methane/air curvature levels seen in other weakly turbulent flows ($-2.5\,\mathrm{mm}^{-1} < \kappa < -2.5\,\mathrm{mm}^{-1}$) are observed for each case. These sudden jumps in curvature tend to occur either before the preheat zone, in which case they are attributed to the weak gradients resulting in the denominator of Equation 4.4 being much smaller than the numerator, or due to noisy OH signal in the equilibrium zone.

5.3 Favre-Averaged Flame Structure

Radial profiles of Favre-averaged temperature, species mole fractions and equivalence ratio measurements are plotted at two axial distances above the burner exit in Figure 5.5. The flat $\widetilde{\Phi}$ profile for the premixed $fs1$ flame demonstrates that there is little to no entrainment of co-flow air within the measurement window, while the moderate mean equivalence ratio gradients for the stratified cases show the structure of the mixing layer between the leaner and richer flows upstream of these axial locations.

The center of the flame brush, taken as the peak in T'' (Figure 5.6), is located significantly farther from the burner centerline in the stratified cases compared to the premixed case. Examination of the $\widetilde{\Phi}$ profiles shows that the position of the flame brush in the stratified flame is dominated by burning through higher equivalence ratios in the upstream portion of the V-flame. The difference in the degree of stratification seen between the $fs4$ and $fs6$ cases is small relative to the premixed $fs1$; this is corroborated by the results in Section 5.4 further on in the present chapter. This suggests that the main effect of stratification on the mean flame position is the balance between the mean heat release rate (which leads to the expansion of the inner V-shape), the mean flame speed at the mean equivalence ratio, and the incoming velocity. Burning mixtures near the stoichiometric point leads to high rates of heat release and greater expansion of the

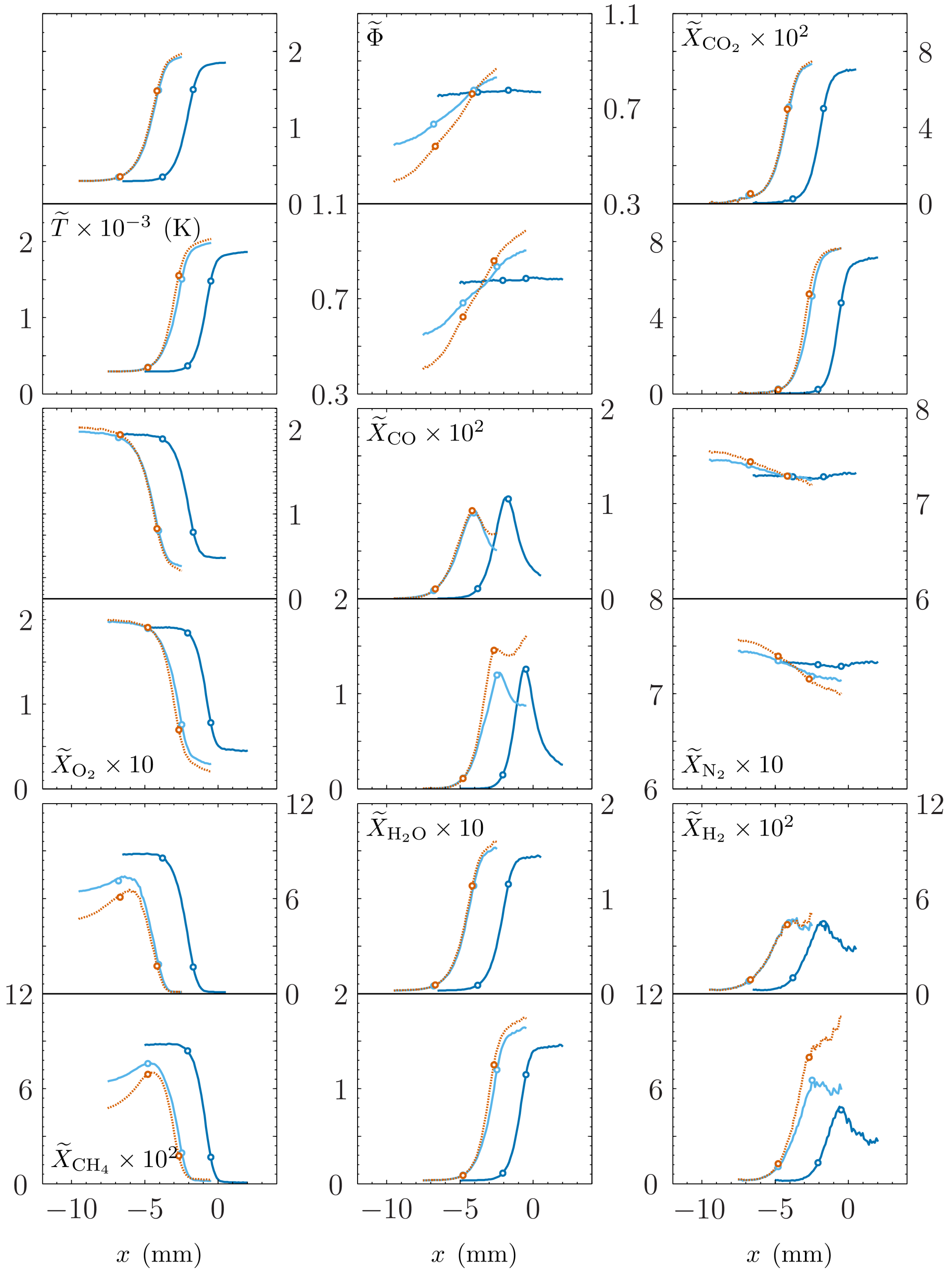

Figure 5.5: Radial profiles of Favre-averaged temperature, equivalence ratio, and mole fractions of major chemical species for premixed, ——, moderately stratified, ——, and highly stratified, ········, cases at $z = 25$ mm (bottom halves) and $z = 30$ mm (top halves). Open circles show the locations of the flame brush as defined by the T'' FWHM positions.

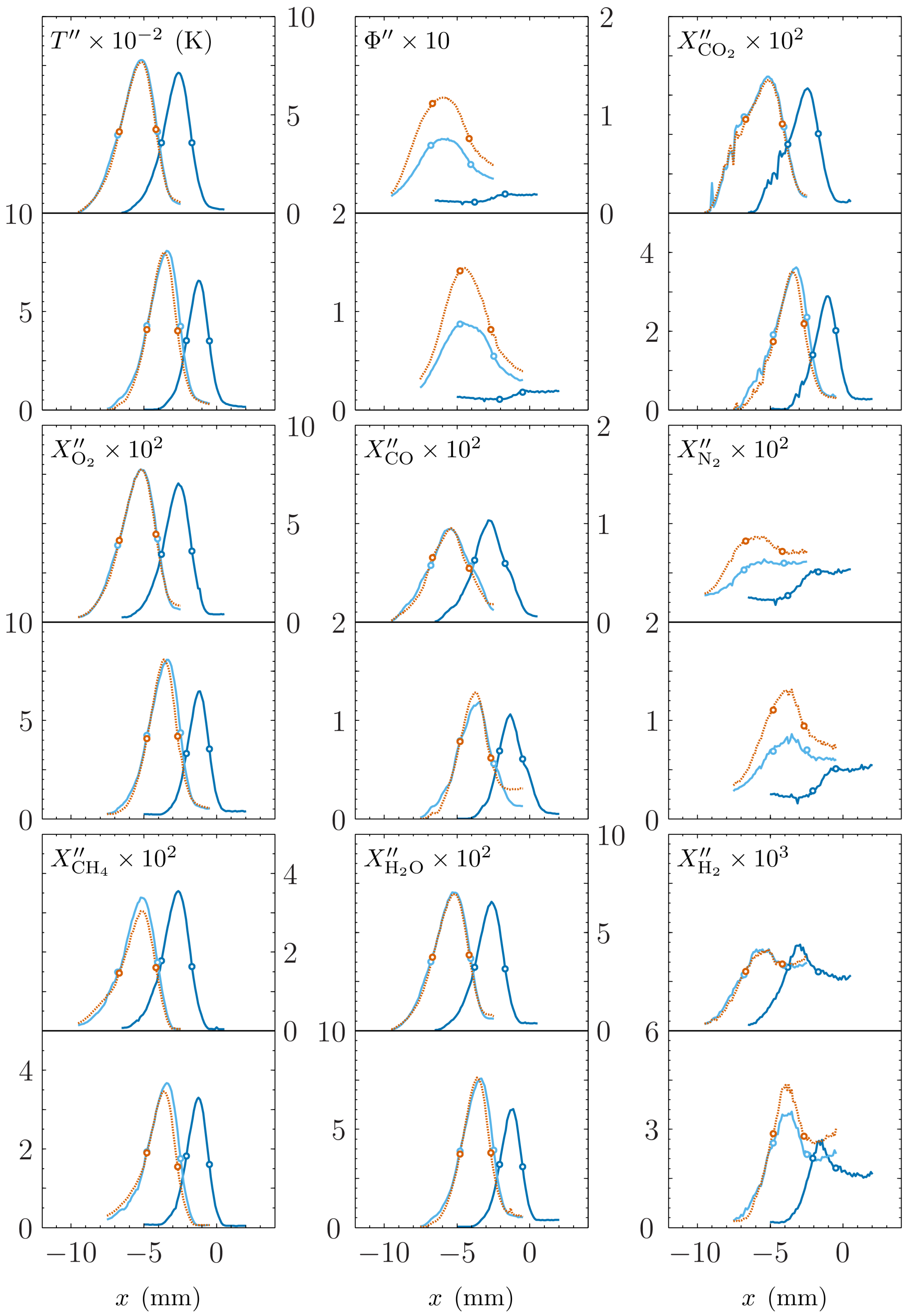

Figure 5.6: Radial profiles of Favre-averaged RMS fluctuation of temperature, equivalence ratio, and mole fractions of major chemical species. Line types and symbols as in Figure 5.5.

V, but by the same token a higher flame speed and thus a larger mean flame brush angle relative to the axial direction.

The values of $\widetilde{\Phi}$ at the center of the flame brush in the stratified cases are fairly close to the premixed value at the $z = 25\,\mathrm{mm}$ location (within $4\,\%$). Further downstream at $z = 30\,\mathrm{mm}$, Favre-averaged equivalence ratios at peak T'' are lower for the stratified cases than the premixed case ($9\,\%$ lower for $fs4_{30}$, $15\,\%$ lower for $fs6_{30}$). The differences in $\widetilde{\Phi}$ at $z = 25\,\mathrm{mm}$ and $z = 30\,\mathrm{mm}$ indicate that results seen in data at the upstream location which have not been conditioned on local equivalence ratio should generally reflect those conditioned on local equivalence ratio at the same location. It may not be possible to draw valid comparisons between the premixed and stratified cases at $z = 30\,\mathrm{mm}$ without applying such conditioning.

Favre-average mole fractions for CO_2 largely mirror the Favre-averaged temperature profiles, as expected for product species and $\widetilde{X}_{H_2O}$. $\widetilde{X}_{O_2}$ is antisymmetric to the profiles of the product species and the temperature. The Favre-averaged $\widetilde{X}_{CH_4}$ profiles follow the equivalence ratio in the non-reacting region and peak just ahead of the flame brush. Finally the intermediates H_2 and CO appear in smaller concentrations, peaking around the center of the flame brush. Interestingly both of these quantities are substantially higher in the equilibrium zone for $fs6$ than $fs4$ at the upstream $z = 25\,\mathrm{mm}$ location, but these differences are almost completely eliminated just $5\,\mathrm{mm}$ farther downstream. Discussion of the correlation of the species and temperature appears in Section 5.5.

5.4 Extent of Stratification

It is not possible to measure the three-dimensional equivalence ratio gradient using the experimental dataset for the slot burner, as there is no information on the three-

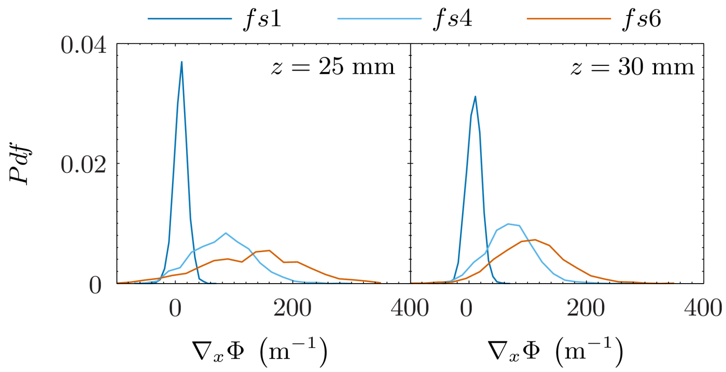

Figure 5.7: Probability density functions of two-dimensional equivalence ratio gradient, $\nabla_x\Phi$, for the slot burner cases at $z = 25\,\mathrm{mm}$ (left plot) and $z = 30\,\mathrm{mm}$ (right plot). Data taken from within the linear bridged region of the flame. Line types as in Figure 5.5.

dimensional equivalence ratio field. However, the two-dimensional projection of the true three-dimensional gradient is given by the gradient of Φ along the line measurement axis. This quantity is denoted as $\nabla_x\Phi$ in the present work. Figure 5.7 shows the probability distributions for $\nabla_x\Phi$ at both axial locations, while Table 5.2 shows some basic statistics for the distributions.

The mean two-dimensional equivalence ratio gradient increases significantly between the $fs4$ and $fs6$ case (63 % and 54 % for $z = 25\,\mathrm{mm}$ and $z = 30\,\mathrm{mm}$ respectively),

Table 5.2: Statistics for equivalence ratio gradients in the slot burner. Equivalence ratio data is linearly bridged (Φ).

Flame	y (mm)	$\nabla_x\Phi_{\mathrm{rms}}$ (m^{-1})	$\overline{\nabla_x\Phi}$ (m^{-1})	γ_1 $(-)$	γ_2 $(-)$
$fs1$	25	9.0	11.8	-0.83	14.7
	30	8.2	12.5	-0.06	0.1
$fs4$	25	80.9	49.3	0.15	-0.1
	30	69.1	39.6	0.12	0.2
$fs6$	25	132.0	80.4	-0.07	-0.2
	30	106.7	55.8	0.13	0.5

though these increases are small in comparison to those relative to the premixed case (743 % to 1 367 %). The near-zero positive gradients exhibited by the premixed case are due to the equivalence ratio being biased slightly high in the product sides in the current experimental data.

5.5 Influence of Stratification on Species Evolution

Scatter plots of major species against temperature are shown in Figs. 5.8-5.10, along with values from laminar flame calculations for unstrained premixed flames at the mean Φ. The local Φ for each data point is shown using the color scale in Figure 5.8. Note that the data are downsampled by a factor of ten to aid clarity. All species in the premixed case (Figure 5.8) are in good agreement on the mean with laminar flame calculations.

In each scatter plot the data are binned in T space, with centers at 100 K intervals starting at $T = 300\,\mathrm{K}$, and the mean equivalence ratio is found within each bin. A multi-dimensional lookup table of unstrained premixed methane/air laminar flame calculations is interpolated in T and Φ to find the corresponding premixed value for each species. It is clear that the premixed calculations give good agreement in the thermal domain with the mean of the experimental scatters with the exception of hydrogen. This is important as it indicates that models whose chemistry is based around the laminar flamelet concept are unlikely to be able to capture the behavior of hydrogen in simulations of stratified flames.

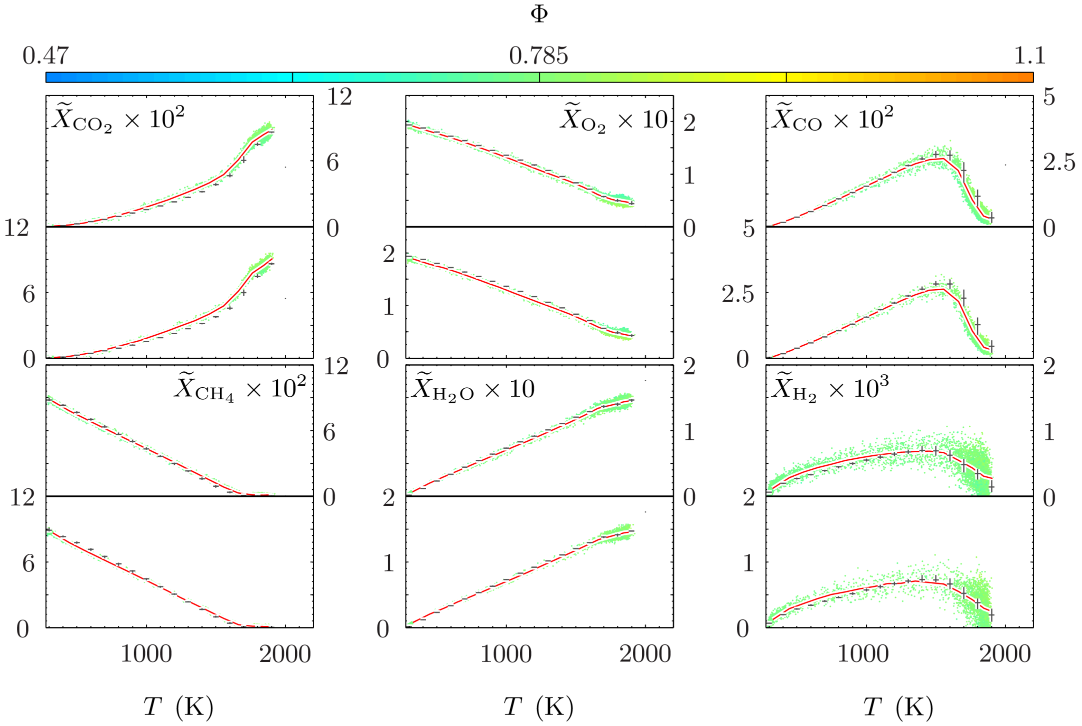

Figure 5.8: Plots of temperature against key scalars for $fs1_{25}$ (bottom row) and $fs1_{30}$ (top row), colored by Φ, as shown in the colorbar. Mean fits are plotted in red. Laminar flame calculations are shown by gray horizontal (value at local mean Φ) and vertical (range of maximum and minimum local Φ) lines.

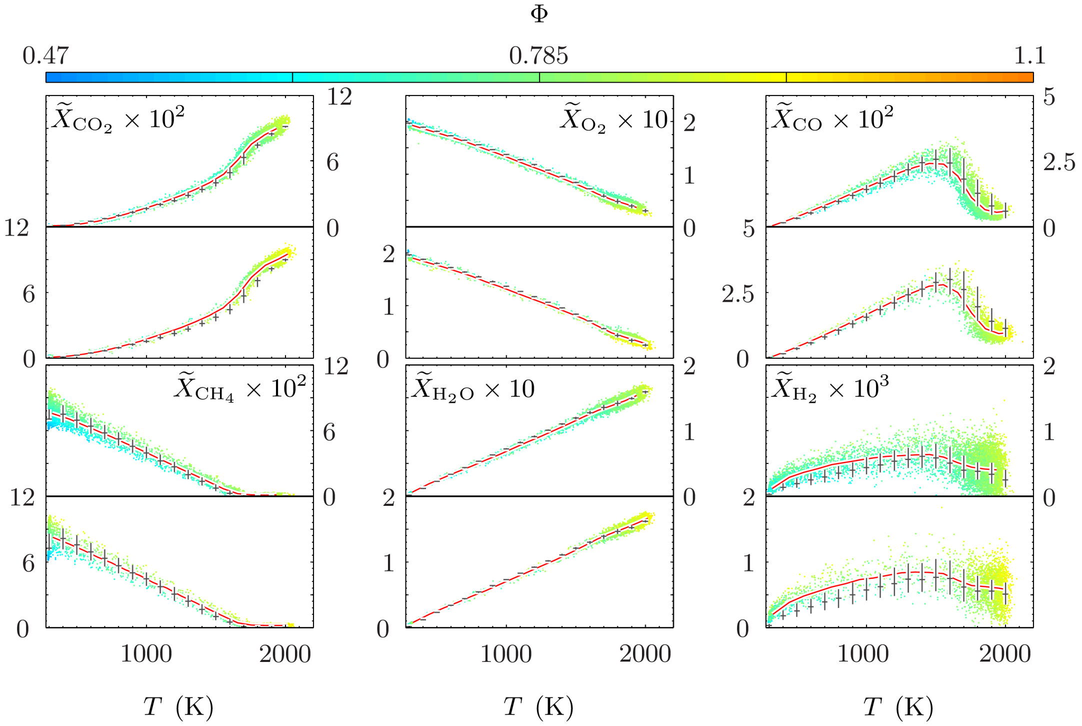

Figure 5.9: Plots of temperature against key scalars for $fs4_{25}$ (bottom row) and $fs4_{30}$ (top row). Symbols as in Figure 5.8

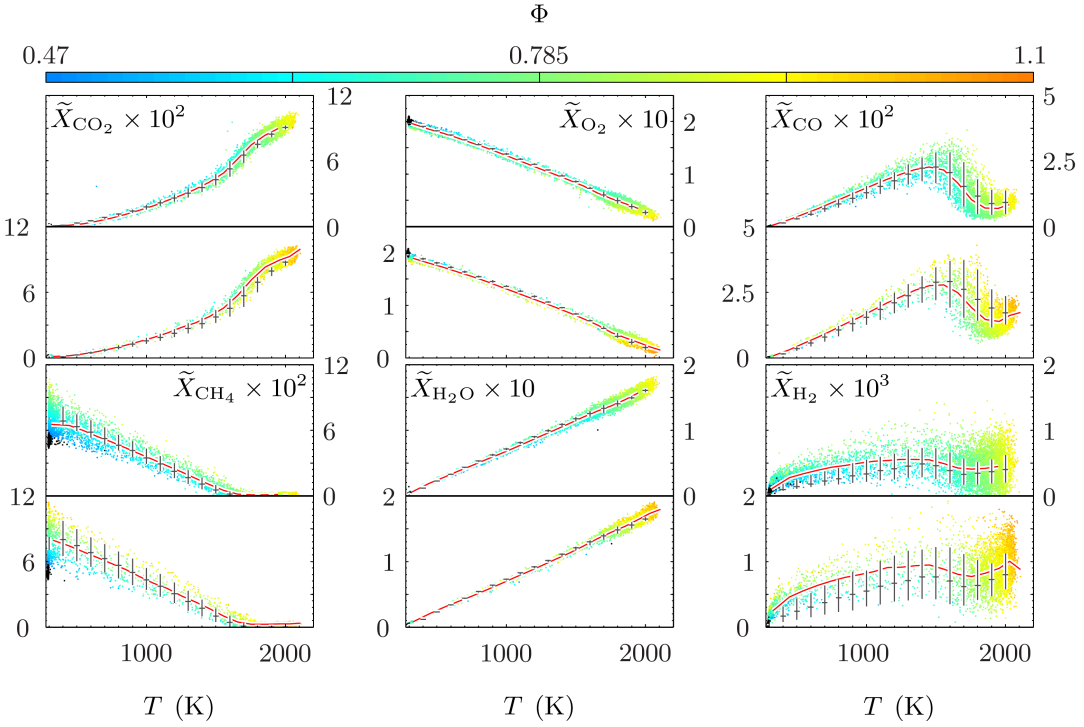

Figure 5.10: Plots of temperature against key scalars for $fs6_{25}$ (bottom row) and $fs6_{30}$ (top row). Symbols as in Figure 5.8

5.6 Curvature

Flame curvature can be obtained from the OH-PLIF images in discrete or continuous two-dimensional forms as described in Section 4.1.4 of Chapter 4. Results for premixed flames have been reported by Shepherd [81], and for stratified flames by Anselmo-Filho [24]. The slot burner used in the current work is the same as that used in the latter study, but the curvature measurements reported previously were obtained from a much larger OH-PLIF measurement window. The work by Shepherd showed that the mean curvature in a turbulent premixed methane/air V-flame is skewed towards positive values. The work in [24] on the current burner as well as that by Renou *et al.* in [21] showed that flame curvature distributions are broadened and shifted closer to a zero mean as stratification increases. Curvature results in the present work are given in both continuous (Section 4.1.4.2 in Chapter 4) and discrete (Section 4.1.4.1 in Chapter 4) forms.

The results of the present work, however, show only partial agreement with previous

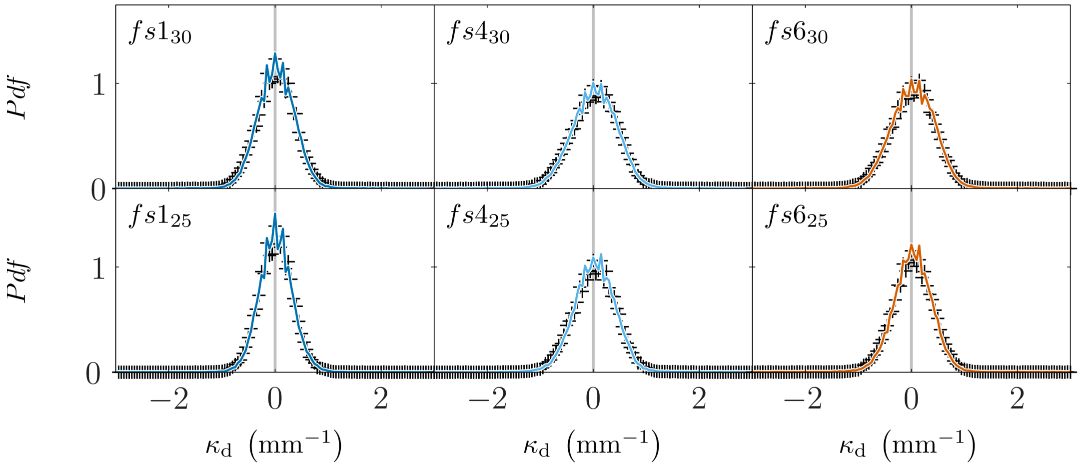

Figure 5.11: Distributions of discrete curvature, κ_d, binned in steps of $\kappa_d = 0.05\,\text{mm}^{-1}$. $\kappa_d = 0\,\text{mm}^{-1}$ is marked with a gray vertical line to aid clarity. Data from planes one and two are shown by solid lines and crosses respectively.

Table 5.3: RMS and excess kurtosis values for discrete and continuous measures of local curvature in the slot burner at 25 and 30 mm downstream of the burner exit. Continuous data is taken from the region $0.1 < c < 0.9$. All curvature data filtered to remove outliers $\left(|\kappa| > 3\,\mathrm{mm}^{-1}\right)$. Data from the second plane is given in parentheses in each case.

Flame	y (mm)	$\overline{\lvert\kappa_\mathrm{d}\rvert}$ $\left(\mathrm{mm}^{-1}\right)$	$\overline{\lvert\kappa_\mathrm{c}\rvert}$ $\left(\mathrm{mm}^{-1}\right)$	$\gamma_{2,\mathrm{d}}$ $(-)$	$\gamma_{2,\mathrm{c}}$ $(-)$
$fs1$	25	0.241 (0.250)	0.349 (0.394)	0.151 (0.342)	5.018 (4.132)
$fs4$		0.304 (0.318)	0.425 (0.485)	0.320 (0.256)	3.830 (2.638)
$fs6$		0.284 (0.298)	0.406 (0.451)	1.424 (1.243)	4.385 (3.417)
$fs1$	30	0.272 (0.285)	0.362 (0.393)	0.104 (0.082)	5.036 (4.188)
$fs4$		0.335 (0.343)	0.375 (0.459)	0.146 (0.202)	4.002 (3.103)
$fs6$		0.325 (0.333)	0.348 (0.437)	0.104 (0.404)	4.352 (3.567)

findings. The pdfs of discrete curvature κ_d shown in Figure 5.11 are similar to the normal distribution in both planes. The discrete distributions are marginally leptokurtic, indicating a slightly peakier distribution than a normal one, with the exception of the highly stratified case at $z = 25$ mm downstream, which exhibits significantly higher levels of kurtosis, as shown in Table 5.3. The reason for the anomalous result in the latter case is uncertain.

The continuous distributions plotted in Figure 5.12 are significantly more leptokurtic than their discrete counterparts, as seen in Table 5.3. One speculative explanation of this behavior is that the continuous data is obtained for a range of locations within the instantaneous thermal ramp of the flame ($0.1 < c < 0.9$), while the discrete data is taken at the location of maximum OH gradient. However limiting the continuous data to smaller intervals of progress variable fails to bring the kurtosis in line with the discrete results, indicating that this alone does not explain the differences.

As the distributions are symmetric and centered close to zero curvature, it seems that the flames undulate such that positive and negative curvatures of similar magnitude

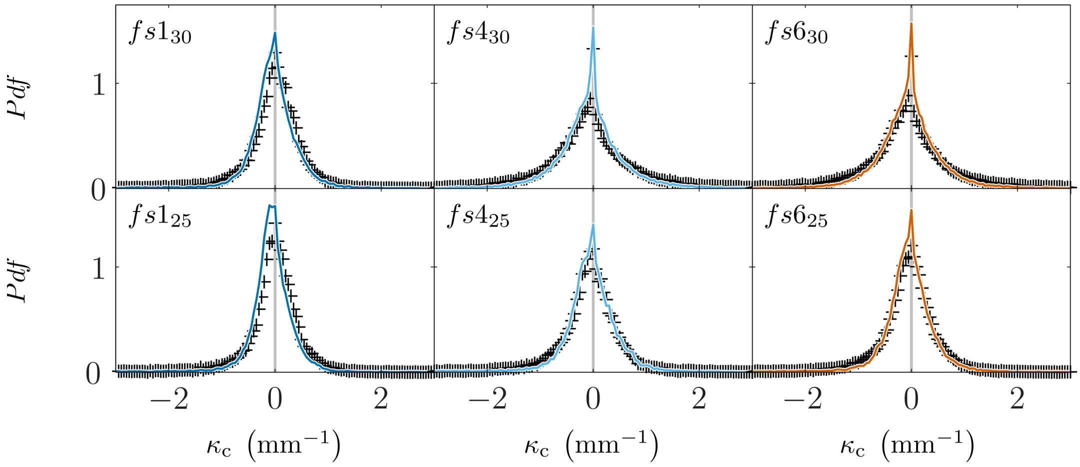

Figure 5.12: Distributions of continuous curvature, κ_c, binned in steps of $\kappa_c = 0.05\,\text{mm}^{-1}$. $\kappa_c = 0\,\text{mm}^{-1}$ is marked with a gray vertical line to aid clarity. Data from planes one and two are shown by solid lines and crosses respectively.

are almost equally distributed within the measurement window. Broadening of the distribution with stratification is observed, in line with the results highlighted earlier. The RMS curvature values (Table 5.3) increase with stratification compared to the premixed case, aside from in the continuous $fs6_{30}$ data. Note that this broadening is not monotonic; while both stratified cases typically have larger RMS values than the premixed case, the $fs4$ case shows higher RMS curvature than the more stratified $fs6$ case.

However, increased stratification appears to shift the mean in the positive direction rather than towards zero. This trend is corroborated by the work of Bonaldo [87], who found that increasing stratification resulted in an increase in the probability of small positive radii of curvature (high positive curvature). The difference between the results presented here and those from [24], which used the same burner, is attributed to the significantly smaller cross planar LIF window size in the present work (10 × 8 mm vs 38 × 25 mm); the previous results may have been affected by a wider variation in local mean Φ.

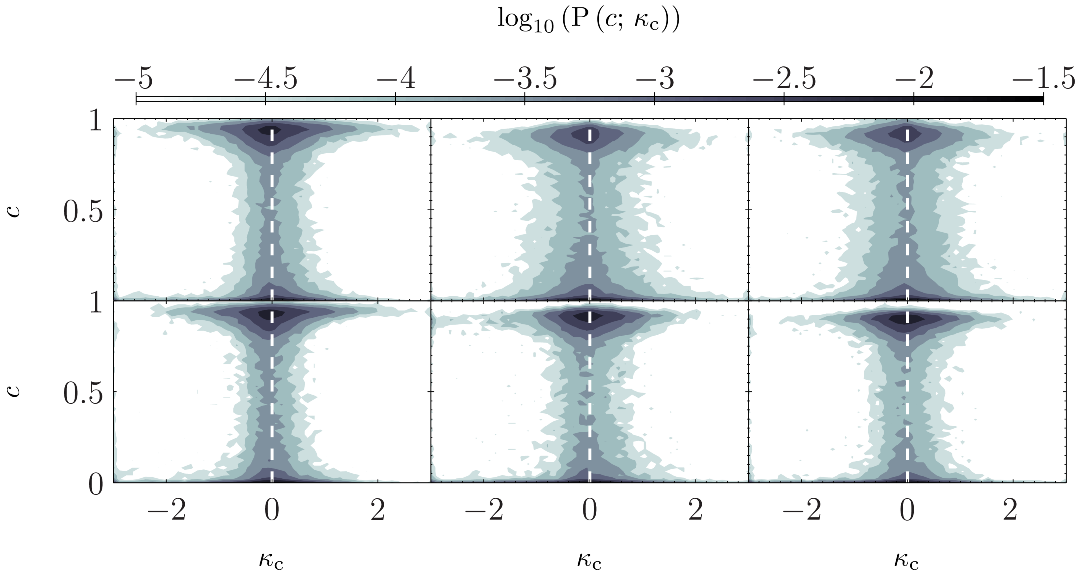

Figure 5.13: Joint pdf of progress variable, c, and continuous curvature, κ_{c}, taken from plane one for premixed (left column), moderately (middle column) and highly (right column) stratified slot burner cases, at $z = 25\,\mathrm{mm}$ (bottom row) and $z = 30\,\mathrm{mm}$ downstream of the burner exit. $\kappa_{\mathrm{c}} = 0\,\mathrm{mm}^{-1}$ is shown by dashed white lines, and the probability $\mathrm{P}(c;\kappa_{\mathrm{c}})$ is expressed on a $\log_{10}$ scale.

It is interesting to note that the continuous curvature is typically smaller in magnitude in the intermediate region of the flame $(0.2 < c < 0.8)$, as shown in the joint pdfs of κ_{c} and c in Figure 5.13, with higher curvature values being more predominant near the progress variable extrema. One possible explanation for this is that the continuous curvature definition (Equation 4.4 in Chapter 4) includes OH signal gradients of first and second order; away from the reaction zone, these quantities will have near-zero values and may result in very high curvatures due to the small value of the denominator of Equation 4.4 in Chapter 4. However, a look at the contour plot of a randomly selected OH-PLIF image from the premixed case shown in Figure 5.14 demonstrates qualitatively that the high curvature values may not be an artifact of near-zero gradients; while similar levels of wrinkling are seen throughout the reaction zone, the contours are significantly more convoluted near the unburned reactants and the burned products.

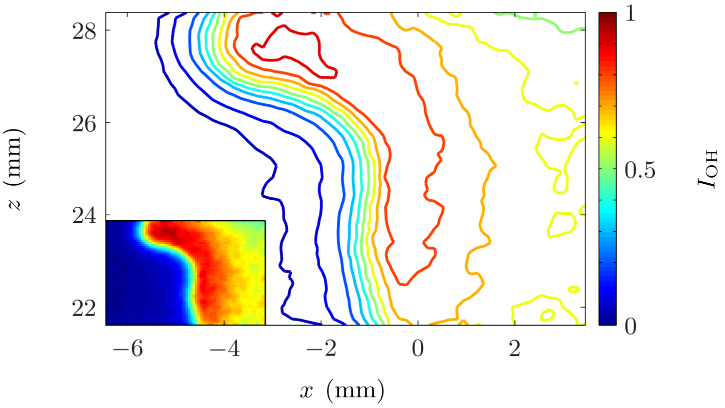

Figure 5.14: Contour plot of I_{OH} from the premixed OH-PLIF image shown in Figure 5.4. The image itself is shown inset for reference.

5.7 Influence of Stratification on Scalar Gradients

5.7.1 Unconditioned

Thermal progress variable, surface density function, and the scalar dissipation rate were calculated using the measured temperature and local equivalence ratio. The resulting unconditioned scatter plots of $|\nabla c|$ and χ_c as a function of progress variable are shown in Figures 5.15 and 5.16 respectively. The data are downsampled by a factor of ten to aid clarity, but are used in full to determine conditional means in progress variable space. Significant levels of scatter are observed, particularly for the $fs6$ case. The mean values are substantially smaller than the calculated unstrained laminar values throughout progress variable space; Sankaran *et al* [73] and more recently Moureau *et al* [74] have reported similar trends in simulations of premixed turbulent flames and their laminar counterparts. In the latter study the turbulent flame was found to be thickened relative to laminar equivalents on both an instantaneous and mean basis, as in the present work. It is interesting that thermal gradients are significantly attenuated even at the low levels of turbulence found in the slot burner.

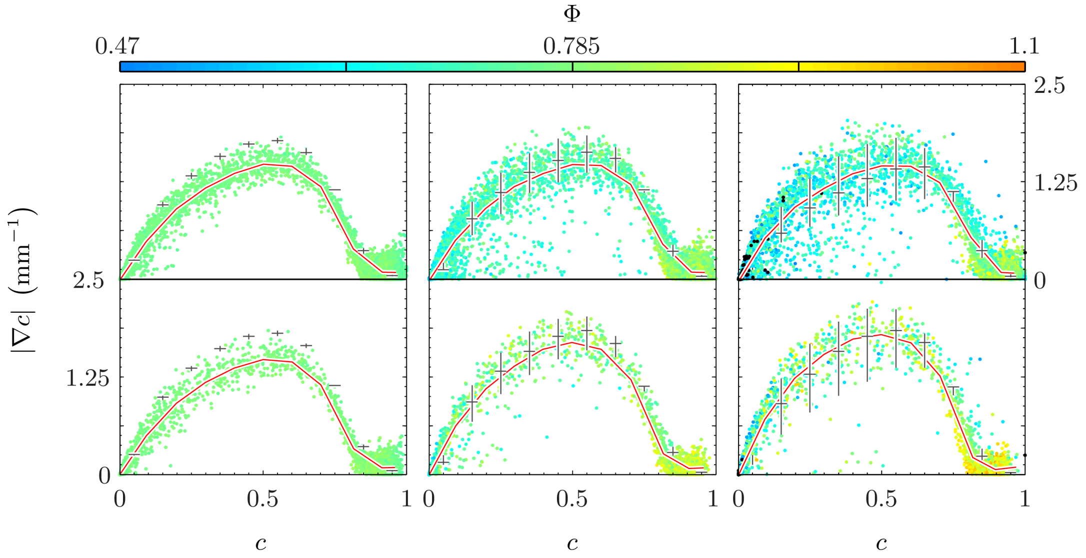

Figure 5.15: Relationship between progress variable c and three-dimensional surface density function $|\nabla c|$ for the premixed (left column), moderately stratified (middle column) and highly stratified (right column) cases at $z = 25\,\text{mm}$ (bottom row) and $z = 30\,\text{mm}$ (top row). Symbols are as in Figure 5.8.

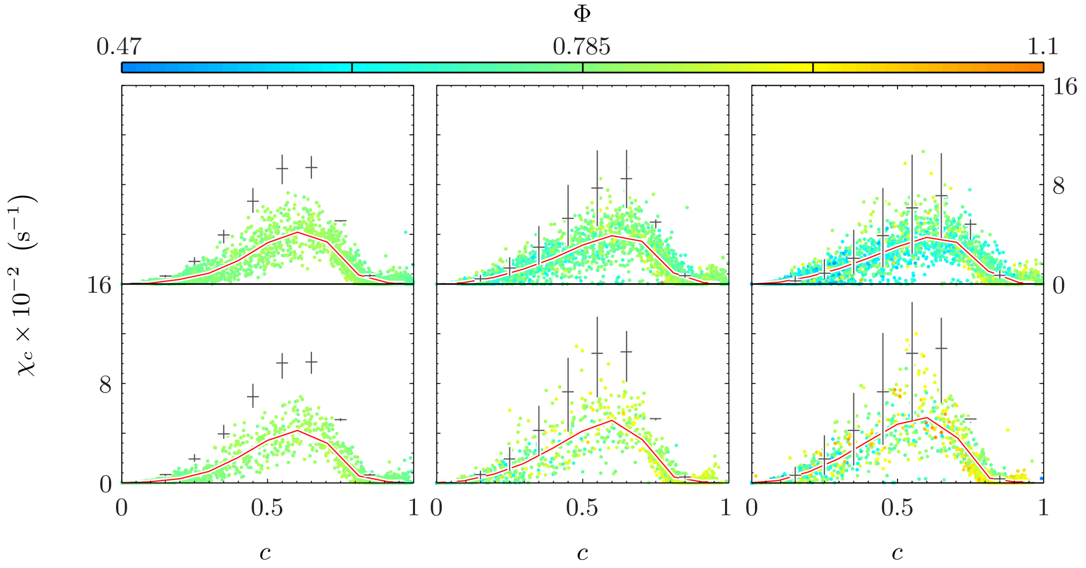

Figure 5.16: Relationship between progress variable c and three-dimensional scalar dissipation rate χ_c for the premixed (left), moderately stratified (middle column) and highly stratified (right column) cases at $z = 25\,\text{mm}$ (bottom row) and $z = 30\,\text{mm}$ (top row). Symbols as in Figure 5.8.

The conditional means of $|\nabla c|$ and χ_c in the premixed case give good agreement with the behavior seen in laminar flame calculations, albeit at significantly reduced values (37 % lower peak $\langle|\nabla c||_c\rangle$, 56 % lower peak $\langle\chi_c|_c\rangle$). This may be due to turbulence thickening the flame relative to unstrained laminar values, as suggested by the DNS simulations in [73, 74]. At each value of instantaneous progress variable c, a broadly positive correlation between gradient terms and equivalence ratio is exhibited by the stratified cases, with higher values of Φ tending to result in thinner flames and higher thermal diffusivities. At the $z = 25\,\mathrm{mm}$ location it appears that both $\langle|\nabla c||_c\rangle$ and $\langle\chi_c|_c\rangle$ are enhanced due to stratification; the former is 9 % (14 %) greater in the $fs4$ ($fs6$) case than the premixed case, and the latter is increased by 17 % (24 %). Further downstream in the flame, no such change is discernible. However as discussed in Section 5.3, only the upstream $z = 25\,\mathrm{mm}$ location is viable for qualitative comparisons between the premixed and stratified cases without further conditioning the data.

5.7.2 Conditioned on local stoichiometry

In order to isolate the effect of stratification from the effects of local equivalence ratio, it is necessary to condition the data on the local Φ. The conditional mean equivalence ratio in progress variable space $\langle\Phi|_c\rangle$ is determined for the premixed case at both locations. The $|\nabla c|$ and χ_c data in all cases, premixed and stratified, are then conditioned such that Φ is within $\pm 1\,\%$ of $\langle\Phi|_c\rangle$ within each progress variable bin. This ensures that any comparisons made between the premixed and stratified cases are unlikely to be influenced by the effect of local equivalence ratio to any significant degree. However this reduces the size of the datasets substantially, with the result that the number of points within each $\bar{c}$ bin ranges from 50 to 60 in the mean thermal ramp ($0.2 \leq \bar{c} \leq 0.8$). This highlights the need to take very large datasets in stratified flows if multiple levels of

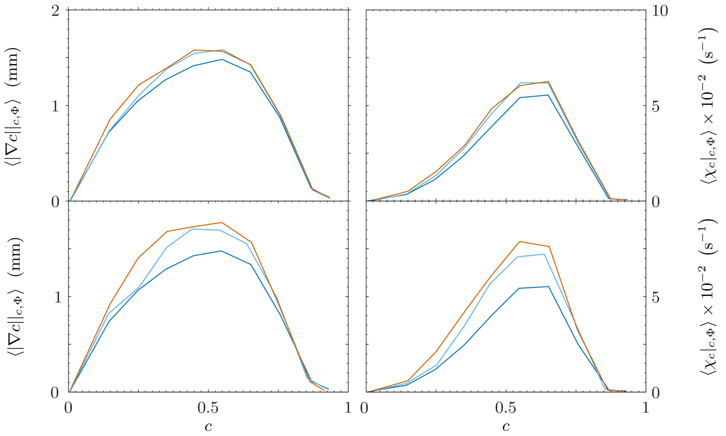

Figure 5.17: Comparison between premixed and stratified cases when conditioned in c-space on local Φ to within $\pm 1\,\%$ of the mean values in the unconditioned premixed data, for premixed, ——, moderately stratified, ——, and highly stratified, ——, cases at $z = 25\,\text{mm}$ (bottom row) and $z = 30\,\text{mm}$ (top row).

conditioning are to be performed.

The doubly conditioned means of surface density function $\left\langle|\nabla c||_{c,\Phi}\right\rangle$ and scalar dissipation rate $\left\langle\chi_c|_{c,\Phi}\right\rangle$ are plotted in Figure 5.17, and the differences in peak amplitudes between the premixed and stratified cases are summarized in Table 5.4. The data show that both surface density function and scalar dissipation rate are enhanced due to stratification relative to the premixed case. The enhancement is modest, but more significant in the upstream location, which may indicate that the effect of stratification on these

Table 5.4: Difference in peak values of doubly conditioned surface density function $\left\langle|\nabla c||_{c,\Phi}\right\rangle$ and scalar dissipation rate $\left\langle\chi_c|_{c,\Phi}\right\rangle$ conditioned on local equivalence ratio Φ for stratified cases expressed relative to equivalent premixed values.

Flame	y	$\left\langle\lvert\nabla c\rvert\rvert_{c,\Phi}\right\rangle$	$\left\langle\chi_c\rvert_{c,\Phi}\right\rangle$
$fs4$	25	+15 %	+31 %
	30	+ 7 %	+ 12 %
$fs6$	25	+20 %	+43 %
	30	+ 7 %	+13 %

quantities is strain sensitive.

5.7.3 Conditioned on local curvature

As both curvature and the thermal gradients within the flame are related to strain, it is interesting to condition the surface density function data on the curvature to see if high positive or negative values of local curvature result in elevated or suppressed levels of $|\nabla c|$. The progress variable and surface density function data were filtered by their continuous curvature values into near zero ($|\kappa_{\mathrm{c}}| < 0.01\,\mathrm{mm}^{-1}$), positive ($\kappa_{\mathrm{c}} > 0.5\,\mathrm{mm}^{-1}$) and negative ($\kappa_{\mathrm{c}} < 0.5\,\mathrm{mm}^{-1}$) sets. Mean fits to these data were obtained and are shown in Figure 5.18.

Local continuous curvature appears to have no significant effect on the surface density function in the cases surveyed. It is possible that this is due to the limits chosen for the positive and negative curvature datasets; correlation between elevated curvature and surface density function may only become apparent at substantially higher curvature

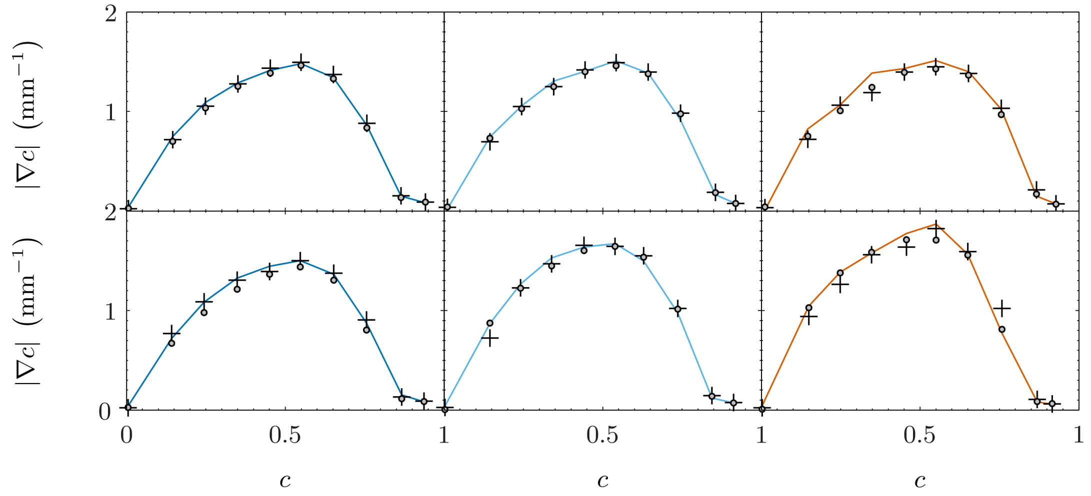

Figure 5.18: Mean fits of surface density function $|\nabla c|$ in progress variable space conditioned on continuous curvature κ_{c} for $fs1_{25}$, $fs4_{25}$ and $fs6_{25}$ (bottom row); and $fs1_{30}$, $fs4_{30}$ and $fs6_{30}$ (top row). Low curvature data are shown in by full lines, highly positive data by crosses, and highly negative by circles.

levels. It is not possible to condition the surface density function at larger curvature values in the present datasets given the paucity of data where $\kappa_c > 0.5$ in the majority of the flame ($0.2 < c < 0.8$). However it is still possible to definitively say that surface density function in the cases under consideration is independent of local continuous curvature to at least $|\kappa_c| = 0.5\,\text{mm}$.

5.8 Flame Surface Density

Flame surface densities calculated using the Pope formulation [8] (detailed in Section 4.3.1 of Chapter 4) are presented in Figure 5.19, demonstrating the trends in Σ across both mean and instantaneous c space. The general behavior is as expected from previous investigations, trending from a positive to negative skew as c increases. Note that the values for high $c = 0.95$ are unphysical, and are due to the noise in the thermal data in the products.

Flame surface density shows similar trends for all cases, with the premixed case appearing elevated relative to the stratified cases at most values of the instantaneous thermal progress variable. This contrasts the behavior expected from the curvature

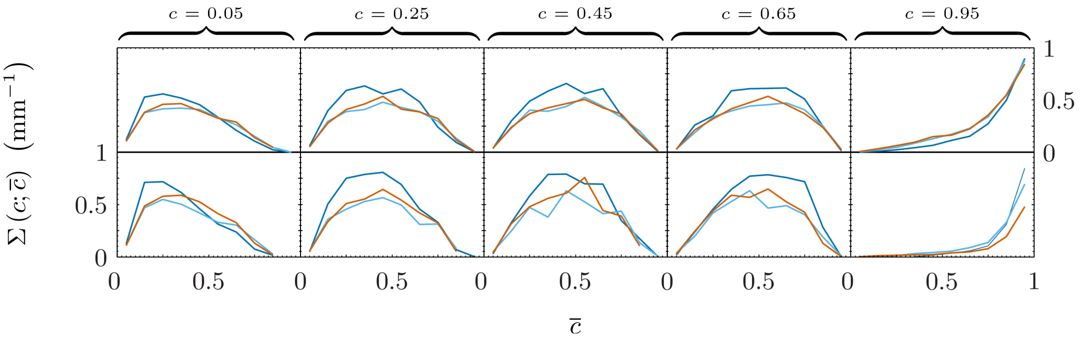

Figure 5.19: Behavior of flame surface density in terms of mean and instantaneous progress variable for $fs1_{25}$, $fs4_{25}$ and $fs6_{25}$ (bottom row); and $fs1_{30}$, $fs4_{30}$ and $fs6_{30}$ (top row). Symbols as in Figure 5.5.

distributions seen in Section 5.6; broader curvature pdfs are associated with thinner flames (due to strain effects), which should result in higher flame surface densities.

There appears to be little difference between the results from the $fs4$ and $fs6$ cases. These are tentative conclusions as the data is rather jittery due to the sample sizes. It is not possible to further condition this data on local equivalence ratio in the slot burner datasets as they are not large enough for such triple conditioning.

5.9 Summary

Line imaging of Raman-Rayleigh scattering and CO-LIF with simultaneous cross-planar OH-PLIF were used to create detailed datasets in premixed and stratified low-turbulence methane/air V-flames. The data[a] have been investigated to determine the effect of stratification on the behavior of species in thermal state space, curvature, surface density function $|\nabla c|$, scalar dissipation rate χ_c, and flame surface density Σ. Specific conclusions are as follows:

i) The distribution of discrete curvature in stratified flames is broader than for premixed flames, in agreement with previous findings, although the mean peak becomes more positive (convex towards the reactants) with stratification, in contrast to prior work.

ii) The curvature distributions obtained using the continuous methodology are significantly more leptokurtic or peaky than the equivalent discrete distributions.

iii) The spread of continuous curvature values within the bulk of the flame ($0.1 < c < 0.8$) is significantly narrower than it is near the unburned reactants and the burned products.

---

[a] The data are available for comparison with model calculations or direct simulations [88].

iv) Turbulent flames are substantially thicker (37%) than premixed unstrained laminar flames at the same equivalence ratio both instantaneously and on the mean. This is perhaps a surprising experimental result, but is substantiated by DNS simulations.

v) Laminar flame calculations of hydrogen mole fraction give poor agreement with the experimental means under stratified conditions. The overall state-space structure of the other measured species is well captured by laminar flamelets on the mean regardless of stratification.

vi) Both the flame surface density function $|\nabla c|$ and scalar dissipation rate χ_c are enhanced relative to the premixed case by stratification.

vii) Curvature shows no significant correlation with the magnitude of surface density function in slot burner data.

Chapter 6

Cambridge Stratified Swirl Burner Results

The stratified swirl burner, SwB, introduced in Section 3.2.1 of Chapter 3 enables the investigation of a range of interesting combustion behaviors. SwB is a more practically relevant burner as it operates at substantially higher levels of turbulence intensity than the slot burner investigated in Chapter 5. The central bluff body induces a recirculation zone above the burner, which produces some interesting deviations from the general behavior seen in the slot burner. The effects of the recirculation zone, in addition to the aforementioned higher turbulence levels, also make this a much more challenging and interesting case for simulations.

A qualitative visual overview of the flames surveyed is given by a series of short- and long-exposure photographs. The flow fields in these cases are explored using the results from the two-dimensional PIV campaign. Key turbulence parameters are given at the locations considered further on when examining the scalar data. The velocity data explain some of the behavior seen in the flame visual survey.

The instantaneous flame structure is examined using profiles of temperature and equivalence ratio, providing a snapshot of the flames surveyed and demonstrating the resolution of the measurements. The thermal and compositional structure of the various cases are considered for various axial distances downstream of the burner exit, enabling the intersection of the mixing layer and the mean flame brush to be identified; significantly larger datasets were taken at these locations to enable the data to be multiply conditioned. The extent of stratification is investigated using the probability distributions of the two-dimensional equivalence ratio gradient.

Representative Favre-averages and fluctuations of temperature, major combustion species and equivalence ratio are presented for each of the cases, and the profiles are compared and contrasted. The influence of stratification on the evolution of these species is examined in temperature space, using both the full datasets and data conditioned on local equivalence ratio. The flame topology is investigated using curvature distributions and statistics for each of the main cases. Progress variable distributions are presented to demonstrate the thickness of the flames. Finally the influence of stratification on the surface density function, turbulent flame thickness and the scalar dissipation rate is considered using both unconditioned data and data conditioned on the local equivalence ratio.

6.1 Flame Visual Survey

Figure 6.1 and Figure 6.2 show photographs of the flames studied in the present work (for long- and short-exposures respectively). The long-exposure photographs in Figure 6.1 demonstrate the mean shape of the flames surveyed through their visible spectrum chemiluminescence. The non-swirling flow cases (top row) demonstrate a non-monotonic broadening of flame angle with increasing stratification. This broadening is attributed to a combination of greater expansion of burnt products and increased flame speeds as the stratified flames burn through higher equivalence ratios than in the premixed cases. The variation in flame angle with stratification is less obvious in cases where the flow is swirling (middle and bottom rows). In all cases the chemiluminescence in the visible spectrum (integrated along the axis perpendicular to the focal plane) shows an increase with stratification. The breadth of the flame increases and the height decreases as swirl is increased (moving down columns).

The turbulent nature of the flames studied is demonstrated by the short-exposure photographs in Figure 6.2. The chemiluminescence indicates that although significant levels of wrinkling are present, the flame fronts are continuous and there is no evidence of local extinction. Again, the distance downstream of the burner exit where high CH excitation is exhibited decreases with increasing swirl for all stratification levels.

6.2 Flow Field Measurements

The velocity fields in the conditions listed in Table 3.3 of Chapter 3 were investigated using two-dimensional particle image velocimetry, as described in Section 3.2.4.

Data is presented for both mean absolute velocity, $\overline{U}$, and velocity fluctuation, u', in a measurement window 25 mm wide and 40 mm tall, starting at $z = 5$ mm downstream of the burner exit. $\overline{U}$ and u' are calculated from the instantaneous two-dimensional velocity fields, with spurious outliers removed. A light shield was used to prevent the illumination of seed particles adhering to the central bluff body; the intensity of light reflected by the bluff body in its absence was sufficient to cause damage to the imaging equipment. The use of the light shield prevented high quality vectors being obtained closer to the burner exit than $z = 5$ mm.

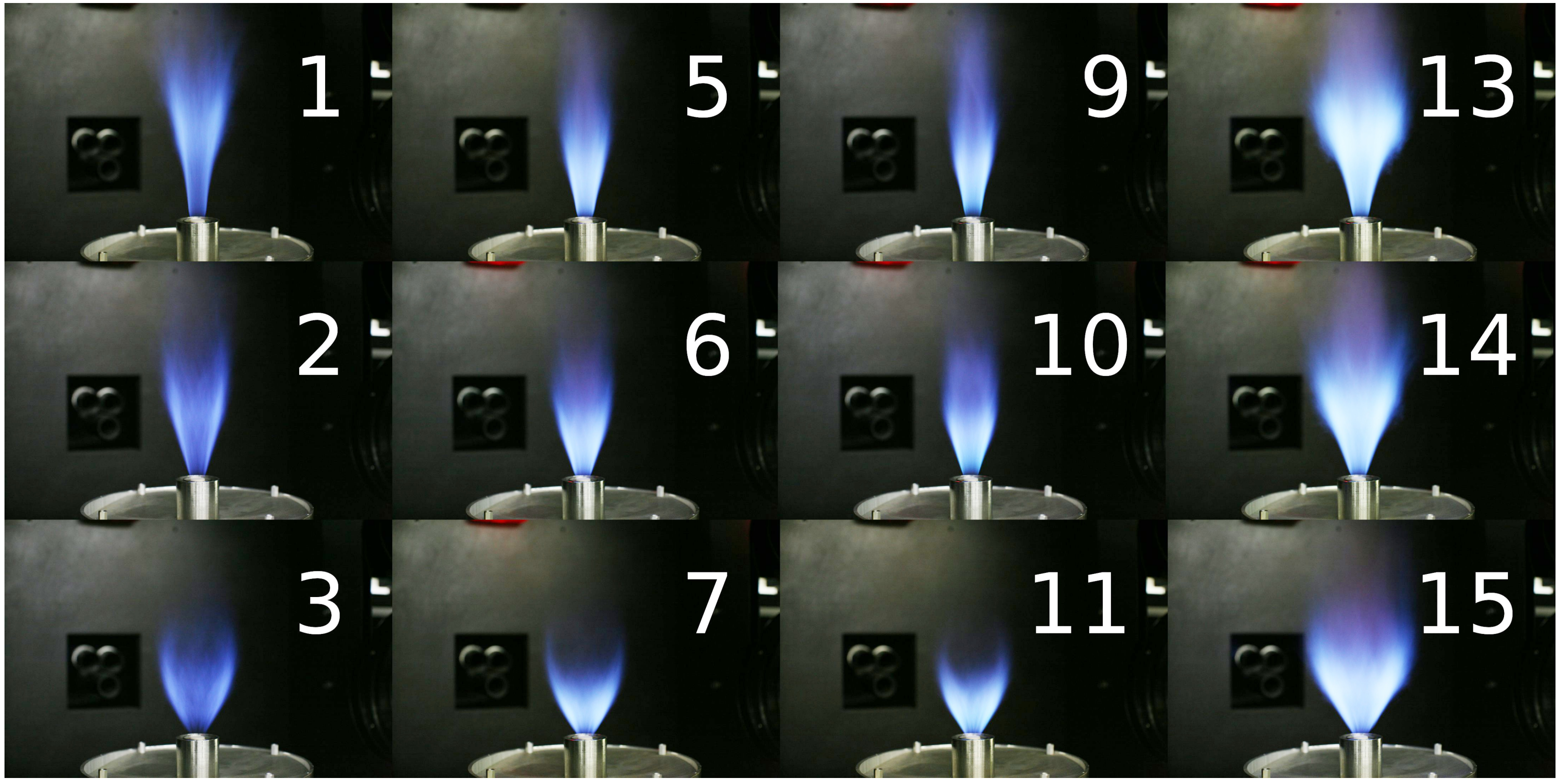

Figure 6.1: Long exposure photos of flame conditions in the swirl burner. Cases are marked by their corresponding numbers; 1 → $SwB1$.

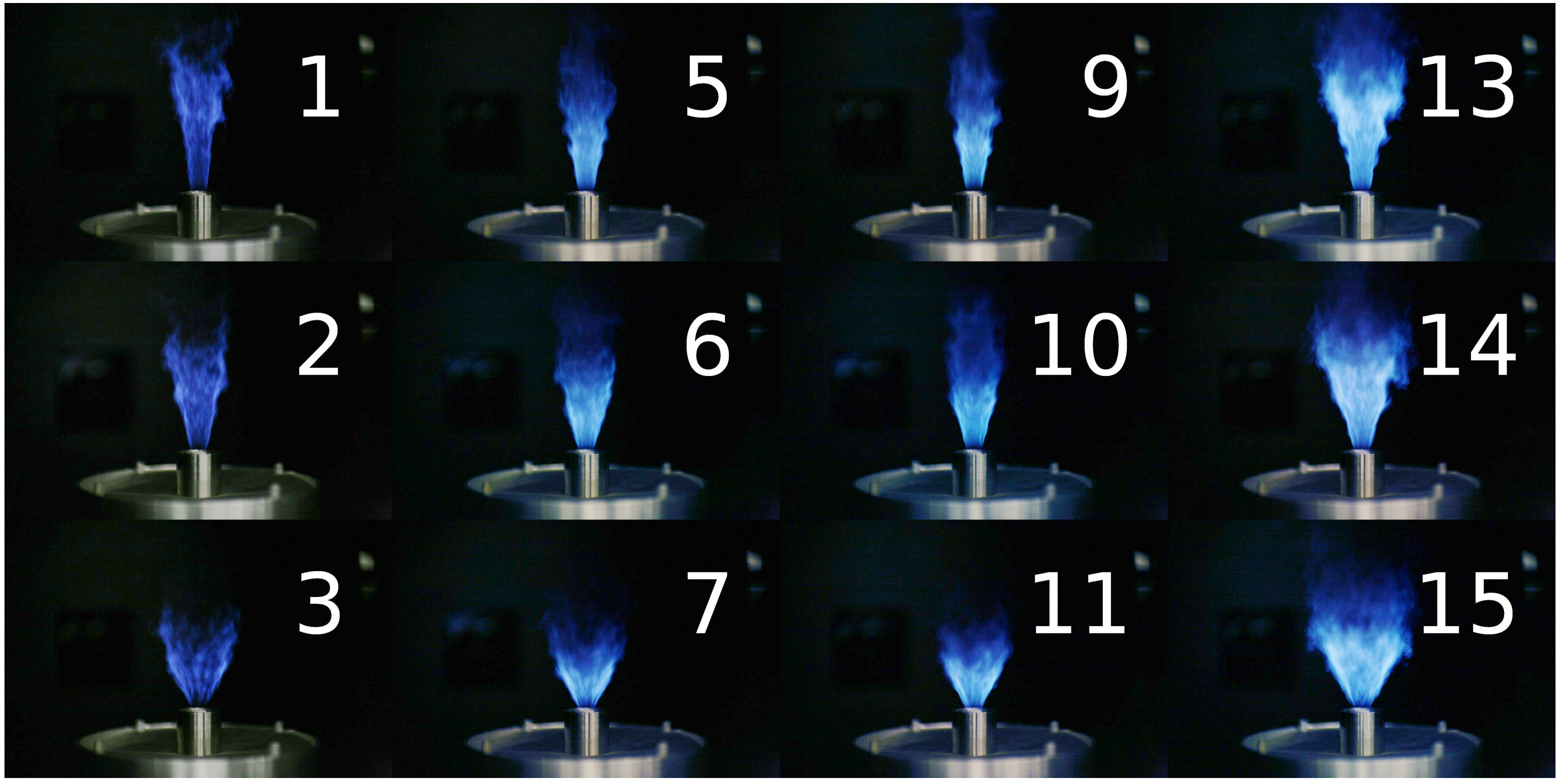

Figure 6.2: Short exposure photos of flame conditions in the swirl burner. Cases are marked by their corresponding numbers; $1 \rightarrow SwB1$.

Mean and fluctuating components of velocity are plotted side by side to give an overall field 50 mm wide, 40 mm tall. Note that both $\overline{U}$ and u' are derived from the same side of the centerline of the experimental images. Under the assumption of radial symmetry, $\overline{U}$ is shown (mirrored) for $r < 0\,\mathrm{mm}$ and u' is shown for $r > 0\,\mathrm{mm}$, with white streak lines to highlight the flow patterns.

6.2.1 Non-Reacting Cases

Non-reacting results are presented in Figure 6.3 for the three flow field patterns; non-swirling, moderately swirling and highly swirling. These velocity fields are presented to illustrate the velocity characteristics due solely to the flows in the burner. The flow near the upstream limit of the measurement window ($z \approx 5\,\mathrm{mm}$) resembles fully developed annular channel flow, with dips between the peak values of $\overline{U}$ corresponding to the inner and outer flows due to the tube wall separating the flows. This can be seen more clearly in the near-exit profiles presented for the reacting cases in Section 6.2.3. These

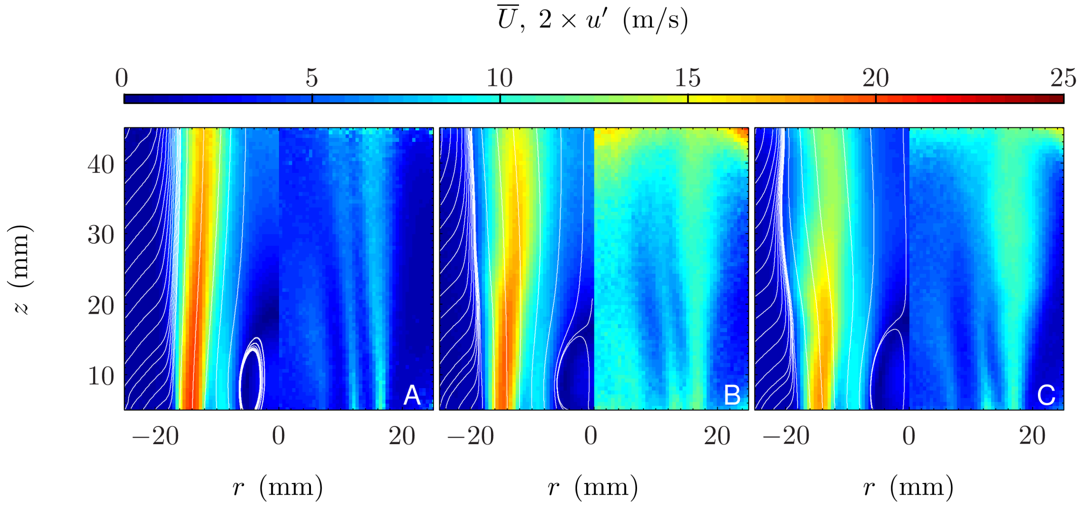

Figure 6.3: Mean absolute ($r < 0\,\mathrm{mm}$) and fluctuating ($r > 0\,\mathrm{mm}$) velocity maps for non-swirling (A), moderately swirling (B), and highly swirling (C) non-reacting swirl burner cases. Streamlines are shown by solid white lines.

peak velocities decay with downstream distance, and the decreases observed increase monotonically with the addition of swirl.

A recirculation zone is seen above the central bluff body, extending from the mouth of the burner to 18.5 mm downstream in each case. The length appears to be independent of the degree of swirl. The width of the recirculation zone is approximately 12.7 mm in diameter, as governed by the size of the central bluff body. The recirculation zones draw the radial position of the peak mean flow from both the inner and outer annuli towards the centerline, and this effect is accentuated as the downstream distance z increases.

The presence of such recirculation zones is important as it affects the results from the multi-scalar measurements presented later. Fully- and partially-reacted combustion products may be transported into the recirculation zone and then back into the reactants from the inner annulus, resulting in deviations from values that would be expected from the nominal stoichiometry detailed in Table 3.3 of Chapter 3.

The plots of u' demonstrate clearly defined shear layers between the recirculation zone, the inner flow, the outer flow, and the co-flow. The breadth and magnitude of these zones indicate that significant turbulent mixing takes place between the streams in all cases. The velocity fluctuations between the co-flow and the outer flow are substantially broadened by the introduction of swirl. It is tempting to assume that the high levels of u' seen in the moderately swirling case for $z > 35$ mm arise from experimental error. However the absence of similar results in either the non-swirling or the highly swirling data implies that this is a real effect.

Significantly higher levels of audible noise experienced when running the burner in the moderately swirling condition than in either the non-swirling or highly swirling conditions. This indicates that the burner operates in an unstable mode under the moderately swirling conditions, and is corroborated by the u' data. The raised levels of turbulence within the recirculation zone can be interpreted as supporting this postulation.

Two additional shear layers form at the middle and outer tube walls, and are visible in the u' profiles (particularly for the non-swirling case). These shear layers generate the mixing layers between the inner annulus, outer annulus, and co-flow streams, resulting in smooth gradients in Φ for the stratified cases.

6.2.2 Reacting Cases

Mean and fluctuating components of velocity are shown for the reacting swirl burner cases in Figure 6.4. The cases are plotted such that the degree of swirl increases along the columns from non-swirling (left column) through moderately swirling (middle column) to highly swirling (right column). The stratification ratios increase moving down the rows from lean premixed (top row) through moderately stratified (2$^{\text{nd}}$ row) to highly stratified (3$^{\text{rd}}$ row); the bottom row shows the stoichiometric premixed cases. The mean velocity demonstrates peaks in mean absolute velocity $\overline{U}$ corresponding to the inner and outer annulus flows, with u' illustrating the shear layers between the various flows. The shear layer between the inner- and outer-flow and the outer- and co-flow merge in most cases by $z = 30\,\text{mm}$, indicating substantial levels of turbulent mixing take place between the fuel/oxidizer streams from the inner and outer annuli by this location.

The radial location of peak $\overline{U}$ is roughly constant in the premixed non-swirling case $SwB1$ for all axial distances in the measurement window, in contrast to the behavior exhibited by the non-reacting non-swirling case (Figure 6.3). This is attributed primarily to the expansion of burnt products in the reacting case.

Considering the other non-swirling cases ($SwB5$, $SwB9$, $SwB13$), the radial position of peak $\overline{U}$ moves progressively farther away from the burner centerline with increasing axial distance (moving down the rows of the left hand column). This is due to the effects of burning through fuel at a higher equivalence ratio than in the lean premixed

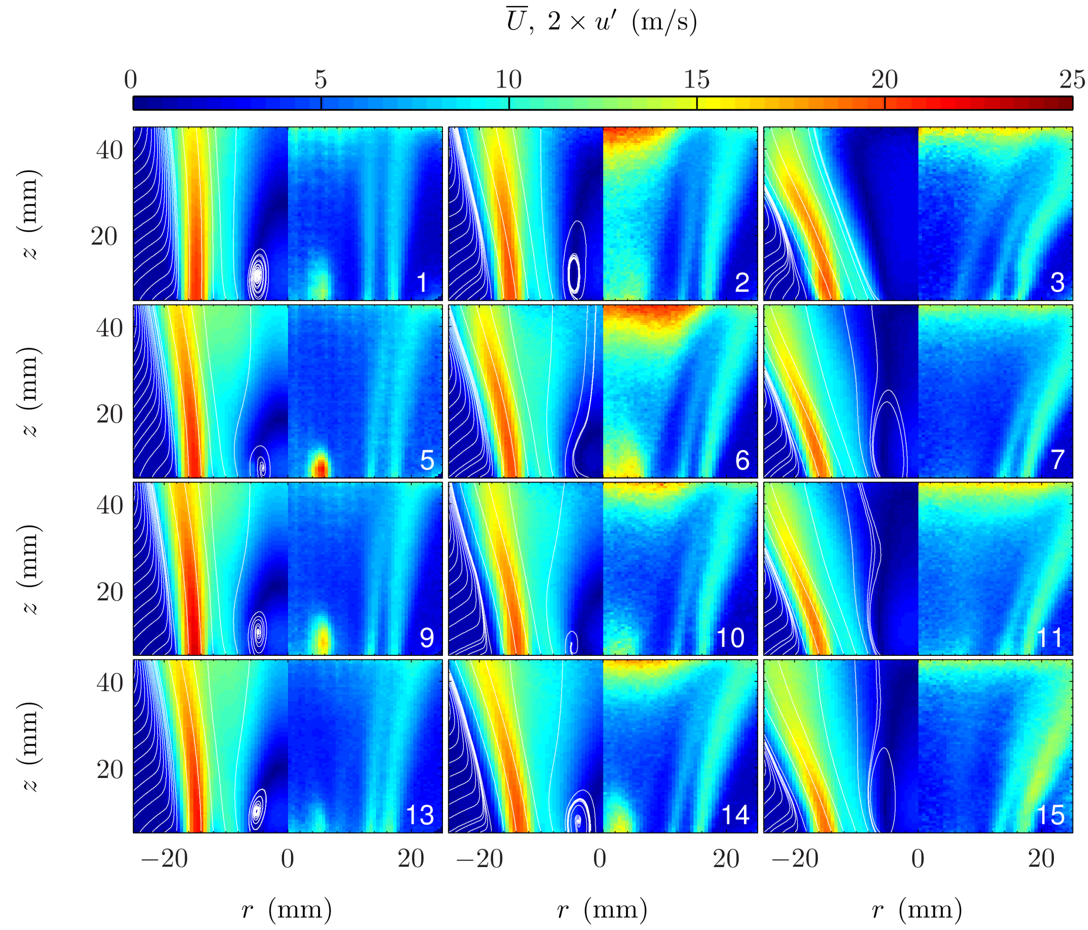

Figure 6.4: Mean absolute ($r < 0\,\mathrm{mm}$) and fluctuating ($r > 0\,\mathrm{mm}$) velocity maps for reacting swirl burner cases. Cases are marked with their corresponding numbers (i.e., $1 \rightarrow SwB1$). Streamlines are shown by solid white lines.

non-swirling case ($SwB1$), resulting in greater temperature changes through the flame and consequently larger changes in density. The greater equivalence ratio also results in an increased flame speed, shifting the radial location of the peak $\overline{U}$ slightly farther out. The radial location of peak $\overline{U}$ at the downstream limit of the measurement window is the same for both levels of stratification.

Again moving down the left column of Figure 6.4, the length of the recirculation zone decreases from roughly 29 mm for the premixed $SwB1$ case to 18 mm to 20 mm in the other cases ($SwB5$, $SwB9$, $SwB13$). The reason for this is not immediately clear. The magnitude of the velocities within the recirculation zones is considerably higher than in the corresponding non-reacting case (35 % to 70 % greater).

In the moderately swirling cases (middle column; $SwB2$, $SwB6$, $SwB10$, $SwB14$), the mean velocity field due to the outer and inner annulus flows are reasonably similar to those in the equivalent non-swirling cases, though the effects of the swirl flow cause the mean flow to diverge outwards significantly more from the axial locations corresponding to the end of the recirculation zone. This effect is more pronounced in the highly swirling cases (right column; $SwB3$, $SwB7$, $SwB11$, $SwB15$), and occurs closer to the burner exit ($z \approx 10\,\mathrm{mm}$).

Examining the mean velocity plot for the premixed moderately swirling $SwB2$, it is clear that the addition of swirl has significantly extended (30 %) the recirculation zone relative to the corresponding non-swirling case, $SwB1$. However the recirculation zones for the other moderately swirling cases (middle column; $SwB6$, $SwB10$, $SwB14$) exhibit recirculation zones which are slightly shorter than their non-swirling equivalents (left column). The reasons for this are unclear, and merit further investigation.

The flow fields of the reacting highly swirling cases (right column; $SwB3$, $SwB7$, $SwB11$, $SwB15$) highlight an interesting phenomenon; the recirculation zone in the premixed $SwB3$ extends farther downstream than the measurement window, and appears to follow the shape of the shear layers within it. This is very different to the behavior seen in the non-swirling (left column) and moderately swirling (middle column) cases, as well as the other highly swirling cases ($SwB7$, $SwB11$, $SwB15$), all of which exhibit more conventional recirculation zones above the central bluff body. This may be due to the balance between the heat release in the reacting case and the degree of swirl causing the recirculation zone interface to move further downstream.

Figure 6.5 provides qualitative visual evidence of this behavior. The photograph was taken during the short exposure flame survey shown in Figure 6.2 while the burner

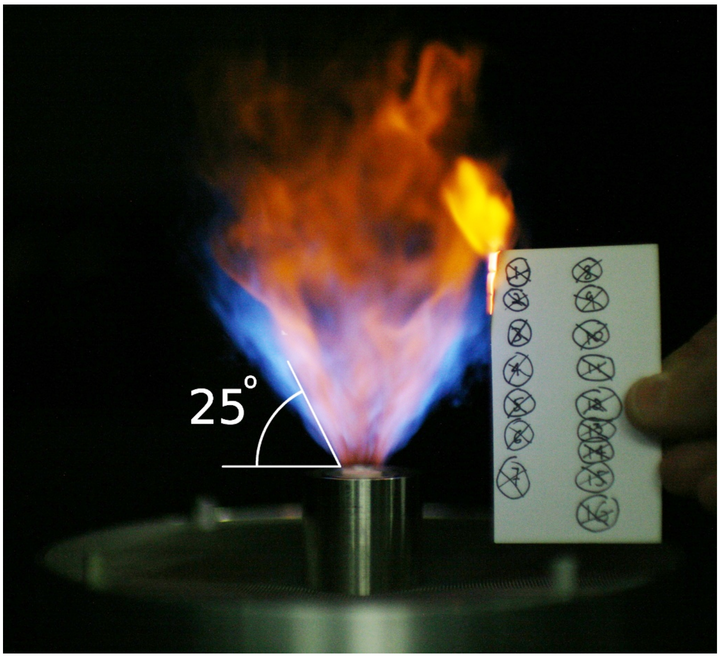

Figure 6.5: Short exposure photograph of very highly swirling stoichiometric case *SwB*16 demonstrating extended recirculation zone.

was operating in the very highly swirling stoichiometric case *SwB*16 (results for this condition are not presented due to difficulties in stabilizing these flames under stratified conditions). The card used to record the current case being recorded is in contact with the flame brush at $z \approx 65\,\mathrm{mm}$ above the burner exit, and is burning, resulting in a yellow/orange sooty flame.

This fortuitous accident demonstrates that the extended recirculation zone proposed earlier is in action, as the cone of yellow/orange chemiluminescence within the blue chemiluminescence of the swirling flame demonstrates that it has entrained products from the card flame down to the bluff body. The yellow/orange cone subtends an angle of 25° to the vertical, which is similar to that subtended by the recirculation zone interface for *SwB*3 (15°). This slight discrepancy is attributed to the different level of swirl between the highly and very highly swirling cases.

The recirculation zones in the non-swirling cases (left column) exhibit a region of high

u' near the edge of the recirculation zone (i.e. above the walls of the central bluff body), with lower levels of u' observed in the interior of the recirculation zone. The moderately swirling cases (middle column) show similar peaks in u', which do not decay to lower levels in the inner region of the recirculation zone. In contrast, the highly swirling case demonstrates substantially lower turbulence in the recirculation zone, echoing the results seen for the non-reacting cases in Section 6.2.1. This apparent decrease in turbulence at high swirl is attributed to the combination of an underestimation of u' in the swirling cases due to the two-dimensional nature of the PIV measurements, as well as a shift back to a stable mode brought about by the further addition of swirl. This latter effect is believed to dominate the former, and is as mentioned previously is corroborated by the noise levels observed when running the burner; significantly lower volumes were experienced when operating the burner for highly swirling cases.

Interestingly, the effect of stratification on the mean flow fields for the swirling cases (middle and right columns) is less pronounced than in the non-swirling cases (left column).

6.2.3 Near-exit Conditions

Profiles of near-exit ($z \approx 5\,\text{mm}$) mean and RMS velocities are presented in Figure 6.6. These profiles are extracted from the data ($\overline{U}$, u') used to produce Figure 6.4. As mentioned in Section 6.2.1, the need to use a light shield to avoid illuminating the central bluff body prevented high quality vectors being obtained nearer to the burner exit than $z = 5\,\text{mm}$. These profiles are presented as they allow the velocities recorded to be separated into their radial and axial components and clearly visualized.

The exit profiles for the reacting cases demonstrate behavior consistent with fully developed annular channel flow, with peaks in $\overline{U}_\text{z}$ (much larger than those for the radial

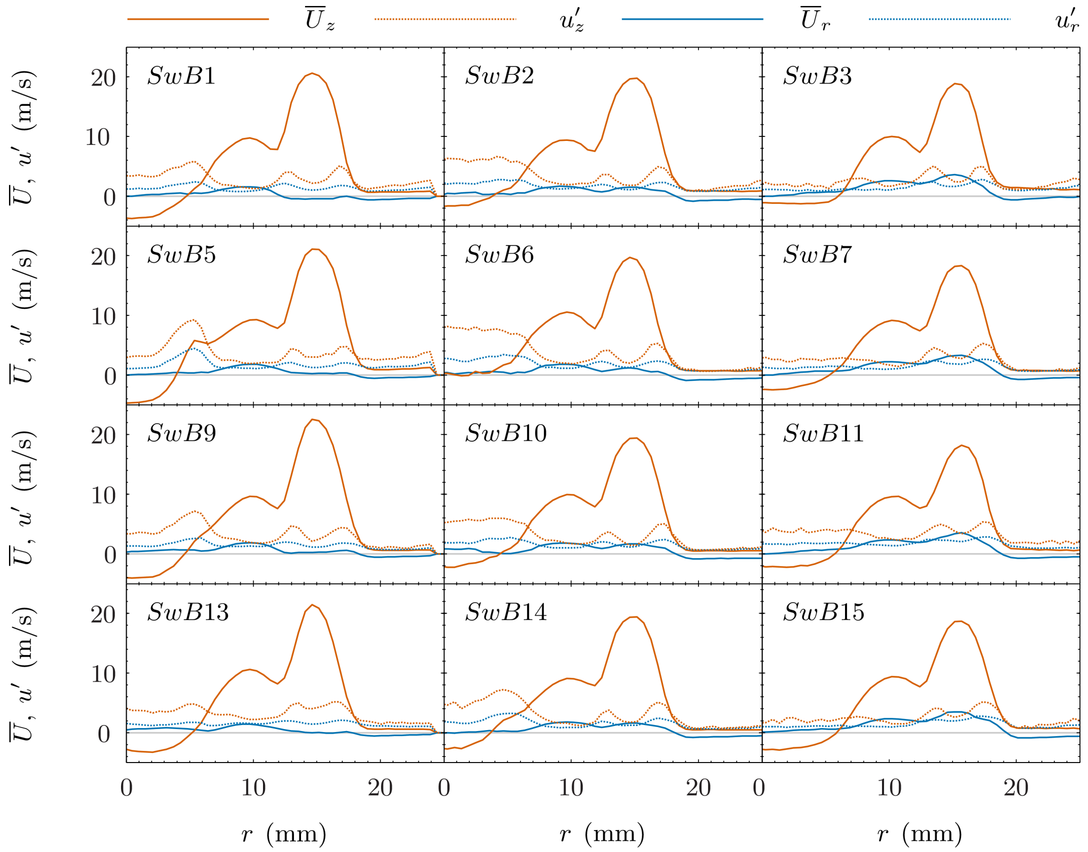

Figure 6.6: Mean and fluctuating velocity profiles near at $z \approx 5$ mm downstream of the burner exit for all reacting cases.

velocity $\overline{U}_\mathrm{r}$) corresponding to flow from the inner and outer annuli . The peak of the outer flow stream is approximately twice that of the inner flow, as expected from the bulk velocities calculated for the annuli. Kaneda *et al* [89] provide a formula for determining the location of peak $\overline{U}_\mathrm{z}$ in a fully developed turbulent annular flow:

$$R_3 = \frac{R_2\,(R_1/R_2)^{0.343} + R_1}{1 + (R_1/R_2)^{0.343}} \tag{6.1}$$

where R refers to a radius and the subscripts 1, 2, and 3 refer to the inner wall of the annulus, the outer wall of the annulus and the location of the peak axial velocity respectively. The exit profiles show good agreement in the non-swirling cases with the values obtained using the geometry detailed in Figure 3.5 of Chapter 3; the peak in $\overline{U}_\mathrm{z}$ is expected to lie near $R_3 = 8.8\,\mathrm{mm}$ for the inner stream and near $R_3 = 14.9\,\mathrm{mm}$ for the outer stream.

All cases except for $SwB6$ exhibit negative $\overline{U}_\mathrm{z}$ for $r < 5\,\mathrm{mm}$ corresponding to the recirculation zones above the burner's ceramic cap, which acts as a central bluff body. A decrease in the magnitude of the positive and negative $\overline{U}_\mathrm{z}$ peaks is seen with increasing swirl, which is expected due to the split between the swirling and non-swirling components of the flow. It should again be noted that the tangential component of velocity is not available in the current datasets.

The extent and strength of the turbulent mixing layers between the inner- and outer-flows and the outer-flow and the co-flow air are shown by u'_z. In the non-swirling cases (left column) there are pronounced peaks in u'_z at the interface between the inner-flow and the recirculation zone, which decay to a reasonably uniform level in the center of the recirculation zone. The magnitude of u'_z is elevated in the bulk of the recirculation zone in the moderate swirl cases (middle column). Again this increase with swirl is non-monotonic; the moderate swirl level appears to result in an unstable mode of operation, while the high swirl cases operate in a stable flow field, as mentioned previously in Section 6.2.2.

The measured radial velocities $\overline{U}_\mathrm{r}$ are small in comparison to the axial velocities at this axial location. The radial fluctuations u'_r are similar to their axial counterparts, albeit reduced by a factor of approximately 2, and show peaks in the shear layers between the inner- and outer-flows and also the outer- and co-flow. Increasing the stratification results in greater levels of radial fluctuation at the interface between the recirculation zone and the inner-flow for the non-swirling cases (left column). This effect is not observed to any significant degree for the swirling cases.

Near to the burner exit it is appears that stoichiometry has limited impact on either the mean or fluctuating components of velocity.

6.2.4 Summary of Turbulence Parameters

The turbulence parameters were calculated using Equation 6.3 through Equation 6.9. The turbulent length scale, L_{t}, is approximated by the hydraulic diameter of the burner as the PIV records were insufficiently long to calculate the autocorrelation coefficient to a satisfactory standard.

$$\begin{aligned}
I &= \frac{u'}{\overline{U}} && (6.2)\\
L_{\mathrm{t}} &= 4\frac{A_{\mathrm{e}}}{P_{\mathrm{w}}} && (6.3)\\
\mathrm{Re}_{\mathrm{t}} &= \frac{uL_{\mathrm{t}}}{\nu} && (6.4)\\
\eta_{\mathrm{K}} &= L_{\mathrm{t}}\mathrm{Re}_{\mathrm{t}}^{-3/4} && (6.5)\\
\nu_{\mathrm{K}} &= u\mathrm{Re}_{\mathrm{t}}^{-1/4} && (6.6)\\
\tau_{\mathrm{K}} &= \frac{\eta_{\mathrm{K}}}{\nu_{\mathrm{K}}} && (6.7)\\
\mathrm{Da} &= \frac{S_{\mathrm{L}}L_{\mathrm{t}}}{u'\delta_{\mathrm{L}}} && (6.8)\\
\mathrm{Ka} &= \frac{\delta_{\mathrm{L}}^2}{\eta_{\mathrm{K}}^2} && (6.9)
\end{aligned}$$

where I is the turbulence intensity, L_{t} is the turbulent length scale, A_{e} is the exit area of the burner, P_{w} is the wetted perimeter of the burner exit, η_{K} is the Kolmogorov length scale, ν_{K} is the Kolmogorov time scale, τ_{K} is the Kolmogorov velocity scale, and all other symbols have their usual meanings. The kinematic viscosity, ν, and laminar flame speed, S_{L}, are calculated for the measured (or in the case of $z = 5\,\mathrm{mm}$, interpolated) values of mean temperature and equivalence ratio.

These turbulence parameters have been calculated for three locations within the flow field, and are listed in Table 6.1 through Table 6.3. The axial positions chosen are: near-exit ($z = 5\,\mathrm{mm}$), the line measurement location closest to the burner exit ($z = 10\,\mathrm{mm}$), and at the intersection of the mixing layer with the mean flame brush ($z = 20\,\mathrm{mm}$ to $50\,\mathrm{mm}$, see Table 6.5 for details). The positions of peak Favre-averaged temperature variation, $\widetilde{T}$, (detailed later on in Section 6.4.1) were used to choose the radial locations considered.

The near-exit case ($z = 5\,\mathrm{mm}$) is included as it is as close to the exit conditions as can be characterized with the current velocity data. As line measurement data is unavailable in this case, the radial position is taken as the linear interpolation between the edge of the bluff body and the center of the flame brush at $z = 10\,\mathrm{mm}$, while relevant quantities such as temperature are approximated by the values at $z = 10\,\mathrm{mm}$. Parameters for $z = 10\,\mathrm{mm}$ are also presented in this section as discussion further on will look at scalar data from these locations. Lastly, the turbulence parameters at the intersection of the mixing layer and the mean flame brush are parametrized as analyses of these data form the crux of the current chapter.

The turbulent parameters are used to plot the region mapped out by the swirl burner cases onto a modified Borghi diagram in Figure 6.7. The swirl burner cases, whether considering data from $z = 5\,\mathrm{mm}$, $z = 10\,\mathrm{mm}$ or the intersection of the mixing layer and the mean flame brush, lie squarely within the thin reaction zone regime, in contrast to the weakly turbulent slot burner cases which were marginally within the wrinkled flamelet regime. It should be noted that the u' used to characterize the flows is obtained from measurements in the axial and radial directions only; the swirl cases, which feature substantial tangential velocity fluctuations, will be lower than their true position on the modified Borghi diagram.

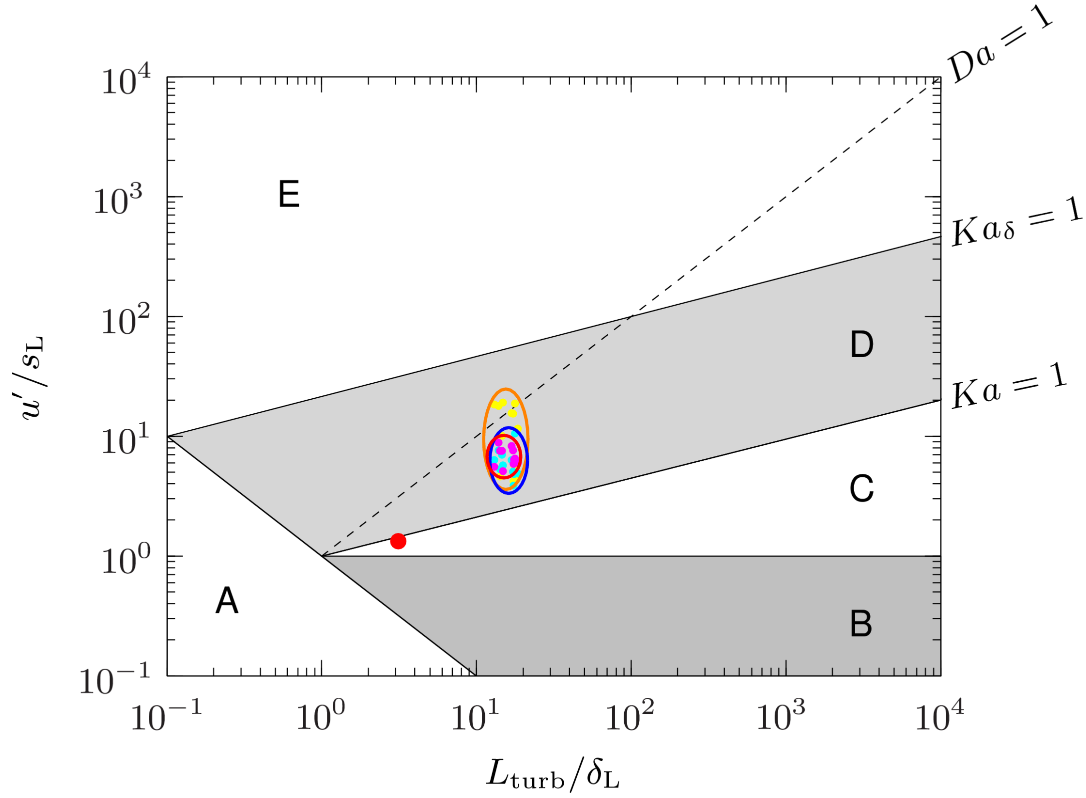

Figure 6.7: Modified Borghi diagram showing both the slot and swirl burner cases: A, laminar flames; B, wrinkled flamelets; C, corrugated flamelets; D, thin reaction zones; E, broken reaction zones. The slot burner condition is marked with a solid red dot, while the swirl burner cases at $z = 5\,\mathrm{mm}$ ($z = 10\,\mathrm{mm}$) [long record locations] are plotted with magenta (cyan) [yellow] full circles, and are enclosed by a red (blue) [orange] ellipse.

Table 6.1: Key turbulence parameters calculated at $z = 5\,\mathrm{mm}$ for the swirl burner cases.

Flame	$\overline{U}$ (m/s)	u' (m/s)	I (%)	$\mathrm{Re_t}$ (−)	L_t (mm)	η_K (µm)	τ_K (µs)	ν_K (m/s)	Da (−)	Ka (−)
$SwB1$	5.66	3.19	56	401	9.97	111	156	0.71	1.18	40
$SwB2$	7.06	3.67	52	496	9.97	95	122	0.78	1.44	51
$SwB3$	6.92	3.14	45	433	9.97	105	153	0.69	1.82	41
$SwB5$	5.71	3.16	55	397	9.97	112	158	0.71	1.98	25
$SwB6$	8.15	3.58	44	568	9.97	86	117	0.73	1.94	46
$SwB7$	6.35	2.74	43	424	9.97	107	177	0.60	2.78	26
$SwB9$	5.36	3.40	63	363	9.97	120	154	0.78	1.48	41
$SwB10$	6.07	3.87	64	525	9.97	91	113	0.81	1.49	62
$SwB11$	7.18	3.75	52	444	9.97	103	126	0.82	1.83	33
$SwB13$	6.17	3.33	54	433	9.97	105	144	0.73	2.12	30
$SwB14$	6.33	3.11	49	536	9.97	90	138	0.65	2.28	40
$SwB15$	5.28	2.84	54	371	9.97	118	182	0.65	2.54	22

Table 6.2: Key turbulence parameters calculated at $z = 10\,\mathrm{mm}$ for the swirl burner cases.

Flame	$\overline{U}$ (m/s)	u' (m/s)	I (%)	Re_t (−)	L_t (mm)	η_K (µm)	τ_K (µs)	ν_K (m/s)	Da (−)	Ka (−)
$SwB1$	6.33	2.46	39	309	9.97	135	231	0.59	1.62	27
$SwB2$	8.23	2.73	33	369	9.97	118	190	0.62	1.58	33
$SwB3$	8.13	2.53	31	351	9.97	123	210	0.58	1.53	30
$SwB5$	6.38	2.68	42	334	9.97	128	204	0.63	2.71	19
$SwB6$	9.44	2.63	28	418	9.97	108	185	0.58	2.67	29
$SwB7$	7.82	2.18	28	338	9.97	126	249	0.51	3.36	18
$SwB9$	6.49	2.91	45	308	9.97	135	195	0.70	1.76	32
$SwB10$	6.83	3.20	47	432	9.97	105	150	0.70	1.71	46
$SwB11$	8.64	3.01	35	356	9.97	122	176	0.69	2.30	24
$SwB13$	8.19	2.68	33	348	9.97	124	199	0.62	2.66	22
$SwB14$	7.58	2.25	30	387	9.97	114	225	0.51	3.20	25
$SwB15$	6.83	2.28	33	298	9.97	139	253	0.55	3.19	16

Table 6.3: Key turbulence parameters calculated at the intersection of the mixing layer and the mean flame brush for the swirl burner cases.

Flame	z (mm)	$\overline{U}$ (m/s)	u' (m/s)	I (%)	Re_t (−)	L_t (mm)	η_K (µm)	τ_K (µs)	ν_K (m/s)	Da (−)	Ka (−)
$SwB1$	30	9.15	2.19	24	332	9.97	128	250	0.51	1.63	30
$SwB2$	30	12.57	2.87	23	377	9.97	117	179	0.65	1.32	34
$SwB3$	30	15.43	3.65	24	541	9.97	89	117	0.76	0.96	57
$SwB5$	50	12.07	7.87	65	985	9.97	57	40	1.41	0.48	98
$SwB6$	40	13.21	4.47	34	557	9.97	87	95	0.92	0.98	44
$SwB7$	30	14.05	3.67	26	383	9.97	115	139	0.83	1.48	22
$SwB9$	50	12.46	7.58	61	762	9.97	69	48	1.44	0.45	123
$SwB10$	40	12.31	4.07	33	486	9.97	96	111	0.87	0.89	55
$SwB11$	30	14.55	3.66	25	417	9.97	108	133	0.81	0.99	30
$SwB13$	30	10.80	2.36	22	332	9.97	128	232	0.55	2.98	20
$SwB14$	30	10.95	2.67	24	327	9.97	130	206	0.63	2.70	19
$SwB15$	20	9.34	2.21	24	269	9.97	150	275	0.54	3.29	14

6.3 Instantaneous Flame Structure

Before beginning any in-depth analysis of the various quantities obtained directly or derived from the multi-scalar line measurements, it is important to give at least a cursory examination of sample instantaneous profiles of these scalars. This allows the general behaviors exhibited by each operating condition to be shown, as well as giving the reader a measure of confidence that the raw data used to calculate derived quantities and conditional means further on in this chapter is sensible. In the interests of brevity, given the volume of material to be covered in the current chapter, instantaneous data presented will be limited to temperature, equivalence ratio (linearly bridged), and OH-PLIF images as these form the basis of the majority of the analysis in the following sections.

Figure 6.8 show instantaneous profiles of temperature and equivalence ratio in the swirl burner cases, using data taken from shots at $z = 30\,\mathrm{mm}$. These data were taken

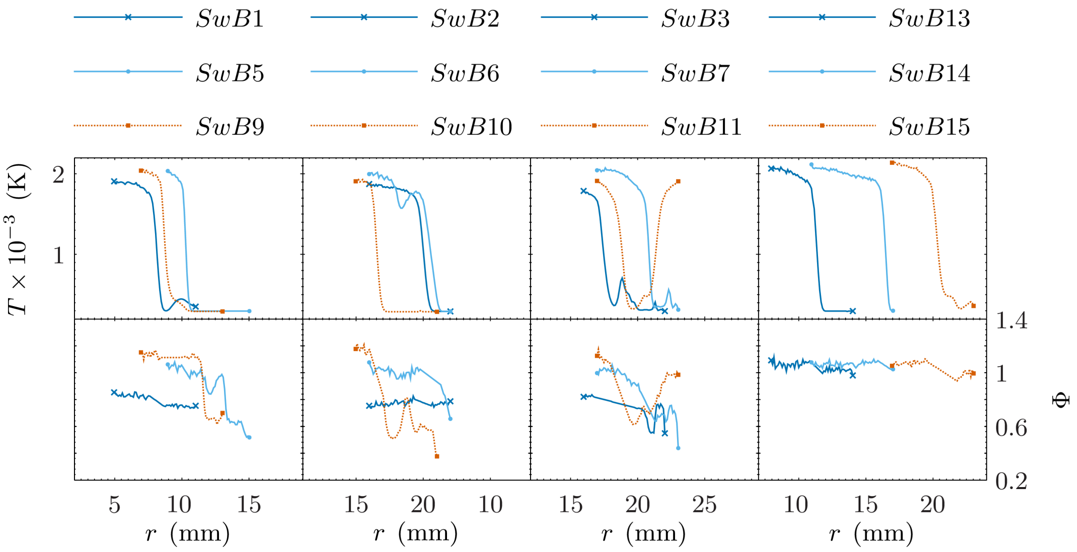

Figure 6.8: Single-shot profiles of temperature (top row) and equivalence ratio (bottom row) at $z = 30\,\mathrm{mm}$ downstream of the burner exit for swirl burner cases.

in initial surveys of the flames detailed in Table 3.3 of Chapter 3, the results of which are presented later on in Section 6.1. These records were relatively short (300 shots at each location, with an additional 1 200 shots at location where the mean flame front is located), at 103 µm resolution, and were taken to establish the locations at which the mixing layer intersected the flame brush. These locations are referred to throughout the present chapter as the long record locations, as larger datasets were subsequently taken at these locations (5 000 shots for premixed cases, 30 000 shots for stratified), using wavelet filtering and oversampling to give 20 µm resolution.

The format of Figure 6.8 merits brief discussion, as it is used extensively from Section 6.7 onwards. The data are presented such that the lean cases ($SwB1$ through $SwB11$) are grouped by flow condition. Hence the first column shows the non-swirling cases ($SwB1$, $SwB5$ and $SwB9$), the second the moderately swirling cases ($SwB2$, $SwB6$, $SwB10$), and the third the highly swirling cases ($SwB3$, $SwB7$ and $SwB11$). The stoichiometric cases ($SwB13$, $SwB14$ and $SwB15$) are grouped in the fourth column. This format allows the effect of stratification at each flow condition to be assessed visually with the minimum of difficulty, as well as highlighting the effects of swirl on the stoichiometric cases, which do not have stratified equivalents.

The instantaneous profiles show some interesting behavior, such as the raised values of equivalence ratio near to the centerline of the burner in the premixed cases. The elevated values result in mild gradients in equivalence ratio along the line measurement axis, $\nabla_x \Phi$[a], as seen in Table 6.4. This curious result is explained in the discussion of the Favre-averaged results later on in Section 6.6.

The profile of equivalence ratio for $SwB9$ demonstrates the necessity of taking data at the intersection of the mixing layer and the flame brush, as the flame in this highly

---

[a] $\nabla_x \Phi$ is the two-dimensional projection of the true three-dimensional equivalence ratio gradient projected onto the line measurement axis.

Table 6.4: Two-dimensional equivalence ratio gradients from instantaneous profiles shown in Figure 6.8.

SwB	1	2	3	5	6	7	9	10	11	13	14	15
$\nabla_x \Phi$ $\left(\mathrm{mm}^{-1}\right)$	73	39	26	159	76	205	-1	340	282	98	67	66

stratified case stabilizes in the rich reactants from the inner annulus, which are not yet well mixed with the leaner reactants from the outer annulus. The equivalence ratio profiles in those stratified cases where this condition has been fulfilled ($SwB10$, $SwB11$) demonstrate large degrees of fluctuation in Φ. This highlights the importance of conditioning on local rather than on mean or global equivalence ratios when considering scalar data later on in this chapter.

The temperature valley seen in the $SwB11$ profile in the third column shows a case where a pocket of lean mixture has penetrated richer flow, causing the flame to stabilize at the interface between the two. This illustrates the need for image processing of the OH-PLIF images to be able to cope robustly with the presence of pockets of unburned mixture in the flame as well as islands or peninsulas of flame.

Figure 6.9 shows profiles of temperature and equivalence ratio in the moderately stratified, highly swirling $SwB7_{30}$ case, using both the 103 µm resolution super-binned data and the 20 µm resolution wavelet filtered data. The data are plotted with markers at each point to demonstrate the increase in fidelity achieved in the wavelet filtered data. It is clear that the wavelet filtered data is substantially smoother than the super-binned data, as well as higher resolution. The implication of this is that gradients obtained from the wavelet filtered data are significantly smoother on a shot to shot basis than the super-binned data. All data at the intersection of the mixing layer with the flame brush (the long record locations mentioned previously) are recorded and processed using the wavelet filtering.

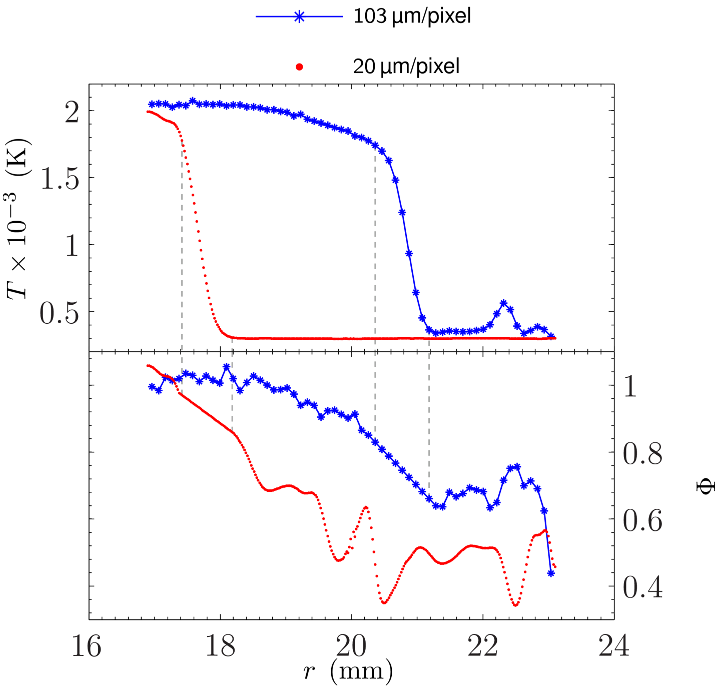

Figure 6.9: Single-shot profiles of temperature (top) and equivalence ratio (bottom) at $z = 30\,\mathrm{mm}$ downstream of the burner exit for $SwB7_{30}$ at both super-binned resolution (103 µm/pixel) and wavelet filtered resolution (20 µm/pixel). The flame brush is mapped from the temperature to the equivalence ratio profiles using gray dashed lines.

Sample OH-PLIF images for $SwB1_{30}$, $SwB6_{30}$, $SwB11_{30}$ and $SwB13_{30}$ are shown in Figure 6.10, along with the continuous curvature along their centerline. The resolution of these images is 48 µm/pixel, which is roughly three times finer than in the slot burner data. These images correspond to the profiles plotted in Figure 6.8; for brevity only four conditions are shown. As in the slot burner data, the continuous curvature results are erratic in both the low (reactants) and high (products) regions of OH due to the effect of small gradients on the denominator of Equation 4.4 (see Section 4.1.4.2 of Chapter 4). The gray regions in Figure 6.10, which mark the instantaneous flame brush, indicate that some caution should be taken when conditioning data on curvature, as there is some disparity between the location of the thermal ramp and the OH reaction zone.

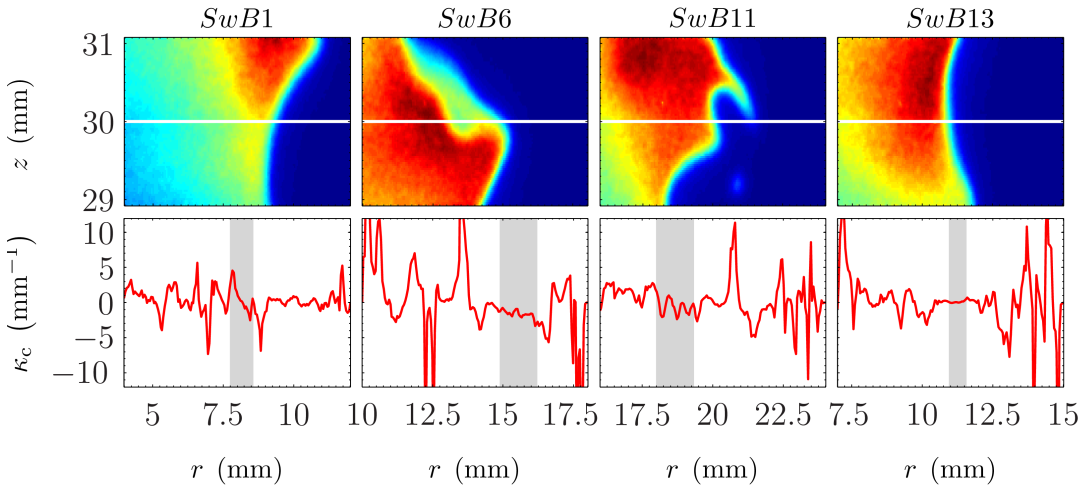

Figure 6.10: Single-shot OH-PLIF images (top row) for $SwB1$, $SwB6$, $SwB11$ and $SwB13$, corresponding to the instantaneous profiles shown in Figure 6.8. Continuous curvature along the line measurement axis (shown by solid white lines in the top row) is shown in the bottom row. Regions corresponding to the instantaneous flame brush are marked in gray.

6.4 Flame Structure and Selection of Long Record Locations

In light of the sparsity of data in the slot burner after conditioning on local equivalence ratio, it was decided that substantially larger datasets would be recorded in the swirl burner cases to allow for multiple conditioning of data without reducing the data by too great an amount. It was not feasible to record large datasets at multiple axial locations in each flame condition due to the time constraints on the use of facilities at Sandia National Laboratories. The intersection of the mixing layer and the mean flame brush was deemed to be the most sensible location to record the large datasets, as the mean equivalence ratio at these locations would be comparable across the relevant cases (i.e. $\overline{\Phi} \approx 0.75$ for the lean cases, $\overline{\Phi} \approx 1$ for the stoichiometric cases). This minimizes data reduction when conditioning on local equivalence ratio is performed. The locations of the intersection of the mixing layer and the mean flame brush are referred to throughout the remainder of the present work as the long record locations. In order to identify these long record locations, it was necessary to determine the radial location of the center of the flame brush for various downstream distances (thermal structure), and also the mean equivalence ratio at these locations (compositional structure).

6.4.1 Thermal Structure

The center of the flame brush was taken to be the location of peak variation of the Favre-averaged temperature, $\widetilde{T}$, and was obtained from the short record[b] temperature and density measurements detailed in Chapter 3. The resulting thermal flame structure for each case is shown in Figure 6.11. The format is as follows: swirl increases from left to right, moving from non-swirling cases (left column) through moderately swirling cases (middle column) to highly swirling cases (right column); stratification increases down the first three rows from lean premixed cases (top row) through moderately stratified cases (2nd row) to highly stratified cases (3rd row), with the stoichiometric premixed cases lying in the bottom row. This format is used extensively throughout the present work. The full width half maximum (FWHM) locations obtained from the T'' profiles are used to quantify the width of the flame brush at each location.

These plots shed more light on the flame structure than the mean and instantaneous shots shown in Section 6.1. In the non-swirling cases, the flame brush angle increases with the addition of stratification (from 5° to 9°), though the difference between the two levels of stratification is minor ($\sim 1^\circ$). The addition of swirl reduces the change in flame angle between the premixed and stratified cases to the point that it is negligible (less

---

[b] The short records consist of 300 to 1 500 shots of data, which were taken to allow complete radial profiles through the flame to be recorded quickly at multiple axial locations. Further details are provided in Figure 3.6 of Chapter 3.

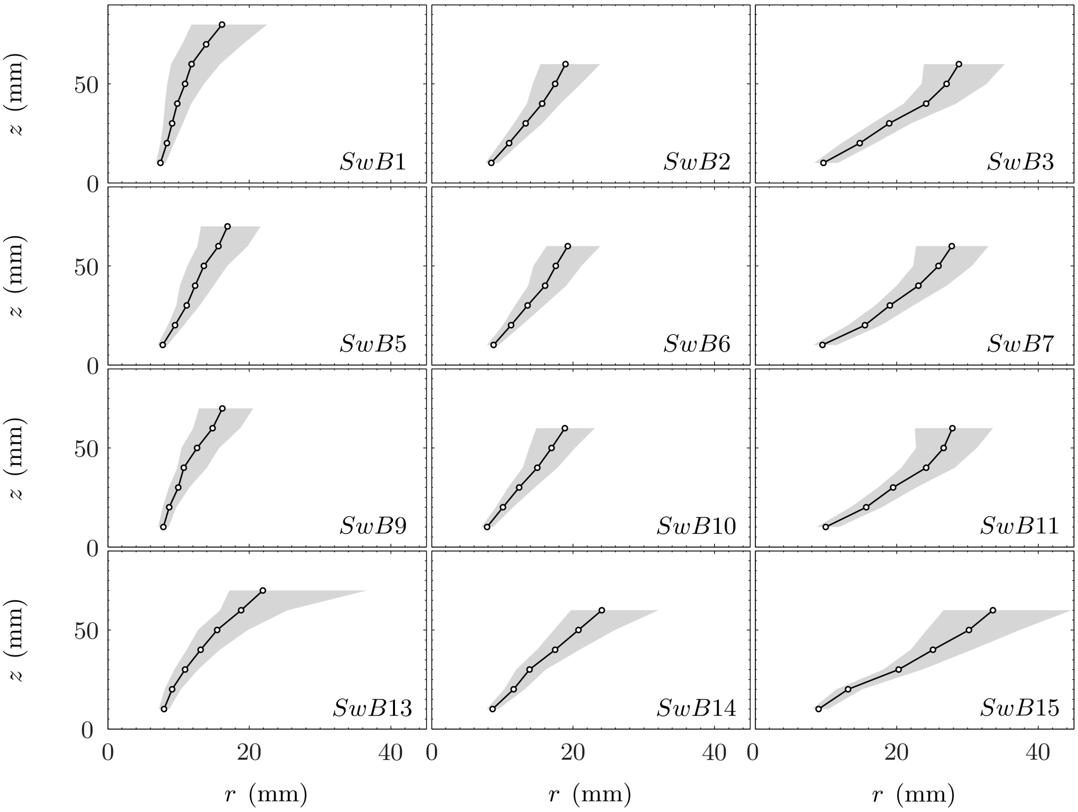

Figure 6.11: Flame brushes in the swirl burner cases. Center of flame brush as defined by peak Favre averaged temperature variation denoted by open circular markers, ○ , with the shaded region showing the associated FWHM.

than 1°).

As swirl is added, the flame brushes shift from being slightly concave towards the reactants in the non-swirling cases, regardless of the fuel/oxidizer composition, straighten out (moderately swirling cases) and eventually become convex towards the reactants (highly swirling cases). This explains the visual differences seen in the flame surveys. Considering only the lean premixed and stratified cases, the mean flame angle increases to $\sim 12^\circ$ for the moderately swirling condition, and increases to $\sim 20^\circ$ for high swirling. The corresponding increases in the stoichiometric premixed cases are to $\sim 17^\circ$ and $\sim 26^\circ$ respectively.

The width of the flame brush also increases regularly with increasing axial distance, in agreement with the broadening of the turbulent mixing layers seen in Figure 6.4. In the non-swirling cases the width is influenced by stratification, with the moderately and highly stratified cases being on average 13 % and 4 % greater than the premixed $SwB1$ case respectively. However the standard deviation of these differences is such that it is difficult to state conclusively that the differences seen between the two levels of stratification are significant; the most salient conclusion from the data is simply that stratification results in a thicker flame brush in non-swirling flow conditions. The effect of stratification on the swirling cases is the opposite to that seen in the non-swirling cases; the addition of stratification results in a reduction in FWHM of $\sim 5\,\%$ on average, with little difference between the moderate and high levels of stratification.

When the composition is held constant and the degree of swirl is varied the flame brush is significantly enlarged. Moving from the non-swirling to moderately swirling cases, increases in FWHM of 17 % to 34 % are seen; the corresponding increases between the non-swirling and highly swirling cases are 74 % to 105 %. Again, this behavior tallies with the velocity fluctuations seen in Figure 6.4.

6.4.2 Compositional Structure

The compositional structure of the flames surveyed is shown in Figure 6.12, using the same layout as the thermal structure plots shown in Figure 6.11. Note that the quantity plotted is the raw unprocessed equivalence ratio, ϕ, and not the linearly bridged equivalent, Φ, as the latter form was not used in the determination of the intersection of the mixing layer with the mean flame brush.

The mean equivalence ratio at the center of the flame brush, defined as for Figure 6.11, decreases with increasing axial distance in all cases. This is due to a combination of the flame stabilizing at wider radial positions further downstream of the exit due

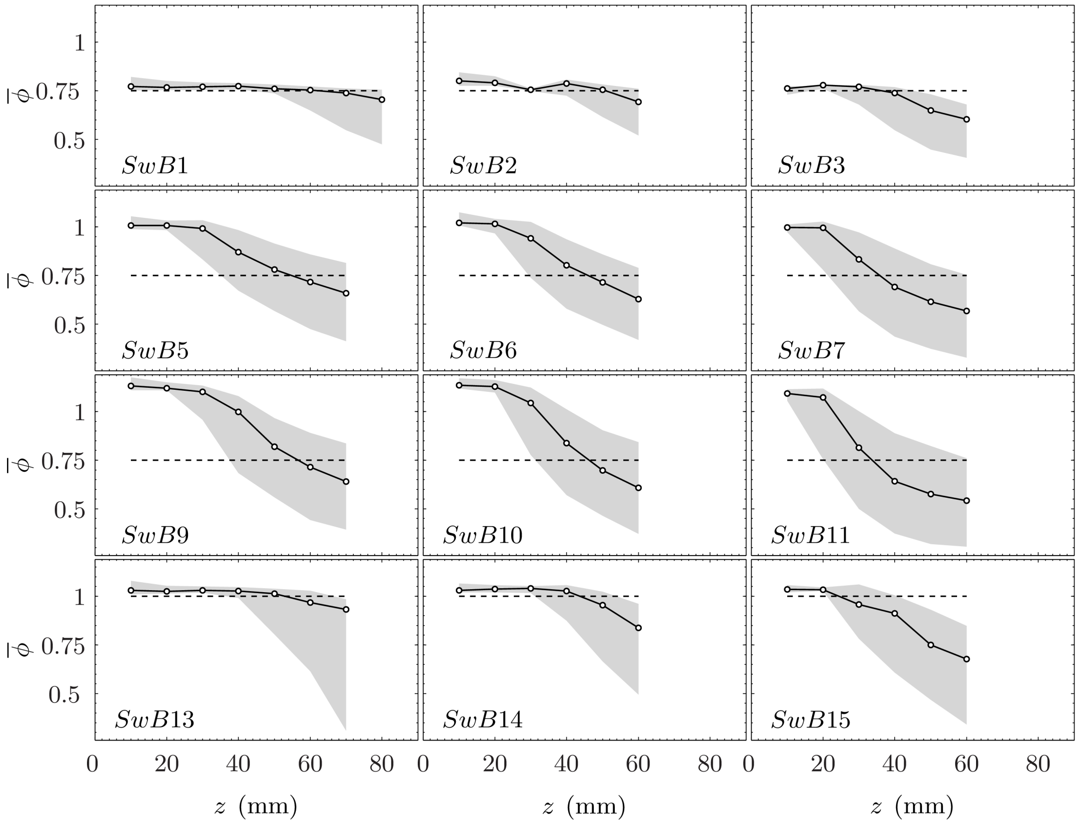

Figure 6.12: Compositional structure of the flames surveyed in the swirl burner. The equivalence ratio at the center of flame brush is denoted by open circular markers, ○ , with the shaded region showing the equivalence ratio values at the associated FWHM points. The nominal stoichiometry is marked by - - - -. Equivalence ratio data is not linear bridged.

to decreasing axial velocity and the increasing width of the turbulent mixing layers. The premixed mean equivalence ratio also decreases with axial distance, albeit significantly less; this is attributed to the dilution of the fuel/oxidizer mix with co-flow air, which becomes more significant as z increases due to the growing mixing layer between the outer- and co-flow streams.

The addition of swirl reduces the mean equivalence ratio as a function of downstream distance. The effect is relatively slight for the lean premixed case, but is substantial in the stratified and stoichiometric cases. The range of mean equivalence ratio encompassed by the FWHM locations at each downstream position show moderate increases with both the degree of stratification and swirl.

6.4.3 Long Record Locations

The nominal mean equivalence ratio ϕ_n was used in conjunction with plots of the compositional structure to determine the radial and axial locations at which to take the long record datasets. The values chosen are listed in Table 6.5. The radial locations are the positions of the peak Favre-averaged temperature variance as in Figure 6.11. The axial locations were selected to ensure the mean equivalence ratio at the center of the flame brush was as close as possible to the nominal value while ensuring that a significant range of equivalence ratio values were experienced within the FWHM window.

Note that in certain cases, such as $SwB11$, it appears from Figure 6.12 that the location listed in Table 6.5 is suboptimal. This is due to slight changes in equivalence ratio resulting from modifications to the processing of the Rayleigh/Raman/CO-LIF line measurement data, altering the ideal axial locations relative to those determined from the initial analysis of the short record data. However the differences are still relatively small, with the mean equivalence ratio being 12 % greater than the nominal value at worst, and on average being within 6 %.

It is worth noting that the spread of Reynolds-averaged equivalence ratio between the FWHM positions, $\Delta_{\overline{\phi}}$, is generally an order of magnitude higher in the stratified cases than in the premixed cases, and that the FWHM flame brush thickness, Δ_T, is small enough that the line measurement window ($\sim$ 6 mm) should encompass most of the temperature variance in all cases. Values for the mean equivalence ratio and corresponding FWHM are also given in the linear bridged form in Table 6.5 for reference, though they were not used in the determination of the long record locations.

Table 6.5: Radial and axial locations of the intersection of the mixing layer and the mean flame brush (long record locations) in the swirl burner, with corresponding FWHM flame brush thickness, Δ_T, Reynolds-averaged equivalence ratio, $\overline{\phi}$, FWHM range of Reynolds-averaged equivalence ratio, $\Delta_{\overline{\phi}}$. Nominal values of equivalence ratio based on the fuel/air flows are $\phi_\mathrm{n} = 0.75$ for the lean cases and $\phi_\mathrm{n} = 1$ for the stoichiometric cases. Corresponding values using linear bridged phi, Φ, are shown in parentheses for reference.

Flame	z (mm)	r (mm)	Δ_T (mm)	$\overline{\phi}$ ($\overline{\Phi}$) (−)	$\Delta_{\overline{\phi}}$ ($\Delta_{\overline{\Phi}}$) (−)
$SwB1$	30	9.1	2.8	0.77 (0.78)	0.04 (0.04)
$SwB2$	30	13.3	4.0	0.76 (0.76)	0.01 (0.01)
$SwB3$	30	18.9	5.4	0.77 (0.77)	0.10 (0.10)
$SwB5$	50	13.6	5.7	0.78 (0.79)	0.35 (0.35)
$SwB6$	40	16.1	5.3	0.80 (0.81)	0.36 (0.36)
$SwB7$	30	19.0	5.4	0.83 (0.85)	0.41 (0.41)
$SwB9$	50	12.6	5.3	0.82 (0.82)	0.41 (0.42)
$SwB10$	40	14.9	4.9	0.84 (0.84)	0.44 (0.45)
$SwB11$	30	19.5	5.3	0.81 (0.83)	0.50 (0.51)
$SwB13$	30	10.9	3.4	1.03 (1.03)	0.03 (0.04)
$SwB14$	30	13.8	3.5	1.04 (1.04)	0.04 (0.04)
$SwB15$	20	13.1	3.2	1.03 (1.05)	0.02 (0.01)

6.5 Extent of Stratification

The Favre-averaged profiles of equivalence ratio shown in Section 6.6 demonstrate that significant degrees of stratification are achieved within the flame brush in the nominally stratified cases at the long record locations. However they also reveal non-negligible spatial gradients of equivalence ratio in the nominally premixed cases, due mainly to the effect of the recirculation zone but also to the measurements of Φ which are known to be biased slightly high in the products.

In order to quantify the extent of stratification at the long record locations, this brief section presents and discusses probability density functions and basic statistics for the cases surveyed at the long record locations. Pdfs of equivalence ratio gradients derived

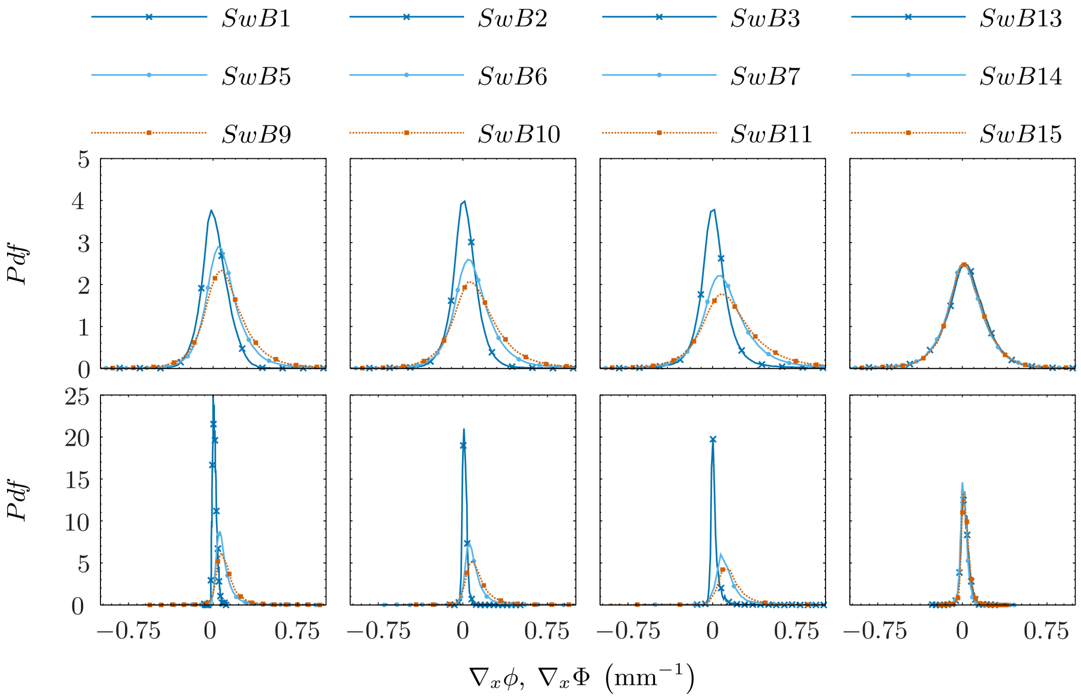

Figure 6.13: Probability density functions of two-dimensional equivalence ratio gradients at the long record locations in the swirl burner. Pdfs of gradients obtained using the raw equivalence ratio data, $\nabla_x \phi$, are shown in the top row, while pdfs generated using linear bridged equivalence ratio gradients, $\nabla_x \Phi$, are shown in the bottom row.

from both raw and linearly bridged equivalence ratio data are presented in Figure 6.13. A word of caution is advised here; the gradients presented are two-dimensional projections of the true equivalence ratio gradient. It is not currently feasible to measure the instantaneous orientation of the equivalence ratio field simultaneous with the other data taking, and hence only the two-dimensional analogue $\nabla_x \Phi$ along the line measurement axis can be presented.

A cursory examination of the top row of this figure reveals the issue with using the raw equivalence ratio data to determine the level of stratification, as even the premixed cases exhibit large positive and negative gradients of ϕ due to the effects of preferential differential diffusion detailed previously in Section 4.2.1.1 of Chapter 4. When the equivalence ratio is linearly bridged to give Φ, more physically sensible results are ob-

Table 6.6: Statistics for two-dimensional equivalence ratio gradients in the swirl burner at long record locations. Equivalence ratio data is linearly bridged.

Flame	z (mm)	$\overline{\lvert\nabla_x\Phi\rvert}$ (m^{-1})	$\overline{\nabla_x\Phi}$ (m^{-1})	γ_1 $(-)$	γ_2 $(-)$
$SwB1$	30	24	14	0.85	1.26
$SwB2$	30	27	16	1.81	27.10
$SwB3$	30	50	19	4.40	41.12
$SwB5$	50	116	92	1.74	6.26
$SwB6$	40	126	96	1.73	6.94
$SwB7$	30	160	125	2.25	23.09
$SwB9$	50	152	118	1.58	5.08
$SwB10$	40	171	129	1.58	5.38
$SwB11$	30	212	169	1.81	11.42
$SwB13$	30	43	22	0.51	2.49
$SwB14$	30	39	17	1.44	9.61
$SwB15$	20	46	27	0.81	2.89

tained (bottom row of Figure 6.13), as the absolute mean gradients are near-zero for the premixed cases.

The main point to note is that the gradient distributions appear similar for both nominal degrees of stratification. This is perhaps a surprising result, given the nominal stoichiometries of the richer inner flow and the lean outer flow are varied symmetrically about $\Phi_\mathrm{g} = 0.75$ while the respective flow rates are kept constant. However an examination of Table 6.6, which summarizes the main statistical moments for $\nabla_x\Phi$, reveals that both the mean and absolute mean gradients are substantially increased moving from the moderate to high stratification levels (28 % to 35 %).

However, these changes are small in comparison to the increases experienced relative to the premixed cases (222 % to 535 %). As such analyses of any given quantity of interest at the two stratification levels are unlikely to exhibit large differences in comparison to those for the premixed equivalent. It is worth noting that the absolute mean gradient, $\overline{|\nabla_x \Phi|}$, for the moderate stratification level is similar to that in the most stratified slot burner case ($\overline{|\nabla_x \Phi|} \sim 123\,\mathrm{m}^{-1}$ in $fs6_{30}$).

The level of swirl also plays a role as it increases the gradients seen in the stratified cases by between 9 % to 39 %. Though these changes in gradient are small relative to those moving from the premixed cases to the stratified ones, they should still be borne in mind when considering figures and discussion in the subsequent sections.

Note that the mean and RMS gradients for the premixed linear bridged equivalence ratio data, while small, are non-negligible and positive. This is also seen in the pdfs in the bottom row of Figure 6.13, which deviate from the expected zero-centered delta functions. These small positive gradients are caused by the elevated levels of Φ seen towards the center of the flow field due to the effects of the recirculation zone, and are not an artifact of the linear bridging function.

To conclude, significant spatial gradients of equivalence ratio are observed in the stratified swirl burner cases. The change in RMS gradient between the two stratification levels is small relative to the change from the premixed cases, but is large enough to justify examining data from both. The premixed data has small positive gradients in equivalence ratio on average due to the elevated Φ in the center of the flow field.

6.6 Favre-Averaged Flame Structure

Radial profiles of Favre-averaged temperature, equivalence ratio and major species at $z = 10\,\mathrm{mm}$ and at the intersection of the mixing layer and the mean flame brush (the long record locations identified in Section 6.4.3) are shown in Figure 6.14 through Figure 6.21. The corresponding fluctuations are plotted in Figure 6.15. Plots at $z = 10\,\mathrm{mm}$ as well as the farther downstream long record locations give a locally resolved picture of the spatial evolution of the measured quantities in the flame. Data are given for radial locations from 0 mm to 25 mm as in the velocity plots in Section 6.2; the behavior of the measured scalars in the flames surveyed is assumed to be radially symmetric.

6.6.1 Non-Swirling Lean Cases

Results from the lean non-swirling cases ($SwB1$, $SwB5$, $SwB9$) are given in Figure 6.14 and Figure 6.15, demonstrating structural differences brought about due to stratification of the inlet flows. The thermal ramps in $\widetilde{T}$ are almost coincident in the $z = 10$ mm cases, despite the substantial differences in $\widetilde{\Phi}$ within the flame brush. This indicates that the effects of burning through higher equivalence ratio are insubstantial at this proximity to the burner exit. As the flame reaches the intersection of the mixing layer and the mean flame brush, the stratified flame brushes have moved radially outwards substantially due to the combined effects of higher flame speed and gaseous expansion inside the flame resulting from the higher levels of $\widetilde{\Phi}$ experienced. At both locations the stratified cases achieve higher temperature in the equilibrium zone, as expected for the higher equivalence ratios.

Interestingly the flame position in the highly stratified $SwB9_{50}$ case stabilizes inside that for the $SwB5_{50}$ case at the long record locations, even though both are measured at the same downstream distance ($z = 50$ mm) and $SwB9$ has a higher peak equivalence ratio. One plausible explanation for this discrepancy is provided by the equivalence ratio burned through by the two cases farther upstream, near the burner exit. Examining the profiles of $\widetilde{\Phi}$ at $z = 10$ mm reveals that the flame brush in the $SwB5_{10}$ spans the range 1 to 1.1 while the more stratified $SwB9_{10}$ spans 1.1 to 1.2; the mean laminar burning velocity in the former is approximately 5 % greater than in the latter. While differences will be observed due to turbulence, the effects should be commensurate due to the similar

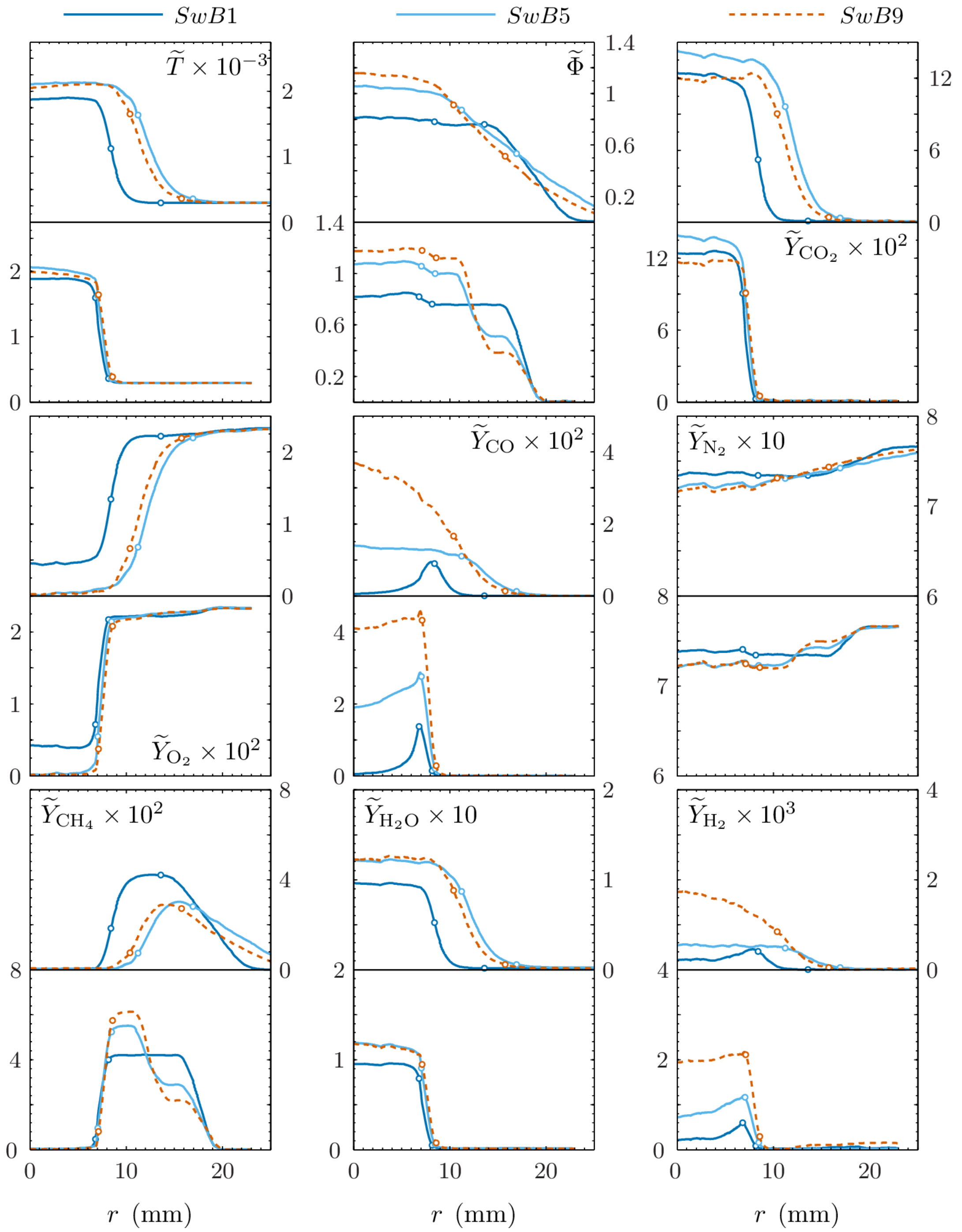

Figure 6.14: Radial profiles of Favre-averaged measurements for the lean non-swirling cases in the swirl burner at $z = 10\,\text{mm}$ (bottom halves) and at the long record locations (top halves). The premixed $SwB1$ case is shown by ——, the moderately stratified $SwB5$ case by ——, and the highly stratified $SwB9$ case by ·········. Locations corresponding to FWHM in T'' are plotted as open circles of the appropriate color. Favre-averaged temperature is in K.

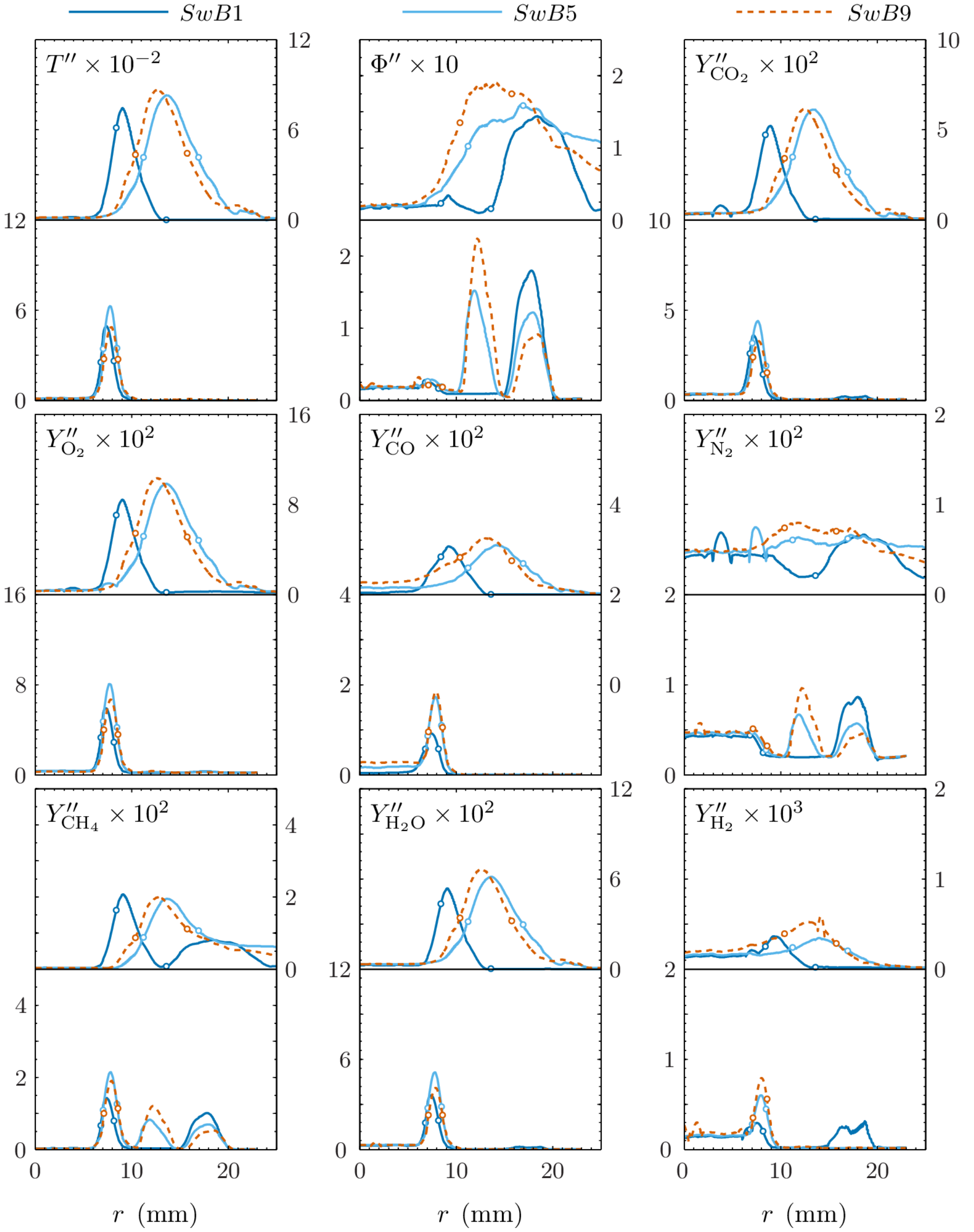

Figure 6.15: Radial profiles of Favre-averaged fluctuations for the lean non-swirling cases in the swirl burner at $z = 10$ mm (bottom halves) and at the long record locations (top halves). Symbols as in Figure 6.14.

turbulence levels experienced by both cases (both have non-swirling flow patterns) and hence the mean equivalence ratios may partially account for the flame brush locations for $SwB5_{50}$ and $SwB9_{50}$ at the long record locations.

The plots of $\widetilde{\Phi}$ show that the central recirculation zones influence the hydrogen-carbon-oxygen balance significantly, resulting in elevated equivalence ratio levels in these regions. The shear layer between the recirculation zones and the inner annulus flow results in a mixing layer between the elevated and nominal inner annulus equivalence ratios, which generates significant equivalence ratio gradients in the flame brushes for all three cases at $z = 10\,\mathrm{mm}$. This is true even in the premixed $SwB1_{30}$ case, despite the inner and outer annulus fuel/air streams being at a constant nominal stoichiometry. The elevated equivalence ratios are attributed to the effect of the central recirculation zone on the hydrogen-carbon balance near the burner exit. This behavior is examined in more detail in a forthcoming (at the time of writing) publication by Barlow *et al* [72]. The Φ'' profiles demonstrate that the flame brushes in the stratified cases do not intersect the mixing layers between the inner- and outer-flows at this location, whereas this is the case at the long record location (by definition).

The Favre-averaged profiles of CO_2, O_2 and H_2O behave similarly to $\widetilde{T}$ (albeit mirrored in the case of O_2), as is expected. Some notable behavior is observed in these species. It is clear at both $z = 10\,\mathrm{mm}$ and the long record locations that for the stratified cases all oxygen is consumed in reactions in the equilibrium zone, in marked contrast to the behavior in the premixed case. This is attributed to the combination of higher $\widetilde{T}$ and $\widetilde{\Phi}$; the behavior of $\widetilde{Y}_{O_2}$ exhibited by all three cases is very similar within the actual flame brush at the long record locations, where $\widetilde{T}$ and $\widetilde{\Phi}$ are much the same for $SwB1$, $SwB5$ and $SwB9$.

The peak values of $\widetilde{Y}_{CO_2}$ attained in the premixed case vary significantly relative to those in the stratified cases moving from the upstream to the long record locations.

Near the burner exit, the premixed value lies between the moderately (higher) and highly (lower) stratified values. Looking further downstream, the difference between the two stratified cases remains consistent but the premixed $\widetilde{Y}_{\mathrm{CO}_2}$ is much closer to the $SwB9$ value.

There is a sharp ramp in the level of CO through the stratified flame brushes at $z = 10\,\mathrm{mm}$, with the peak level in $SwB5_{10}$ ($SwB9_{10}$) being $202\,\%$ ($323\,\%$) higher than in the premixed $SwB1_{10}$. This decreases rapidly in the premixed case, and declines at a more gradual rate in the stratified cases. Farther downstream at long record locations similar values of $\widetilde{Y}_{\mathrm{CO}}$ are observed within the flame brush for all cases, at much lower magnitudes than the stratified cases at $z = 10\,\mathrm{mm}$. The profile for $SwB1_{30}$ is similar to that at $z = 10\,\mathrm{mm}$, though the peak is smeared out. In contrast, the moderately stratified $SwB5_{50}$ shows a gentle increase towards the centerline of the burner on the product side of the flame brush, while $SwB9_{50}$ increases substantially in the post-flame region. The behavior seen in the stratified cases tracks the stoichiometry of the products.

$\widetilde{Y}_{\mathrm{H}_2}$ is seen to trend similarly to $\widetilde{Y}_{\mathrm{CO}}$. The low levels of $\widetilde{Y}_{\mathrm{H}_2}$ in $SwB1$ are due to the lean stoichiometry of the flow. The higher levels of H_2 seen in the post-flame region for the stratified cases may be attributed to the lack of additional O_2 in these regions, preventing the formation of additional H_2O in addition to the effects of stoichiometry.

$\widetilde{Y}_{\mathrm{CH}_4}$ and $\widetilde{Y}_{\mathrm{N}_2}$ are relatively unremarkable, with the former following $\widetilde{\Phi}$ in the pre-flame region before dropping to zero through the flame, and the latter being relatively invariant in the flame brush.

6.6.2 Moderately Swirling Lean Cases

Favre-averaged and fluctuating components of temperature, equivalence ratio and major species are plotted for $SwB2$, $SwB6$ and $SwB10$ in Figure 6.16 and Figure 6.17. The

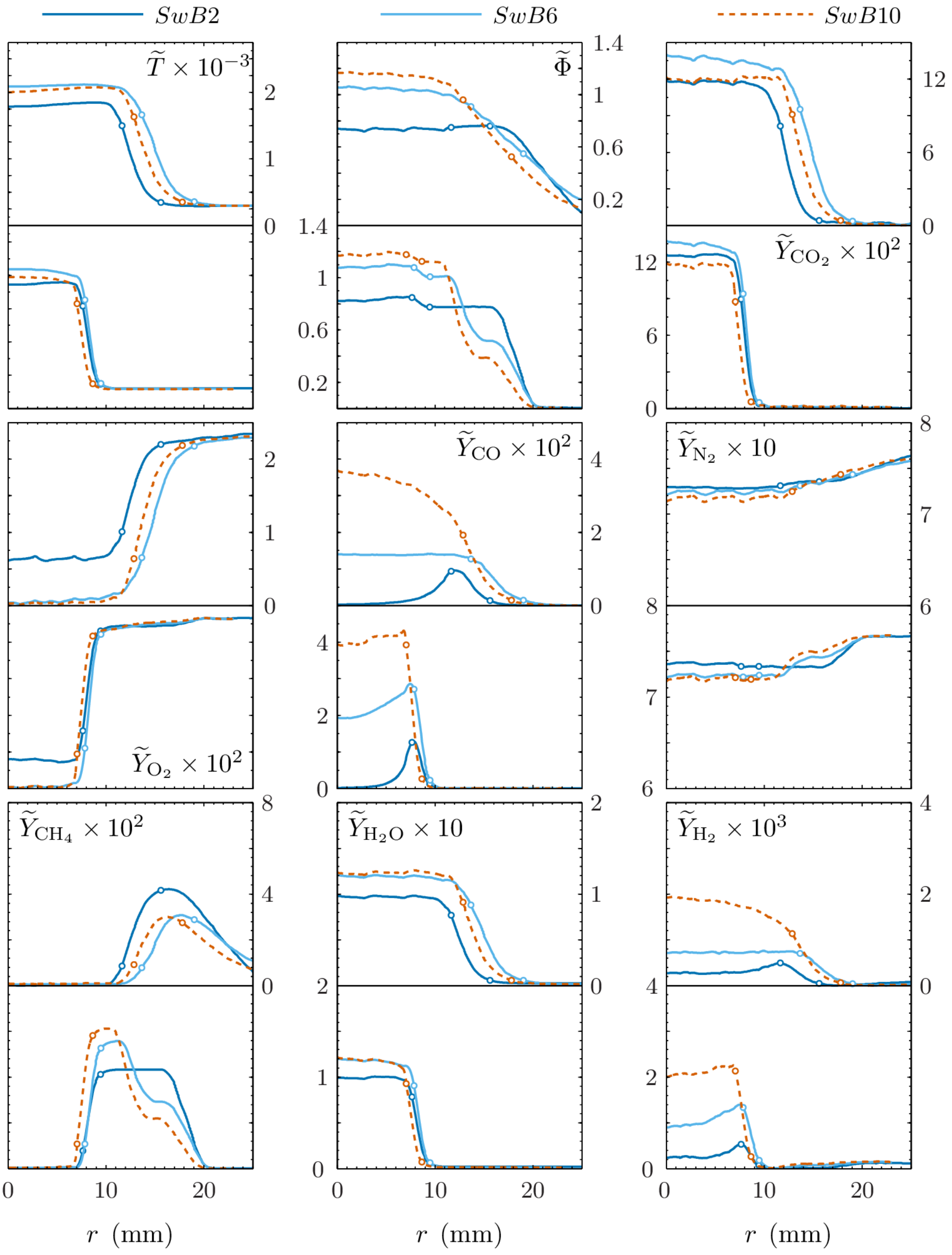

Figure 6.16: Radial profiles of Favre-averaged measurements for the lean moderately swirling cases in the swirl burner at $z = 10$ mm (bottom halves) and at the long record locations (top halves). Symbols as in Figure 6.14.

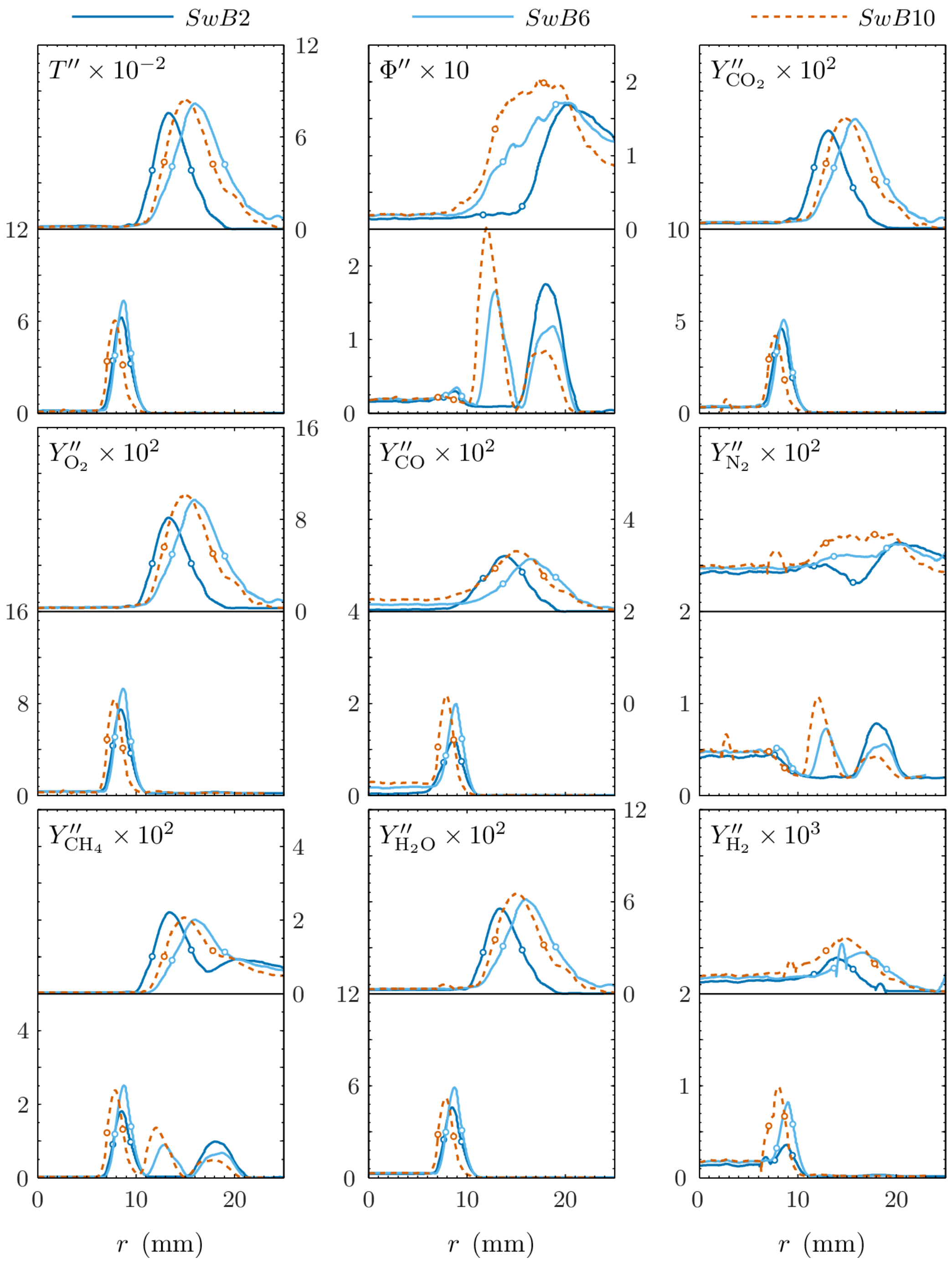

Figure 6.17: Radial profiles of Favre-averaged fluctuations for the lean moderately swirling cases in the swirl burner at $z = 10\,\text{mm}$ (bottom halves) and at the long record locations (top halves). Symbols as in Figure 6.14.

addition of moderate swirl to the lean non-swirling cases has little effect on the shape or magnitude of the profiles of the averaged quantities. The most notable change is that both the average and fluctuating profiles are shifted radially outwards, as expected from the thermal flame structure shown in Figure 6.11. The profiles of the fluctuations are also similar to those seen in the non-swirling cases, though shifted radially outwards, with slightly elevated levels at the $z = 10\,\mathrm{mm}$ location for most species.

Outside of this, some slight differences are observed in the profiles of $\widetilde{\Phi}$, $\widetilde{Y}_{\mathrm{O}_2}$, and $\widetilde{Y}_{\mathrm{CH}_4}$ for the premixed $SwB2$ case. The higher degree of mixing between the recirculation zone and the inner annulus flow eliminates the $\widetilde{\Phi}$ ramp seen between these two regions at $z = 10\,\mathrm{mm}$ by the time the flow reaches the intersection of the mixing layer with the mean flame brush (long record locations). This gives a much flatter $\widetilde{\Phi}$ profile across the flame brush of $SwB2_{30}$ than was seen in $SwB1_{30}$ at the same axial location ($z = 30\,\mathrm{mm}$).

The post-flame region of the $\widetilde{Y}_{\mathrm{O}_2}$ profile at the long record location for the premixed $SwB2_{30}$ is elevated by $25\,\%$ compared to the non-swirling $SwB1_{30}$ case. The reasons for this relatively large change are unclear as alterations of a similar magnitude are not seen in any single other species; it is assumed that the variation is balanced by slight alterations in all oxygen-based reactions, rather than any specific mechanism.

Lastly, the Favre-averaged CH_4 profile at the downstream location is substantially smoothed out by the addition of swirl, with the plateau evident in the $SwB1_{30}$ case being absent for $SwB2_{30}$.

6.6.3 Highly Swirling Lean Cases

The behavior exhibited by the Favre-averaged quantities in the highly swirling lean cases ($SwB3$, $SwB7$, $SwB11$) are markedly different to those seen in the non- and moderately-swirling cases, as shown in Figure 6.18 and Figure 6.19. These differences

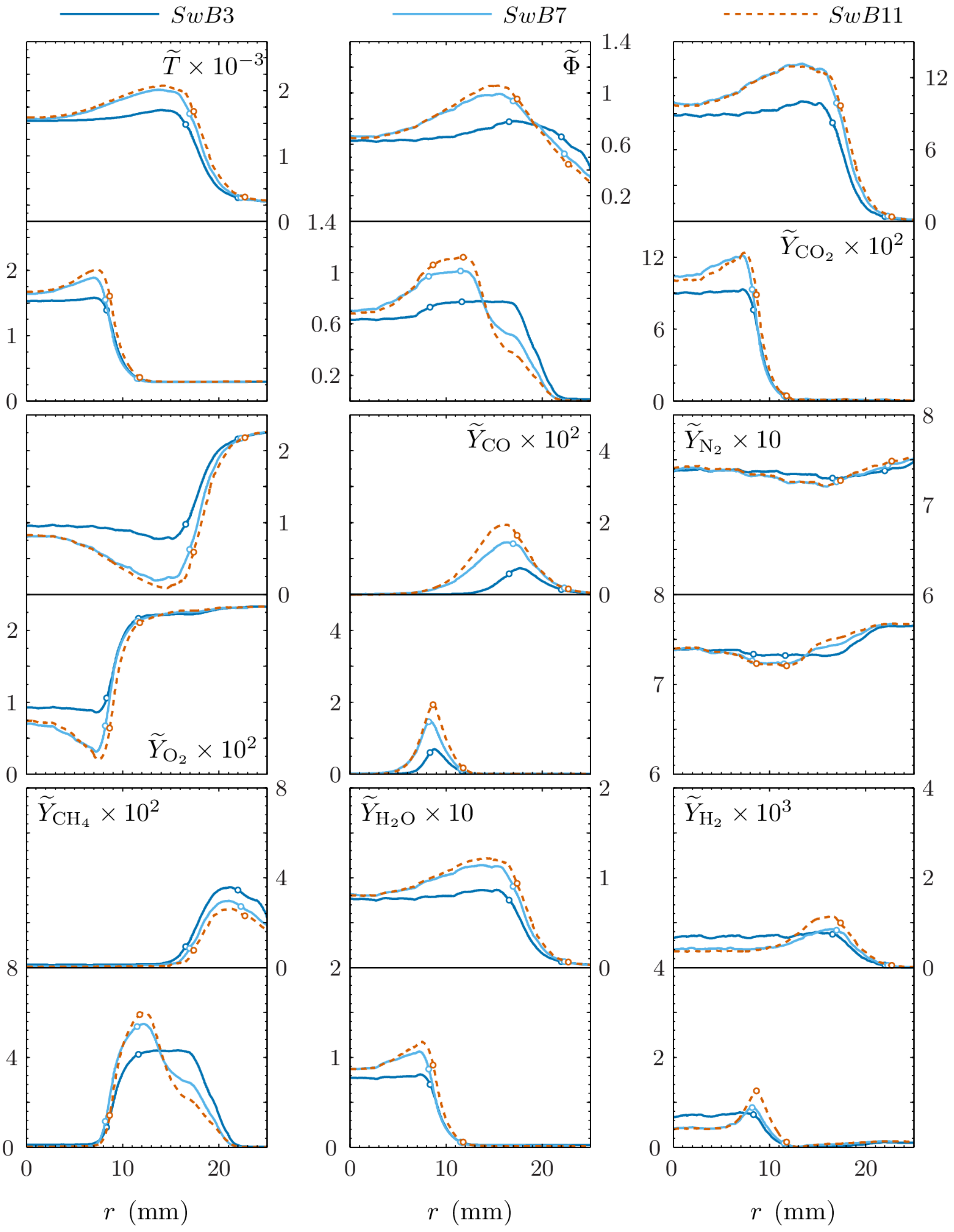

Figure 6.18: Radial profiles of Favre-averaged measurements for the lean highly swirling cases in the swirl burner at $z = 10$ mm (bottom halves) and at the long record locations (top halves). Symbols as in Figure 6.14.

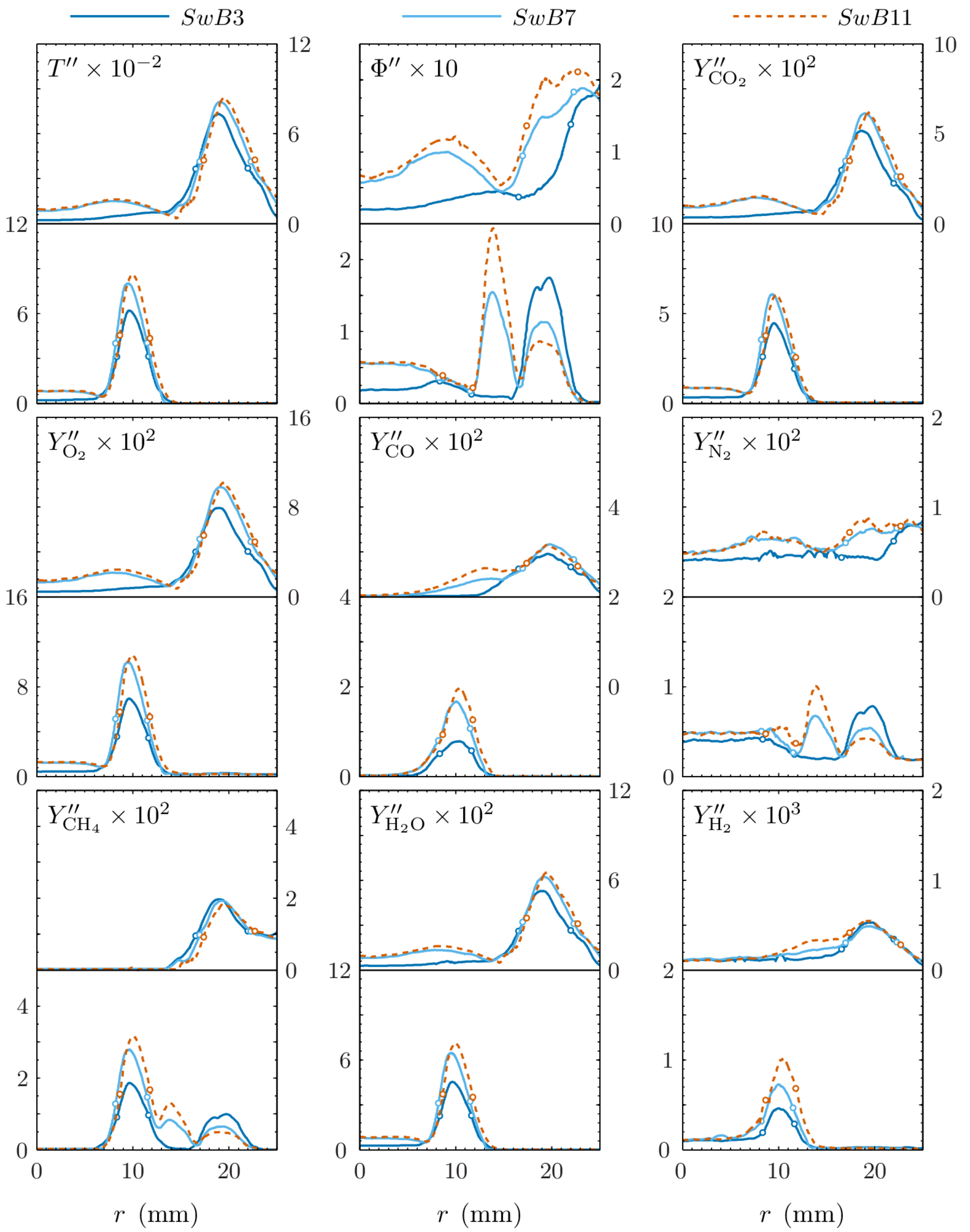

Figure 6.19: Radial profiles of Favre-averaged fluctuations for the lean highly swirling cases in the swirl burner at $z = 10\,\mathrm{mm}$ (bottom halves) and at the long record locations (top halves). Symbols as in Figure 6.14.

are attributed to the entrainment of co-flow air into the recirculation zone, which does not take place for the other flow fields.

The Favre-averaged profiles show dips in $\widetilde{T}$ in the post-flame region at both $z = 10\,\mathrm{mm}$ and the long record locations, with the effect in the latter being more significant. These changes are particularly pronounced for the stratified cases, which attain higher peak $\widetilde{T}$ due to the higher values of $\widetilde{\Phi}$. Similar dips are not seen for the non-swirling or the moderately swirling lean cases in Figure 6.14 and Figure 6.16 respectively. It appears that the recirculation zone for the highly swirling cases entrains co-flow air, whereas the recirculation zones in the other cases consists solely of hot products. The oxygen levels in the premixed $SwB3$ case are substantially (200 %) raised in comparison to those in $SwB1$, while the values in the stratified highly swirling cases show a minimum and then steadily increase moving towards the centerline instead of bottoming out to zero as for the other flow patterns. Combined with the zero levels of $\widetilde{Y}_{\mathrm{CH}_4}$ in the post-flame region, this indicates that the entrained fluid is air from the co-flow and not fuel/oxidizer from the pre-flame region.

The mean $\widetilde{\Phi}$ gradients seen at the $z = 10\,\mathrm{mm}$ location are slightly negative in the premixed and stratified cases due to the reduced $\widetilde{\Phi}$ in the recirculation zone caused by the entrainment of co-flow air described previously. Further downstream at the long record locations the premixed $\widetilde{\Phi}$ shows a positive slope in the flame brush as the flame is stabilizing in the shear layer between the outer annulus flow and the co-flow air. The gradients in $SwB7$ and $SwB11$ are similar to those in the corresponding non-swirling and moderately swirling cases.

Relative to the non-swirling cases, the production of $\widetilde{Y}_{\mathrm{H}_2}$ through the flame front is enhanced for the premixed $SwB3$ and significantly attenuated for both $SwB7$ and $SwB11$.

The behavior of $\widetilde{Y}_{\mathrm{CO}}$ is changed significantly relative to the previously examined flow conditions by the addition of high swirl. The profiles all resemble the premixed behavior, following an approximately Gaussian profile, with the result that the $\widetilde{Y}_{\mathrm{CO}}$ rapidly decays to zero in the post flame region.

$\widetilde{Y}_{\mathrm{CO}_2}$ and $\widetilde{Y}_{\mathrm{H}_2\mathrm{O}}$ trend similarly to the profiles seen for the non-swirling and moderately swirling cases, but with dips in the post-flame region which as with the plots of $\widetilde{T}$ are more pronounced for the stratified cases. The profiles of $\widetilde{Y}_{\mathrm{CH}_4}$ in the highly swirling cases resemble those in the moderately swirling configuration.

The fluctuating components of the measured quantities behave similarly to the cases associated with the other flow conditions, but with significant levels of fluctuation in the post flame regions for T'', Φ'', Y''_{O_2}, Y''_{CO_2} and $Y''_{\mathrm{H}_2\mathrm{O}}$.

6.6.4 Stoichiometric Cases

The effects of the addition of swirl to a stoichiometric flame are shown in Figure 6.20 and Figure 6.21. The differences between $SwB13$, $SwB14$ and $SwB15$ are negligible at the upstream $z = 10\,\mathrm{mm}$ location. The profiles of $\widetilde{\Phi}$ at this axial position are elevated in the recirculation zone, indicating that there is no significant entrainment of air from the co-flow the data shown.

Looking at the long record profiles ($z = 20\,\mathrm{mm}$ for $SwB15$, $z = 30\,\mathrm{mm}$ otherwise), the behavior exhibited is generally very similar, with the major differences being the radial shift outwards associated with increasing swirl. However, some interesting deviations are seen in the highly swirling $SwB15$ case. Firstly, the $\widetilde{T}$ profile shows a gradual decline in the post-flame region, akin to that seen in the highly swirling lean premixed $SwB3$ case in Section 6.6.3. A similar trend is observed in $\widetilde{\Phi}$, indicating that there is some entrainment of air from the co-flow at this point. Oddly the levels of $\widetilde{Y}_{\mathrm{O}_2}$ in the $SwB15$ post-flame region are only slightly elevated, in contrast to the behavior seen in $SwB3$.

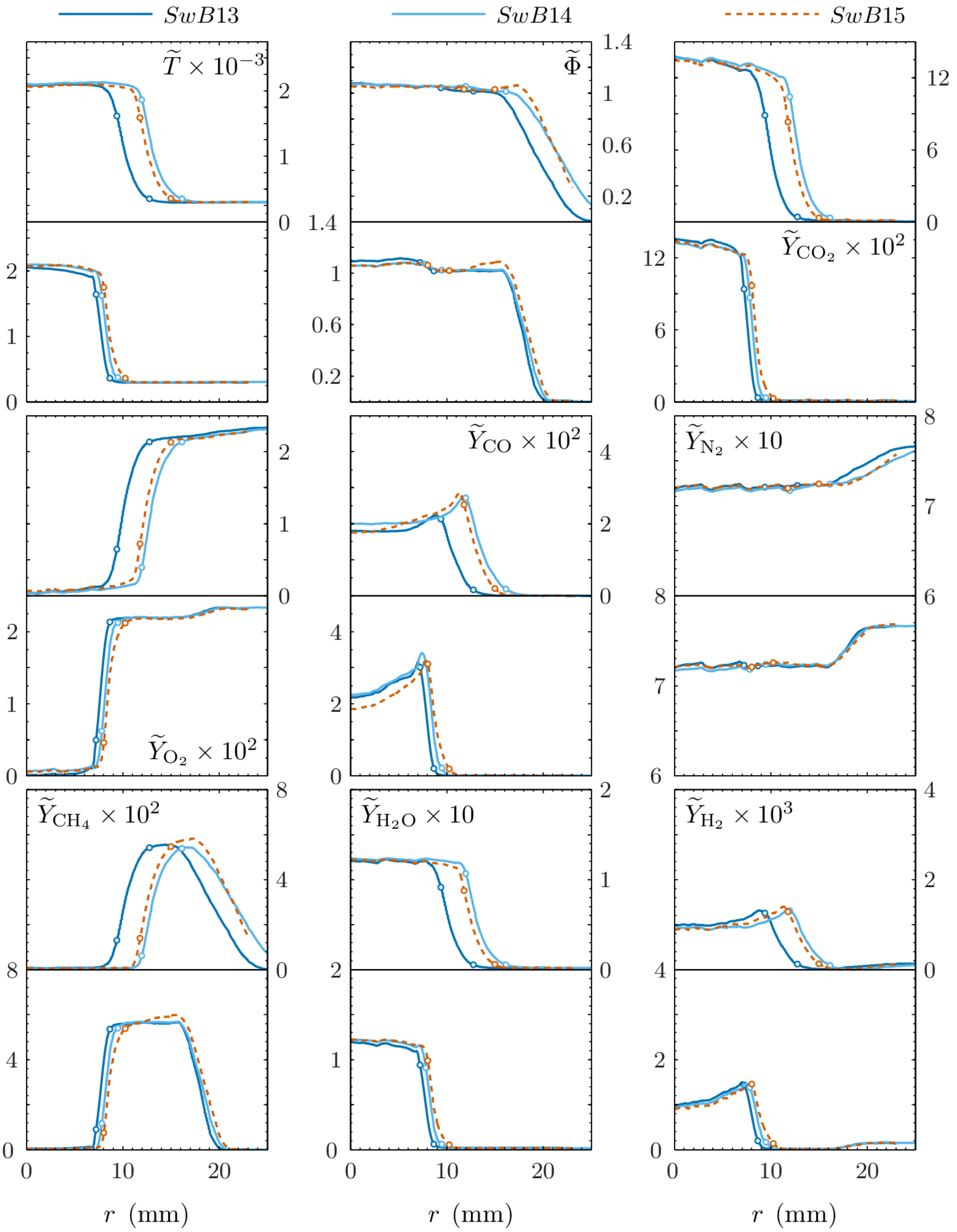

Figure 6.20: Radial profiles of Favre-averaged measurements for the stoichiometric cases in the swirl burner at $z = 10\,\text{mm}$ (bottom halves) and at the long record locations (top halves). Symbols as in Figure 6.14.

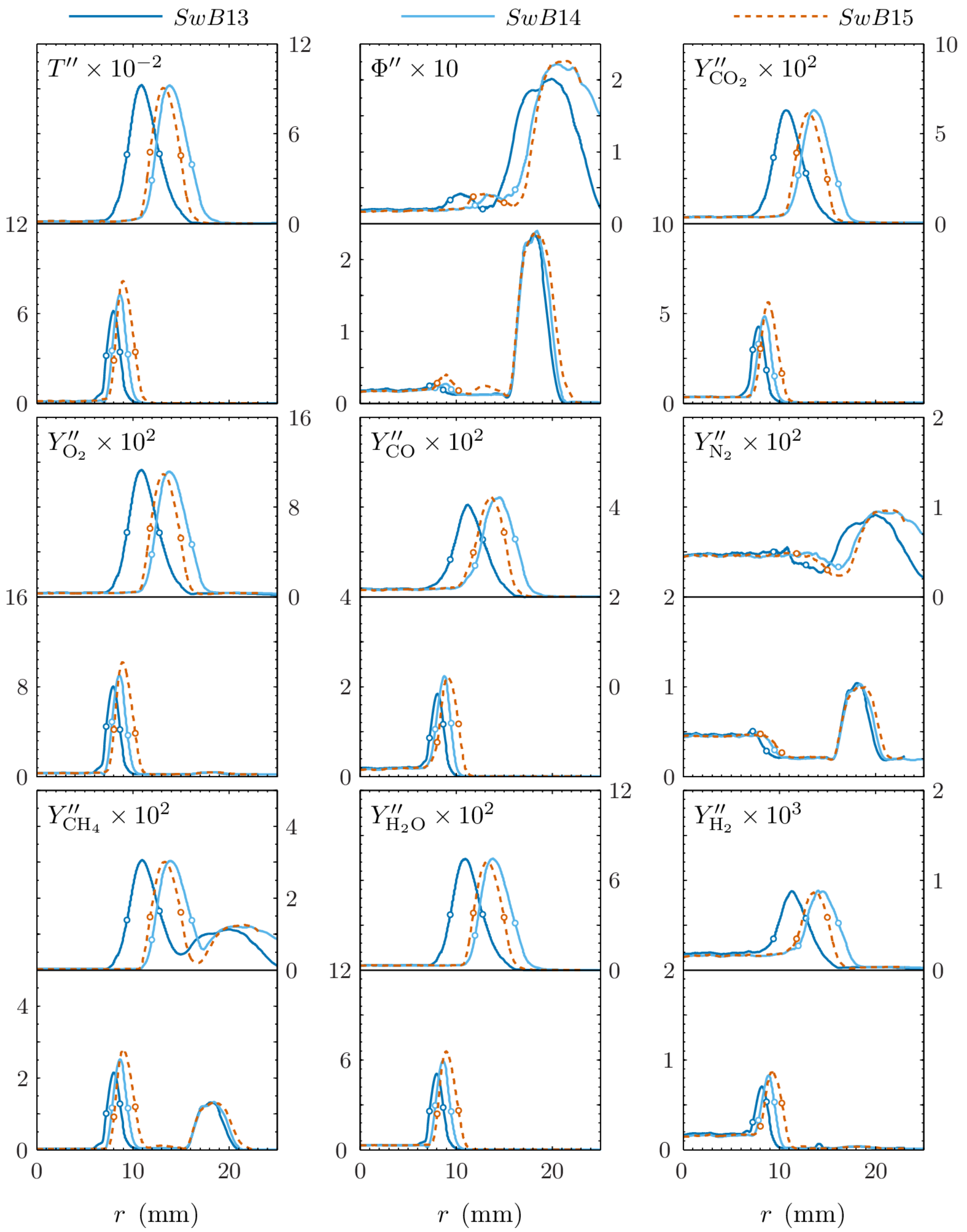

Figure 6.21: Radial profiles of Favre-averaged fluctuations for the stoichiometric cases in the swirl burner at $z = 10\,\text{mm}$ (bottom halves) and at the long record locations (top halves). Symbols as in Figure 6.14.

Both $SwB13_{30}$ and $SwB14_{30}$ stabilize at a flat near-stoichiometric $\widetilde{\Phi}$, with low levels of fluctuation. The flame brush in the highly swirling $SwB15_{20}$ stabilizes in the gently sloping $\widetilde{\Phi}$ region generated by the shear layer between the stoichiometric flows and the co-flow air. As a result the Φ'' is significantly higher for this highly swirling case than for $SwB13_{30}$ or $SwB14_{30}$. Stabilization of the flame in the mixing layer also explains the attenuation of the $\widetilde{Y}_{\mathrm{CH_4}}$ and $\widetilde{Y}_{\mathrm{N_2}}$ profiles seen for the highly swirling case at the long record location.

The values of $\widetilde{Y}_{\mathrm{CO}}$ plateau in the post-flame region for both the non-swirling and moderately swirling cases at the long record location. In contrast $\widetilde{Y}_{\mathrm{CO}}$ in the highly swirling case tapers to near zero after peaking on the product side of the flame brush. Similar behavior is also seen in the profiles of $\widetilde{Y}_{\mathrm{H_2}}$, though rather than tapering to zero the $SwB15_{20}$ case decays to approximately half the value of $SwB13_{30}$ or $SwB14_{30}$.

The Favre-averaged fluctuations are very similar for these three cases, with the exception of those for Φ'' and $Y''_{\mathrm{N_2}}$. These discrepancies are explained by the reasons given in the discussion of the averaged quantities for the differences observed there.

6.7 Influence of Stratification on Species Evolution

Section 6.6 highlighted significant differences in the behavior of the mass fractions of certain species when considering Favre averages and fluctuations. The evolution of the major species involved in combustion reactions is intrinsically temperature dependent. This section examines the trends exhibited by the various species mass fractions in temperature space, with the intent of identifying the influence of stratification. First, in Section 6.7.1, unconditioned data are used to investigate the mean behavior of the key combustion species in the swirl burner. These results are compared with laminar flame calculations at the local mean equivalence ratio to highlight differences between cases, and also to demonstrate the ability of ensembles of laminar unstrained calculations to capture the behavior of the turbulent flames surveyed. Data is then conditioned on local equivalence ratio in Section 6.7.2 to facilitate a more quantitative assessment of the influence of stratification and swirl on the thermal response of these species.

6.7.1 Unconditioned Results

The instantaneous data from the swirl burner is used to generate mean fits of T and the scalar under consideration, at both the $z = 10\,\mathrm{mm}$ and the long record locations. The data is not conditioned on equivalence ratio, and so there is a spread in the values of local equivalence ratio. The range of Φ values are shown in Figure 6.12, and the magnitude of the ranges in the long record locations are summarized in Table 6.5.

Data at $z = 10\,\mathrm{mm}$ is binned in temperature space in steps of $50\,\mathrm{K}$, while the long record data is binned in steps of $20\,\mathrm{K}$. The bin sizes were empirically chosen to give smooth mean fits in the unconditioned data, and differ due to the variation in the amount of data available. In addition to determining the mean species mass fraction within each temperature bin, the mean equivalence ratio is also calculated. The probability distribution of Φ within each bin is used to determine the 10^{th} and 90^{th} percentiles of equivalence ratio, which are taken as a measure of the minimum and maximum Φ respectively. Laminar flame calculations corresponding to these Φ values are plotted for comparison with the experimental data.

The experimental data sets are too large to plot all points in a scatter plot without introducing a large degree of redundancy and obfuscation due to points overlapping each other. To counteract this, 100 points were randomly selected from each temperature bin, and only these are plotted in the scatter plots in this section. Note that the mean values within each bin are derived using the full dataset. The points selected are recorded to ensure the scatter plots show the same data points for each species. The scatter data is also colored by the local equivalence ratio to give a qualitative impression of both the composition and the degree of stratification. All data points below the lean flammability limit[c] for laminar methane/air flames ($\Phi = 0.47$) are plotted in black to highlight these data.

The figures are arranged such that subplots in the left, middle and right columns correspond to non-swirling, moderately swirling and highly swirl cases respectively. Similarly the top, second and third rows of subplots show the lean premixed, moderately stratified and highly stratified cases, while the stoichiometric cases are shown on the bottom row. This format is used throughout the current section, though where data is subject to conditioning (for example on local equivalence ratio) only data from the long record locations are presented as the datasets at $z = 10\,\mathrm{mm}$ are insufficiently large to produce satisfactory multiply conditioned results.

Figure 6.22 shows the evolution of $Y_{\mathrm{CO_2}}$ in the various swirl burner flames. The uniformity of color in the scatter data for $z = 10\,\mathrm{mm}$ demonstrates that there is little variation in equivalence ratio in any of the cases surveyed, regardless of the degree of stratification. As mentioned in Section 6.6, this is due to the flame brush stabilizing at this axial location such that the majority of it lies within the inner annulus flow, before it has mixed to any large degree with the outer annulus flow. This is also shown by the differences between the $Y_{\mathrm{CO_2}}$ values obtained from the laminar flame calculations; in general the difference between values corresponding to the local mean, 10^{th} and 90^{th} percentile Φ are negligible.

While the general trend observed in the mean fit to $Y_{\mathrm{CO_2}}$ at $z = 10\,\mathrm{mm}$ is similar to that in the laminar flame calculations — showing a steady increase with temperature

---

[c] The lean flammability limit is taken to be $\Phi = 0.47$ based on the experimental findings of Shoshin *et al* [90]. There is a degree of variation in the lean limit found, depending on the experimental configuration used, but typically it has been found to be in the range $0.45 < \Phi < 0.51$ [90–93].

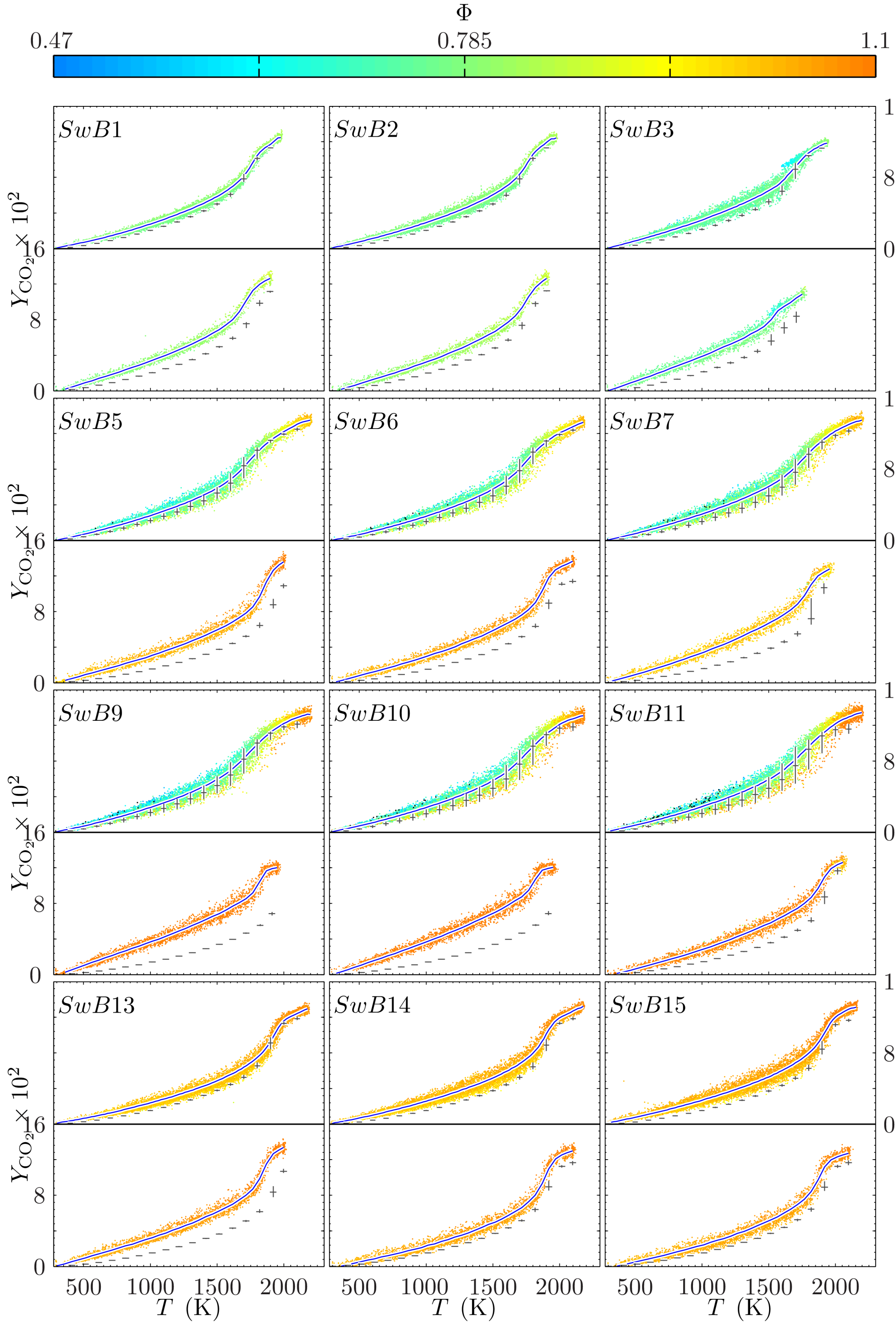

Figure 6.22: Plots of temperature against Y_{CO_2} for the swirl burner at both $z = 10\,\text{mm}$ (bottom halves) and long record (top halves) locations, colored by Φ, as shown in the colorbar. Data below the lean flammability limit ($\Phi = 0.47$) are plotted in black. Mean fits are shown by solid blue lines. Laminar flame calculations are shown by gray horizontal (value at local mean Φ) and vertical (range of maximum and minimum local Φ) lines.

before a sharp ramp near the beginning of the equilibrium zone — the magnitudes in the experimental data are substantially higher than the laminar values. Looking across the columns, no consistent trend with swirl is observed. Looking down the rows however, the effect appears more pronounced in the stratified cases and in the stoichiometric cases.

This effect decreases with axial distance, as shown by the long record data which are much closer to their calculated values, though still slightly elevated. The raised $Y_{\mathrm{CO_2}}$ at $z = 10\,\mathrm{mm}$ is attributed to preferential molecular transport, which is exacerbated by the presence of the recirculation zone. This effect is investigated in detail by Barlow *et al* [72] using data from a single annulus bluff-body burner of similar dimensions to the swirl burner. They observed that this effect is highly dependent on the bulk velocity, U_{b}, in the annulus; species mass fractions were in good agreement with laminar calculations for $U_{\mathrm{b}} < 2.6$, while similarly elevated $Y_{\mathrm{CO_2}}$ was seen for $U_{\mathrm{b}} = 7.7\,\mathrm{m/s}$ ($U_{\mathrm{b}} = 7.5\,\mathrm{m/s}$ in the inner annulus of the swirl burner). They propose that the primary hydrogen-containing species (H_2 and H_2O) are preferentially diffused ahead of carbon-containing species (CO_2 and CO) away from the products, and are subsequently carried away from the flame flame front as the flow moves downstream. The recirculation zone results in increased residence time for the hydrogen-depleted products, amplifying the elevated CO_2 levels. These findings will be referred back to in the analysis of relevant species later on in this section.

It is worth noting that the behavior exhibited by both $SwB5_{10}$ and $SwB13_{10}$ is virtually identical (both are stabilized in streams with a nominal equivalence ratio of $\Phi_{\mathrm{n}} = 1$). As both are subject to similar mean velocities (see Table 6.2) this indicates that the increasingly raised $Y_{\mathrm{CO_2}}$ seen with increasing stratification in the lean cases is due to the magnitude of the upstream equivalence ratio, and not the degree of stratification. This dependence was not observed in [72] as the swirl burner data was taken exclusively from the lean premixed $SwB1_{10}$ and $SwB2_{10}$ cases.

Further downstream, at the long record locations, the agreement between the experimental means and the laminar calculations is substantially better, with the computational values underestimating the experimental data slightly but lying within the bounds of the scatter data. The spread of values expected based on the 10th and 90th percentiles of equivalence ratio are also in good agreement with the spread seen in the stratified experimental data.

The preferential molecular transport detailed previously is also evident in the profiles of Y_{CO}, though the difference relative to comparable calculated laminar values is significantly less. In general, with the exception of $SwB3_{10}$, the agreement between the mean experimental Y_{CO} and the calculated values at the mean Φ is very good below $T = 1\,500\,\mathrm{K}$ for $z = 10\,\mathrm{mm}$. Past this point the mean experimental values typically undershoot the peak laminar Y_{CO} by up to $20\,\%$, though the $SwB14_{10}$ shows good agreement with the calculated values. In the premixed lean highly swirling $SwB3_{10}$ case this undershoot is exhibited throughout the flame brush.

Interestingly in the highly stratified cases (third row down), very different behavior is observed for the non- and moderate-swirl cases (first and second column from left) than in the high swirl case (third column). The laminar values of Y_{CO} in the former continue to rise in the equilibrium zone, whereas they dip in the latter. The scatter data indicates that the equivalence ratio in $SwB9_{10}$ and $SwB10_{10}$ is higher than in $SwB11_{10}$, which may account for this discrepancy.

The lower equivalence ratio values in the equilibrium regions of the highly swirling lean cases (top three rows, third column) as seen qualitatively in Figure 6.23 and more explicitly in the Favre averages in Figure 6.18 attenuates the magnitude of the mean Y_{CO} for high temperatures, indicating the importance of conditioning the data on the local Φ before drawing hard conclusions from the data.

Further downstream at the long record locations the agreement seen between the ex-

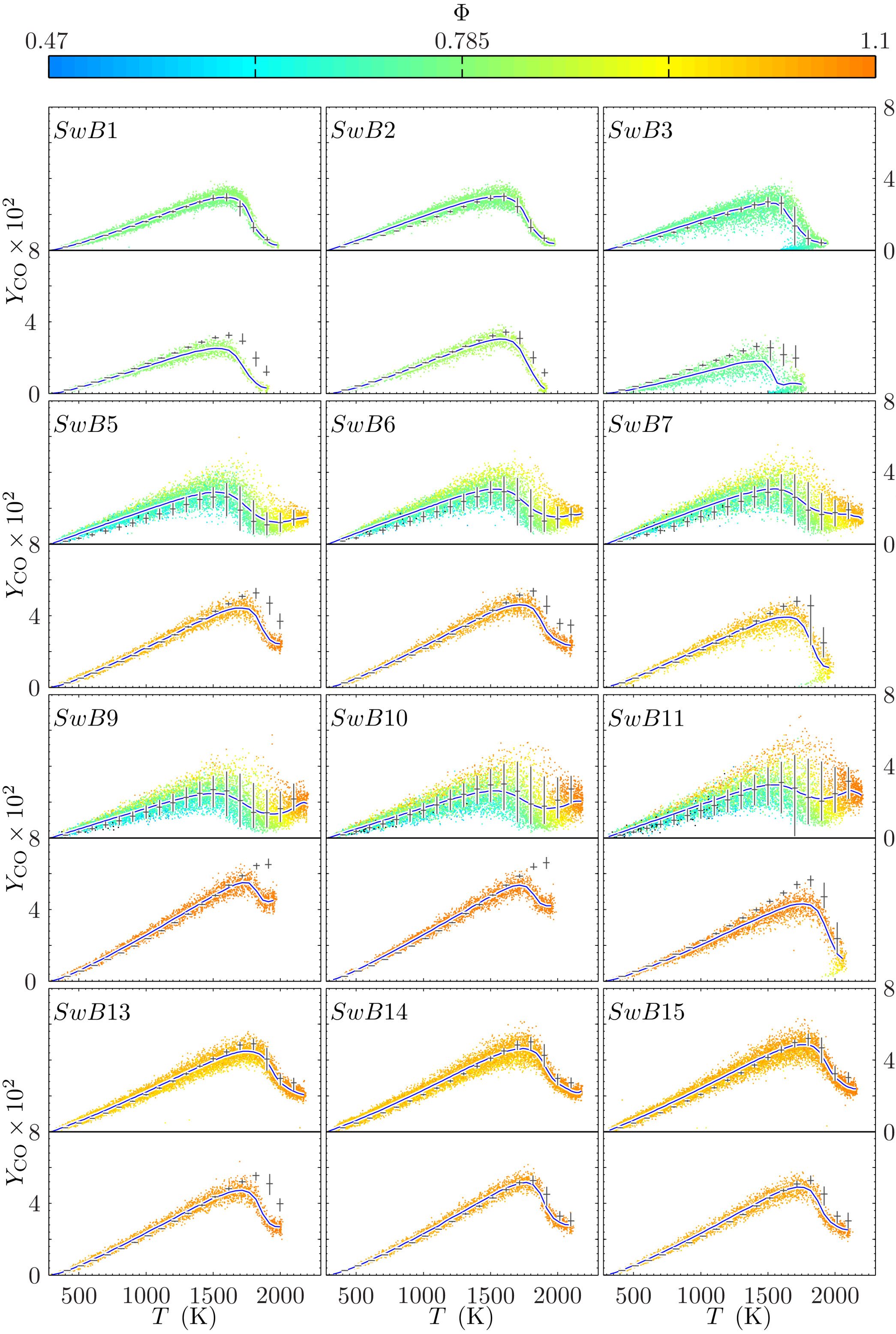

Figure 6.23: Plots of temperature against Y_{CO} for the swirl burner. Symbols and format as in Figure 6.22.

perimental means and the corresponding laminar calculated values is excellent throughout the entire temperature space. This indicates that the effect of the preferential molecular transport, which was already lower than for CO_2 at $z = 10\,\mathrm{mm}$, is virtually negligible for CO by the time the mixing layer intersects with the flame brush. Additionally, the range of values spanned by the scatter data in the stratified cases is matched almost exactly by the spread of the 10^{th} and 90^{th} percentile calculated values. It appears at this point that mean behavior of CO in the turbulent flame is well captured by laminar flamelet calculations, regardless of the level of stratification or swirl.

The experimental Y_{H_2} data shown in Figure 6.24 is reasonably well modeled on the mean by the laminar calculations, with the latter falling within the limits of the scatter data in the majority of the temperature space of the cases surveyed.

The main differences seen at the upstream location across the various cases is that the rate of production of H_2 in the experimental data is less than expected from the laminar values in the premixed zone up to $T \sim 600\,\mathrm{K}$. This is attributed to the preferential transport of the H_2 away from the reactants as detailed by Barlow *et al* [72]. This relationship is then inverted in the reaction zone, with the experimental Y_{H_2} trending above the anticipated values, before again dipping below them in the equilibrium zone. $SwB3_{10}$ again provides an exception, with the measured data trending significantly above the laminar calculated values for all T.

Considering the long record locations, the lean premixed cases (top row) are observed to trend almost exactly in line with the laminar values. This is also true of the stoichiometric premixed cases (bottom row), though to a lesser degree. The stratified cases (middle rows) trend higher than the laminar values throughout temperature space. The extent of this difference appears magnified by the stratification, being up to 66 % higher for the highly stratified cases compared to 33 % higher for the moderately stratified cases. The spread of values in the stratified cases is reasonably well captured by

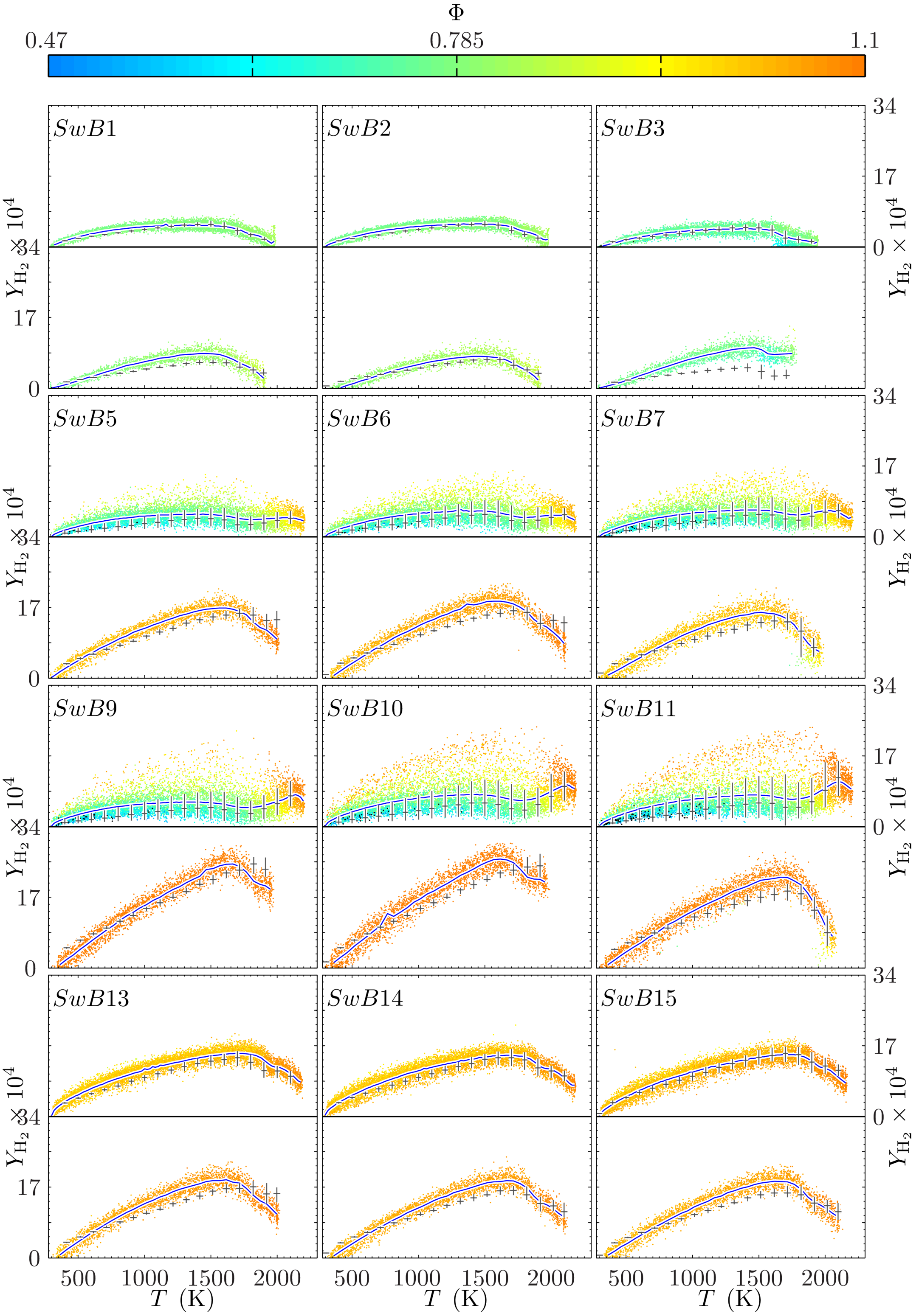

Figure 6.24: Plots of temperature against Y_{H_2} for the swirl burner. Symbols and format as in Figure 6.22.

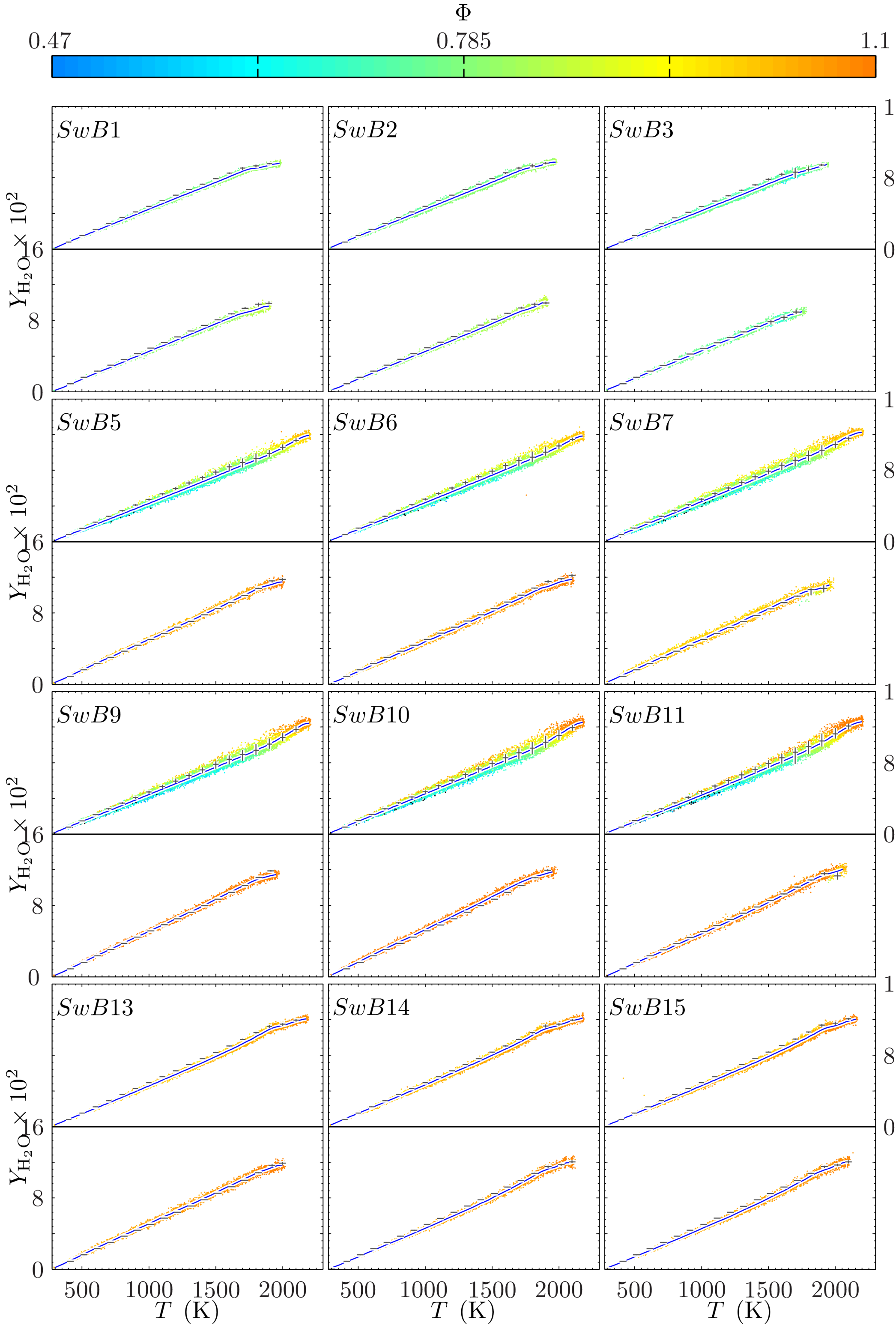

Figure 6.25: Plots of temperature against Y_{H_2O} for the swirl burner. Symbols and format as in Figure 6.22.

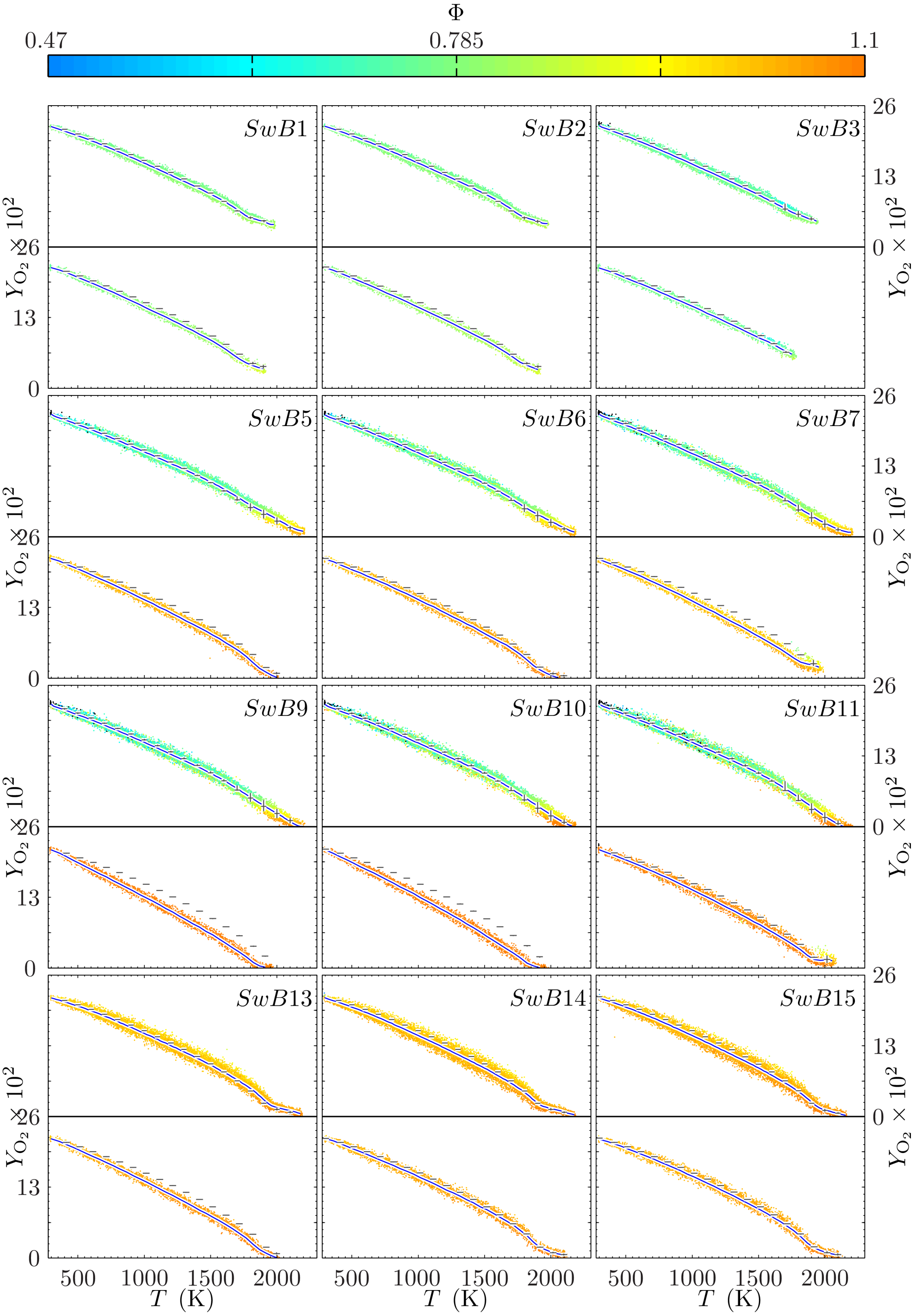

Figure 6.26: Plots of temperature against Y_{O_2} for the swirl burner. Symbols and format as in Figure 6.22.

the laminar calculations, though not to the same degree as for Y_{CO}.

Excellent agreement is seen between the laminar calculations and experimental means for $Y_{\mathrm{H_2O}}$ (Figure 6.25) and $Y_{\mathrm{O_2}}$ (Figure 6.26) at both $z = 10\,\mathrm{mm}$ and the long record locations.

Figure 6.22 through Figure 6.26 indicate that in general the thermal evolution of the key combustion species a short distance downstream of the burner exit is well captured on the mean by laminar flame values at the mean local equivalence ratio. The agreement seen is relatively insensitive to the degree of stratification or swirl.

6.7.2 Results Conditioned on Local Equivalence Ratio

The results observed in Section 6.7.1 pose the question as to whether the stratification in the swirl burner has a noticeable influence on the relationship between temperature and species. In order to better assess this issue it is necessary to condition the data on the local equivalence ratio in order to insulate the results from the influence of composition. The present section focuses solely on the long record location data as the datasets are much larger than at $z = 10\,\mathrm{mm}$, and thus the means and deviations obtained from the conditioned data are more accurate than would be the case for the $z = 10\,\mathrm{mm}$ datasets.

Figure 6.27 shows mean fits for species data conditioned on the local equivalence ratio such that $\Phi = 0.79$ for the lean cases and $\Phi = 1$ for the stoichiometric cases ($\pm 1\,\%$). $Y_{\mathrm{CO_2}}$ shows negligible influence of stratification under non-swirling flow conditions. The influence of stratification shows a slight swirl dependency, with both stratified cases trending slightly below the corresponding premixed case. The effect of stratification on $Y_{\mathrm{CO_2}}$ increases moving from the moderate to high swirl level. The addition of swirl has no noticeable impact on the behavior of the premixed cases. In all cases the experimental means are elevated relative to the equivalent laminar values through the majority of the

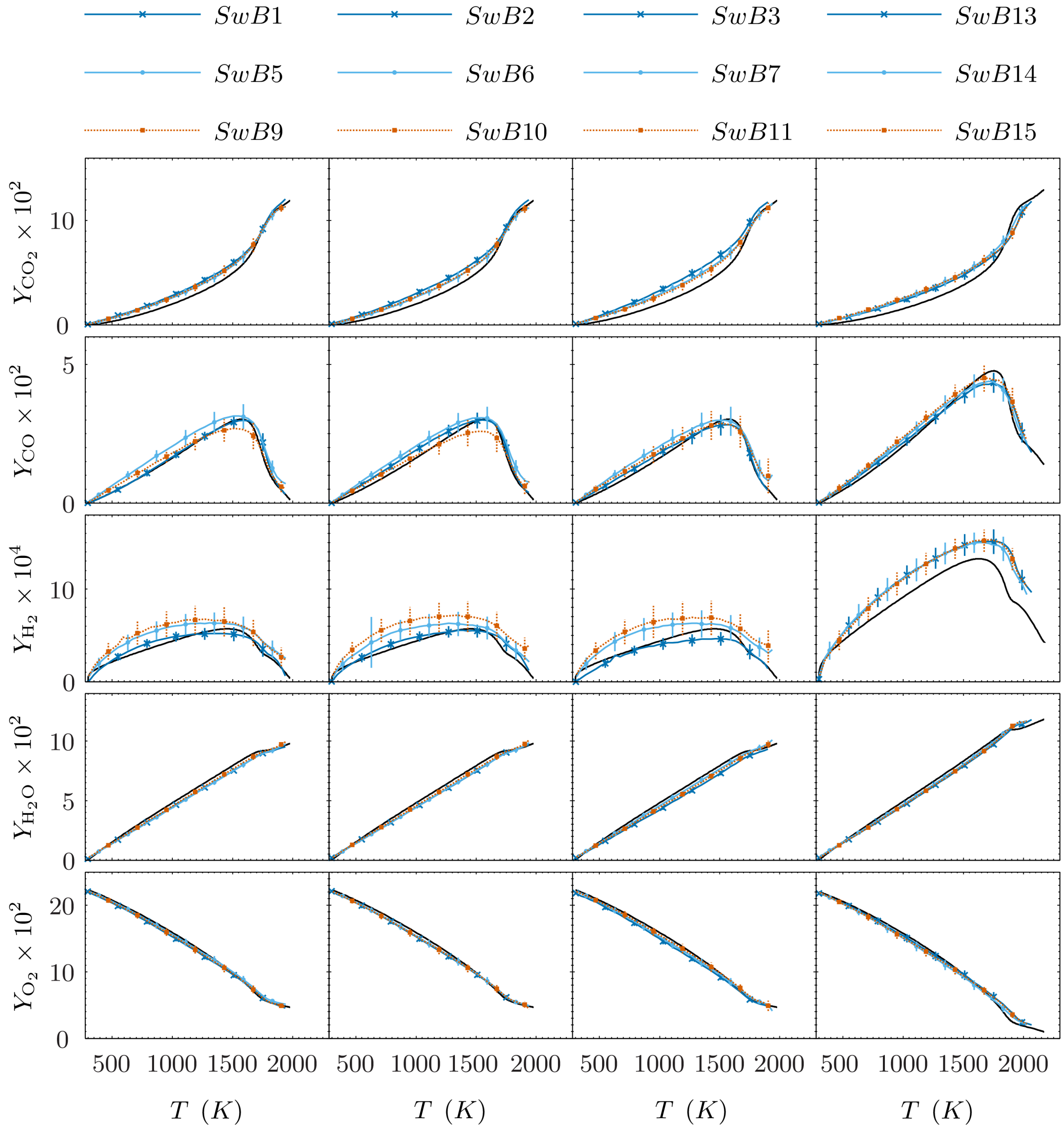

Figure 6.27: Plots of temperature against key combustion species for the swirl burner at the long record locations. Data is conditioned on local equivalence ratio to be within ±1 % of the nominal stoichiometry. Corresponding laminar flame calculations are shown by solid black lines.

temperature range. The maximum differences are seen for the premixed cases, which are up to 8 % greater in the middle of the flame than the corresponding values from laminar flame calculations.

Laminar flame calculations capture the behavior of the conditioned premixed *SwB*1

Y_{CO} data very well, but as swirl is introduced the production of carbon monoxide is increased relative to the non-swirling case in the middle of the flame ($\sim 14\,\%$). Interestingly while both the premixed and moderately stratified lean cases peak at similar magnitudes to the laminar calculations, the highly stratified cases show reduced peaks ($-12\,\%$ for $SwB9$, $-15\,\%$ for $SwB10$) for the non-swirling and moderate swirl flows. This effect is not as pronounced in the highly swirling $SwB11$ case. The stoichiometric cases appear relatively insensitive to the degree of swirl, and are all relatively well modeled by laminar calculations for $\Phi = 1$, though the calculated peak is in excess of the experimental means.

The hydrogen profiles in Figure 6.27 show the largest deviations from the corresponding laminar values. The lean premixed cases are reasonably well captured by the laminar calculations, but both levels of stratification exhibit markedly different behavior in the reaction zone; whereas the calculated $Y_{\mathrm{H_2}}$ increases at a constant rate with increasing temperature in this region, the stratified cases show an elevated and parabolic profile. This is true regardless of the degree of swirl. A speculative explanation for this is that the preferential transport of hydrogen away from the flame front near the burner exit results in elevated levels of $Y_{\mathrm{H_2}}$ further downstream at the long record location. As the long record locations are further downstream for the stratified cases than the premixed, there may be a larger accumulation of $Y_{\mathrm{H_2}}$ resulting in the differences seen in the plots. The stoichiometric cases trend much higher than the corresponding calculations, and show no evidence of being influenced by swirl.

Excellent agreement is seen in $Y_{\mathrm{H_2O}}$ and $Y_{\mathrm{O_2}}$, both between the premixed and stratified experimental means, and between the experimental means and laminar calculations (all flow conditions). The conclusions taken from this are that the consumption of oxygen and the production of water in the current burner are insensitive to the degree of stratification or swirl, and hence may be accurately modeled using ensembles of laminar flame calculations.

The main conclusions of this section are that on the mean the production and consumption of key species is well captured by ensembles of laminar flame calculations, particularly at the intersection of the mixing layer and the mean flame brush, despite the obvious differences in turbulence characteristics and stratification levels between the various cases. When conditioned on local equivalence ratio, stratification appears to have negligible effect on the behavior of $Y_{\mathrm{O_2}}$ or $Y_{\mathrm{H_2O}}$, and only a minor effect on Y_{CO} and $Y_{\mathrm{CO_2}}$. The mass fractions of hydrogen appear to be enhanced significantly in the stratified cases relative to the premixed; however, it is unclear as to whether this effect is due to the spatial gradients of equivalence ratio in and of themselves or instead is an artifact of preferential differential molecular transport of $\mathrm{H_2}$ away from the flame front into the reactants near to the burner exit.

6.8 Curvature

Stratification has typically been found to broaden the curvature distributions of turbulent methane/air flames, as detailed in Section 5.6 of Chapter 5. The mean of these distributions also tends to shift towards zero as the stratification increases. A broadening effect was observed in the slot burner, though the mean shifted away from zero. The present section will investigate the effect of stratification on curvature in the more turbulent swirl burner. The initial analysis will make use of both discrete and continuous forms of curvature, κ_{d} and κ_{c} respectively. Subsequent analysis is based upon continuous data only, as it can be multiply conditioned without becoming too sparse for sensible conclusions to be drawn.

Based on the findings in the slot burner, which showed only minor differences in the distributions of curvature for the two OH-PLIF planes (Figure 5.11), the data investigated in this section is taken from the first plane only.

Figure 6.28 demonstrates the spatial evolution of curvature in the swirl burner cases. Mean absolute discrete curvature[d], $\overline{|\kappa_\mathrm{d}|}$ is plotted against axial distance z using data taken from the short records used to show thermal and compositional flame structure in Section 6.4. The general trends exhibited are the same regardless of the composition or degree of swirl; mean absolute curvature rises steeply near the burner exit before reaching a plateau at $\overline{|\kappa_\mathrm{d}|} \sim 1.25\,\mathrm{mm}^{-1}$, and decays gradually with increasing downstream distance. In the initial region of quasi-linear increase, the curvature increases rapidly as the annular jets at the burner exit interact with their surroundings and become more wrinkled. Surface generation attains a maximal value before gradually decaying as both velocities and turbulence levels decrease further downstream.

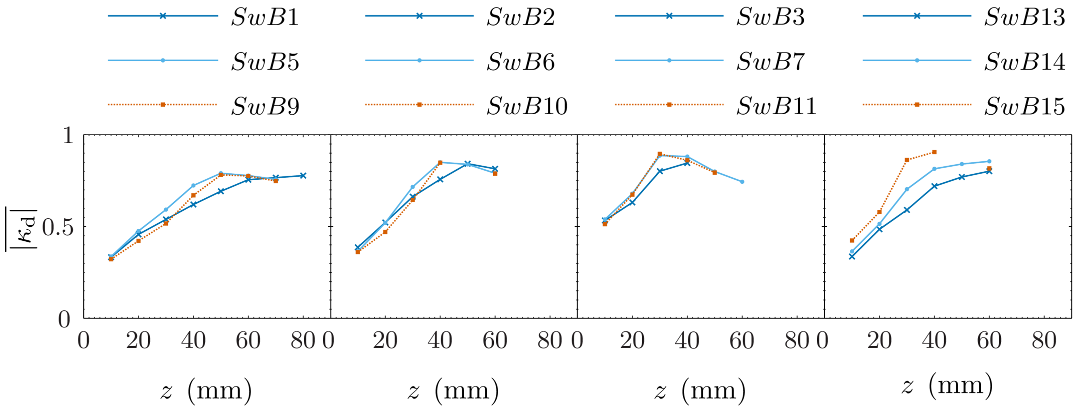

Figure 6.28: Relationship between mean absolute discrete curvature, $\overline{|\kappa_\mathrm{d}|}$, and axial distance for the swirl burner cases. Data is taken from the short data records used in Section 6.4, and is conditioned to remove outliers such that $|\kappa_\mathrm{d}| < 6\,\mathrm{mm}^{-1}$.

The influence of stratification is not immediately apparent from these plots as they are not conditioned on local equivalence ratio, and also are effectively premixed close to

---

[d] Continuous curvature is omitted from Figure 6.28 to improve the clarity of the figure, but similar behavior is observed.

the burner exit as seen in Figure 6.14. However, considering the behavior of the stratified systems as a whole, rather than data conditioned at a specific equivalence ratio gradient, the effect of stratification appears mild, perhaps resulting in the mean absolute curvature peak to be reached further upstream than in the corresponding premixed cases.

Some tentative conclusions about the influence of swirl may be drawn from this figure; the addition of swirl results in additional surface generation (as would be expected due to the increased turbulence), leading to increased values of mean absolute curvature. This is best illustrated by the rightmost column of Figure 6.28, which shows consistent increases in the mean absolute curvature of the stoichiometric cases with increasing swirl for all distances.

Similar trends are observed scanning the other columns from left to right, though this is less immediately clear. Considering the discrete mean absolute curvature values at $z = 30\,\mathrm{mm}$ the addition of moderate swirl increases $\overline{|\kappa_\mathrm{d}|}$ by 20 % to 27.5 % relative to the non-swirling cases, while the high swirl level results in an increase of 40 % to 70 %.

Pdfs of curvature at the long record locations (where the mixing layer intersects the flame brush) are shown in Figure 6.29, and basic statistics are summarized in Table 6.7. The most noticeable aspect of the continuous curvature distributions is how little effect stratification appears to have, regardless of whether flow is non-swirling or swirling. This is in contrast to the discrete distributions, where stratification clearly results in slightly broader distributions of curvature. The latter result is in line with the findings of Anselmo-Filho *et al* [24] and Renou *et al* [21]. It is speculated that the insensitivity of the continuous distributions to stratification is due to the fact that the results are not conditioned on a specific progress variable value, whereas the discrete curvature is located at a progress variable close to the peak gradient in OH in each instantaneous shot.

Looking at the mean absolute values of discrete curvature listed in Table 6.7, it ap-

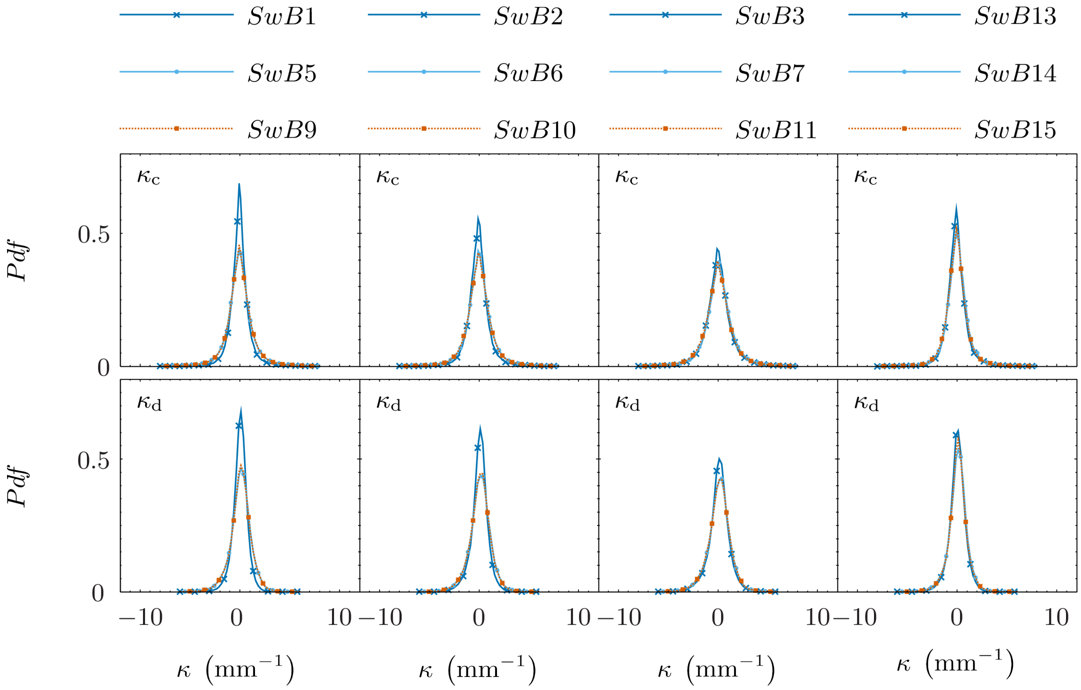

Figure 6.29: Local curvature probability density functions for continuous curvature κ_c (top row) and discrete curvature κ_d (bottom row) from the long record locations in the swirl burner cases.

pears that the addition of swirl increases $\overline{|\kappa_d|}$, though the increase seen is not monotonic in the stoichiometric case. However caution is advised in interpreting these curvature results as the long record locations are at various axial distances from the burner exit; thermal iso-surfaces are liable to exhibit different degrees of wrinkling and by extension curvature depending on the downstream distance. A more considered analysis follows.

The lean premixed cases (all at $z = 30\,\text{mm}$) demonstrate sizable increases in mean curvature modulus with increasing swirl, with $SwB2_{30}$ and $SwB3_{30}$ being 20 % and 49 % greater than the $SwB1_{30}$ case respectively. The intersection of the mixing layer and the flame brush moves steadily towards the burner exit with increasing swirl in the lean stratified cases, with the result that it is not possible to make a similar comparison conditioned on a single level of stratification. The stoichiometric non-swirling and moderately swirling premixed cases are both measured at $z = 30\,\mathrm{mm}$, and an increase of 15 % is seen with the addition of swirl, which is comparable to the increase seen between the corresponding lean cases. Note that the highly swirling stoichiometric case $SwB15_{20}$, which shows an increase in $\overline{|\kappa_\mathrm{d}|}$ (15 %), is located closer to the burner exit ($z = 20\,\mathrm{mm}$). Flames become more convoluted with downstream distance as the bulk velocities decay and interaction with the environment increases, and hence the highly swirling lean premixed case is expected to show a greater difference in mean absolute curvature at $z = 30\,\mathrm{mm}$.

Comparing $SwB5_{50}$ to $SwB9_{50}$, as well as $SwB6_{40}$ to $SwB10_{40}$ and $SwB3_{30}$ to both $SwB7_{30}$ and $SwB11_{30}$, enables tentative conclusions to be drawn as to the effect of stratification on mean absolute curvatures. Negligible differences are observed between the two levels of stratification at the long record locations for either discrete or continuous mean absolute values, regardless of flow type. This is to be expected given the similar levels of stratification found between the cases. In the highly swirling lean cases, increases of 9 % relative to the premixed $SwB1_{30}$ are demonstrated for both stratification levels. The marginal differences seen between the two stratification levels regardless of the degree of swirl again indicates that the relative difference in spatial gradients of equivalence ratio is insufficient to generate significant differences in curvature. The results in the highly swirling case quantitatively show the broadening of the curvature distribution with stratification, in line with the findings in the literature. The influence of stratification (at the levels found in the current work) is significantly weaker than that of swirl.

The continuous statistics are based on local curvature values throughout the flame front, rather than simply at the location of the peak OH gradient (as is the case for the discrete curvature). This will naturally have an effect on the values reported, so caution is advised in the interpretation of the values shown in Table 6.7.

Table 6.7: Statistics for discrete and continuous measures of local curvature in the swirl burner at long record locations. Continuous data is taken from data within the thermal ramp across the flame front. Data in parentheses is taken from short record locations to aid discussion of results.

Flame	z (mm)	$\overline{\lvert\kappa_\mathrm{d}\rvert}$ $\left(\mathrm{mm}^{-1}\right)$	$\overline{\lvert\kappa_\mathrm{c}\rvert}$ $\left(\mathrm{mm}^{-1}\right)$	$\overline{\kappa_\mathrm{d}}$ $\left(\mathrm{mm}^{-1}\right)$	$\overline{\kappa_\mathrm{c}}$ $\left(\mathrm{mm}^{-1}\right)$	$\gamma_{1,\mathrm{d}}$ $(-)$	$\gamma_{1,\mathrm{c}}$ $(-)$	$\gamma_{2,\mathrm{d}}$ $(-)$	$\gamma_{2,\mathrm{c}}$ $(-)$
$SwB1$	30	0.74	1.08	0.02	0.02	−0.39	−0.56	2.68	7.56
$SwB2$	30	0.89	1.17	0.05	0.06	−0.50	−0.29	3.29	5.79
$SwB3$	30	1.10	1.45	0.10	−0.06	−0.36	−0.24	2.84	3.74
$SwB5$	50 (30)	1.09 (0.81)	1.45 (1.03)	0.07	0.03	−0.39	−0.10	2.25	4.03
$SwB6$	40 (30)	1.13 (0.99)	1.44 (0.92)	0.10	−0.01	−0.32	−0.10	2.01	3.92
$SwB7$	30	1.19	1.57	0.11	−0.13	−0.32	−0.19	2.05	3.19
$SwB9$	50 (30)	1.09 (0.70)	1.43 (0.80)	0.07	0.01	−0.39	−0.15	2.27	4.02
$SwB10$	40 (30)	1.12 (0.89)	1.44 (1.03)	0.08	0.01	−0.34	−0.14	2.06	3.83
$SwB11$	30	1.19	1.57	0.10	−0.02	−0.32	−0.06	2.07	3.12
$SwB13$	30	0.83	1.10	0.04	0.05	−0.37	−0.55	2.42	6.16
$SwB14$	30	0.96	1.20	0.07	−0.01	−0.38	−0.32	2.58	5.10
$SwB15$	20 (30)	0.95 (1.15)	1.21 (1.54)	0.06	0.04	−0.31	−0.37	3.07	5.09

The investigation of local curvature in the slot burner revealed that high values of continuous curvature were more likely to be found outside of the intermediate region of the flame ($0.2 < c < 0.8$). Figure 6.30 shows the bivariate pdf of progress variable c and continuous curvature κ_c for the swirl burner cases at the long record locations. The data is conditioned on local equivalence ratio to within ±1 % of the nominal values — $\Phi = 0.79$ for lean cases, $\Phi = 1$ for stoichiometric — to isolate any differences due to stratification from the effects of local stoichiometry.

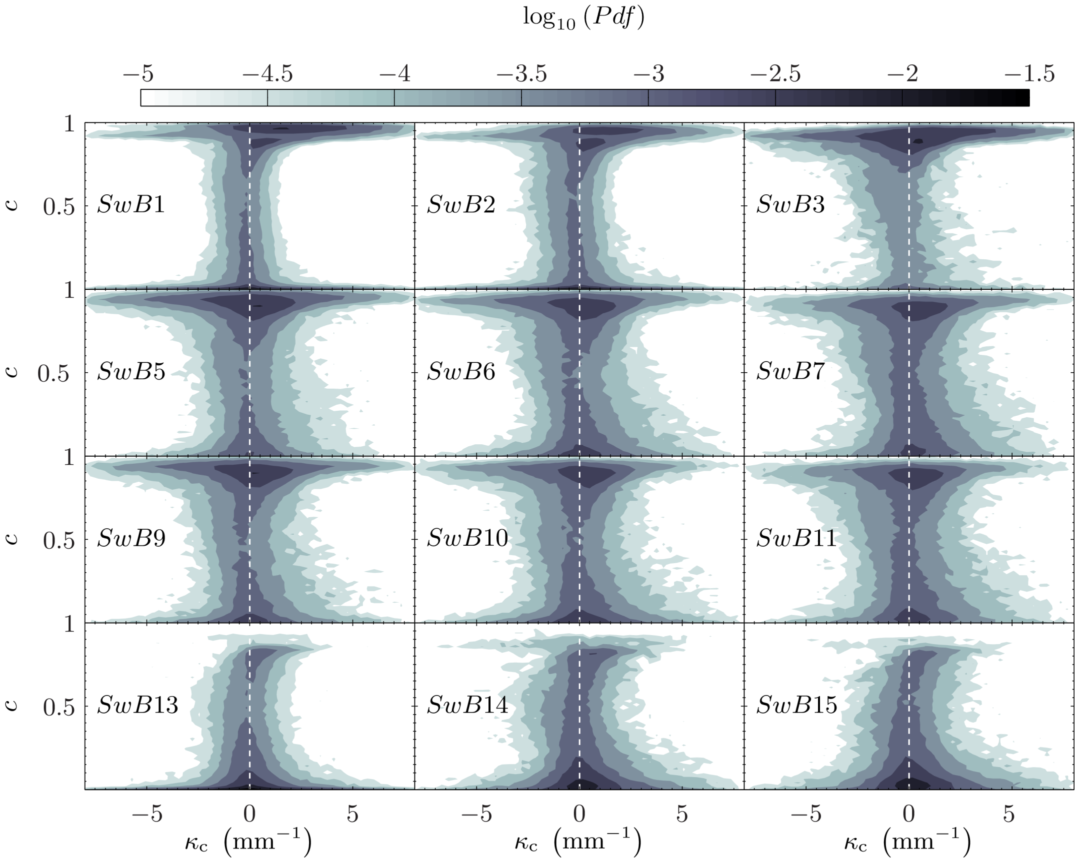

Figure 6.30: Bivariate pdfs of continuous curvature κ_c and progress variable c for the swirl burner cases at the long record locations. $\kappa_c = 0\,\text{mm}^{-1}$ is plotted with a dashed white line to highlight asymmetries in the distributions with respect to c. Data is conditioned such that $\Phi = 0.79$ and $\Phi = 1$ for the lean and stoichiometric cases respectively (±1 %).

The reduction in data points due to this conditioning accounts for the relative roughness of the probability contours. It is readily apparent from the bivariate pdfs that in the intermediate regions the continuous curvature values exhibit similar behavior to the discrete pdfs seen in Figure 6.29, with the distributions at any given progress variable $0.2 < c < 0.8$ showing peaks at near-zero (negative) curvature and negligible probability past $|\kappa_\mathrm{c}| = 2.5\,\mathrm{mm}^{-1}$. Stratification broadens these distributions in all cases, though the effect is most pronounced in the non-swirling flow cases.

The addition of swirl also typically has a broadening effect. Interestingly the high swirl premixed lean case $SwB3_{30}$ appears to show a trend towards increasingly negative values of continuous curvature moving towards the products, with a weak negative correlation $R^2 = -0.22$ ($c < 0.7$). An explanation for this behavior in light of its absence both in the stratified and stoichiometric highly swirling cases is not immediately apparent. Note that the lack of contours for high c values in the lean cases is due to the high positive correlation between Φ and c in the stoichiometric cases resulting in a lack of data for $c > 0.9$ following equivalence ratio conditioning.

In conclusion, it is clear that discrete mean absolute curvature is substantially increased by the addition of swirl in both the lean and stoichiometric premixed cases. Stratification also influences $\overline{|\kappa_\mathrm{d}|}$, though the increases seen relative to the premixed cases are similar for both levels of stratification.

6.9 Progress Variable PDFs

PDFs of progress variable provide useful information as they allow the similarity between the flames under investigation and an ideal laminar flame to be quickly assessed; the latter is characterized by a double delta function, with peaks at $c = 0$ and $c = 1$. PDFs of progress variable for the swirl burner cases are presented in Figure 6.31. It is clear

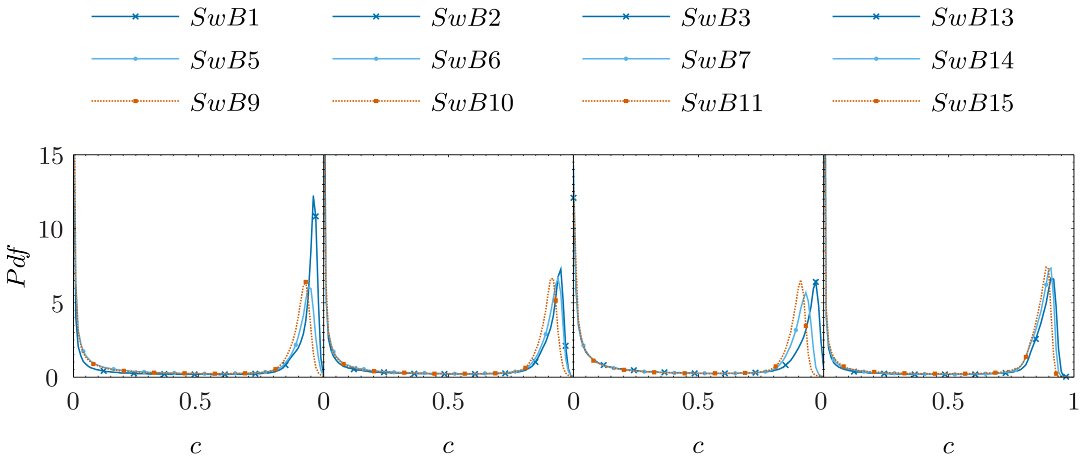

Figure 6.31: Probability density function of progress variable c for the swirl burner cases at the long record locations. Nominal equivalence ratio for lean ($\Phi = 0.79$) and stoichiometric ($\Phi = 1$) are shown by dashed white lines.

that the studied flames deviate substantially from the idealized behavior, as expected from their turbulent nature.

The addition of stratification shifts the near-unity progress variable peak back towards the zero peak. This effect is observed for all conditions; lean or stoichiometric, non-swirling or swirling.

Interestingly the addition of swirl only reduces the near-unity peak of the premixed lean cases when moving from non-swirling flow to moderate swirl; the shift to high swirl has little further effect. The implication of this is that the addition of swirl increases the instantaneous flame thickness of premixed flames but that above a certain level the further addition of swirl fails to increase the thickness of the flame. One possible explanation is that the production of small eddies — which may penetrate and thicken the reaction zone — either plateaus at/below the moderate swirl level or does not increase monotonically with swirl.

Note that none of the distributions shows a peak at $c = 1$, with only the $SwB3_{30}$ showing any significant percentage of flames attaining said value. This can be further elucidated by looking at the bivariate pdf of progress variable and equivalence ratio, shown in Figure 6.32. The probability density function for $SwB3_{30}$ shows a distinct hook towards lower equivalence ratios as the progress variable approaches unity. This is attributed to the effect of co-flow air being entrained by the recirculation zone, reducing the local equivalence ratio, as seen in the Favre-averages in Figure 6.18. Although the entrained air also reduces the local temperature, again evident in Figure 6.18, the balance between that effect and the reduction of the local equivalence ratio is such that higher values of local progress variable are attained.

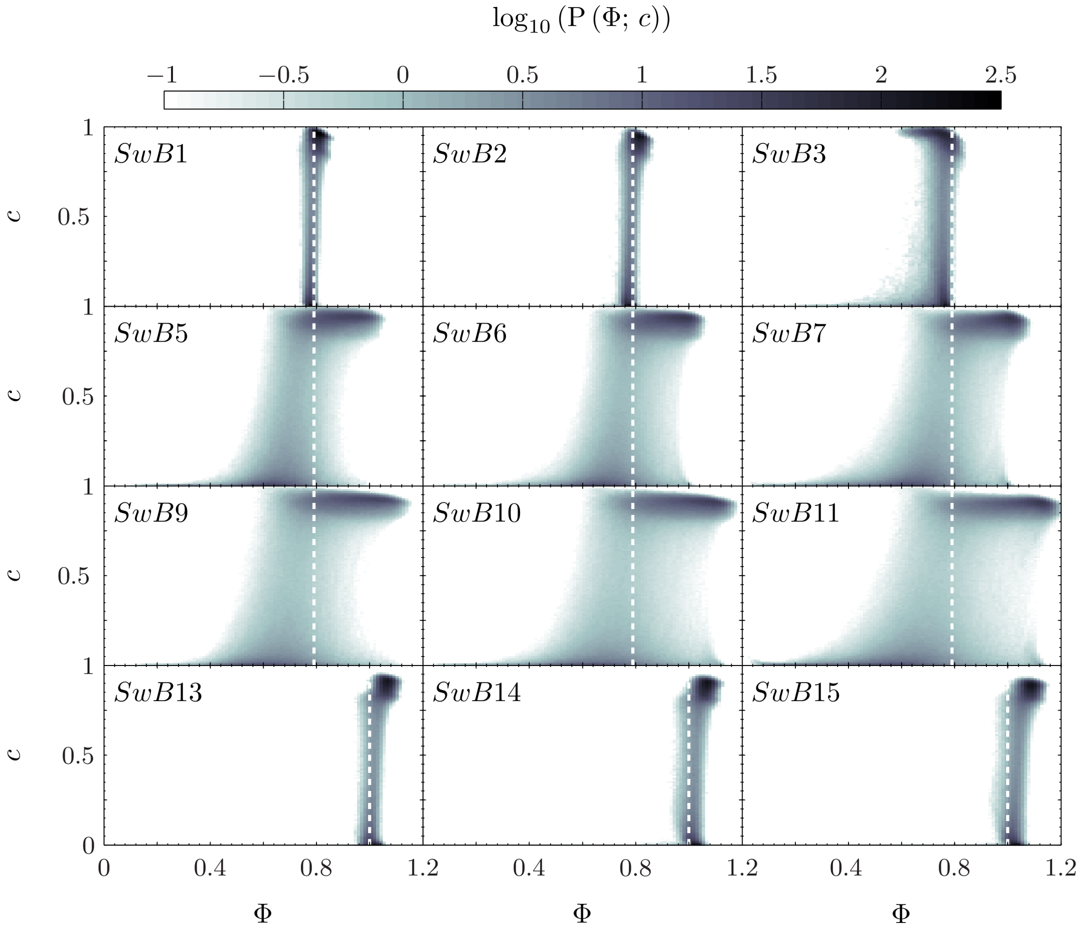

Figure 6.32: Bivariate probability density function of progress variable c and equivalence ratio Φ for the swirl burner cases at the long record locations. Vertical dashed white lines are plotted at the mean lean and stoichiometric Φ values (0.79 and 1).

In contrast, the equivalence ratio tends towards higher values in the equilibrium zone for the other cases. This is expected in the stratified cases as they are back-supported (the spatial gradient of equivalence ratio is positive moving from reactants to products), and hence the flames do not attain temperatures sufficient for the local progress variable to reach unity. In the stoichiometric cases the equivalence ratio is slightly higher than unity near the burner centerline, as detailed in Section 6.6.4, again accounting for the failure to attain unity progress variable. It should also be noted that the local equilibrium temperature T_e is obtained from calculations which are unstrained and adiabatic. The effect of strain in the experimental data will reduce the true value of T_e, and while efforts have been made to ensure the experiments are close to adiabatic, deviations from this will account in part for the attenuated peak progress variable values seen in the data.

6.10 Influence of Stratification on Scalar Gradients

This section will consider the following quantities, all of which are highly dependent on temperature gradients: surface density function, $|\nabla c|$; thermal scalar dissipation rate, χ_c; turbulent flame thickness, δ_t; and flame surface density Σ. The general approach will be first to consider the unconditioned data, to show the behavior on the mean, and then to condition the data on local equivalence ratio to isolate the effects of stratification (i.e. local equivalence ratio gradients) from those due to local stoichiometry.

6.10.1 Surface Density Function & Scalar Dissipation Rate

Surface density function, $|\nabla c|$, and scalar dissipation rate, χ_c, are very closely related ($\chi_c \propto |\nabla c|^2$) Scatter plots of surface density function, $|\nabla c|$, against progress variable c are provided in Figure 6.33. The data is colored by the local equivalence ratio to highlight any composition dependent effects. Points below the lean flammability limit

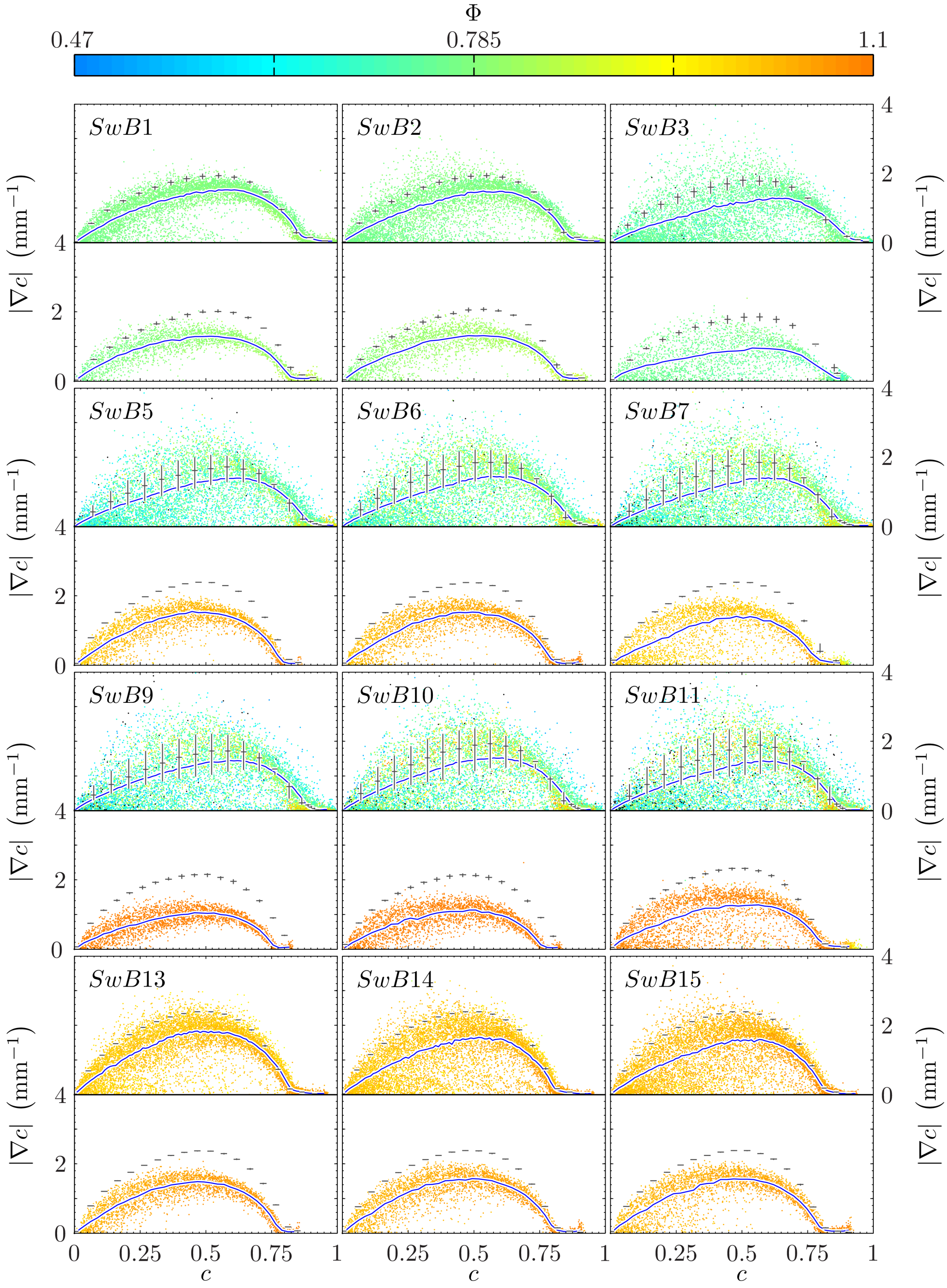

Figure 6.33: Plots of progress variable c against surface density function $|\nabla c|$ for the swirl burner at both $z = 10\,\mathrm{mm}$ (bottom halves) and long record (top halves) locations, colored by Φ, as shown in the colorbar. Data below the lean flammability limit ($\Phi = 0.47$) are plotted in black. Mean fits are shown by solid blue lines. Laminar flame calculations are shown by gray horizontal (value at local mean Φ) and vertical (range of maximum and minimum local Φ) lines.

($\Phi = 0.47$) are plotted in black to illustrate any extension of the lean limit. Note that few such points are visible even in the highly stratified case due to the fact that the scatter data has been downsampled such that a hundred points are plotted within each progress variable bin. The aim of this down-sampling is to reduce the degree of redundancy in plotting and also to highlight the range of equivalence ratios experienced, and not to provide an approximation to the bivariate pdf by virtue of point density.

The conditional mean fits are significantly lower than laminar unstrained values at the corresponding nominal stoichiometries. Comparable turbulence-induced thickening has been reported in the modeling literature by Sankaran *et al* [73] and more recently by Moureau *et al* [74]. The magnitude of the disparities seen in the swirl burner results appear to have a fairly strong equivalence ratio dependence; Φ values are nearly constant at the $z = 10\,\mathrm{mm}$ locations, and the differences are much larger in the richer cases. The agreement is better in the stratified cases at the long record locations, but large differences are still seen for the premixed cases. This indicates that the use of ensembles of unstrained laminar flame calculations is unsuitable for capturing the behavior of surface density function on the mean, particularly for premixed cases; an unsurprising result as such a method fails to take into account any potential thickening of the flame front (and hence attenuation of $|\nabla c|$) by the entrainment of small eddies into the preheat zone. Evidence of such eddies penetrating the flame front are provided by the instantaneous temperature profiles, where small local peaks and troughs are regularly observed within the overall thermal ramp.

The peak $|\nabla c|$ in the experimental data typically occurs closer to the equilibrium zone (high c) than in the numerical values. The rapid evolution of $|\nabla c|$ seen in the laminar flame calculations is attenuated in the regions preceding the $|\nabla c|$ peak, and the experimental means exhibit quasi-linear slopes for much of this progress variable space. This slope, observed in many of the mean fits, is attributed to the effect of eddies

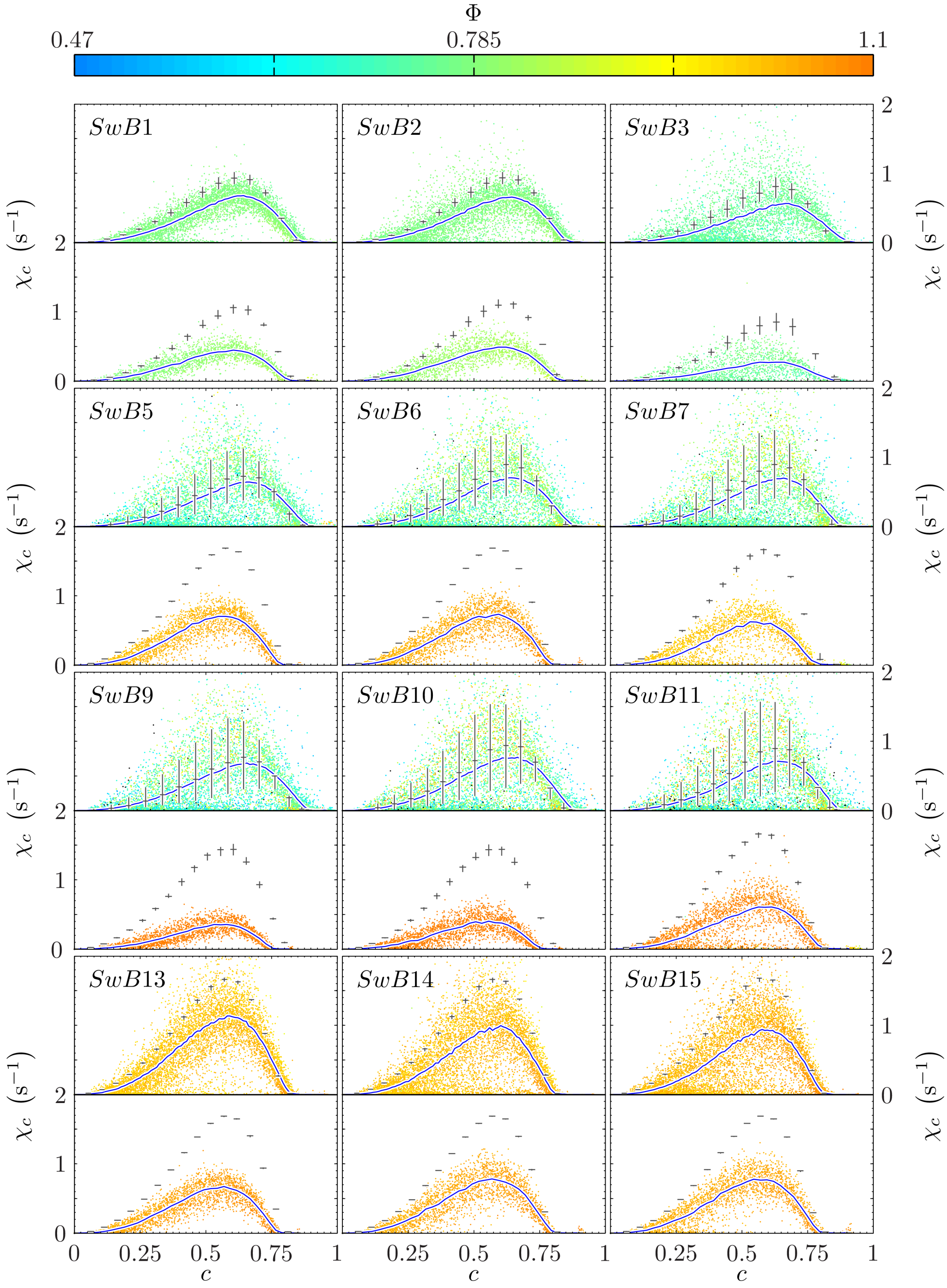

Figure 6.34: Plots of progress variable c against scalar dissipation rate χ_c for the swirl burner at both $z = 10\,\mathrm{mm}$ (bottom halves) and long record (top halves) locations, colored by Φ, as shown in the colorbar. Data below the lean flammability limit ($\Phi = 0.47$) are plotted in black. Mean fits are shown by solid blue lines. Laminar flame calculations are shown by gray horizontal (value at local mean Φ) and vertical (range of maximum and minimum local Φ) lines.

penetrating the preheat zone; the flame may be locally thickened, reducing the rate at which $|\nabla c|$ increases in c space, and leading to a near-linear slope of $|\nabla c|$ against c.

The $|\nabla c|$ mean fits all return to zero for progress variable values that are substantially below unity. This indicates that the shift of the second delta in the progress variable pdfs towards the reactants seen in Figure 6.31 is not due to the flames failing to reach equilibrium within the line measurement window, and may be attributed to the effects of elevated equivalence ratios (due to stratification or preferential molecular transport) and non-idealities (i.e. non-adiabatic conditions).

Figure 6.34 shows conditional mean fits of scalar dissipation rate in progress variable space, using the same conventions as Figure 6.33. Again, the data is not conditioned on equivalence ratio as the objective is to examine the behavior on the mean. As χ_c is closely related to $|\nabla c|$, detailed analysis will be reserved for conditioned data. Unsurprisingly, the squared term in the formula for χ_c results in the differences seen for the quasi-premixed conditions at $z = 10\,\text{mm}$ being amplified; agreement with corresponding laminar calculations is very poor in all cases.

The long record locations show somewhat more interesting behavior. The differences seen in the premixed cases remain relatively large, particularly for the stoichiometric case. However the conditional means in the stratified cases trend closely with their laminar unstrained values, and the spread of the scatter data is well captured by the laminar values at the 10^{th} and 90^{th} percentiles of local equivalence ratio within each progress variable bin.

Figure 6.35 shows the behavior of $|\nabla c|$ and χ_c in progress variable space when data is conditioned such that the local equivalence ratio is within $\pm 1\,\%$ of the mean equivalence ratio ($\Phi = 0.79$ for the lean cases, $\Phi = 1$ for the stoichiometric). This ensures that any trends observed are unlikely to be influenced unduly by stoichiometry effects. The profiles of $|\nabla c|$ again trend below their laminar unstrained calculated equivalents, with

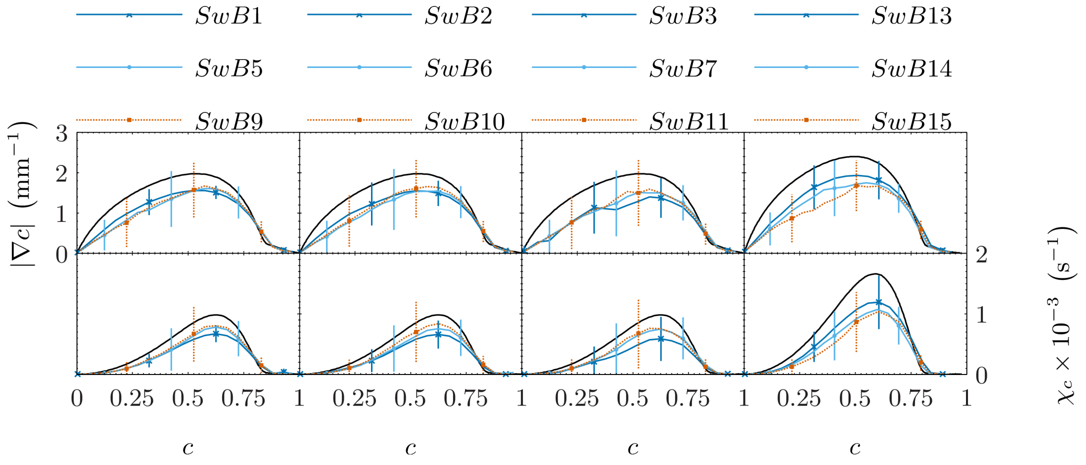

Figure 6.35: Conditional mean fits of surface density function (top row) and scalar dissipation rate (bottom row) in progress variable space for the swirl burner cases at the long record locations. Data is conditioned such that $\Phi = 0.79$ and $\Phi = 1$ ($\pm 1\,\%$) in the lean and stoichiometric cases respectively. Vertical lines show standard deviations at that location. Laminar flame calculations at the specified equivalence ratio are shown by solid black lines.

the latter lying approximately one standard deviation above the experimental conditional means.

Given the degree of variance seen within the experimental data it is difficult to know whether differences seen between the means are significant. However it does appear that stratification shifts the location of peak surface density function towards the products for the lean cases. The stoichiometric cases show decreases in peak amplitudes with increasing swirl, which is not noticeable in the lean cases save for $SwB3$. It appears that the flame structure is more sensitive to turbulence at the stoichiometric point than at the leaner conditions experienced for the other conditions.

The scalar dissipation rate shows a more convincing trend with increasing stratification, with the premixed lean cases consistently undershooting the peak levels seen in their stratified equivalents. Interestingly the locations of peak χ_c are less sensitive to the degree of stratification than for the surface density function. In all cases the peaks attained are substantially lower than the laminar calculations. The heightened turbulence sensitivity noted for $|\nabla c|$ in the stoichiometric cases is also observed in the χ_c profiles.

6.10.2 Turbulent Flame Thickness

The turbulent flame thickness is of interest in stratified flames as the presence of equivalence ratio gradients is expected to result in fluctuations in local propagation speed, with an associated change in flame area. Any such changes effect the degree of stretch in the flame, and subsequently the turbulent flame thickness δ_t. The definition of turbulent flame thickness used in the following analysis is based on the Rayleigh temperature measurements, specifically the ratio of the magnitude of the thermal ramp across the flame front to the maximum thermal gradient within the flame:

$$\delta_\mathrm{t} \quad = \quad \frac{T_\mathrm{b} - T_\mathrm{u}}{|\nabla T|_\mathrm{max}} \tag{6.10}$$

where subscripts have their usual meanings.

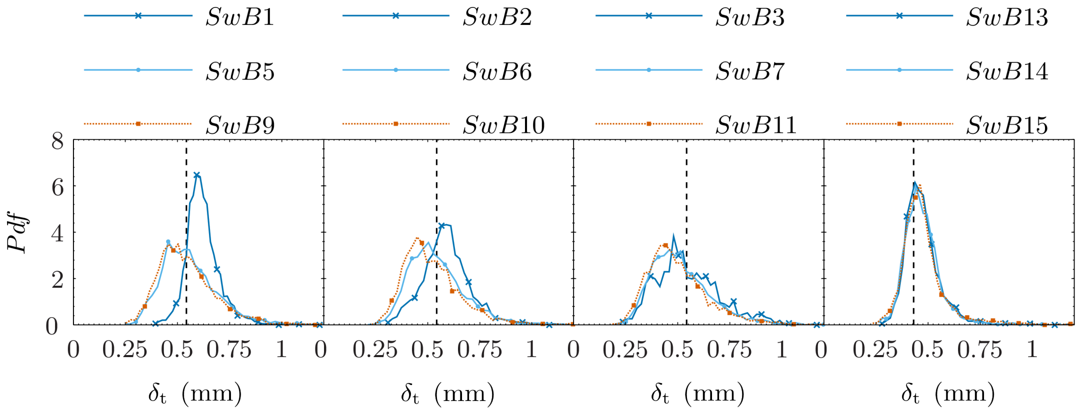

Figure 6.36: Probability density functions of turbulent flame thickness δ_t for the swirl burner cases at the long record locations. Data is conditioned such that $\Phi = 0.79$ and $\Phi = 1$ in the lean and stoichiometric cases respectively ($\pm 2.5\,\%$). The corresponding laminar flame thicknesses δ_L are marked with a vertical dashed line, - - - -.

Table 6.8: Statistics for turbulent flame thickness δ_{t} in the swirl burner at long record locations. Data is conditioned such that $\Phi = 0.79$ and $\Phi = 1$ in the lean and stoichiometric cases respectively ($\pm 2.5\,\%$) at the location of peak temperature gradient. Values in parentheses are taken from short records.

Flame	z (mm)	$\overline{\delta_{\mathrm{t}}}$ (mm)	$\sigma_{\delta_{\mathrm{t}}}$ (mm)	γ_1 (–)	γ_2 (–)
$SwB1$	30	0.62	0.08	1.05	3.53
$SwB2$	30	0.59	0.12	0.80	2.69
$SwB3$	30	0.55	0.15	0.80	1.09
$SwB5$	50 (30)	0.56 (0.53)	0.14	1.23	3.17
$SwB6$	40 (30)	0.54 (0.51)	0.14	1.17	3.05
$SwB7$	30	0.52	0.15	1.27	3.32
$SwB9$	50 (30)	0.54 (0.42)	0.14	1.13	2.50
$SwB10$	40 (30)	0.52 (0.50)	0.14	1.21	2.85
$SwB11$	30	0.50	0.15	1.26	3.04
$SwB13$	30	0.47	0.09	1.89	8.77
$SwB14$	30	0.47	0.09	1.73	7.01
$SwB15$	20 (30)	0.47 (0.52)	0.11	2.01	7.65

Probability density functions for the swirl burner cases at the long record locations are presented in Figure 6.36, and the corresponding principle moments are given in Table 6.8 for reference. The flame thickness distributions highlight some interesting behavior. Firstly, the premixed cases are consistently thicker than the stratified, in agreement with the results in the slot burner data and also the findings of Robin *et al* [23]. Note that flame thickness in the latter is derived using the temperature difference between T_{u} and the temperature at the location of peak temperature gradient, which is analogous to the thickness of the preheat zone [94]. However, the trends observed are expected to be similar to those seen for the turbulent flame thickness defined in Equation 6.10.

The influence of swirl is quite interesting, as it only appears to have a significant effect on the lean premixed flames. The distributions of δ_t progressively broaden and shift to lower mean values moving from $SwB1$ to $SwB3$, yet no significant difference is observed with flow type for either the stratified or the stoichiometric distributions. Figure 6.36. The mean turbulent flame thickness in the premixed cases decreases moving from the lean $\Phi_\mathrm{n} = 0.79$ to the stoichiometric $\Phi_\mathrm{n} = 1$, which is in line with the behavior of laminar flame calculations for $\Phi < 1.1$.

Finally, the lean stratified cases appear to have values of δ_t which are equal to or lower than the equivalent laminar flame value. This is interesting as it seems contrary to the surface density results seen in Figure 6.35 of Section 6.10.1, which showed attenuated values of mean $|\nabla c|$ relative to laminar calculations, implying thickened flame fronts in agreement with the modeling literature [73, 74]. This disparity is attributed to the definition of δ_t given by Equation 6.10; as the formula is dependent on the temperature range spanned by the flame, and the peak thermal gradient, it fails to take into account any broadening of the physical flame front which may arise if there are local peaks and troughs inside the overall thermal ramp (e.g. due to eddy penetration).

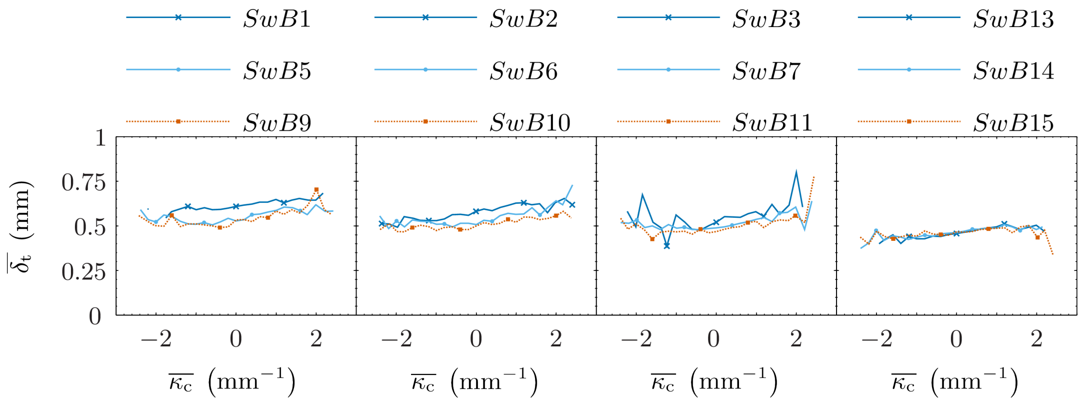

Figure 6.37: Conditional mean fit of turbulent flame thickness against continuous curvature for the swirl burner cases at the long record locations. Data is conditioned such that $\Phi = 0.79$ and $\Phi = 1$ in the lean and stoichiometric cases respectively ($\pm 2.5\,\%$).

Figure 6.37 illustrates the variation of mean turbulent flame thickness with mean continuous curvature. Note that the data (particularly for the highly swirling cases) is relatively sparse after conditioning on local equivalence ratio, with the result that the conditional means are somewhat noisy. However, the general behavior exhibited indicates that there is a weak positive correlation between curvature and flame thickness in the swirl burner cases ($0.08 < R < 0.22$). The noted correlation for positive values of mean curvature is significantly less than that reported by Robin *et al* [23], and it is reasonable to say that continuous curvature is for all practical purposes decoupled from the turbulent flame thickness in the swirl burner. Note that the trends exhibited in similar analyses in the literature [23, 95] show substantial differences both within and across the studies. This is particularly well highlighted by the results seen in [23], where the relationship between curvature and turbulent flame thickness is heavily modified by the type of turbulent grid used, the nominal equivalence ratio, and the degree of stratification.

6.10.3 Flame Surface Density

Flame surface densities calculated using the Pope formulation [8] (detailed in Section 4.3.1 of Chapter 4) are presented in Figure 6.38, demonstrating the trends in Σ across both mean and instantaneous c space in the swirl burner cases at the long record locations. The profiles trend similarly to those in the slot burner data in Section 5.8 of Chapter 5, exhibiting a shift from positive to negative skew as c increases. The values for high $c = 0.95$ are again unphysical, but are attributed to the shift of the unity peak in the progress variable pdfs towards the reactants (Section 6.9 of Section 6.9) rather than noise in the product temperature data, as the latter is essentially eliminated by the wavelet filtering.

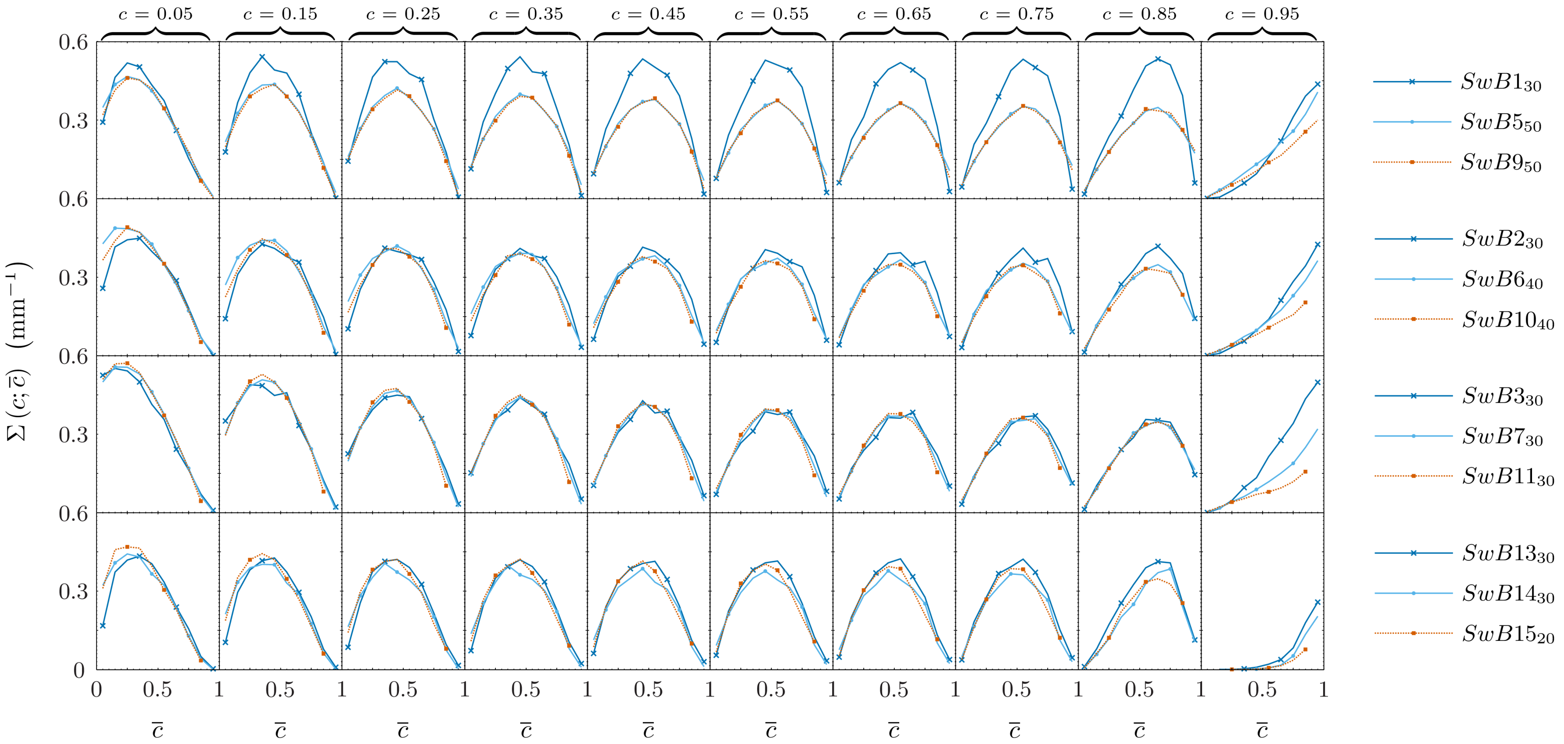

Figure 6.38: Behavior of flame surface density in terms of mean and instantaneous progress variable for lean non-swirling (top row), moderately swirling (2nd row), highly swirling (3rd row) and stoichiometric cases (bottom row) in the swirl burner at the long record locations.

Flame surface density appears quite sensitive to whether or not the conditions are premixed or stratified in the non-swirling cases, more so than the equivalent data in the slot burner. This may indicate that the effect of stratification on flame topology has a degree of turbulence dependence. The premixed $SwB1_{30}$ profiles peak at values between 8 % to 51 % greater than the corresponding stratified cases. This is a peculiar result given the broader curvature pdfs seen for the stratified cases in Figure 6.29; the expectation would be that the higher frequency of large curvature, more wrinkled flames in these cases would result in a greater surface area and a corresponding larger flame surface density. The differences between the two levels of stratification in $SwB5_{50}$ and $SwB9_{50}$ are comparatively tiny, between -1 % to 2 %.

Interestingly the addition of swirl decreases the differences seen between the premixed and stratified cases, indicating that the effects of stratification on flame surface density have a turbulence dependency. The stratified cases trend higher for low instantaneous values of progress variable (-9 % to -2 % for $c \leq 0.25$) and increasingly lower for higher values of progress variable (5 % to 26 % for $0.35 \leq c \leq 0.85$). These differences are almost eliminated moving to the high swirl conditions, with the stratified cases peaking between -8 % to 4 % relative to the premixed values. The effect of swirl on the stratified cases themselves small compared to that seen for the premixed cases, with peak amplitudes in stratified conditions being increased (contrast with the behavior in the premixed cases) by 0 % to 15 %.

6.11 Summary of Results

This chapter has presented results from a new turbulent swirling stratified methane/air burner. An experimental matrix encompassing three degrees of stratification and swirl in lean cases and three levels of swirl in stoichiometric premixed cases were investigated using a variety of techniques. Axial and radial flow fields were revealed using two-dimensional PIV, while the thermo-chemical structure was probed within the flame front using high resolution Rayleigh/Raman/CO-LIF line measurements with simultaneous cross-planar OH-LIF. The main results of these analyses are summarized as follows:

- The turbulence levels are substantially greater than those seen in the slot burner in Chapter 5, and the flames surveyed fall within the thin reaction zone regime on the modified Borghi diagram.
- The addition of swirl influences the stability of the flow field. The moderate swirl cases appears to generate instabilities and operate in an unstable mode, resulting in higher u' relative to equivalent non-swirling and highly swirling cases.
- The flames surveyed feature large recirculation zones above the central bluff body, which has significant impact on the species concentrations within the flame.
- Significant levels of stratification are achieved within the flame front, as shown in Section 6.5, with the moderately stratified cases showing RMS gradients of Φ comparable to the most highly stratified slot burner cases.
- Favre averaged results in Section 6.6 reveal elevated equivalence ratio levels within the recirculation zone, which is attributed to the effects of preferential molecular transport of hydrogen away from the flame front near to the burner exit.
- The mean behavior of key combustion species in the swirl burner flames at the intersection of the mixing layer with the flame brush is well captured by the use of ensembles of unstrained laminar flame calculations, with the exception of H_2. Significant differences are seen further upstream in H_2 and CO_2 due to the effects of preferential molecular transport.

- When conditioned on local equivalence ratio, H_2 is well modeled in the lean premixed cases by laminar calculations but is under-predicted through much of the temperature space for the stratified and stoichiometric conditions. This has important implications for models attempting to capture the behaviour of stratified flames using simple laminar flame models in their chemistry.

- Discrete curvature pdfs are broadened by the addition of stratification, in line with results seen elsewhere in the literature.

- Surface density function and scalar dissipation rate are significantly attenuated relative to their corresponding laminar unstrained values, which is reflected in the mean turbulent flame thicknesses. The peak surface density function values are similar between stratified and premixed cases when conditioned on local equivalence ratio, but are shifted towards the products under stratified conditions. Scalar dissipation rate is enhanced by stratification in all cases.

- Flame surface density appears to show a strong turbulence dependence in the lean cases, which seems to be moderated under stratified conditions. The premixed lean case $SwB1$ peaks significantly higher than all other cases through mean and instantaneous progress variable space.

Chapter 7

Flame Surface Density Metrics

This aim of this chapter is slightly different from from the previous two in that it is the underlying methodology of deriving flame surface density that is under investigation, rather than the behavior of the data itself. Over course of this chapter the values obtained using the three FSD metrics described in Section 4.3 of Chapter 4 are compared and contrasted. The metrics considered are the statistical expression derived by Pope [8] (Equation 4.11 of Chapter 4), Σ_1, the geometric method proposed by Shepherd [81] (Equation 4.12 of Chapter 4), Σ_2, and a geometric method which extends the Shepherd method to the entirety of c space [27] (Equation 4.13 of Chapter 4), Σ_3. Raw data from the slot burner (Chapter 5) and the swirl burner (Chapter 6) are used to ensure that any conclusions drawn are robust, and not simply an artifact of considering data from a single (perhaps fortuitous) condition.

7.1 Slot Burner Results

The purpose of the present chapter is to provide a systematic comparison of the relative behavior of various flame surface density measures, rather than to comment on the behavior of FSD itself in CH_4/air flames at different operating conditions. Stratification, turbulence intensity, curvature and swirl level may have an influence on the behavior of Σ. Variations in local flame speed and density due to spatial gradients in ϕ might be expected to affect FSD. The use of a large number of experimental cases allows robust comparison of the various FSD measures across a range of conditions.

True values of FSD for each experimental case are not known a priori. However, the general behaviour of Σ in both c and $\bar{c}$ space is known from results presented in both the experimental and modeling combustion literature [80, 81, 85, 96, 97]. For example, FSD should show a positive skew against $\bar{c}$ for low values of c. Hence a given measure is deemed to perform better than another if the measured behavior follows the expected physical behavior to a greater degree than the other.

Figure 7.1 shows the various flame surface density measures derived from the slot

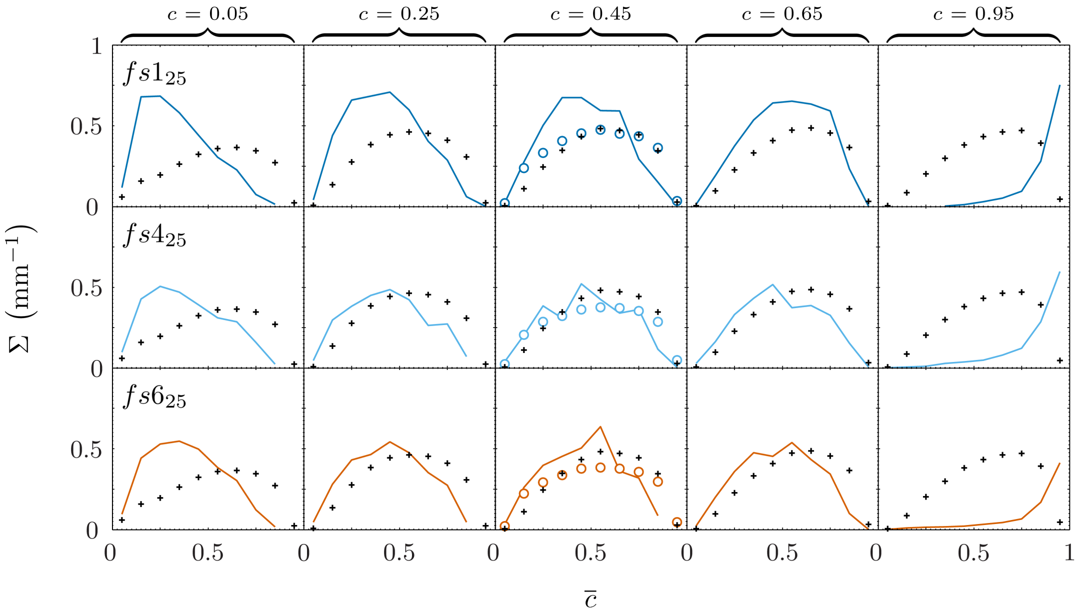

Figure 7.1: Flame surface density measurements from $fs1$ (top row), $fs4$ (middle row) and $fs6$ (bottom row). $\Sigma_1\,(c_T, \bar{c}_T)$ is shown by ——, $\Sigma_2\,(c_{\mathrm{OH}} = 0.5, \bar{c}_{\mathrm{OH}})$ by ○ , and $\Sigma_3\,(c_{\mathrm{OH}}, \bar{c}_{\mathrm{OH}})$ by +. Colors (and rows) delineate premixed, moderately stratified and highly stratified cases.

burner data. The data are plotted using absolute values rather than relative differences in order to show the trends in Σ with c and $\bar{c}$. The statistical $\Sigma_{1,T}$ and the geometric $\Sigma_{3,\mathrm{OH}}$ show good agreement at intermediary values of progress variable, but very poor at the extremes. In general $\Sigma_{3,\mathrm{OH}}$ reaches slightly lower values than $\Sigma_{1,T}$. The coarse resolution of the OH measurements compared to the thermal measurements in the slot burner data (Section 3.1.3 in Chapter 3) may account for part of this attenuation: the calculation of areas and contour lengths from the c_{OH} data is inherently sensitive to the experimental resolution. Resolution effects (spatial averaging) in $\Sigma_{1,T}$ are expected to be small due to the corrections applied (Section 4.2.4).

At high c, the geometric method gives more physically realistic results than those for $\Sigma_{1,T}$, which tends to explode as high $\bar{c}$ values are reached. This is attributed to two factors: the presence of non-zero gradients of c_T in the high $\bar{c}_T$ regions as the investigation window fails to encapsulate burnout and noise in the c_T measurements in this region, giving non-zero gradients. For low c, $\Sigma_{1,T}$ gives much better results than the geometric $\Sigma_{3,\mathrm{OH}}$. The Shepherd measure, $\Sigma_{2,\mathrm{OH}}$, is in good agreement with $\Sigma_3\,(c_{\mathrm{OH}} = 0.45, \bar{c}_{\mathrm{OH}})$, which is expected as $\Sigma_{3,\mathrm{OH}}$ is analogous to $\Sigma_{2,\mathrm{OH}}$ near $c_{\mathrm{OH}} = 0.5$.

7.2 Swirl Burner Results

$\Sigma_{1,T}$, $\Sigma_{2,\mathrm{OH}}$ and $\Sigma_{3,\mathrm{OH}}$ are similarly compared for the swirl burner data in Figure 7.2. Moderately swirling cases are omitted for brevity but exhibit similar behavior to highly swirling cases. The agreement between the surveyed metrics is substantially better for the premixed swirl burner data than that seen for the slot burner. Additionally the stratified cases show excellent agreement between $\Sigma_{1,T}$, $\Sigma_{2,\mathrm{OH}}$ and $\Sigma_{3,\mathrm{OH}}$. This is attributed primarily to the refinement of the OH image resolution by a factor of three for the swirl burner datasets relative to those for the slot burner experiments (due to improvements in the laser diagnostics described in Chapter 3). Again, $\Sigma_{1,T}$ is found to increase rapidly with $\overline{c}_T$ for high c_T, with similar explanations as for the slot burner. The behavior of $\Sigma_{3,\mathrm{OH}}$ for low c_{OH} is markedly improved in comparison to that in the slot burner datasets. $\Sigma_{2,\mathrm{OH}}$ and $\Sigma_{3,\mathrm{OH}}$ are almost identical for $c_{\mathrm{OH}} = 0.45$, again as expected.

The behavior of $\Sigma_3\left(c_{\mathrm{OH}} = 0.95, \overline{c}_{\mathrm{OH}}\right)$ is significant, as it shows substantially more realistic behavior than $\Sigma_1\left(c_T = 0.95, \overline{c}_T\right)$ in Figure 7.2. This may be attributed to the lack of noise at high c_{OH} due to the use of the OH progress images (Section 4.1.5 of Chapter 4). This contrasts with the high c_T gradients experienced at high c_T due to noise in the Rayleigh measurement in the products. This indicates that smoothing or denoising is necessary in high c_T data if sensible results for FSD are to be obtained in said data.

A note of caution in these comparisons is that c in Figure 7.1 and Figure 7.2 is defined using a different scalar depending on the FSD measure. It is perhaps surprising that such good agreement is seen despite the use of two different scalars. It is necessary to use the same scalar to derive Σ_1 and Σ_3 in order to isolate disparities due to methodology alone. $\Sigma_{1,\mathrm{OH}}$ and $\Sigma_{3,\mathrm{OH}}$ are compared for a selection of SwB operating conditions in Figure 7.3. A subset of conditions is shown for brevity; similar trends are observed throughout.

Very good agreement is found between $\Sigma_{1,\mathrm{OH}}$ and $\Sigma_{3,\mathrm{OH}}$ for $c_{\mathrm{OH}} > 0.1$, demonstrating that the two measures of FSD behave in a near-identical manner when using the same scalar. $\Sigma_{1,\mathrm{OH}}$ and $\Sigma_{3,\mathrm{OH}}$ tend to diverge at the low extreme of c_{OH} for $\overline{c}_{\mathrm{OH}} < 0.5$, with $\Sigma_{1,\mathrm{OH}}$ being significantly higher than the geometric measure. This is attributable to the fact that while ∇c_{OH} is small for low c_{OH}, it is still non-zero. This means that the product of the scalar gradient with the $\mathrm{P}\left(c_{\mathrm{OH}}; \overline{c}_{\mathrm{OH}}\right)$ (high when both c_{OH} and $\overline{c}_{\mathrm{OH}}$ are low) fails to decay towards zero as $\overline{c}_{\mathrm{OH}}$ decreases.

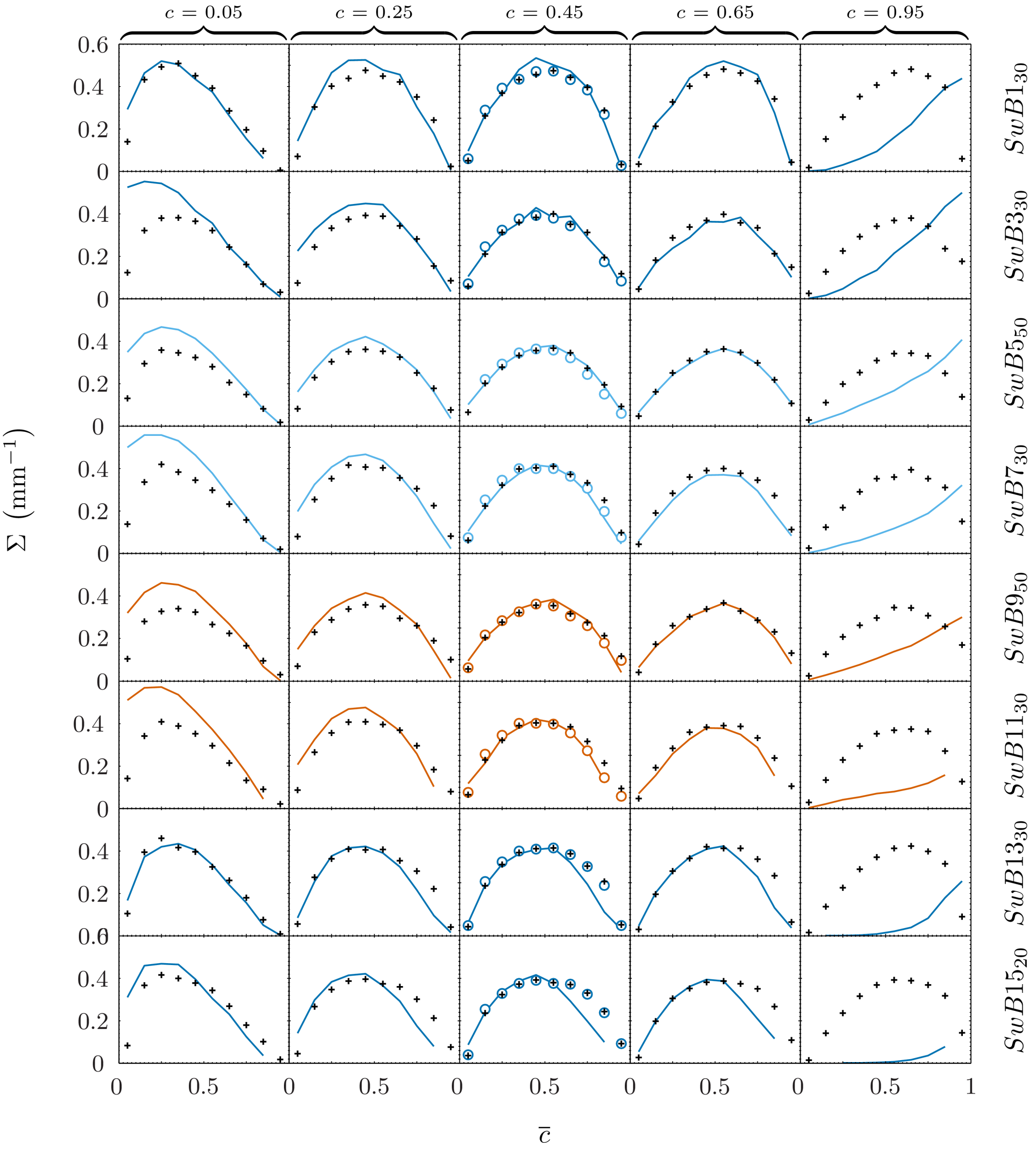

Figure 7.2: Flame surface density measurements from the swirl burner. $\Sigma_1\left(c_T, \bar{c}_T\right)$ is shown by ——, $\Sigma_2\left(c_{\mathrm{OH}} = 0.5, \bar{c}_{\mathrm{OH}}\right)$ by ○ , and $\Sigma_3\left(c_{\mathrm{OH}}, \bar{c}_{\mathrm{OH}}\right)$ by +. Colors delineate premixed, moderately stratified and highly stratified cases.

Figure 7.4 demonstrates the sensitivity of Σ_1 to the choice of scalar using data from $SwB1$. The ratio of the conditional progress variable probability in terms of c_{OH} to c_T is compared to corresponding ratio for the conditionally-averaged progress variable gradient from Equation 4.11. If Σ_1 is independent of the choice of scalar, then the data should collapse the dashed reciprocal curve in Figure 7.4. The data lie close to this curve for c_T, $c_{\mathrm{OH}} < 0.9$, demonstrating that Σ_1 shows little dependence on whether c is defined using temperature or OH. The data for $c > 0.9$ deviate substantially from the curve, showing $\Sigma_{1,\mathrm{OH}}$ to trend substantially higher and lower than $\Sigma_{1,T}$. This corresponds to the differences seen in Figure 7.2 for $c = 0.95$. It is difficult to determine whether probability or gradient ratios dominate this effect.

7.3 Conclusions

A quantitative comparison has been made between measures of flame surface density based on the statistical method proposed by Pope (Σ_1), the geometric method derived by

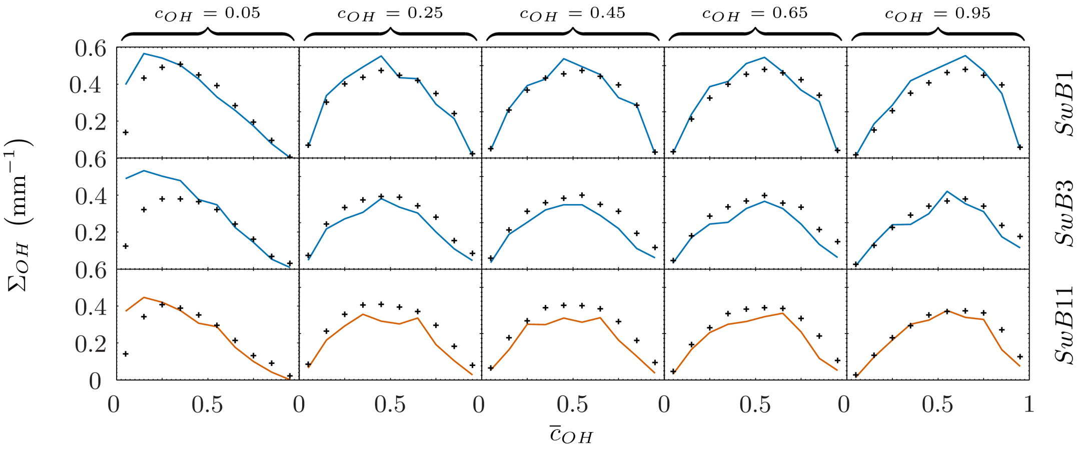

Figure 7.3: Flame surface density measurements from the swirl burner for cases $SwB1$ (uniformly premixed, non-swirling), $SwB3$ (uniformly premixed, highly swirling), and $SwB7$ (moderately stratified, highly swirling). $\Sigma_1(c_{\mathrm{OH}}, \bar{c}_{\mathrm{OH}})$ is shown by —— and $\Sigma_3(c_{\mathrm{OH}}, \bar{c}_{\mathrm{OH}})$ by +. Colors delineate premixed and highly stratified cases.

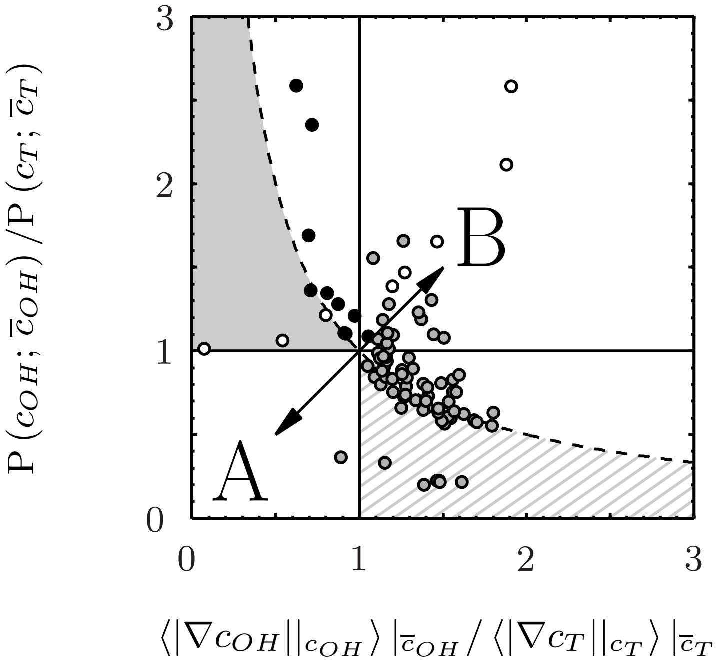

Figure 7.4: Ratio of mean progress variable gradients against ratio of conditional progress variable probabilities (OH:T) for *SwB*1. Low values $c < 0.1$ are shown by ●, intermediate c points where $0.1 \leq c \leq 0.9$ are shown by ●, and points where $c > 0.9$ are shown by ○ . The dashed curve corresponds to $\Sigma_{1,\mathrm{OH}} = \Sigma_{1,T}$. $\Sigma_{1,\mathrm{OH}} < \Sigma_{1,T}$ on the side of the dashed curve marked A, and vice-versa on the side marked B.

Shepherd (Σ_2), and a novel extension of the latter (Σ_3) in both premixed and stratified turbulent CH_4/air flames, using both T and OH as measurands of progress of reaction. Two different burners were used in separate experiments in order to obtain robust results that are insensitive to geometry or Reynolds number. A slot burner provided weakly turbulent V-flames, varying from uniformly premixed to highly stratified. A swirl burner provided 12 turbulent flames with varying stratification, swirl strength and global equivalence ratio. Measurements of local temperature, equivalence ratio flame orientation and flame tomography were made using simultaneous multi-scalar line diagnostics and cross plane OH-PLIF imaging.

The results demonstrate that geometric methods (Σ_2, Σ_3) and statistical methods (Σ_1) give virtually identical results at intermediate values of c for the swirl burner data, and demonstrate negligible dependence on stratification levels. Poorer agreement is seen in the slot burner data, and this is attributed to OH-LIF resolution being three times coarser in these experiments (150 µm/pixel) than in the swirl burner experiments (48 µm/pixel). Geometric methods are more sensitive to experimental resolution than the statistical method, for which a simple correction can partially compensate for spatial averaging effects.

Deriving Σ_1 requires simultaneous dual-plane Rayleigh (temperature), Mie or LIF imaging in order to determine the true three-dimensional gradients of progress variable instead of their projection on the line measurement axis, while Σ_3 achieves comparable results using experimentally simpler single sheet imaging, provided the resolution is sufficiently fine. Flame surface density values derived using these two methods appear to agree regardless of whether or not they are calculated using the same scalar, though suitable smoothing or filtering of data is required for Σ_1 due to the gradient terms involved.

Chapter 8

Conclusions

The goals of this project were as follows:

- to develop a burner to enable the investigation of stratified flames under more turbulent conditions than seen in the slot burner.
- to investigate the effects of stratification on combustion.
- to acquire and develop the experimental, data processing, and analytical skills required to accomplish these goals.

These objectives have been met over the last three and a half years, and have been detailed in the previous chapters. The effects of stratification on key combustion species, scalar gradients, and curvature have been investigated through the analysis of multi-scalar data from both the weakly turbulent slot burner (Chapter 5) and the more turbulent swirl burner (Chapter 6). The data processing skills acquired during the course of the project also enabled a detailed comparison of some of the key metrics used to measure flame surface density in experimental data (Chapter 7). The primary conclusions drawn from the work are given in the following section, with potential avenues of future work presented in the subsequent section.

Primary Conclusions:

- The equivalence ratio (derived from a mass fraction balance of hydrocarbons to oxygen in Chapter 4) is not viable for conditioning data within the flame front as substantial deviations from nominal stoichiometry is observed even in premixed flame calculations due to differential diffusion effects. This issue is exacerbated in stratified flows, as it also becomes impossible to separate instantaneous spatial gradients of equivalence ratio due to the stratification from those due to the differential diffusion effects. In the present work this issue is overcome by the use of a linear bridging function within the flame front (Section 4.2.3.2 of Chapter 4), providing a robust first-order solution to the problem.

- The evolution of the major combustion species in thermal space is well captured on the mean by ensembles of unstrained laminar flame calculations in both the slot and swirl burner datasets, with the exception of hydrogen.

- Stratification influences the surface density function (conditioned on local equivalence ratio), though this effect varies depending on the burner and flow conditions. $|\nabla c|$ is consistently elevated in the slot burner data under stratified conditions, while the swirl burner shows only a shift in the c values associated with peak $|\nabla c|$ towards the products for stratified cases.

- Scalar dissipation rate is consistently increased in stratified cases relative to equivalent premixed conditions. This is seen in both the slot and swirl burner data.

- The swirl burner is significantly more turbulent than the slot burner and displays some interesting behavior in terms of thermo-chemistry near the burner exit due to the combined effects of the recirculation zone above the central bluff body and preferential transport of species away from the flame front. The extensive experimental datasets already available on this burner mark it as a potentially interesting candidate for numerical modeling.

- The geometric flame surface density formula provided by Shepherd has been shown to be consistent with the formal derivation of Pope, and an extension to the Shepherd method has been proposed and validated which enables the comparison of the methods across both mean and instantaneous progress variable space.

Future Work:

- One interesting avenue of future work is to investigate the feasibility of extracting three-dimensional curvature data from cross-planar images. This is of practical relevance to the experimental combustion field as there are numerous existing cross-planar datasets, as well as labs where such measurements are likely to be taken in the future. Some preliminary work has been done on this, with early indications being that it may be possible to calculate the three-dimensional curvature through careful application of coordinate system transforms and the least squares solution of a Taylor series expansion for the temperature field. However, further work on the implementation of this technique is required before any concrete conclusions are drawn.

- The use of a linear bridging function to overcome the effects of differential diffusion on equivalence ratio within the flame front provides a robust basis for the analysis of stratified flames, but may not be an optimal strategy. It is suggested that both linear bridging and other potential methods to correct for differential diffusions effects be investigated further.

- The flow field in the swirl burner has been characterized in the axial and radial directions using PIV, as shown in Section 6.2 of Chapter 6. The absence of velocity data in the tangential direction is unsatisfactory, and it is proposed that a high speed stereo PIV campaign be undertaken with the current burner to ensure full three-dimensional characterization of these flames.

- High temporal resolution velocity measurements such as laser Doppler velocimetry (LDV) could be performed to improve calculations of the turbulent length scale.
- Qualitative imaging of the equivalence ratio field using acetone PLIF would provide useful information on the mixture fraction field, and allow the investigation of the effect of local pockets of high/low equivalence ratio on curvature on a larger scale than in the multi-scalar laser diagnostics.
- One major issue experienced during the experimental work was the difficulty in achieving consistent seeding. Commercial grade seeding chambers are not financially viable when multiple seeders are required in a single experiment. Additionally there appears to be a lack of consensus on good seed chamber design within the department. This could potentially be an interesting avenue of research during an experimental PhD student's first year; the goal would be the design and implementation of a seed chamber capable of giving consistent seeding at a range of flow rates. It may also be a promising candidate project for 4th year engineering students, as the work could be built on over successive years until a sufficiently good design (and set of design parameters and underlying physics) is established.

Appendix A

List of Publications

A.1 Journal Publications

- Sweeney, M. S., Hochgreb, S., and Barlow, R. S. (2011) The Structure of Premixed and Stratified Low Turbulence Flames, *Combustion and Flame*, **158**, 5, 935–948
- Barlow, R. S., Dunn, M. J., Sweeney, M. S., Hochgreb, S. (2011) Effects of preferential transport in turbulent bluff-body-stabilized lean premixed CH_4/air flames, *Combustion and Flame*, *In Press*
- Sweeney, M. S., Hochgreb, S., Dunn, M. J., and Barlow, R. S. (2010) A Comparative Analysis of Flame Surface Density Metrics in Premixed and Stratified Flames, *Proceedings of the Combustion Institute*, **33**, 1, 1419–1427
- Sweeney, M. S. and Hochgreb, S. (2009) Autonomous extraction of optimal flame fronts in OH planar laser-induced fluorescence images, *Applied Optics*, **48**, 19, 3866–3877
- Barlow, R. S., Wang, G. H., Anselmo-Filho, P., Sweeney M. S., and Hochgreb, S. (2008) Application of Raman/Rayleigh/LIF diagnostics in turbulent stratified flames, *Proceedings of the Combustion Institute*, **32**

A.2 Conference Publications

- Sweeney, M. S., Hochgreb, S., Dunn, M. J., and Barlow, R. S. (2011) A New Series Of Turbulent Stratified Flames: Preliminary Findings, *Proceedings of the Meditteranean Combustion Symposium*

- Barlow, R. S., Dunn, M. J., Sweeney, M. S., and Hochgreb, S. (2010) Multiscalar Measurements on a Variable Swirl Burner Operating in Premixed and Stratified Modes, *AFRC Pacific Rim Combustion Symposium*

- Sweeney, M. S., Darbyshire, O. R., Hochgreb, S., and Barlow, R. S. (2009) Premixed and Stratified Flame Diagnostics Based on 3D Flame Orientation, 4th *European Combustion Meeting*

- Barlow, R. S., Wang, G. H., Anselmo-Filho, P., Sweeney M. S., and Hochgreb, S. (2008) Application of Multiscalar Laser Diagnostics to Turbulent Stratified Methane/Air Flames, 46th *AIAA Aerospace Sciences Meeting and Exhibit*

Appendix B

Error propagation formulas

The error formulae used to calculate the propagated error in the derived quantities (e.g. $|\nabla c|$ and χ_c) in the slot and swirl burner datasets are detailed in this appendix in the interests of transparency. The calculated propagated errors are shown in Table 4.2 of Chapter 4 for the slot and swirl burner datasets.

The precision in the equilibrium temperature conditioned on local equivalence ratio, $T\left(\phi\right)$ is given by:

$$\sigma_{T_{\mathrm{e}}} = \frac{\partial T_{\mathrm{e}}}{\partial \phi}\sigma_{\phi} \tag{B.1}$$

For the progress variable, c:

$$\sigma_c = \left[\left(\frac{\partial c}{\partial T}\sigma_T\right)^2 + \left(\frac{\partial c}{\partial \phi}\sigma_{\phi}\right)^2\right]^{\frac{1}{2}} \tag{B.2}$$

For the thermal diffusivity conditioned on local temperature and equivalence ratio, $\alpha_c\left(T,\phi\right)$:

$$\sigma_{\alpha_c} = \left[\left(\frac{\partial\alpha_c}{\partial T}\sigma_T\right)^2 + \left(\frac{\partial\alpha_c}{\partial\phi}\sigma_\phi\right)^2\right]^{\frac{1}{2}} \tag{B.3}$$

$$\tag{B.4}$$

For the gradient of c it is necessary to consider the temperature and equivalence ratio to be independent variables at the local point k, the preceding point $k-1$ and the subsequent point $k+1$:

$$\begin{aligned}\sigma_{|\nabla c|_k} &= \left[\left(\frac{\partial|\nabla c|_k}{\partial\phi_{k-1}}\sigma_{\phi_{k-1}}\right)^2 + \left(\frac{\partial|\nabla c|_k}{\partial T_{k-1}}\sigma_{T_{k-1}}\right)^2\right.\\ &+ \left(\frac{\partial|\nabla c|_k}{\partial\phi_k}\sigma_{\phi_k}\right)^2 + \left(\frac{\partial|\nabla c|_k}{\partial T_k}\sigma_{T_k}\right)^2\\ &+ \left.\left(\frac{\partial|\nabla c|_k}{\partial\phi_{k+1}}\sigma_{\phi_{k+1}}\right)^2 + \left(\frac{\partial|\nabla c|_k}{\partial T_{k+1}}\sigma_{T_{k+1}}\right)^2\right]^{\frac{1}{2}}\end{aligned} \tag{B.5}$$

Similar considerations apply to the uncertainties in thermal scalar dissipation χ_c:

$$\begin{aligned}\sigma_{\chi_c} &= \left[\left(\frac{\partial\chi_c}{\partial\phi_{k-1}}\sigma_{\phi_{k-1}}\right)^2 + \left(\frac{\partial\chi_c}{\partial T_{k-1}}\sigma_{T_{k-1}}\right)^2\right.\\ &+ \left(\frac{\partial\chi_c}{\partial\phi_k}\sigma_{\phi_k}\right)^2 + \left(\frac{\partial\chi_c}{\partial T_k}\sigma_{T_k}\right)^2\\ &+ \left.\left(\frac{\partial\chi_c}{\partial\phi_{k+1}}\sigma_{\phi_{k+1}}\right)^2 + \left(\frac{\partial\chi_c}{\partial T_{k+1}}\sigma_{T_{k+1}}\right)^2\right]^{\frac{1}{2}}\end{aligned} \tag{B.6}$$

List of References

[1] A. Mansour. Gas turbine fuel injection technology. *Proceedings ASME Turbo Expo*, 2:141–149, 2005.

[2] D. A. Nickolaus, D. S. Crocker, D. L. Black, and C. E. Smith. Development of a lean direct fuel injector for low emission aero gas turbines. *International Gas Turbine Initiative*, 2002.

[3] H. J. Bauer. New low emission strategies and combustor designs for civil aeroengine applications. *Progress in Computational Fluid Dynamics*, 4(3-5):130–142, 2004.

[4] A. C. Alkidas. Combustion advancements in gasoline engines. *Energy Conservation and Management*, 48(11):2751–2761, 2007.

[5] M. C. Drake and D. C. Haworth. Advanced gasoline engine development using optical diagnostics and numerical modeling. *Proceedings of the Combustion Institute*, 31:99–124, 2007.

[6] R. S. Cant and E. Mastorakos. *An introduction to turbulent reacting flows*. Imperial College Press, 2008.

[7] K. N. C. Bray, P. A. Libby, and J. B. Moss. Unified modelling approach for premixed turbulent combustion part 1 — general formulation. *Combustion and Flame*, 61: 143–172, 1985.

[8] S. B. Pope. The evolution of surfaces in turbulence. *International Journal of Engineering Science*, 26(5):445–469, 1988.

[9] S. M. Candel and T. J. Poinsot. Flame stretch and the balance equation for the flame area. *Combustion Science and Technology*, 70(1-3):1–15, 1990.

[10] N. Peters. The turbulent burning velocity for large-scale and small-scale turbulence. *Journal of Fluid Mechanics*, 384(1):107–132, 1999.

[11] D. Veynante and L. Vervisch. Turbulent combustion modeling. *Progress in Energy and Combustion Science*, 28(3):193–266, 2002.

[12] T. Echekki and E. Mastorakos. *Turbulent combustion modeling: Advances, new trends and perspectives.* Springer Verlag, 2010.

[13] W. Meier, P. Weigand, X. R. Duan, and R. Giezendanner-Thoben. Detailed characterization of the dynamics of thermoacoustic pulsations in a lean premixed swirl flame. *Combustion and Flame*, 150(1-2):2–26, 2007.

[14] A. X. Sengissen, J. F. Van Kampen, R. A. Huls, G. G. M. Stoffels, J. B. W. Kok, and T. J. Poinsot. LES and experimental studies of cold and reacting flow in a swirled partially premixed burner with and without fuel modulation. *Combustion and Flame*, 150(1-2):40–53, 2007.

[15] C. Duwig and C. Fureby. Large eddy simulation of unsteady lean stratified premixed combustion. *Combustion and Flame*, 151(1-2):85–103, 2007.

[16] T. Kang and D. C. Kyritsis. Methane flame propagation in compositionally stratified gases. *Combustion Science and Technology*, 177:2191–2210, 2005.

[17] S. R. Turns. *An introduction to combustion.* McGraw-Hill, 2000.

[18] R. K. Green and C. C. Zavier. Charge stratification in a spark ignition engine. *Proceedings of the IMechE, Part A: Journal of Power and Energy*, 206(11):59–64, 1992.

[19] C. Arcoumanis, M. R. Gold, J. H. Whitelaw, and H. M. Xu. Local mixture injection to extend the lean limit of spark-ignition engines. *Experiments in Fluids*, 26(1):126–135, 1999.

[20] C. Galizzi and D. Escudié. Experimental analysis of an oblique laminar flame front propagating in a stratified flow. *Combustion and Flame*, 145(3):621–634, 5 2006.

[21] B. Renou, E. Samson, and A. Boukhalfa. An experimental study of freely propagating turbulent propane/air flames in stratified inhomogeneous mixtures. *Combustion Science and Technology*, 176:1867–1890, 2004.

[22] N. Pasquier, B. Lecordier, M. Trinité, and A. Cessou. An experimental investigation of flame propagation through a turbulent stratified mixture. *Proceedings of the Combustion Institute*, 31(1):1567–1574, 2007.

[23] V. Robin, A. Mura, M. Champion, O. Degardin, B. Renou, and M. Boukhalfa. Experimental and numerical analysis of stratified turbulent v-shaped flames. *Combustion and Flame*, 153(1–2):288–315, 2008.

[24] P. Anselmo-Filho, S. Hochgreb, R. S. Barlow, and R. S. Cant. Experimental measurements of geometric properties of turbulent stratified flames. *Proceedings of the Combustion Institute*, 32(2):1763–1770, 2009.

[25] F. Seffrin, F. Fuest, D. Geyer, and A. Dreizler. Flow field studies of a new series of turbulent premixed stratified flames. *Combustion and Flame*, 157(2):384–396, 2010.

[26] B. Böhm, J. H. Frank, and A. Dreizler. Temperature and mixing field measurements in stratified lean premixed turbulent flames. *Proceedings of the Combustion Institute*, 33(1):1583–1590, 2011.

[27] M. S. Sweeney, S. Hochgreb, M. J. Dunn, and R. S. Barlow. A comparative analysis of flame surface density metrics in premixed and stratified flames. *Proceedings of the Combustion Institute*, 33(1):1419–1427, 2011.

[28] C. Galizzi and D. Escudié. Experimental analysis of an oblique turbulent flame front propagating in a stratified flow. *Combustion and Flame*, 157(12):2277–2285, 2010.

[29] P. C. Vena, B. Deschamps, G. J. Smallwood, and M. R. Johnson. Equivalence ratio gradient effects on flame front topology in a stratified iso-octane/air turbulent v-flame. *Proceedings of the Combustion Institute*, 33(1):1551–1558, 2011.

[30] A. P. da Cruz, A. M. Dean, and J. M. Grenda. A numerical study of the laminar flame speed of stratified methane/air flames. *Proceedings of the Combustion Institute*, 28(2):1925–1932, 2000.

[31] Y M Marzouk. Dynamic response of strained premixed flames to equivalence ratio gradients. *Proceedings of the Combustion Institute*, 28(2):1859–1866, 2000.

[32] E. S. Richardson, V. E. Granet, A. Eyssartier, and J. H. Chen. Effects of equivalence ratio variation on lean, stratified methane-air laminar counterflow flames. *Combustion Theory and Modeling*, 14(6):775–792, 2010.

[33] J. Hélie and A. Trouvé. Turbulent flame propagation in partially premixed combustion. *Proceedings of the Combustion Institute*, 27(1):891–898, 1998. Sysposium (International) on Combustion.

[34] T. Poinsot, D. Veynante, A. Trouve, and G. Ruetsch. Turbulent flame propagation in partially premixed flames. *Proceedings of the CTR Summer Program*, 1996.

[35] D. C. Haworth, R. J. Blint, B. Cuenot, and T. J. Poinsot. Numerical simulation of turbulent propane-air combustion with nonhomogeneous reactants. *Combustion and Flame*, 121(3):395–417, 2000.

[36] C. Jiménez, B. Cuenot, T. Poinsot, and D. C. Haworth. Numerical simulation and modeling for lean stratified propane-air flames. *Combustion and Flame*, 128(1–2):1–21, 2002.

[37] V. Robin, A. Mura, M. Champion, and P. Plion. A multi-Dirac presumed pdf model for turbulent reactive flows with variable equivalence ratio. *Combustion Science and Technology*, 178:1843–1870, 2006.

[38] K. N. C. Bray, P. Domingo, and L. Vervisch. Role of the progress variable in models for partially premixed turbulent combustion. *Combustion and Flame*, 141:431–437, 2005.

[39] Z. Tan and R. D. Reitz. An ignition and combustion model based on the level-set method for spark ignition engine multidimensional modeling. *Combustion and Flame*, 145(1-2):1–15, 2006.

[40] E. Knudsen and H. Pitsch. A general flamelet transformation useful for distinguishing between premixed and non-premixed modes of combustion. *Combustion and Flame*, 156(3):678–696, 3 2009.

[41] P. D. Nguyen, L. Vervisch, V. Subramanian, and P. Domingo. Multidimensional flamelet-generated manifolds for partially premixed combustion. *Combustion and Flame*, 157(1):43–61, 1 2010.

[42] A. C. Eckbreth. *Laser diagnostics for combustion temperature and species*. CRC, 1996.

[43] A. Buschmann, F. Dinkelacker, T. Schäfer, M. Schäfer, and J. Wolfrum. Measurement of the instantaneous detailed flame structure in turbulent premixed combustion. In *Symposium (International) on Combustion*, volume 26, pages 437–445. Elsevier, 1996.

[44] F. O'Young and R. W. Bilger. Scalar gradient and related quantities in turbulent premixed flames. *Combustion and Flame*, 109(4):682–700, 1997.

[45] Y. C. Chen and R. W. Bilger. Experimental investigation of three-dimensional flame-front structure in premixed turbulent combustion I: hydrocarbon/air bunsen flames. *Combustion and Flame*, 131(4):400–435, 2002.

[46] M. J. Dunn, A. R. Masri, and R. W. Bilger. A new piloted premixed jet burner to study strong finite-rate chemistry effects. *Combustion and Flame*, 151(1-2):46–60, 2007.

[47] R. S. Barlow, G. H. Wang, P. Anselmo-Filho, M. S. Sweeney, and S. Hochgreb. Application of Raman/Rayleigh/LIF diagnostics in turbulent stratified flames. *Proceedings of the Combustion Institute*, 32(1):945–953, 2009.

[48] M. A. Gregor, F. Seffrin, F. Fuest, D. Geyer, and A. Dreizler. Multi-scalar measure-

ments in a premixed swirl burner using 1D Raman/Rayleigh scattering. *Proceedings of the Combustion Institute*, 32(2):1739–1746, 2009.

[49] O. Degardin, B. Renou, and A. Boukhalfa. Simultaneous measurements of temperature and fuel mole fraction using acetone planar induced fluorescence and Rayleigh scattering in stratified flames. *Experiments in Fluids*, 40:452–463, 2006.

[50] A. C. Eckbreth, P. A. Bonczyk, and J. F. Verdieck. Combustion diagnostics by laser Raman and fluorescence techniques. *Progress in Energy and Combustion Science*, 5(4):253–322, 1979.

[51] A. R. Masri, R. W. Dibble, and R. S. Barlow. The structure of turbulent non-premixed flames revealed by Raman-Rayleigh-LIF measurements. *Progress in Energy and Combustion Science*, 22(4):307–362, 1996.

[52] D. Geyer, A. Kempf, A. Dreizler, and J. Janicka. Turbulent opposed-jet flames: A critical benchmark experiment for combustion LES. *Combustion and Flame*, 143 (4):524–548, 2005.

[53] T. W. Lee, G. L. North, and D. A. Santavicca. Surface properties of turbulent premixed propane/air flames at various Lewis numbers. *Combustion and Flame*, 93 (4):445–456, 1993.

[54] S. A. Filatyev, J. F. Driscoll, C. D. Carter, and J. M. Donbar. Measured properties of turbulent premixed flames for model assessment, including burning velocities, stretch rates, and surface densities. *Combustion and Flame*, 141(1-2):1–21, 2005.

[55] P. Anselmo-Filho. *Experimental investigations of turbulent stratified V-flames using laser diagnostics*. PhD thesis, University of Cambridge, Cambridge, UK, 2008.

[56] A. N. Karpetis, T. B. Settersten, R. W. Schefer, and R. S. Barlow. Laser imaging system for determination of three-dimensional scalar gradients in turbulent flames. *Optics Letters*, 29(4):355–357, 2004.

[57] A. N. Karpetis and R. S. Barlow. Measurements of flame orientation and scalar dissipation in partially premixed methane flames. *Proceedings of the Combustion Institute*, 30(1):665–672, 2005.

[58] G. H. Wang and N.T. Clemens. Effects of imaging system blur on measurements of flow scalars and scalar gradients. *Experiments in Fluids*, 37(2):194–205, 2004.

[59] A. Johnstone, M. Uddin, and A. Pollard. Calibration of hot-wire probes using non-uniform mean velocity profiles. *Experiments in Fluids*, 39(3):527–534, 2005.

[60] O. R. Darbyshire, N. Swaminathan, and S. Hochgreb. The effects of small-scale

mixing models on the prediction of turbulent premixed and stratified combustion. *Combustion Science and Technology*, 182(9):1141–1170, 2010.

[61] M. J. Dunn and R. S. Barlow. A wavelet based denoising algorithm optimized for high resolution line imaging in fluid mechanics. *Experiments in Fluids*, 2011. Paper in preparation.

[62] M. S. Sweeney and S. Hochgreb. Autonomous extraction of optimal flame fronts in OH planar laser-induced fluorescence images. *Applied Optics*, 48(19):3866–3877, 2009.

[63] M. S. Sweeney, S. Hochgreb, and R. S. Barlow. The structure of premixed and stratified low turbulence flames. *Combustion and Flame*, 158(5):935–948, 2011.

[64] Open Source. GNU Image Manipulation Program. Online, 2011. http://www.gimp.org/.

[65] M. Kass, A. Witkin, and D. Terzopoulos. Snakes: Active contour models. *International Journal of Computer Vision*, 1(4):321–331, 1988.

[66] F. J. Canny. A computational approach to edge detection. *IEEE Transactions on Pattern Analysis and Machine Intelligence*, 8(6):679–698, 1986.

[67] L. Lam, S. W. Lee, and C. Y. Suen. Thinning methodologies — a comprehensive survey. *IEEE Transactions on Pattern Analysis and Machine Intelligence*, pages 869–885, 1992.

[68] R. W. Bilger, S. H. Stårner, and R. J. Kee. On reduced mechanisms for methane/air combustion in nonpremixed flames. *Combustion and Flame*, 80(2):135–149, 1990.

[69] R. S. Cant, S. B. Pope, and K. N. C. Bray. Modelling of flamelet surface-to-volume ratio in turbulent premixed combustion. *Proceedings of the Combustion Institute*, 23(1):809–815, 1991.

[70] Sandia National Laboratories. Chemkin. Online, 2011. http://www.ca.sandia.gov/chemkin/.

[71] G. P. Smith and D. M. Golden. GRI-Mech 3.0. Online, 2010. URL `http://www.me.berkeley.edu/gri_mech/`.

[72] R. S. Barlow, M. J. Dunn, M. S. Sweeney, and S. Hochgreb. Effects of preferential transport in turbulent bluff-body-stabilized lean premixed CH_4/air flames. *Combustion and Flame*, Submitted, 2011.

[73] R. Sankaran, E. R. Hawkes, J. H. Chen, T. Lu, and C. K. Law. Structure of a spatially developing turbulent lean methane-air Bunsen flame. *Proceedings of the Combustion Institute*, 31(1):1291–1298, 2007.

[74] V. Moureau, P. Domingo, and L. Vervisch. From large-eddy simulation to direct numerical simulation of a lean premixed swirl flame: filtered laminar flame-pdf modeling. *Combustion and Flame*, 158(7):1340–1357, 2011.

[75] S. M. Martin, J. C. Kramlich, G. Kosály, and J. J. Riley. The premixed conditional moment closure method applied to idealized lean premixed gas turbine combustors. *Journal of Engineering for Gas Turbines and Power*, 125:895, 2003.

[76] A. Y. Klimenko and R. W. Bilger. Conditional moment closure for turbulent combustion. *Progress in Energy and Combustion Science*, 25(6):595–688, 1999.

[77] R. W. Bilger. The structure of diffusion flames. *Combustion Science and Technology*, 13(1):155–170, 1976.

[78] N. Peters. Laminar diffusion flamelet models in non-premixed turbulent combustion. *Progress in Energy and Combustion Science*, 10(3):319–339, 1984.

[79] R. W. Bilger. Conditional moment closure for turbulent reacting flow. *Physics of Fluids A: Fluid Dynamics*, 5:436, 1993.

[80] M. S. Sweeney, O. R. Darbyshire, S. Hochgreb, and R. S. Barlow. Premixed and stratified flame diagnostics based on 3D flame orientation. 4^{th} *European Combustion Meeting*, 2009.

[81] I. G. Shepherd. Flame surface density and burning rate in premixed turbulent flames. *Proceedings of the Combustion Institute*, 26(1):373–379, 1996.

[82] I. G. Shepherd and R. K. Cheng. The burning rate of premixed flames in moderate and intense turbulence. *Combustion and Flame*, 127(3):2066–2075, 2001.

[83] J. Kiefer, Z. S. Li, J. Zetterberg, X. S. Bai, and M. Aldén. Investigation of local flame structures and statistics in partially premixed turbulent jet flames using simultaneous single-shot CH and OH planar laser-induced fluorescence imaging. *Combustion and Flame*, 154(4):802–818, 2008.

[84] C. Cohé, F. Halter, C. Chauveau, I. Gokalp, and O. L. Gulder. Fractal characterization of high-pressure and hydrogen-enriched CH_4-air turbulent premixed flames. *Proceedings of the Combustion Institute*, 31(1):1345–1352, 2007.

[85] D. Veynante, J. M. Duclos, and J. Piana. Experimental analysis of flamelet models for premixed turbulent combustion. *Proceedings of the Combustion Institute*, 25(1): 1249–1256, 1994.

[86] Y. Dong, C. M. Vagelopoulos, G. R. Spedding, and F. N. Egolfopoulos. Measurement of laminar flame speeds through digital particle image velocimetry: Mixtures

of methane and ethane with hydrogen, oxygen, nitrogen, and helium. *Proceedings of the Combustion Institute*, 29(2):1419–1426, 2002.

[87] A. Bonaldo and J. B. Kelman. Experimental annular stratified flames characterisation stabilised by weak swirl. *Combustion and Flame*, 156(4):750–762, 2009.

[88] M. S. Sweeney, S. Hochgreb, and R. S. Barlow. Cambridge stratified slot burner dataset. Online, 2010. URL `http://www.dspace.cam.ac.uk/handle/1810/226470`.

[89] M. Kaneda, B. Yu, H. Ozoe, and S. W. Churchill. The characteristics of turbulent flow and convection in concentric circular annuli part I: Flow. *International Journal of Heat and Mass Transfer*, 46(26):5045–5057, 2003.

[90] Y. Shoshin, L. Tecce, and J. Jarosinski. Experimental and computational study of lean limit methane-air flame propagating upward in a 24 mm diameter tube. *Combustion Science and Technology*, 10(11):1812–1828, 2008.

[91] Y. Shoshin, G. Gorecki, J. Jarosinski, and T. Fodemski. Experimental study of limit lean methane/air flame in a standard flammability tube using particle image velocimetry method. *Combustion and Flame*, 157(5):884–892, 2010.

[92] A. Levy. An optical study of flammability limits. *Proceedings of the Royal Society of London. Series A. Mathematical and Physical Sciences*, 283(1392):134, 1965.

[93] E. von Lavante and R. A. Strehlow. The mechanism of lean limit flame extinction. *Combustion and Flame*, 49(1–3):123–140, 1983.

[94] J. Gottgens, F. Mauss, and N. Peters. Analytic approximations of burning velocities and flame thicknesses of lean hydrogen, methane, ethylene, ethane, acetylene, and propane flames. *Symposium (International) on Combustion*, 24(1):129–135, 1992.

[95] D. Thévenin. Three-dimensional direct simulations and structure of expanding turbulent methane flames. *Proceedings of the Combustion Institute*, 30:629–637, 2005.

[96] I. G. Shepherd and W. T. Ashurst. Flame front geometry in premixed turbulent flames. *Proceedings of the Combustion Institute*, 24(1):485–491, 1992.

[97] F. C. Gouldin and P. C. Miles. Chemical closure and burning rates in premixed turbulent flames,. *Combustion and Flame*, 100(1–2):202–210, 1995.

List of Figures

List of Tables

Author Index

Colophon

This thesis is typeset in Computer Modern[a] using LaTeX 2_ε with the hepthesis[b] class with modifications made by the author. American English is used throughout. Figures are generated using Matlab[c], GNU Image Manipulation Program[d], Pro/ENGINEER[e], and Xfig[f].

---

[a] http://www.tug.dk/FontCatalogue/cmr/

[b] http://www.ctan.org/tex-archive/help/Catalogue/entries/hepthesis.html

[c] http://www.matlab.com/

[d] http://www.gimp.org

[e] http://www.ptc.com/products/creo-elements-pro/

[f] http://www.xfig.org/